

Electronic Thesis and Dissertation Repository

3-6-2013 12:00 AM

Carbon Nitride and Conjugated Polymer Composite Materials

Josh Byers

The University of Western Ontario

Supervisor

Oleg Semenikhin


The University of Western Ontario

Graduate Program in Chemistry

A thesis submitted in partial fulfillment of the requirements for the degree in Doctor of Philosophy

© Josh Byers 2013

Follow this and additional works at: <https://ir.lib.uwo.ca/etd>

 Part of the [Condensed Matter Physics Commons](#), [Materials Chemistry Commons](#), [Physical Chemistry Commons](#), [Polymer and Organic Materials Commons](#), [Polymer Chemistry Commons](#), and the [Semiconductor and Optical Materials Commons](#)

Recommended Citation

Byers, Josh, "Carbon Nitride and Conjugated Polymer Composite Materials" (2013). *Electronic Thesis and Dissertation Repository*. 1135.

<https://ir.lib.uwo.ca/etd/1135>

This Dissertation/Thesis is brought to you for free and open access by Scholarship@Western. It has been accepted for inclusion in Electronic Thesis and Dissertation Repository by an authorized administrator of Scholarship@Western. For more information, please contact wlsadmin@uwo.ca.

CARBON NITRIDE AND CONJUGATED POLYMER COMPOSITE MATERIALS

(Spine title: Carbon Nitride and Conjugated Polymer Composite Materials)

(Thesis format: Integrated Article)

by

Joshua Byers

Graduate Program in Chemistry

A thesis submitted in partial fulfillment
of the requirements for the degree of
Doctor of Philosophy

The School of Graduate and Postdoctoral Studies
The University of Western Ontario
London, Ontario, Canada

© Joshua Byers 2013

Abstract

The semiconductor and photovoltaic properties of carbon nitride (CN_x) thin films prepared using a reactive magnetron sputtering technique were investigated both individually and as composites with the organic conjugated polymers polybithiophene (PBT) and poly(3-hexylthiophene) (P3HT). At low nitrogen content, the film structure was dominated by graphitic sp² percolation networks, whereas at higher nitrogen contents CN_x films started to demonstrate semiconductor properties, as evidenced by the occurrence of photoconductivity and the development of a space charge region. When CN_x was deposited onto a PBT substrate, it was found to function as an acceptor material improving the photocurrent generation both in solution and in solid state photovoltaic devices, with the external quantum efficiencies reaching 1% at high nitrogen contents. The occurrence of the donor–acceptor charge transfer was further evidenced by suppression of the n-doping of the PBT polymer by CN_x. Nanoscale atomic force microscopy (AFM) and current-sensing AFM data suggested that CN_x may form a bulk heterojunction with PBT. Thermal annealing of nitrogen rich CN_x films led to n-type semiconductor materials consisting of a graphitic carbon nitride network as determined using X-ray photoelectron spectroscopy, and these materials exhibited photovoltaic properties.

Intensity modulated photocurrent (IMPS) and photovoltage (IMVS) spectroscopies were used to study the mechanism of photoprocesses in P3HT:PCBM ([6,6]-phenyl C₆₁ butyric acid methyl ester) bulk heterojunction organic solar cells at various light intensities. The use of the frequency domain techniques allowed us to separate the bulk and interfacial processes and gain valuable insight into the mechanism of losses in these devices. The results provide direct evidence that interfacial nongeminate recombination is one of the dominant loss and aging mechanisms in bulk heterojunction organic solar cells. The trapping of photoexcited holes in the P3HT phase was found to contribute to the increased recombination rate. It was determined that interfacial recombination occurs at the P3HT/PCBM interface and that higher PCBM contents help to improve charge carrier extraction. The results suggest that promising ways of improving the efficiency of bulk heterojunction solar cells may be reducing the charge trapping both at and near the P3HT:PCBM interface, as well as improving the efficiency of charge extraction at the contacts.

Keywords

Carbon nitride, solar, photovoltaic, conjugated polymer, intensity modulated photocurrent spectroscopy, electrochemical impedance spectroscopy, semiconductor, bulk heterojunction

Co-Authorship Statement

All of the experimental work was carried out by Joshua Byers under the direction and supervision of Dr. Oleg Semenikhin except where noted below. All of the chapters in this thesis were originally written, edited, and revised by Joshua Byers under the supervision of Dr. Oleg Semenikhin who was actively involved in all steps through the entire process.

Chapter 3. A. Pailleret assisted with editing and revising the manuscript. F. Billon deposited CNx substrates for XPS collection and analysis by C. Debiemme-Chouvy for the data shown in the supporting information for Chapter 3 in the appendix. S. Borensztajn carried out SEM of CNx films for thickness determination shown in the supporting information for Chapter 3 in the appendix.

Chapter 4. M. Biesinger carried out XPS experiments and peak fitting.

Chapter 5. S. Ballantyne prepared bulk heterojunction photovoltaic devices and characterized them using an AM 1.5 Solar Simulator.

Chapter 6. T. Heiser prepared bulk heterojunction photovoltaic devices and characterized them using an AM 1.5 Solar Simulator.

Acknowledgments

First and foremost I must sincerely thank my supervisor Dr. Oleg Semenikhin for providing an excellent research environment along with tremendous opportunity to explore several related areas of research to the work presented. I have learned a tremendous amount under your mentorship and guidance over the years and greatly enjoyed your enthusiasm for science. I would also like to thank all of the members of the Semenikhin group (Trissa, Kevin, Radu, Adam, John, Mike) over the years for making the lab/office more than just an enjoyable place to be each day.

This work represents the effort of several collaborative projects and I would like to thank all of those involved. Dr. Alain Pailleret is gratefully acknowledged for his host supervision during several extended visits to his laboratory at the University of Pierre and Marie Curie where I was able to benefit from his experience and knowledge in the fabrication of carbon nitride thin films. As well, I must thank Alex Mann and Konstantin Rodionov who I had the pleasure of working with and for providing a glimpse into the exciting world of a start-up company.

Finally, I must thank my family and in particular my wife Danielle who has been an unwavering source of support over this entire journey. I dedicate this work to you.

Funding provided from the Department of Chemistry, The University of Western Ontario, the Ontario Graduate Scholarship program and the France Government are gratefully acknowledged.

Table of Contents

Abstract.....	ii
Acknowledgments	v
List of Tables.....	ix
List of Figures	x
List of Appendices.....	xvii
List of Abbreviations	xviii
Chapter 1.....	1
1 Introduction	1
1.1 Motivation for this work	2
1.2 Scope of thesis	4
1.3 References	6
Chapter 2.....	7
2 Background.....	7
2.1 Organic Photovoltaics	8
2.2 Bulk Heterojunction Polymer Solar Cells	11
2.3 Loss Mechanisms.....	15
2.4 Methods of Improvement	17
2.5 Carbon Thin Film Materials	19
2.6 Carbon Nitride	20
2.7 Methods to Study Photovoltaic Devices	24
2.7.1 Steady-State Current-Voltage Measurements.....	24
2.8 Frequency Domain Techniques	27
2.8.1 Electrochemical Impedance Spectroscopy	27
2.8.2 Mott-Schottky Plots.....	31

2.8.3 Intensity Modulated Photocurrent Spectroscopy	32
2.9 References	39
Chapter 3.....	43
3 Photocurrent Generation in Carbon Nitride and Carbon Nitride/Conjugated Polymer Composites	43
3.1. Introduction.....	44
3.2. Experimental.....	46
3.3 Results and Discussion.....	49
3.4 Conclusions.....	65
3.5 References	66
Chapter 4.....	71
4 Nitrogen Rich Carbon Nitride Photovoltaic Materials	71
4.1 Introduction	72
4.2 Experimental.....	75
4.3 Results and Discussion.....	77
4.4 Conclusions	104
4.5 References	105
Chapter 5.....	109
5 The Mechanism of Recombination Losses in Bulk Heterojunction P3HT:PCBM Solar Cells Studied Using Intensity Modulated Photocurrent Spectroscopy	109
5.1 Introduction	110
5.2 Experimental.....	113
5.3 Results and Discussion.....	117
5.4 Conclusions	136
5.5 References	138
Chapter 6.....	141

6	Influence of Preparation Conditions of Bulk Heterojunction Solar Cells Studied using Intensity Modulated Photocurrent Spectroscopy	141
6.1	Introduction	142
6.2	Experimental.....	144
6.3	Results	145
6.4	Discussion.....	159
6.5	References	170
Chapter 7	172
7	Conclusions	172
7.1	Conclusions	173
7.2	Future Work.....	175
Curriculum Vitae	186

List of Tables

Table 4-1. CN _x film composition determined for XPS survey spectra.....	97
Table 4-2. Binding energies and peak areas for peaks used to fit N 1s spectra.....	100
Table 4-3. Binding energies and peak areas for peaks used to fit C 1s spectra.....	100
Table 6-1. Device efficiencies for bulk heterojunction devices measured shortly after fabrication.....	147
Table 6-2. Device efficiencies for bulk heterojunction devices measured aging.....	149
Table 6-3. Values for the low frequency ReJ_0 , high frequency g_{ac} , and $(I - \gamma)$ determined from the IMPS plots.....	156
Table 6-4. Values for the rate constant for charge transfer k_{tr} from the surface states to the Al electrode along with a rate constant for interfacial recombination k_{rec}	167

List of Figures

Figure 2-1. Bi-layer architecture. (a) Two materials with different ionization potentials/electron affinities. (b) Light absorption and exciton formation (c) Charge transfer and exciton dissociation.	10
Figure 2-2. (A) Left: Absorption of light by donor material. Right: Solid state photovoltaic device. (B) Right: Exciton splitting at donor acceptor interface. Left: Exciton diffusion in donor material to acceptor interface. Dark area is acceptor material. Light area is donor material. (C) Right: Electron is transported to cathode through the LUMO and hole is transported to anode through the HOMO. Left: Electron transport through acceptor material to cathode and hole transport through donor material to anode.	13
Figure. 2-3. Chemical structures of (A) poly(3-hexylthiophene), (B) poly(3,4-ethylenedioxythiophene) and (C) phenyl-C ₆₁ -butyric acid methyl ester.	14
Figure 2-4. Bulk heterojunction active layer showing donor (white) and acceptor (grey) interface. Illustration of (i) exciton decay, (ii) charge transfer state formation and (iii) exciton dissociation in an organic bulk heterojunction device. Adapted from Ref. 21.	16
Figure 2-5. Different possible bonding arrangements in nitrogen doped t:aC and carbon nitride. Only bonding arrangements (B), (D), and (G) in the centre column represent the possible doping configurations.	22
Figure 2-6. Illustration of the magnetron sputtering process.	24
Figure 2-7. Illustration of a JV curve obtained under illumination showing the open circuit voltage V_{oc} , the short-circuit current I_{sc} , the point along the curve where the maximum power is generated P_{max} . The dotted square represents the area covered within the fill factor FF . ..	25
Figure 2-8. Example of a (A) Nyquist plot and corresponding Bode plots of (B) the impedance magnitude $ Z $ and phase angle ϕ . The values for the elements used to generate this plot were $R_s = 100$, $R_p = 1 \times 10^6$ and $C_p = 5 \times 10^{-9}$..	29

Figure 2-9. Randles equivalent circuit that consists of a resistance R_s in series with a parallel capacitance C_p and resistance R_p . This type of equivalent circuit is often used to represent an organic solar cell and can be used to fit the data shown in Figure 2-8.....	30
Figure 2-10. Photocurrent transients on the left and their complex plot representation on the right. (A) Left: Light is switched on and immediately reaches steady state. Right: Corresponding IMPS plot is located on real axis with no phase shift. (B) Left: Photocurrent spikes when light is switched on and then decays. Right: IMPS plot is located in the first quadrant in this case (C) Left: Photocurrent lags light intensity and slowly rises with time. Right: The IMPS plot is located in the fourth quadrant in this case.....	35
Figure 2-11. A typical IMPS spectrum shown in Nyquist plot representation. The IMPS curve begins at the origin at a high frequency and moves across the fourth quadrant until it crosses over at the real axis into the first quadrant and eventually reaches the steady-state value ReJ_0	36
Figure 2-12. Schematic illustrating (i) charge carrier collection at the electrodes, and (ii) charge carrier trapping at an interfacial state leading to (iia) extraction or (iib) interfacial recombination. Adapted from Ref. 59.	37
Figure 3-1. Conductivity of CN _x films as a function of N ₂ content in the gas mixture for films prepared with a deposition power of 25 W (plot 1), 50 W (plot 2), 100 W (plot 3) during deposition. The deposition time for all films was 20 minutes. The lines are guides for the eye.	50
Figure 3-2. Dark conductivity (plot 1) and photoconductivity (plot 2) for ITO/CN _x /Au. CN _x was prepared at 100 W and 50 % N ₂	52
Figure 3-3. (A) Mott-Schottky plot for CN _x on an ITO substrate in aqueous 0.1 M KCl. CN _x was prepared at 50 W and 25 % N ₂ . (B) Donor density determined from slopes of Mott-Schottky plots for CN _x films as a function of nitrogen content for deposition powers of 25 W (■), 50 W (●) and 100 W (▲).....	55
Figure 3-4. Energy level diagram of a CN _x /PBT interface illustrating the proposed photoinduced electron transfer from PBT to CN _x	58

Figure 3-5. Net photocurrent generation of PBT/CN _x composites on ITO substrates in aqueous 0.1 M KCl. CN _x films were prepared at 25 W and nitrogen contents of 5 % (plot 1), 25 % (plot 2), and 50 % (plot 3). Photocurrent generation of a pristine PBT film is included for comparison (plot 4).	59
Figure 3-6. Current-Voltage plot of a solid state ITO/PEDOT/PBT/CN _x /Al (plot 1) and a ITO/PEDOT/PBT/Al (plot 2) photovoltaic device. CN _x film was prepared at 25 W and 10 % N ₂	60
Figure 3-7. Quantum efficiency of PBT/CN _x composites on ITO substrates in aqueous 0.1 M KCl. CN _x films were prepared at 25 W and nitrogen contents of 5 % (plot 1), 25 % (plot 2), and 50 % (plot 3). A pristine PBT film is included for comparison (plot 4). Scan rate: 100 mV s ⁻¹	61
Figure 3-8. 500 nm by 500 nm topography (left) and CS-AFM current (right) images of a CN _x film on PBT. A bias of + 500 mV was applied to the tip. Height scale bar: 200 nm. CS-AFM current scale bar: 50 pA.	63
Figure 3-9. Cyclic voltammograms of (1) ITO/PBT and (2) ITO/PBT/CN _x in acetonitrile and 0.1 M TBAPF ₆	64
Figure 4-1. Dark J-V plots of CN _x films prepared at (A) 25 W, (B) 50 W, (C) 100 W and (D) 150 W for nitrogen plasma compositions indicated.	79
Figure 4-2. Dark J-V plots of CN _x films prepared using a deposition power of 25 W and nitrogen contents of (A) 1 % N ₂ , (B) 50 % N ₂ , (C) 100 % N ₂	81
Figure 4-3. (A) Nyquist plot and (B) Bode plot of CN _x films prepared at 25 W and nitrogen content of 1 % N ₂ , 5 % N ₂ and 100 % N ₂ (1 Pa total pressure). (C) Equivalent circuit element used to fit the data. Applied potential was 0 V in dark.	82
Figure 4-4. Illuminated (1) and dark (2) J-V plots of a CN _x film prepared using a deposition power of 25 W in a 100% (1 Pa total pressure) nitrogen discharge plasma.	84

Figure 4-5. Dark J-V plots of a CNx film prepared using a deposition power of 25 W in a 100 % nitrogen discharge plasma for a (1) fresh film and an (2) aged film (1 Pa total pressure). Note the current density of the aged film has been multiplied by a factor of 10^3	85
Figure 4-6. Nyquist plot of an aged CNx film prepared using a deposition power of 25 W in a 100 % nitrogen discharge plasma.....	86
Figure 4-7. Dark (1) and illuminated (2) J-V plots of a CNx film prepared using a deposition power of 25 W in a 100 % nitrogen containing plasma at 1 Pa after aging.....	87
Figure 4-8. (A) Photocurrent and (B) photovoltage transients for photoconductive (plot 1 - fresh) and photovoltaic (plot 2 - aged) CNx films prepared in 100 % N ₂ plasma at 1 Pa.....	88
Figure 4-9. Dark current-voltage plots of CNx prepared at 1 Pa (plot 1), 3 Pa (plot 2) and 5 Pa (plot 3) pure nitrogen plasma discharge pressures. Current density values for films prepared at 3 Pa and 5 Pa have been multiplied by a factor of 25 and 500 respectively to more clearly display on the same plot.	90
Figure 4-10 Values for the (A) parallel capacitance and (B) parallel resistance as a function of annealing temperature determined using a Randles equivalent circuit for CNx films prepared at 1 Pa, 3 Pa, and 5 Pa pure nitrogen plasma discharge pressures. All films were annealed for 60 minutes. (C) Figure 4-10A re-plotted as a function of total plasma pressure.	92
Figure 4-11. Typical J-V plot under illumination for CNx films prepared at 3 Pa (plot 1) and 5 Pa (plot 2) pure nitrogen plasma discharge pressures. The films were annealed for 60 minutes at 150°C.	94
Figure 4-12. Photocurrent transient for a CNx film at an applied bias of – 70 mV. The film was prepared in a 5 Pa pure nitrogen discharge plasma and annealed for 60 minutes at 150°C.	96
Figure 4-13. (A) C 1s XPS spectrum for an as deposited CNx film prepared in a 5 Pa discharge plasma. (B) N 1s XPS spectrum for an as deposited CNx film prepared in a 5 Pa discharge plasma.	99

Figure 4-14. (A) C 1s XPS spectrum for an annealed CNx film prepared in a 5 Pa discharge plasma. Films were annealed for 60 minutes at 150°C. (B) N XPS 1s spectrum for an annealed CNx film prepared in a 5 Pa discharge plasma. Films were annealed for 60 minutes at 150°C.....102

Figure 4-15. Photocurrent transients for a CNx single layer device (plot 1), P3HT single layer device (plot 2) and a CNx-P3HT heterojunction device (plot 3) measured at short-circuit conditions. All films were annealed at 150°C for 60 minutes.104

Figure 5-1. Experimental I-V curves for two P3HT:PCBM cells after fabrication (plot 1, cell B; plot 2, cell A) prepared on the same photovoltaic slide.118

Figure 5-2. (A) Experimental IMPS spectra obtained at short-circuit conditions for two P3HT:PCBM photovoltaic cells (plot 1, cell A; plot 2, cell B) prepared on the same photovoltaic slide. (D) Comparison of experimental IMPS spectra for cell A (1) after fabrication and (2) after ageing for 2 months. The arrows indicate the direction of increasing frequency. IMPS spectra are presented as Bode plots of (B,E) the imaginary and (C,F) the real components of the photocurrent response vs. the modulation frequency. The *dc* light intensity for all spectra was $8.2 \times 10^{15} \text{ s}^{-1} \text{ cm}^{-2}$122

Figure 5-3. The intensity dependence of IMPS spectra measured at short-circuit conditions for photovoltaic cell A. The *dc* light intensities were (1) $8.2 \times 10^{15} \text{ s}^{-1} \text{ cm}^{-2}$; (2) $2.2 \times 10^{16} \text{ s}^{-1} \text{ cm}^{-2}$; (3) $3.5 \times 10^{16} \text{ s}^{-1} \text{ cm}^{-2}$; (4) $5.0 \times 10^{16} \text{ s}^{-1} \text{ cm}^{-2}$ and (5) $6.4 \times 10^{16} \text{ s}^{-1} \text{ cm}^{-2}$. The IMPS spectra are presented as (A) a Nyquist complex plane plot as well as Bode plots of (B) the imaginary and (C) the real components of the photocurrent response vs. the modulation frequency. The arrow indicates the direction of increasing frequency.....126

Figure 5-4. The intensity dependence of IMVS spectra measured at open-circuit conditions for photovoltaic cell A. The *dc* light intensities were (1) $8.2 \times 10^{15} \text{ s}^{-1} \text{ cm}^{-2}$; (2) $2.2 \times 10^{16} \text{ s}^{-1} \text{ cm}^{-2}$; (3) $3.5 \times 10^{16} \text{ s}^{-1} \text{ cm}^{-2}$; (4) $5.0 \times 10^{16} \text{ s}^{-1} \text{ cm}^{-2}$ and (5) $6.4 \times 10^{16} \text{ s}^{-1} \text{ cm}^{-2}$. The IMVS spectra are presented as (A) a Nyquist complex plane plot as well as Bode plots of (B) the imaginary and (C) the real components of the photovoltage response vs. the modulation frequency. (D) Comparison of the frequency dependencies of the imaginary components of (1) IMVS

photovoltage and (2) IMPS photocurrent response at a *dc* light intensity of $8.2 \times 10^{15} \text{ s}^{-1} \text{ cm}^{-2}$.
.....128

Figure 5-5. (A) Experimental IMPS spectra obtained at cell biases of 0.0 V (plot 1), +0.25 V (plot 2), +0.5 V (plot 3) as well as Bode plots of (B) the imaginary and (C) the real components of the photocurrent response obtained at these bias values vs. the modulation frequency.....130

Figure 5-6. Mott-Schottky plots for photovoltaic cell A measured in the dark (plot 1) and as a function of the *dc* light intensity (plots 2-6). The light intensity values were (2) $8.2 \times 10^{15} \text{ s}^{-1} \text{ cm}^{-2}$; (3) $2.2 \times 10^{16} \text{ s}^{-1} \text{ cm}^{-2}$; (4) $3.5 \times 10^{16} \text{ s}^{-1} \text{ cm}^{-2}$; (5) $5.0 \times 10^{16} \text{ s}^{-1} \text{ cm}^{-2}$ and (6) $6.4 \times 10^{16} \text{ s}^{-1} \text{ cm}^{-2}$. The inset shows an enlarged Mott-Schottky plot at a *dc* light intensity of $5.0 \times 10^{16} \text{ s}^{-1} \text{ cm}^{-2}$. 132

Figure 5-7. Dependencies on the *dc* light intensity of (A) interfacial recombination rate constant derived from the IMPS plots and (B) trap density obtained from the Mott-Schottky plots for photovoltaic cell A. For each graph, plot 1 corresponds to the photovoltaic cell after ageing for 2 months and plot 2 corresponds to a photovoltaic cell after fabrication.134

Figure 6-1. J-V plots of encapsulated bulk heterojunction devices containing a P3HT:PCBM mass ratio of (A) 1:0.5, (B) 1:0.6, (C) 1:0.7, and (D) 1:0.8.....146

Figure 6-2. J-V plots of non-encapsulated bulk heterojunction devices containing a P3HT:PCBM mass ratio of (A) 1:0.5, (B) 1:0.6, (C) 1:0.7, and (D) 1:0.8.147

Figure 6-3. J-V plots of aged non-encapsulated bulk heterojunction devices containing a P3HT:PCBM mass ratio of (A) 1:0.5, (B) 1:0.6, (C) 1:0.7, and (D) 1:0.8.149

Figure 6-4. Experimental IMPS spectra obtained at short-circuit conditions for a P3HT:PCBM ratio of 1:0.7 in (A) Nyquist and (B,C) Bode plot representation. The *dc* light intensity used was (1) 3.07×10^{16} , (2) 1.62×10^{17} , and (3) $2.95 \times 10^{17} \text{ s}^{-1} \text{ cm}^{-2}$ 151

Figure 6-5. The value of the rate constant for recombination ω^* for P3HT:PCBM mass ratios of 1:0.5, 1:0.6, 1:0.7 and 1:0.8 as a function of the *dc* light intensity. The line is not a fit and is a guide for the eyes.....152

Figure 6-6. Experimental IMPS spectra obtained at short-circuit conditions for P3HT:PCBM ratios of (1) 1:0.5, (2) 1:0.6, (3) 1:0.7, and (4) 1:0.8 in (A) Nyquist and (B,C) Bode plot representation. The dc light intensity for all spectra was $1.62 \times 10^{-17} \text{ s}^{-1} \text{ cm}^{-2}$154

Figure 6-7. Normalized IMPS spectra (from Figure 6-6 (A)) obtained at short-circuit conditions for P3HT:PCBM ratios of (1) 1:0.5, (2) 1:0.6, (3) 1:0.7, and (4) 1:0.8 in Nyquist plot representation. The dc light intensity for all spectra was $1.62 \times 10^{-17} \text{ s}^{-1} \text{ cm}^{-2}$. The high frequency intercept g_{ac} , low frequency intercept $I-\gamma$ and the maximum of the imaginary photocurrent ω^* are indicated155

Figure 6-8. Experimental IMPS spectra of aged films obtained at short-circuit conditions for P3HT:PCBM ratios of (1) 1:0.5, (2) 1:0.6, (3) 1:0.7, and (4) 1:0.8 in (A) Nyquist and (B,C) Bode plot representation. The dc light intensity for all spectra was $1.62 \times 10^{-17} \text{ s}^{-1} \text{ cm}^{-2}$157

Figure 6-9. Normalized IMPS spectra of aged films obtained at short-circuit conditions for P3HT:PCBM ratios of (1) 1:0.5, (2) 1:0.6, (3) 1:0.7, and (4) 1:0.8 in (A) Nyquist and (B,C) Bode plot representation. The dc light intensity for all spectra was $1.62 \times 10^{-17} \text{ s}^{-1} \text{ cm}^{-2}$159

Figure 6-10. (A) Short-circuit current density and (B) open-circuit voltage as a function of PCBM content for (1) fresh cells and (2) aged cells. A light intensity of $1.62 \times 10^{-17} \text{ s}^{-1} \text{ cm}^{-2}$ was used.160

Figure 6-11. Schematic showing the possible interfaces where interfacial recombination may occur in a bulk heterojunction P3HT:PCBM device.162

Figure 6-12. (A) Values for the (1) high frequency intercept g_{ac} and the (2) low frequency intercept ReJ_0 for aged cells as a function of PCBM content in the film. (B) Fraction of charge carriers collected as a function of PCBM content for (1) fresh cells and (2) aged cells. A light intensity of $1.62 \times 10^{-17} \text{ s}^{-1} \text{ cm}^{-2}$ was used.164

List of Appendices

Appendix A: Supporting Information for Chapter 3: Photocurrent Generation in Carbon Nitride and Carbon Nitride Conjugated/Polymer Composites	177
Appendix B: Copyright Release from Publisher for Chapter 3	184
Appendix C: Copyright Release from Publisher for Chapter 5	185

List of Abbreviations

Abbreviation	Definition
A	electrode surface area
AFM	atomic force microscopy
AM	air mass
BDD	boron doped diamond
BE	binding energy
BT	2,2-Bithiophene
Bu ₄ NPF ₆	tetrabutylammonium hexafluorophosphate
CB	conduction band
CELIV	charge extraction by linearly increasing voltage
cm	centimetre
CN _x	carbon nitride
C	capacitance
C _p	parallel capacitance
CS-AFM	current-sensing atomic force microscopy
C _{sc}	space-charge capacitance
CV	cyclic voltammetry
DC	direct current
DLC	Diamond like carbon
e _o	elementary charge
e ⁻	electron
E _f	Fermi level
E _{fb}	flat-band potential
E _g	band-gap
EIS	electrochemical impedance spectroscopy
ε	dielectric constant
ε _o	permittivity of free space
eV	electron volt
g _{ac}	high frequency photocurrent
f	frequency

fs	femtosecond
FF	fill factor
h^+	hole
HOMO	highest occupied molecular orbital
Hz	hertz
I_{\max}	photocurrent at maximum power
IMPS	intensity modulated photocurrent spectroscopy
IMVS	intensity modulated photovoltage spectroscopy
I_{SC}	short-circuit current density
ITO	indium tin oxide
j	imaginary part
J	current density
κ	Boltzmann constant
kHz	kilohertz
LUMO	lowest unoccupied molecular orbital
M	molar
m	metre
μA	microampere
ml	millilitre
mm	millimetre
mV	millivolt
mW	milliwatt
η_e	efficiency
N	newton
N_A	acceptor density
N_D	donor density
nm	nanometre
ω	circular frequency
Ω	ohm
OPV	organic photovoltaic
P3HT	poly(3-hexylthiophene)
Pa	pascal

PBT	polybithiophene
PCBM	[6,6]-phenyl C ₆₁ butyric acid methyl ester
PEDOT:PSS	poly(3,4-ethylenedioxythiophene):polystyrene sulfonate
Φ	phase shift
P_{in}	power in
P_{Max}	maximum power point
π	pi bonding orbital
π^*	pi antibonding orbital
ps	picosecond
σ	sigma bonding orbital
σ^*	sigma antibonding orbital
ReJ_0	low frequency photocurrent
RF	radiofrequency
R_p	parallel resistance
R_s	serial resistance
s	second
SCCM	standard cubic centimeters per minute
SCE	saturated calomel electrode
SEM	scanning electron microscope
t:aC	tetrahedral amorphous carbon
T	absolute temperature
TOF	time of flight
V	volt
V_{max}	voltage at maximum power
V_{OC}	open-circuit voltage
VB	valence band
W	watt
XPS	X-ray photoelectron spectroscopy
Z	impedance

Chapter 1

1 Introduction

1.1 Motivation for this work

As the demand for energy continues to grow it is evident that new sources will be needed in the future to continue to satisfy the world's energy needs. Furthermore, it is becoming increasingly clear that anthropogenic green house gases are having a detrimental impact on our climate, which makes the development of sustainable energy sources an important global goal. It has been suggested, that by 2050, the world energy demand could reach 60 terawatts, which is the equivalent of 900 million barrels of oil per day. The anticipated need for this overwhelmingly large amount of energy has been referred to as "The Terawatt Challenge".¹ This type of demand will undoubtedly only be met through a combination of traditional energy sources such as oil, hydroelectric, coal, gas, and fission, along with renewables such as wind, solar and geothermal energy playing an increasingly prevalent role. Ultimately, economics will to a large extent determine the most likely energy sources that are used in the future and therefore the development of renewable energy sources using low cost and high-throughput methods represent a promising path towards this goal.

Photovoltaic devices represent a vital part of a sustainable future and are based on the separation of charge at the interface of two materials as a result of light absorption in one or both materials. Commercially available solar cells, often referred to as generation one and generation two devices, use solid state architectures made from inorganic materials. The main drawbacks of these technologies include high processing costs, the use of toxic materials in some cases and an inability to generate a large and significant source of energy due to manufacturing limitations.^{2,3} However, third generation devices, which take advantage of nanostructured films and organic materials are being intensely investigated for potential low cost, high throughput solar energy generation for large scale exploitation.⁴ The realization of efficient and practical photovoltaic systems for energy conversion requires the continued development and understanding of new materials that can be used on a large scale, while remaining economically viable. Photovoltaic devices based on conjugated polymers continue to generate significant interest due to their potential application as a low cost material combined with high throughput manufacturing for solar energy production. Single layer device efficiency is

approaching 10 %, which is considered the minimum efficiency needed for commercialization.^{5,6} This extremely encouraging result highlights the significant potential of organic solar cells. However, the lifetimes of these devices are still very low and remain a significant barrier toward their large scale production. The understanding and knowledge of the loss mechanisms in these devices is much more limited and represents an important area of research where new methods and techniques are needed to study these nanostructured devices.

The generation of free charge carriers in organic photovoltaic devices is quite different from that of many other traditional solar cells such as silicon due to the increased exciton binding energy in organic materials. Organic photovoltaic devices typically consist of a conjugated polymer mixed with a fullerene derivative to maximize charge carrier generation by solar radiation. The most efficient polymer solar cells combine these two materials with a nanoscale phase separation on the order of 10's of nm's to form a composite photoactive layer. The photoactive layer is sandwiched between two selective contacts for electron and hole extraction resulting in the formation of a bulk heterojunction organic solar cell. To improve charge carrier extraction, interfacial materials between the anode and/or cathode are often employed. The introduction of these layers increases the number of thin film materials and interfaces in these devices that photogenerated charge carriers must be efficiently transported to and across. It is very important to understand the dynamics of charge transport across these interfaces to develop more effective interfacial materials that will continue to improve the efficiency of organic solar cells. A powerful technique that had not been applied to the investigation of bulk heterojunction polymer photovoltaic devices at the commencement of this thesis was intensity modulated photocurrent spectroscopy (IMPS). Intensity modulated photocurrent spectroscopy is a technique where the complex ratio of photocurrent flux to incident light flux is measured over many decades of frequency using a frequency response analyzer. Analysis of these spectra provides insight into the parameters that control charge transport and recombination at the interfaces in bulk heterojunction organic solar cells.

The vast majority of organic photovoltaic devices employ a fullerene derivative as an acceptor material in combination with a donor conjugated polymer. However, in polymeric photovoltaic devices, the majority of light absorption is due to the p-type donor polymer and not fullerenes. One of the advantages of using conjugated organic polymers is a high absorption coefficient that can be tuned to match the solar spectrum. Due to the large volume of fullerenes in these devices, the amount of light absorbing polymer is greatly reduced in the active layer, which ultimately limits the amount of light that can be absorbed. The constraints of high loading ratios combined with the low solar absorbance of fullerenes present an important area of improvement for future devices. Therefore new materials that can act as effective electron acceptor materials similar to fullerenes while also contributing a significant amount towards photocurrent generation represents an extremely important goal in the realization of more efficient organic photovoltaic devices. Another disadvantage of fullerenes is that they are small molecules rather than continuous materials, and therefore any nanostructure formed with fullerenes will be prone to morphological changes, phase segregation, etc. Carbon nitride (CN_x) is a potentially promising material for this type of application as it has been shown to exhibit semiconductor properties that could be beneficial for use in a photovoltaic device. However, very little work has been done in this area with no reports of composite organic photovoltaic devices based on these materials having been studied prior to the commencement of this thesis. It is shown in this work for the first time that n-type carbon nitride materials can be developed that exhibit photovoltaic properties and function as an electron acceptor material when combined with a conjugated polymer.

1.2 Scope of thesis

This thesis examines two very important issues in the development of photovoltaic solar cells including the development of new photovoltaic materials and new methods for studying charge transport and recombination in these devices.

Chapter 2 provides a brief overview of the development of organic solar cells and the key milestones that have guided research in this field. As mentioned, there is a need for the development of alternative acceptor and semiconductor materials for photovoltaic solar cells. The photovoltaic properties of carbon nitride prepared using reactive magnetron

sputtering are examined in detail in this work and an overview of their preparation and the influence of the bonding and structure on the electronic and optical properties is provided. Many of the measurements carried out in this thesis use frequency resolved techniques to study the dynamic processes occurring in organic photovoltaic materials and devices, and an overview of their application to photovoltaic devices is included.

In Chapters 3 and 4 the semiconductor and photovoltaic properties of carbon nitride (CN_x) thin films prepared using a reactive magnetron sputtering technique were investigated both individually and as composites with the organic conjugated polymers, poly(2,2'-bithiophene) (PBT) and poly(3-hexylthiophene) (P3HT). When CN_x was combined with a conjugated polymer they were shown to function as an acceptor material leading to an increase in photocurrent generation in the composite materials. The influence of the deposition conditions (target power, nitrogen partial pressure, and total pressure) was studied to understand their role on the resulting optical and electronic properties of the thin film materials. The elimination of graphitic percolation networks accompanied by improved structural ordering led to nitrogen rich carbon nitride materials that exhibited photoconductive and photovoltaic properties. Structural ordering was promoted through film relaxation using thermal annealing that led to fabrication of single layer photovoltaic carbon nitride thin film materials. This represents the first demonstration of a photovoltaic effect in carbon nitride thin film materials prepared using reactive magnetron sputtering. A prototype p-n heterojunction device made up of a p-type P3HT layer and n-type CN_x layer was shown to exhibit enhanced photovoltaic properties relative to either of the single layer devices demonstrating the potential of CN_x as a new type of photovoltaic solar cell material.

In Chapters 5 and 6 intensity modulated photocurrent (IMPS) and photovoltage (IMVS) spectroscopies were used to study the mechanism of photoprocesses in P3HT:PCBM (Phenyl-C₆₁-Butyric-Acid-Methyl Ester) bulk heterojunction organic solar cells containing varying amounts of P3HT and PCBM in the active layer. The use of the frequency domain techniques allowed us to separate the bulk and interfacial processes and gain valuable insight into the mechanism of losses in these devices. The results provide direct evidence that interfacial nongeminate recombination is one of the

dominant loss and aging mechanisms in bulk heterojunction organic solar cells. It is also shown that high loading ratios of PCBM are beneficial for the enhanced stability of organic solar cells with device aging. This is attributed to improved carrier extraction at the interface between PCBM and the metal cathode, which limits the amount of charge carriers that are lost to interfacial recombination. These results demonstrate the importance of the PCBM content on device stability, an important aspect, which is often overlooked in the search for alternative acceptor materials.

Chapter 7 summarizes the main conclusions reached in this thesis and considers their significance in the context of the development of high stability and efficient organic solar cells and discusses future directions of research that build upon the results presented.

1.3 References

- (1) Smalley, R. E. *MRS Bulletin*. **2005**, *30*, 412.
- (2) Zweibel, K. *Science* **2010**, *328*, 699.
- (3) Peter, L. M. *Philosophical Transactions of the Royal Society, A* **2011**, *369*, 1840.
- (4) Kamat, P. V. *Journal of Physical Chemistry C* **2007**, *111*, 2834.
- (5) Small, C. E.; Chen, S.; Subbiah, J.; Amb, C. M.; Tsang, S. W.; Lai, T. H.; Reynolds, J. R.; So, F. *Nature Photonics* **2012**, *6*, 115.
- (6) Sondergaard, R.; Hosel, M.; Angmo, D.; Larsen-Olsen, T. T.; Krebs, F. C. *Materials Today* **2012**, *15*, 36.

Chapter 2

2 Background

2.1 Organic Photovoltaics

Organic photovoltaic devices are a promising platform for the conversion of solar energy into electricity as these materials can be synthetically tailored permitting molecular control of the electronic and optical properties. Many of the early organic solar cells were fabricated using small organic molecules such as phthalocyanines and merocyanines.¹ The simplest device architectures consisted of a single molecular organic active layer sandwiched between two electrodes with different work functions, which were typically a transparent semi-metallic material such as indium tin oxide (ITO) combined with a second metal electrode. The difference in work function of the two electrodes generated an electric field across the thin organic layer and helped to direct and transport the photogenerated charge carriers through the active layer. While early devices demonstrated the potential of organic materials in solar cells, their efficiencies were quite low. These low efficiencies were attributed to the formation of excitons, instead of separated electrons and holes as in conventional solar cell devices.² An exciton is an uncharged coulombically bound electron-hole pair and it is necessary to dissociate the exciton into free charge carriers to generate a photocurrent. Exciton dissociation can occur at the interface between two different materials. In the case of a single layer organic solar cell, this interface is created between the organic material and the electrode.³ Due to the short exciton lifetime and diffusion length, photocurrent generation is confined to the organic/electrode interface representing a small fraction of the film, which reduces the amount of material that can generate an electric current.

The formation of excitons in organic solar cells emphasizes the importance of different dynamic processes compared to conventional solar cells such as silicon. The important parameters affecting organic photovoltaic device efficiency include:

- (1) Exciton generation
- (2) Exciton diffusion length
- (3) Charge separation at an interface

(4) Charge transport through the active layer

(5) Charge extraction at the electrodes

The electrically neutral exciton has a limited diffusion length of approximately 5 – 10 nm in conjugated polymers.⁴ Recombination of an exciton can occur if it is not separated into a free electron and a hole, limiting the maximum attainable photocurrent. Typical binding energies of an exciton are approximately 0.3 eV requiring a similar difference in energy at the interface for dissociation to occur.⁵ Upon exciton dissociation, the negative and positive charges must be transported across the active layer, to the proper electrodes. Charge transport of free charge carriers across the film and their extraction at contacts, represents a serious loss mechanism in these devices, especially with aging, and a part of this thesis includes the development and use of the technique intensity modulated photocurrent and photovoltage spectroscopy (IMPS/IMVS) to bulk heterojunction organic solar cells to address these issues in further detail.⁶

A significant milestone in the development of organic photovoltaic devices occurred through the demonstration of a bi-layer arrangement that significantly enhanced photocurrent generation.⁷ This innovative device architecture consisted of two different organic materials in the active layer. Due to differences in ionization potentials and electron affinities in these materials, the dissociation of excitons at the organic/organic interface was much more efficient. This led to increased photocurrent generation, with device efficiencies approaching approximately 1 %. The bi-layer device architecture is illustrated below in Figure 2-1 to demonstrate how excitons are generated and dissociated at the interface of two different organic materials. The majority of organic solar cells today exploit the differences in the HOMO/LUMO levels of two different materials to maximize photocurrent generation.

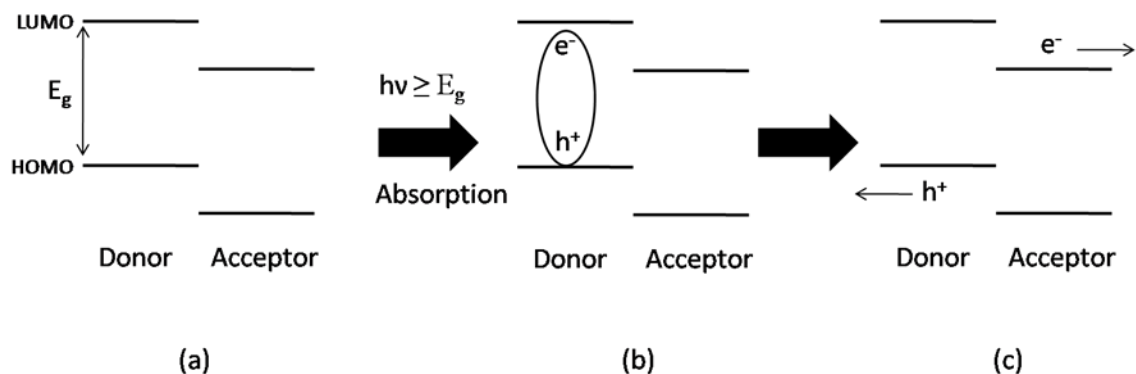


Figure 2-1. Bi-layer architecture. (a) Two materials with different ionization potentials/electron affinities. (b) Light absorption and exciton formation (c) Charge transfer and exciton dissociation.

Figure 2-1A shows that before illumination the highest occupied molecular orbital (HOMO) and lowest unoccupied molecular orbital (LUMO) of each organic material are offset. The material with a smaller ionization potential is known as the electron donor, while the material with a larger electron affinity is referred to as the electron acceptor. Illumination of the organic materials with visible light leads to formation of an exciton, which diffuses to the interface of the two organic materials (Fig. 2-1B). Dissociation of the exciton at the donor-acceptor interface generates a negatively charged electron on the acceptor material and a positively charged hole on the donor material. These charged species then travel across the active layer towards the cathode and anode respectively to generate a photocurrent (Fig. 2-1C). The bi-layer architecture marked a significant advancement in the efficiencies of organic photovoltaic devices, but it still did not overcome the problem of the short diffusion length of excitons in organic materials. Excitons created farther away from this interface still did not contribute to the photocurrent and limited the region of the light harvesting active layer to the immediate vicinity of the donor-acceptor interface. Therefore, the conversion of photons into electrons could not occur across the entire film, placing a significant limit on the maximum achievable photocurrent in these devices. This was, amongst other reasons, one of the major motivating factors for the development and application of conjugated organic polymers in organic solar cells as discussed in further detail in the next section.

2.2 Bulk Heterojunction Polymer Solar Cells

Due to their extended conjugated structure, conjugated polymers exhibit a high absorption coefficient that is on the order of 10^5 cm^{-1} and as a result, a film of only ca. 200 nm is needed to absorb all photons at the peak absorption.⁸ Similar to organic small molecules, their electronic and optical properties can be controlled through chemical and electrochemical modification leading to materials with electronic properties that exhibit exceptionally high conductivities similar to metals, as well as semi-conducting and insulating properties.⁹ The use of conjugated organic polymers opens the door towards the development of materials that combine the processability of polymers with useful electronic and optical properties. Moreover, these materials can be deposited onto a substrate directly from solution, which allows for the development of high-throughput deposition techniques such as ink-jet printing, spray coating, electrochemical deposition, etc.¹⁰ All of these factors highlight the significant driving force behind the development and use of conjugated polymer materials in organic solar cells.

Two concepts demonstrated 15 – 20 years ago still underline the design and architecture of the majority of organic polymer photovoltaic devices today. The first was the demonstration that fullerenes were found to be extremely effective materials for promoting the photoinduced electron transfer from a conjugated polymer to a fullerene molecule as observed by photoluminescence quenching that was almost 100% efficient.¹¹ Later it was shown that a similar bi-layer device containing a donor conjugated polymer combined with a fullerene acceptor thin film generated a heterojunction device that exhibited promising semiconductor and photovoltaic properties.¹² While these devices were still limited by the short diffusion length of excitons, this early result paved the road toward the formation of an interpenetrating bulk heterojunction active layer, which opened the way towards high efficiency organic solar cells. A major shift in the fabrication of polymer solar cells occurred following the demonstrations that a donor and acceptor conjugated polymer, or a donor conjugated polymer mixed with a soluble fullerene acceptor phenyl-C₆₁-butyric acid methyl ester (PCBM), can be cast from the same solution to form a nanoscale interpenetrating donor-acceptor network that exhibited improved device efficiencies.^{13,14} These interpenetrating

networks formed a 3-dimensional bulk heterojunction photoactive layer and maximized the interfacial area between the two different materials, which led to significantly enhanced exciton dissociation and photocurrent generation. It is the bulk heterojunction active layer that is used in the vast majority of polymer solar cell architectures today, with fullerenes and their derivatives being ubiquitous in their use in the most highly efficient devices.¹⁵

The left hand side of Figure 2-2A illustrates the absorption of light by a semiconducting conjugated polymer in a bulk heterojunction solar cell leading to the formation of an exciton. The right hand side of Figure 2-2A shows the multi-layer structure that is typical of a bulk heterojunction organic solar cell. A transparent conductor indium tin oxide is coated onto a glass slide and this is the side of the photovoltaic device where light enters. The light is absorbed by the photoactive layer, eventually leading to charge carriers being generated, with holes being extracted at the ITO electrode and electrons being collected at the low work function metal electrode, which is often aluminum in organic solar cells. As mentioned above, dissociation of an exciton is necessary to create a free electron and hole to generate a photocurrent. In polymer bulk heterojunction solar cells the conjugated polymer is responsible for light absorption and this is where the exciton is formed, as shown in Figure 2-2B. To separate the exciton, an acceptor material with a LUMO that is lower in energy is combined in the bulk heterojunction to increase charge carrier generation. In the right hand side of the diagram, the donor material (grey shading) is poly(3-hexylthiophene) (P3HT) and the acceptor material (black shading) is PCBM, which are two commonly used materials. Their structures along with the hole transport material poly(3,4-ethylenedioxythiophene):polystyrene sulfonate (PEDOT:PSS) are shown below in Figure 2-3. The free charge carriers produced in these devices occur due to the separation of excitons at the donor/acceptor interface. Upon dissociation, the negative and positive charge carriers must be transported to the proper electrodes through percolation pathways in the bulk heterojunction. The positively charged holes are transported by the donor material while the negatively charged electrons are transported by the acceptor material to their respective electrodes as shown in Figure 2-2C. Due to the high surface area of the heterojunction between the donor and acceptor materials, transport across the film is extremely sensitive to film morphology and composition, and

significant efforts have been directed towards their optimization to realize improvements in device efficiency.

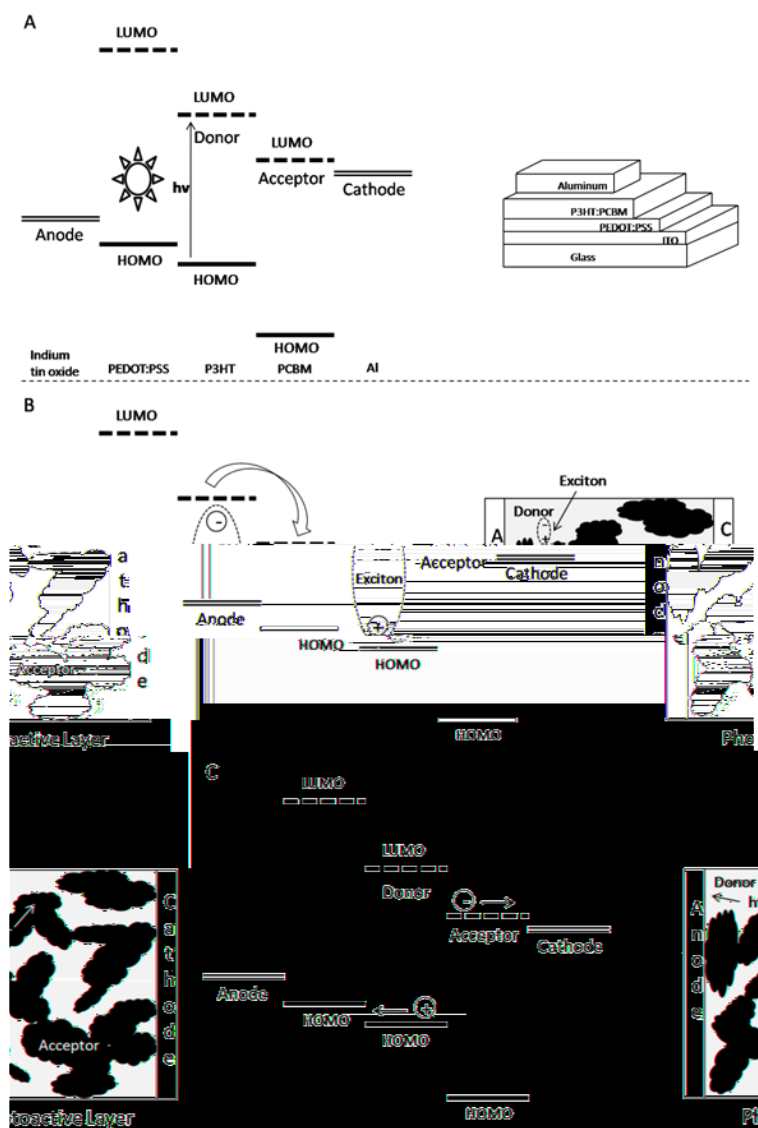


Figure 2-2. (A) Left: Absorption of light by donor material. Right: Solid state photovoltaic device. (B) Right: Exciton splitting at donor acceptor interface. Left: Exciton diffusion in donor material to acceptor interface. Dark area is acceptor material. Light area is donor material. (C) Right: Electron is transported to cathode through the LUMO and hole is transported to anode through the HOMO. Left: Electron transport through acceptor material to cathode and hole transport through donor material to anode.

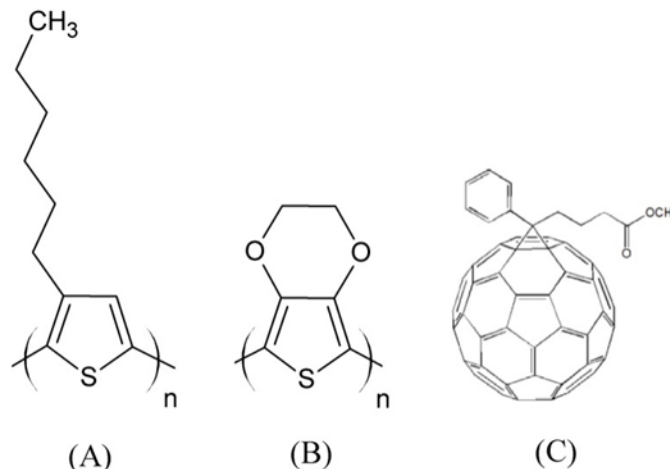


Figure. 2-3. Chemical structures of (A) poly(3-hexylthiophene), (B) poly(3,4-ethylenedioxythiophene) and (C) phenyl-C₆₁-butyric acid methyl ester.

The ideal morphology of bulk heterojunction solar cells should contain phase segregated domains that are about twice the exciton diffusion length (10 – 20 nm) in size, and these domains should also form a percolation network across the bulk of the film (100 – 200 nm) to ensure the transport of charge carriers to the corresponding electrodes.⁸ The film morphology is a critical aspect that governs the interactions between the donor and acceptor phases in the active layer.^{16,17} The photocurrent generation in films prepared using the same composition of donor and acceptor materials but deposited from different solvents can be markedly different, and this has been directly attributed to differences in film morphology.¹⁸ This example highlights the extreme importance of film morphology and composition on the efficiency of organic solar cells. Photoactive layers that do not possess an optimum morphology can result in significantly reduced efficiencies due to decreased photocurrent generation, charge carrier transport and poor contact formation with the electrodes. All of these factors can limit device efficiency. However, methods that are available to investigate the influence of film morphology and composition on carrier transport and other dynamic processes under normal working conditions of bulk heterojunction organic solar cells are not readily available, which has limited their detailed study.

2.3 Loss Mechanisms

The time scales of the various processes occurring in organic solar cells span from the femtosecond timescale to as long as several hundred milliseconds.^{19,20} The initial processes of exciton formation and dissociation in bulk heterojunction active layers occur on a very fast time scale and have been extensively studied using transient absorption optical techniques.²¹ Figure 2-4 (as adapted from Ref. 21) highlights the different possible paths that can lead to charge carrier extraction and the possible loss mechanisms that can occur in a device following light absorption in the conjugated polymer.

Initially, there are three possible outcomes that can be considered for an exciton following light absorption:

- (i) Exciton recombination
- (ii) Exciton separation at the donor/acceptor interface into an electron and a hole that remain spatially correlated
- (iii) Separation of an exciton into a free electron and hole

In case (i), light absorption by the polymer leads to exciton formation and subsequent radiative decay before it is able to reach the donor/acceptor interface. In case (ii), an exciton can reach the donor acceptor interface and form a charge transfer state that remains electrically neutral. It is possible for this spatially correlated exciton to recombine without generating a photocurrent (iia). This type of recombination is referred to as geminate recombination because the electron recombines with the hole that it was initially separated from. Alternatively, after forming this so called charge transfer state, the exciton can be separated, leading to the generation of free charge carriers, which may be transported across the film and extracted at the electrodes (iiib). It is also possible that once created, the free charge carriers will not reach the electrodes upon their separation. Instead, as shown in case (iiia), a positive and negative charge carrier that were independently generated can recombine without being collected. This is referred to as nongeminate recombination.²² Nongeminate recombination can occur for a variety of reasons including poor charge transport, unfavourable film morphology, poor contact

formation, as well as interfacial states due to defects present in the film and at the electrodes. Nongeminate recombination becomes an increasingly important problem in organic photovoltaic devices when considering their long term stability.

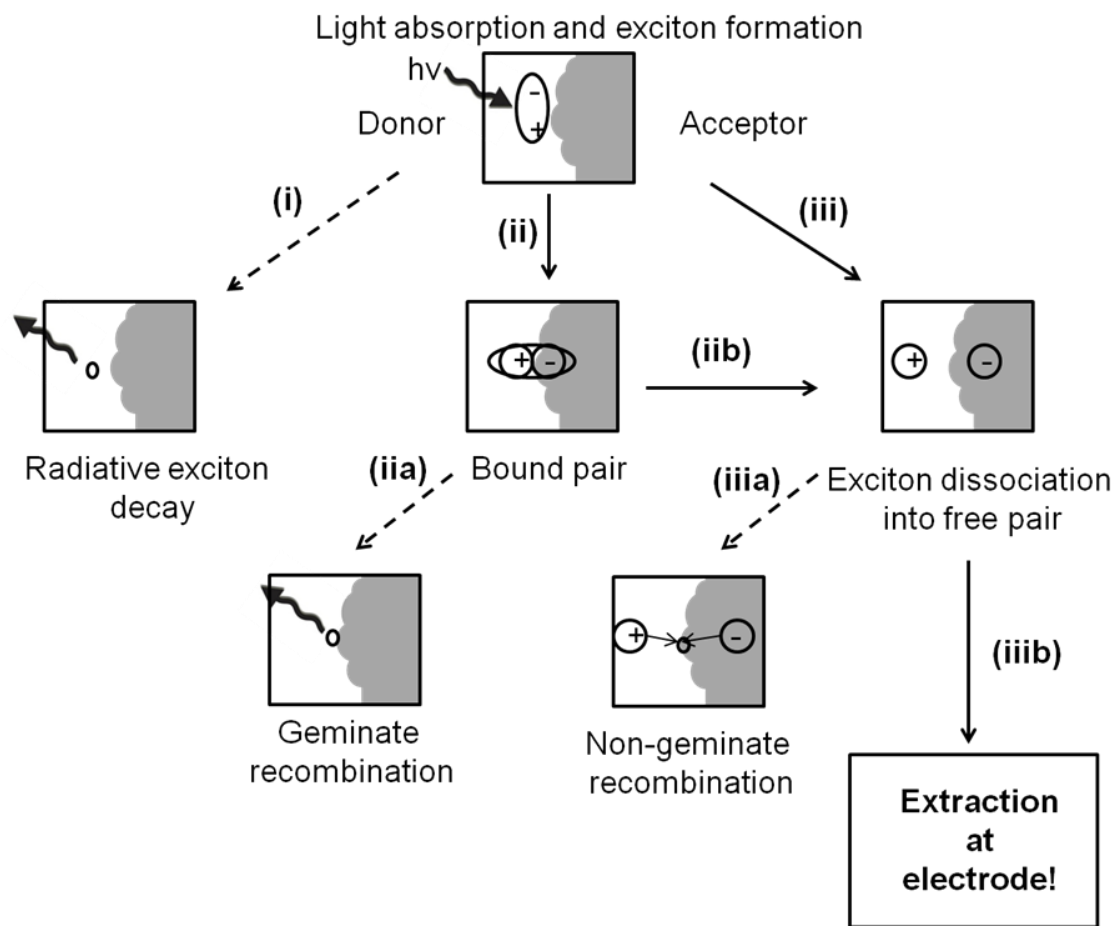


Figure 2-4. Bulk heterojunction active layer showing donor (white) and acceptor (grey) interface. Illustration of (i) exciton decay, (ii) charge transfer state formation and (iii) exciton dissociation in an organic bulk heterojunction device. Adapted from Ref. 21.

The realization of practical organic photovoltaic devices is not only limited by their low efficiencies but also their short service life.²³ However, the degradation of organic solar cells has not been as well investigated, especially the dynamic processes such as recombination and charge carrier transport. Typically, steady-state current voltage plots of degraded devices are carried out in combination with a second analytical technique

such as atomic force microscopy (AFM), transmission electron microscopy (TEM), scanning electron microscopy (SEM), or optical absorption measurements to better understand the chemical and physical processes that accompany a decrease in efficiency. While these techniques provide valuable insight into modifications of the active layer morphology and interfacial degradation, they do not provide details of the processes that limit the efficiency. Due to the high surface area interpenetrating nanoscale morphology, there are many possible interfaces throughout the bulk of the film as well as at the charge collecting electrodes where losses may occur. The identification of the loss mechanisms is extremely important as it can provide insight into new methods and device architectures that could be used to improve device stability. As discussed in further detail in this thesis, intensity modulated photocurrent spectroscopy (IMPS) is a powerful technique for probing processes that occur on a longer time scale, which represent significant loss mechanisms in organic photovoltaic devices, especially with respect to device stability. Using IMPS it is possible to probe and separate the dynamic processes of charge carrier transport and interfacial recombination, which are not readily determined using steady-state techniques such as current-voltage measurements under illumination.

2.4 Methods of Improvement

Improvements for organic photovoltaic devices have included the design and synthesis of low band-gap polymers for absorption of a larger part of the solar spectrum,²⁴ development of tandem or multilayer cells,²⁵ improved light absorption of the electron acceptor,²⁶ optical spacers,²⁷ processing additives,²⁸ and control of the nanoscale phase separation.²⁹ A combination of these effects in a single layer device that exploits an inverted architecture has led to the best reported efficiency in a polymer photovoltaic solar cell in excess of 9%,³⁰ and greater than 10 % in a tandem cell configuration.³¹ These efficiencies are extremely encouraging and illustrate the tremendous potential of organic solar cell devices. However, increasingly it is becoming more important that these types of efficiencies are sustainable over several years, highlighting the need to understand how and why efficiency decreases with time.²³

A dramatic improvement in efficiency was realized through the bulk heterojunction architecture by maximizing the interaction between a donor polymer and a PCBM

acceptor. PCBM is the ubiquitous acceptor material in organic photovoltaics and its overwhelming use is due to the excellent electron transport and exceptional electron accepting abilities of fullerenes.^{32,33} However, PCBM is itself a molecule and not a polymer. As a result, high loading ratios of PCBM are required to create conducting paths throughout the network of the film to achieve high photocurrents. In polymeric photovoltaic devices, the majority of light absorption is due to the p-type polymer and not PCBM. One of the advantages of using conjugated organic polymers is a high absorption coefficient that can be tuned to match the solar spectrum.

Identifying the properties that make PCBM an ideal acceptor material in organic photovoltaics can guide the search for alternatives. The most significant attributes of fullerenes are the low lying LUMO that make it an effective electron acceptor and the ability to effectively transport electrons throughout the active layer. The low lying LUMO of fullerenes provides an effective energy difference between the LUMO levels of the donor polymer and PCBM acceptor permitting efficient exciton dissociation.³⁴ Alternative electron acceptors should also contain a LUMO level capable of efficient exciton dissociation. The electron transport in fullerene derivatives can be quite high due to beneficial packing and formation of crystalline structures.^{35,36} For other materials to be used in organic photovoltaics, electron transport through a well defined structure is important. A third benefit of PCBM is the increased stability that is observed in bulk heterojunction devices for high loading ratios.³⁷ This factor is often overlooked when considering alternative acceptor materials but should also be considered when exploring new device architectures. Reflecting on these properties, it is possible to consider alternatives to PCBM that can overcome the limitations imposed by fullerenes. The search for alternative n-type materials and different active layer compositions is an important challenge in the development of next generation photovoltaic technologies. In this work, carbon nitride thin films, which represent a new type of carbon photovoltaic material, are explored as an alternative to fullerenes.

2.5 Carbon Thin Film Materials

The different allotropes of carbon exhibit distinctly different bonding in the bulk as reflected in the case of sp^2 hybridized graphite or sp^3 hybridized diamond. Diamond is the hardest known naturally occurring material, is optically transparent to visible light and electrically insulating. On the other hand, graphite is relatively soft and can be used as a lubricant due to the weak van der Waals forces between the individual graphene sheets. It also strongly absorbs visible light and is an electrical conductor, which is in stark contrast to diamond. The differences in the physical properties of these materials are directly related to the hybridization of the carbon atoms and their long range order. While diamond is an isotropic material that exhibits tetrahedral sp^3 covalent bonding, graphite is an anisotropic material made up of stacks of individual sp^2 graphene sheets. Carbon nanostructures expand the number of possible allotropes that carbon may form including 0 dimensional fullerenes,^{34,38} the ubiquitous acceptor material in bulk heterojunction organic solar cells, 1 dimensional carbon nanotubes which are a single graphene sheet that is rolled up to form a tube,³⁹ and 2 dimensional graphene which is an individual sheet of graphite that is only one monolayer thick.⁴⁰ Aside from diamond, all of these carbon allotropes exhibit sp^2 hybridized bonding. In addition to these nanostructured materials there are also amorphous carbon thin films, which are an extremely interesting class of materials that exhibit both sp^2 and sp^3 hybridized bonding giving rise to physical properties intermediate between those of graphite and diamond.⁴¹ Their properties can be controlled and modified by adjusting the ratio of sp^2 and sp^3 fractions within the thin film creating the opportunity to develop and study novel materials that possess a combination of diamond and graphite. Films that contain predominantly sp^3 bonding (> 90 %) are typically referred to as diamond like carbon (DLC) or tetrahedral amorphous carbon (ta:C), whereas films that contain a significant fraction of sp^2 carbon are typically referred to as amorphous carbon. Through variations of the sp^2/sp^3 bonding in these films it is possible to control the physical properties such as film hardness, transparency, conductivity and electrochemical reactivity. It is the sp^2 states that control the electronic and optical properties and which are important for photovoltaic applications.

Further control of the electronic structure of carbon thin films is possible through the intentional addition of dopant heteroatoms such as B, N, P and S. Boron doped diamond (BDD) is a well known example of a doped carbon thin film and has found many applications, particularly in electrochemistry.⁴² The addition of the group 13 boron to group 14 carbon leads to p-type doping of diamond. Alternatively, group 15 elements such as N and P can be added to carbon to create an n-type semiconductor.⁴³ While BDD has been extensively characterized and studied for electronic and electrochemical applications, n-type carbon materials have received significantly less research attention for their electronic applications with the majority of research so far having focused on their mechanical properties.⁴⁴ As highlighted above, there is a great need to replace fullerenes in organic solar cells and n-type carbon nitride thin films represent a promising alternative material.

2.6 Carbon Nitride

Nitrogen can be incorporated into highly sp^3 hybridized diamond as well as sp^2 hybridized amorphous carbon to create nitrogen doped t:aC and carbon nitride thin films respectively.⁴¹ The focus of this thesis is exclusively on the development of highly sp^2 hybridized carbon nitride thin films, however some general discussion of the nitrogen doped t:aC is also included here to illustrate how nitrogen adjusts the physical properties of carbon thin films. Addition of nitrogen strongly alters the electronic properties of the native carbon materials by introducing and modifying the distribution of the π and π^* orbitals and bands. In sp^3 hybridized diamond, an electronic insulator with a band-gap of 5.5 eV, there are no π and π^* states and one of the main effects of the addition of nitrogen into this material is to introduce sp^2 bonding into the material with increasing nitrogen content. This significantly increases the electronic conductivity of nitrogen doped t:aC, which can also be accompanied by a decrease in the optical gap depending upon the amount of nitrogen introduced into the material. At the other extreme is highly sp^2 hybridized amorphous carbon whose optical and electronic properties are more similar to graphite. The main difference is that these materials do not exhibit the same long range order as graphite due to the smaller and more disordered cluster sizes.⁴⁵ The addition of a small amount of nitrogen into these materials can further increase the electronic

conductivity through the introduction of more π and π^* states. For higher nitrogen containing films these materials are converted from a highly conductive semi-metal to a semiconductor material with an increased optical gap due to structural modification.⁴⁶ However, a significant amount of graphitic material is often still present, which can be detrimental to their semiconductor properties and is an important consideration in their development for practical applications.

The deposition of nitrogen doped t:aC and carbon nitrides can be realized using a variety of vacuum deposition techniques resulting in a wide number of different possible bonding configurations in these materials as shown in Figure 2-5.⁴⁷ The modification of the bonding and structure of carbon thin films by nitrogen can also result in n-type doping configurations.⁴³ However, only a few of the possible bonding arrangements shown in Figure 2-5 (B, D, G) can lead to n-type doping. In nitrogen doped t:aC there are two possible doping regimes, corresponding to low nitrogen doping concentrations and high nitrogen doping concentrations. Throughout the doping process for low nitrogen concentrations, the optical gap does not change and the sp^3 fraction remains constant and is not significantly distorted.⁴⁸ However, for concentrations greater than 2 %, the sp^3 fraction in these films is significantly reduced and the electronic properties of these materials become dominated by the sp^2 content in the film, which is typically located at the grain boundaries. While these materials exhibit interesting physical properties, and demonstrate how nitrogen is able to modify the electronic properties, they are not ideal for photovoltaic devices because they do not absorb visible light. It is the highly sp^2 hybridized carbon nitride thin films which contain as much as 50 % nitrogen stoichiometrically that represent an extremely promising class of semiconductor materials. However, very little work has been done in the area of photovoltaics.

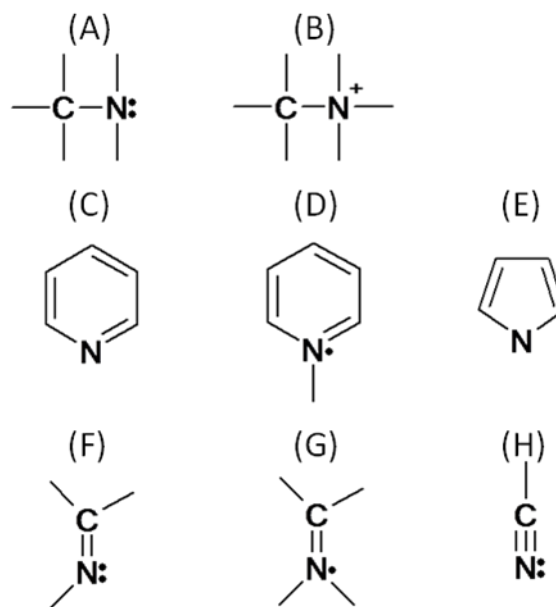


Figure 2-5. Different possible bonding arrangements in nitrogen doped t:aC and carbon nitride. Only bonding arrangements (B), (D), and (G) in the centre column represent the possible doping configurations.

Carbon nitride thin films can be considered carbon nitrogen alloys that may contain some amount of nitrogen in a doping configuration. These materials consist primarily of aromatic structures such as pyrrole, pyridine and nitrogen substituted graphitic clusters.⁴⁹ Of the possible aromatic bonding arrangements in carbon nitride, only when nitrogen substitutes for a graphitic carbon is n-type doping possible (structure G). Doping does not occur for pyridine-like and pyrrole-like bonding configurations, which are also present in a large amount in these materials.⁴³

As mentioned above, the choice of deposition technique strongly impacts the resulting structure of nitrogen containing carbon thin films. In general, techniques carried out at elevated temperatures with low nitrogen contents favour the formation of diamond-like materials, whereas lower energy techniques with high nitrogen contents favour the formation of carbon nitride materials.⁴⁷ Direct-current (DC) and radiofrequency (RF) magnetron sputtering are two well developed techniques for the deposition of carbon nitride thin film materials. Magnetron sputtering is also an industrially practical deposition technique that can be used to deposit conductors, semiconductors, and

insulators made from elemental and compound materials. In view of high-throughput manufacturing of photovoltaic devices, this makes magnetron sputtering of carbon nitride thin films a very valuable deposition process. Prior to the commencement of this thesis there were not any reports of the deposition of carbon nitride thin films using magnetron sputtering that exhibited photovoltaic properties. As shown in Chapter 4, we have created photovoltaic carbon nitride thin films using RF magnetron sputtering that demonstrate promising photovoltaic properties.

Magnetron sputtering is a physical vapour deposition technique that relies on the momentum transfer of positively charged ions to eject matter from a target material towards a substrate where deposition occurs. A custom built RF magnetron sputter deposition vacuum system was developed in this thesis to prepare carbon nitride thin films. Figure 2-6 illustrates the sputter deposition of a graphite target using an Ar gas source. The target material to be sputtered is held at a negative bias (typically hundreds of volts) relative to the substrate and vacuum chamber, which are grounded. An inert gas source such as argon is introduced into the vacuum chamber which causes the pressure to increase. Some argon atoms can become ionized, which in the presence of a strong electric field between the target and substrate leads to the formation of a plasma. The plasma is a quasi-neutral gas that consists of equal numbers of positive and negative charges along with neutral atoms and/or molecules. Due to the large negative bias that is applied to the target, the positively charged ions are accelerated towards the target, collide with it, and eject some of the material by ion bombardment. The target material is ejected upward by momentum transfer towards the substrate where it is deposited to create a thin film. Magnetron sputtering utilizes magnets placed behind the target to confine the charged plasma near the surface of the target material which increases ion bombardment and sputter deposition rate. It is also possible to use a gas which is not inert and will react with the target material. In this work, nitrogen is used to react with the carbon target material to generate carbon nitride thin films. The use of a reactive gas during the sputter deposition process is referred to as reactive magnetron sputtering.

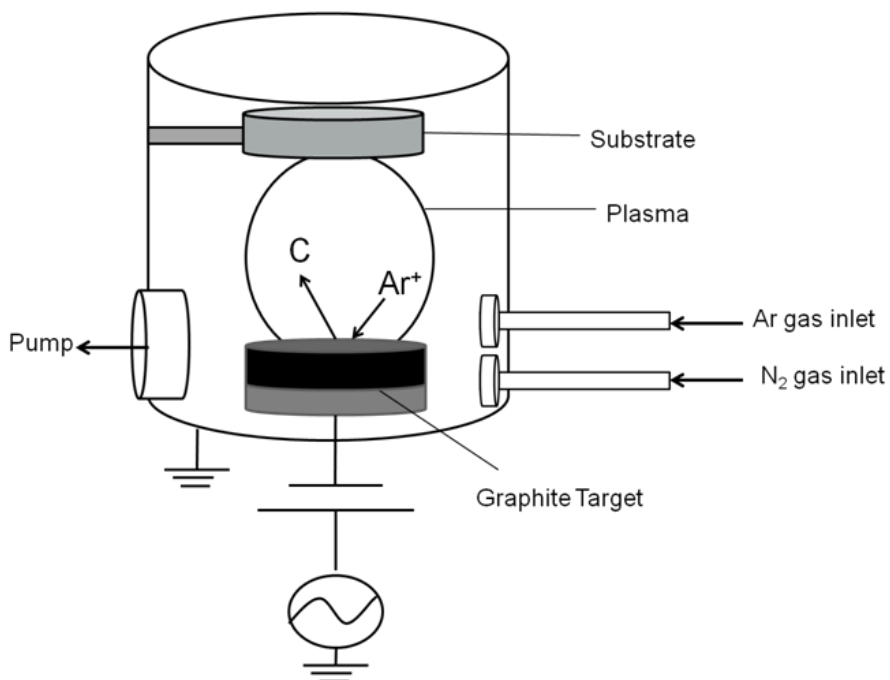


Figure 2-6. Illustration of the magnetron sputtering process.

2.7 Methods to Study Photovoltaic Devices

2.7.1 Steady-State Current-Voltage Measurements

Steady-state current-voltage measurements carried out under constant illumination are typically used to report device efficiency and performance.⁵⁰ The efficiency of an organic photovoltaic device can be determined by illuminating the solar cell with light of known intensity and energy, and measuring the current as a function of the voltage. The important parameters that can be obtained from these plots include the short-circuit current density I_{sc} , the open-circuit voltage V_{oc} , and the fill factor FF . An illustration of a typical current-voltage curve is shown below in Figure 2-7 highlighting the important parameters obtained from these plots.

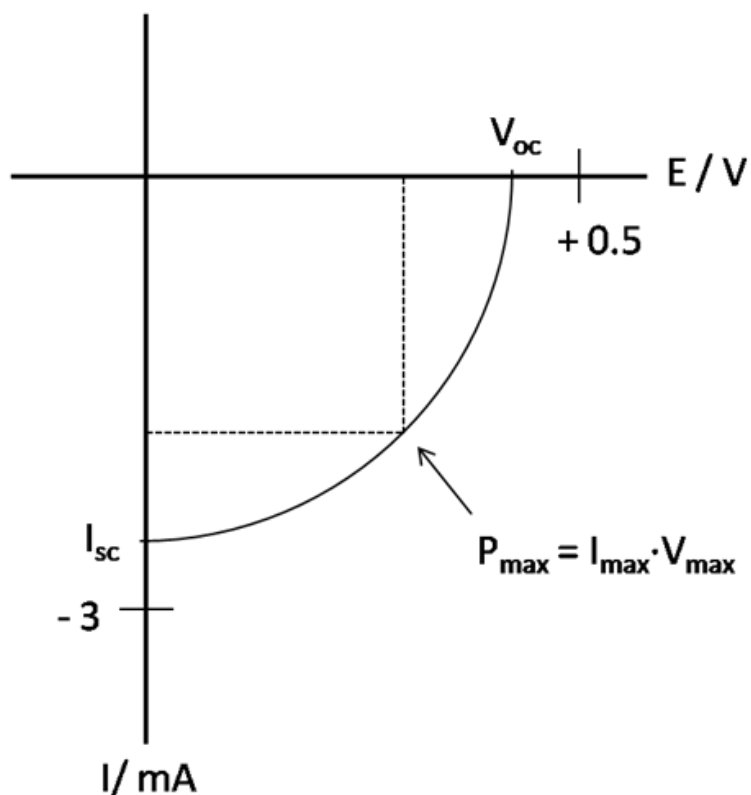


Figure 2-7. Illustration of a JV curve obtained under illumination showing the open circuit voltage V_{oc} , the short-circuit current I_{sc} , the point along the curve where the maximum power is generated P_{max} . The dotted square represents the area covered within the fill factor FF .

The open-circuit voltage represents the voltage across the cell when the current density in the device is zero. The open-circuit voltage of a bulk heterojunction device is determined by the difference in energy between highest occupied molecular orbital of the donor material and the lowest unoccupied molecular orbital of the acceptor material. The short-circuit current density represents the current density that can be extracted when the voltage across the cell is zero. The maximum power P_{max} that can be generated by the cell is determined from the point along the current-voltage curve where the product of the current I_{max} and the voltage V_{max} is at a maximum. The fill factor represents the area of the measured current-voltage curve that is defined by I_{max} and V_{max} as illustrated in Figure 2-7. A more efficient solar cell will exhibit a higher fill factor, which can be determined using the following equation:

$$FF = \frac{I_{max} \cdot V_{max}}{V_{oc} \cdot I_{sc}} \quad (1)$$

Measurements of the efficiency of solar cells can be compared using a standard incident light intensity that reflects the Sun's spectral light intensity on the Earth's surface. The standard spectral light intensity used is the AM (Air Mass) 1.5 spectrum and represents the intensity of the Sun at an angle of 48.2° with that of the Earth's surface and an intensity of 1000 W m^{-2} .⁵¹ Knowing the incident power striking a solar cell it is possible to determine its efficiency using the parameters described above through the following equation:

$$\eta_e = \frac{V_{oc} \cdot I_{sc} \cdot FF}{P_{in}} \quad (2)$$

Where η_e represents the efficiency and P_{in} represents the input power of the incident light source. While steady state measurements as those just described are useful for analyzing the efficiency of a device, they do not provide insight into the origin of the underlying mechanisms for differences observed in the shapes of the curves. As mentioned above this is increasingly important upon device aging where methods of measurement are much more limited. A normal organic photovoltaic architecture consists of an indium tin oxide electrode, composite photoactive layer and a metal contact, which makes necessary to develop methods to study interfacial degradation and active layer segregation under normal working cell conditions.

There are several techniques available that can probe charge transport and recombination in organic photovoltaic devices such as transient photocurrent and photovoltage measurements,⁵² time of flight (TOF),⁵³ photo-CELIV (charge extraction by linearly increasing voltage),⁵⁴ impedance spectroscopy (EIS),⁵⁵ and intensity modulated photocurrent and photovoltage spectroscopy (IMPS/IMVS).⁵⁶ In transient photocurrent/photovoltage techniques, a pulse of light is used to generate a photocurrent/photovoltage in a photovoltaic device and the decay of the curves is measured as a function of time, and used to extract information related to charge transport and recombination. However, different processes may not be easily separated

using time domain techniques, making it difficult to identify the individual contributions of interfacial and bulk recombination processes for example. For time of flight and photo-CELIV measurements, a thick photoactive layer is used to measure the time required for a charge carrier packet to drift from one side of the sample to the other and blocking contacts may be necessary to prevent current injection. So far the use of these techniques have been limited to measurements of pristine samples that have not been degraded and very little work is available that has examined the dynamics of organic solar cells under these conditions. IMPS can overcome some of these limitations because it is a frequency domain technique and can be used to study organic solar cells in their as prepared working configuration.

2.8 Frequency Domain Techniques

In this thesis, the frequency resolved perturbation techniques EIS and IMPS are used to study the dynamics of charge transport and carrier recombination in organic solar cells. Frequency resolved measurements offer an advantage over time domain techniques as it is possible to probe separate processes occurring on very different time scales. In addition, these devices can be studied in their normal working architecture, which is not always the case using other techniques. This is a distinct advantage for organic solar cells, where interfaces between the active layer and at the electrodes can significantly modify device efficiency and represent sites where interfacial recombination could occur, making it highly beneficial to probe these processes under normal conditions.

2.8.1 Electrochemical Impedance Spectroscopy

Impedance spectroscopy is a valuable technique for the characterization of the electronic properties of thin film materials and their interfaces with an electrode or electrolyte. In a typical impedance spectroscopy measurement a small alternating voltage at a specific frequency, superimposed on a background dc potential, is applied to the working electrode and the amplitude and phase shift of the alternating current is measured at the same frequency. The measured alternating current may or may not exhibit a phase shift relative to the input potential depending upon the system that is being measured and the frequency being used. These measurements can be made over a range of frequencies to

determine the impedance of the system as a function of the frequency. While the amplitude of the alternating voltage is usually quite small (ca. 5 – 20 mV), the dc potential can be varied over a wide range of values and impedance measurements can also be made as a function of the applied potential. A specific example of this type of potential dependent measurement is Mott-Schottky analysis where the impedance of the system is measured for a specific frequency over a range of dc potentials. The application of this technique to semiconductor materials is discussed in further detail below.

The frequency dependent impedance Z can be represented in a manner similar to Ohm's law as shown in equation 3:

$$Z(\omega) = \frac{V}{I} \quad (3)$$

Where ω is the angular frequency, V is the voltage and I is the current. Due to a phase shift between the applied alternating voltage and the measured alternating current, the frequency dependent impedance Z is a complex value and can be represented as a sum of the frequency dependent real Z_{Re} and imaginary Z_{Im} parts as given by equation 4:

$$Z(\omega) = Z_{Re} + jZ_{Im} \quad (4)$$

Where j is the imaginary unit. Impedance spectra are often represented as Nyquist plots, which plot the frequency dependent imaginary part Z_{Im} versus the frequency dependent real part Z_{Re} . Figure 2-8A shows a typical Nyquist plot, which consists of many discrete measurements at different frequencies. One of the disadvantages of the Nyquist representation is that the frequency values are not included in the plot. It can be more useful to represent the data as a Bode plot where the magnitude of the impedance $|Z|$, or the phase angle ϕ are plotted as a function of the frequency.

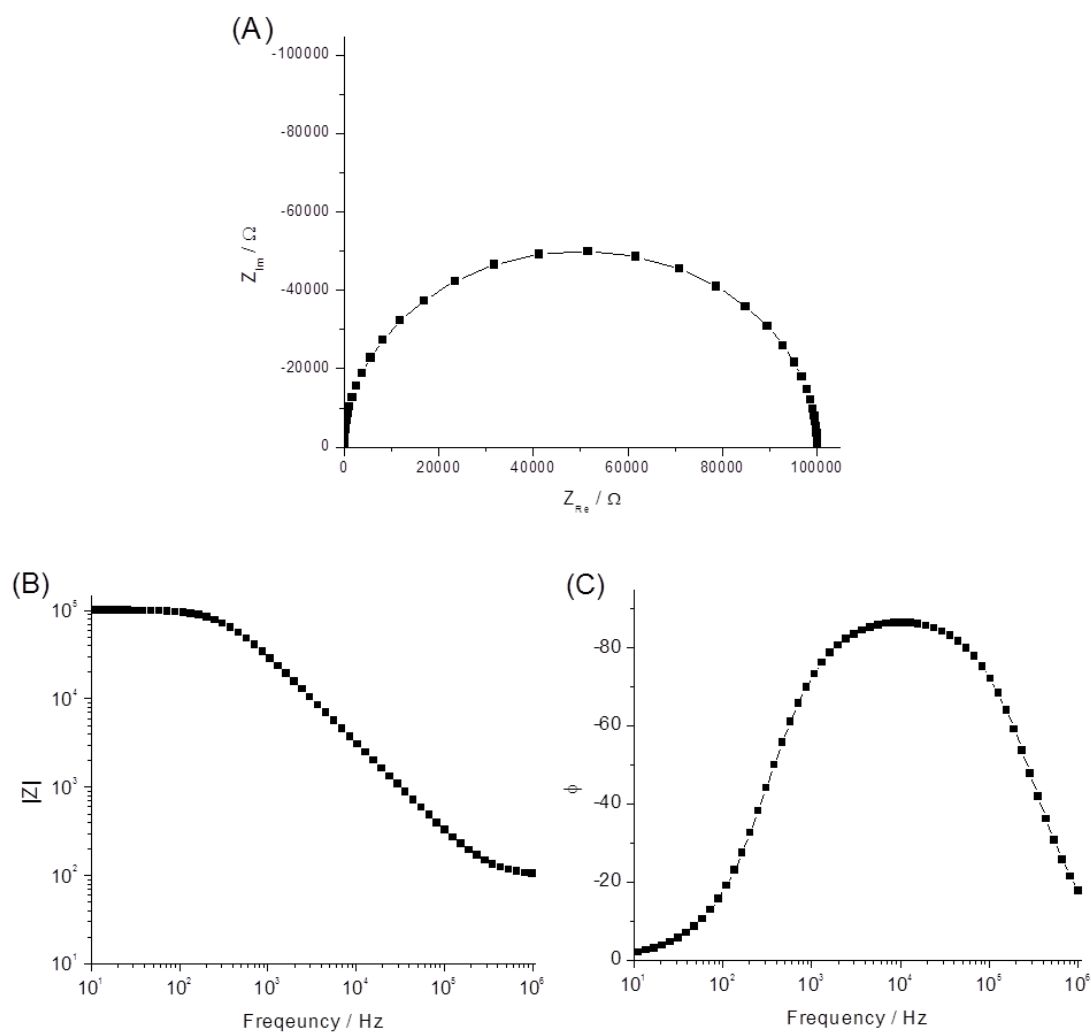


Figure 2-8. Example of a (A) Nyquist plot and corresponding Bode plots of (B) the impedance magnitude $|Z|$ and phase angle ϕ . The values for the elements used to generate this plot were $R_s = 100$, $R_p = 1 \times 10^6$ and $C_p = 5 \times 10^{-9}$.

The measured impedance values can be fitted using equivalent circuits that represent physical properties of the system. Capacitors and resistors are typically used but other circuit elements such as inductors may also be included. The Randles equivalent circuit (Fig. 2-9) can be used to fit impedance data like those illustrated in Figure 2-8 above.

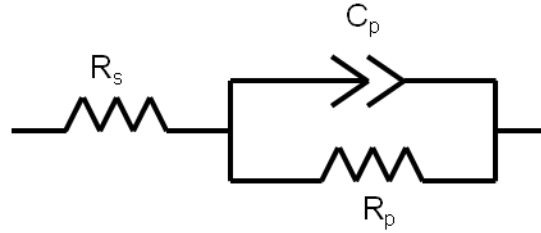


Figure 2-9. Randles equivalent circuit that consists of a resistance R_s in series with a parallel capacitance C_p and resistance R_p . This type of equivalent circuit is often used to represent an organic solar cell and can be used to fit the data shown in Figure 2-8.

The three circuit elements used in the equivalent circuit are R_s , R_p and C_p and these values can be determined from the Nyquist and Bode plots. In the case of an organic layer sandwiched between two electrodes in a solid state photovoltaic device, the parameters R_s , R_p and C_p are assigned to the contact resistance, film resistance and film capacitance respectively.⁵⁵ The impedance Z for this arrangement can be represented as:

$$Z(\omega) = R_s + \frac{R_p}{1 + j\omega R_p C_p} \quad (5)$$

Where ω is the frequency with units of s^{-1} . In the limiting case of infinitely high frequency, the impedance is due solely to the serial resistance R_s . In the other limiting case at zero frequency, the impedance is represented by the sum of the serial resistance R_s and parallel resistance R_p . The real and imaginary terms can be separated from one another for the above expression and are given by:

$$Z_{Re}(\omega) = R_s + \frac{R_p}{1 + (\omega R_p C_p)^2} \quad (6)$$

$$Z_{Im}(\omega) = -j \frac{\omega(RC)^2}{1 + (\omega RC)^2} \quad (7)$$

From equations 6 and 7 it is possible to generate the Bode plots in Figures 2-8B and 2-8C, which plot the magnitude $|Z(\omega)| = [(Z_{Re}(\omega))^2 + (Z_{Im}(\omega))^2]^{1/2}$ of the impedance and the phase angle $\varphi(\omega) = \tan^{-1}(Z_{Im}(\omega)/Z_{Re}(\omega))$ respectively as a function of the frequency. From these frequency dependent measurements, it is possible to generate the plots shown in Figure 2-8 and determine the values of R_s , R_p and C_p individually.

2.8.2 Mott-Schottky Plots

As mentioned above, impedance measurements can also be made at a single frequency over a wide range of dc potentials. For measurements made at a high enough frequency to exclude effects due to leakage currents in a semiconductor material, it is possible to fit the data using a serial R-C circuit and determine the film capacitance as a function of the applied potential as given by:

$$Z = R + \frac{1}{j\omega C_{sc}} \quad (8)$$

Where R represents the electrolyte or contact resistance, while C_{sc} represents the space charge capacitance in the semiconductor material. In this work, Mott-Schottky measurements are performed in solution as well as for solid state devices and depending upon the experimental arrangement R will represent the electrolyte or contact resistance respectively, while C represents the space charge capacitance in the semiconductor material. In a Mott-Schottky plot, the value of the inverse capacitance squared C^{-2} is plotted as a function of the applied potential E . For an ideal semiconductor electrode, the dependence of C^{-2} will be linear over a broad range of potentials. The slope of this curve is inversely proportional to the dopant density in the semiconductor film and the point of intersection along the x-axis represents the flat-band potential E_{fb} for the semiconductor film, which corresponds to the situation where no electric field exists across the

semiconductor device. Examples of these types of plots can be found in Chapters 3 and Chapter 5.

2.8.3 Intensity Modulated Photocurrent Spectroscopy

Intensity modulated photocurrent spectroscopy is a dynamic technique where a small harmonic perturbation of the steady state light intensity of a monochromatic light source is used to study frequency dependent processes in a semiconductor electrode.⁵⁷ IMPS is similar to electrochemical impedance spectroscopy described above which employs a small harmonic perturbation of the applied voltage and measures the resulting current response. For IMPS measurements the excitation is a modulated light source superimposed on a steady state dc background. Excitation of an organic solar cell through the ITO side generates charge carriers throughout the volume of the film, which are collected as a modulated ac photocurrent superimposed on a steady-state dc photocurrent at the aluminum electrode. A light source with constant and small sinusoidal modulation intensity can be represented by:

$$I(t) = I + \tilde{I} \cdot \sin(\omega t) \quad (9)$$

Where I is the continuous background light intensity with units photons $\text{s}^{-1} \text{cm}^{-2}$ and \tilde{I} is the modulation amplitude, t is time and $\omega = 2\pi f$ is the circular frequency, where f is the modulation frequency. For sufficiently small modulation amplitude the resulting photocurrent is also a function of time and is given by:

$$j(t) = j + \tilde{j} \cdot \sin(\omega t + \varphi) \quad (10)$$

where \tilde{j} is the amplitude of the photocurrent density and φ is the phase of the photocurrent density. These two terms are frequency dependent and are measured using a frequency response analyzer. Figure 2-10 illustrates three different possible scenarios that can be observed using IMPS. The left hand side of the diagram illustrates the photocurrent response as a function of time for a square wave light pulse, while the right hand side of the diagram shows the corresponding Nyquist plot representation of the imaginary photocurrent $Im(J_{photo})$ vs. the real photocurrent $Re(J_{photo})$. Similar to EIS,

IMPS spectra may be expressed as a Bode plot as well. It is important to highlight for Figure 2-10 that a square wave light pulse is being used to illustrate the relationships between the time domain response and the frequency domain response of the photocurrent density.

2.8.3.1 Photocurrent in Phase with Light Source

In Figure 2-10A, the light is switched on and a steady state photocurrent is immediately achieved in the left hand side of the diagram. This scenario corresponds to the ideal case where no transport or recombination losses occur, and no shift in phase of the photocurrent in the IMPS plot is observed in the right hand side of Figure 2-10A. In this case a single point that lies along the real axis would be obtained.

2.8.3.2 Photocurrent Exhibits Positive Phase Shift Relative to Light Source

It is also possible for the photocurrent to lead the light intensity. This is illustrated in the left hand side of figure 2-10B and shows that when the light is switched on, the photocurrent exhibits a sharp peak that decays with time. The decay of the photocurrent with time is due to interfacial recombination of charge carriers. At high enough frequencies the photocurrent is located on the real axis, without a phase shift as mentioned above. This corresponds to the case where no interfacial recombination is occurring and represents ideal carrier generation and collection. However, as the frequency decreases the value of the real photocurrent also decreases and exhibits a positive phase shift leading to a semicircle that is located in the upper right hand quadrant of the IMPS plot. With continued decreasing frequency, the IMPS plot passes through a maximum before reaching a steady-state value on the real axis, which represents the decreased value of collected carriers in steady-state conditions. The frequency at the maximum of the semicircle of the IMPS plot corresponds to the pseudo first order rate constant for the interfacial recombination of photogenerated charge carriers. This type of response corresponds to what was observed in bulk heterojunction organic solar cells, which will be studied in further detail in this thesis.

2.8.3.3 Photocurrent Exhibits Negative Phase Shift Relative to Light Source

It is also possible for the photocurrent to lag the light intensity as shown in the right hand side of Figure 2-10C. This is often observed for dye sensitized solar cells due to the slow transport of electrons through the nanoporous TiO₂ layer.⁵⁸ In this case when the light is switched on, the photocurrent transient rises with time as shown in the left hand side of Figure 2-10C. Due to the small size of the TiO₂ nanoparticles, an electric field is not present across the semiconductor material and electrons diffuse from the electrolyte/semiconductor interface, where they are generated, to the back electrode where they are collected. This leads to a phase lag between the light intensity and the measured photocurrent, and is observed as a semi-circle that is located in the lower right hand corner of the complex plane plot. At high frequencies these spectra begin at the origin and grow in size with decreasing frequency, passing through a minimum, and reaching a steady state value for low frequencies, which is located on the real axis. The frequency at the minimum of this plot corresponds to the recombination rate constant for the electrons, and its inverse represents the pseudo first order lifetime of the electron.

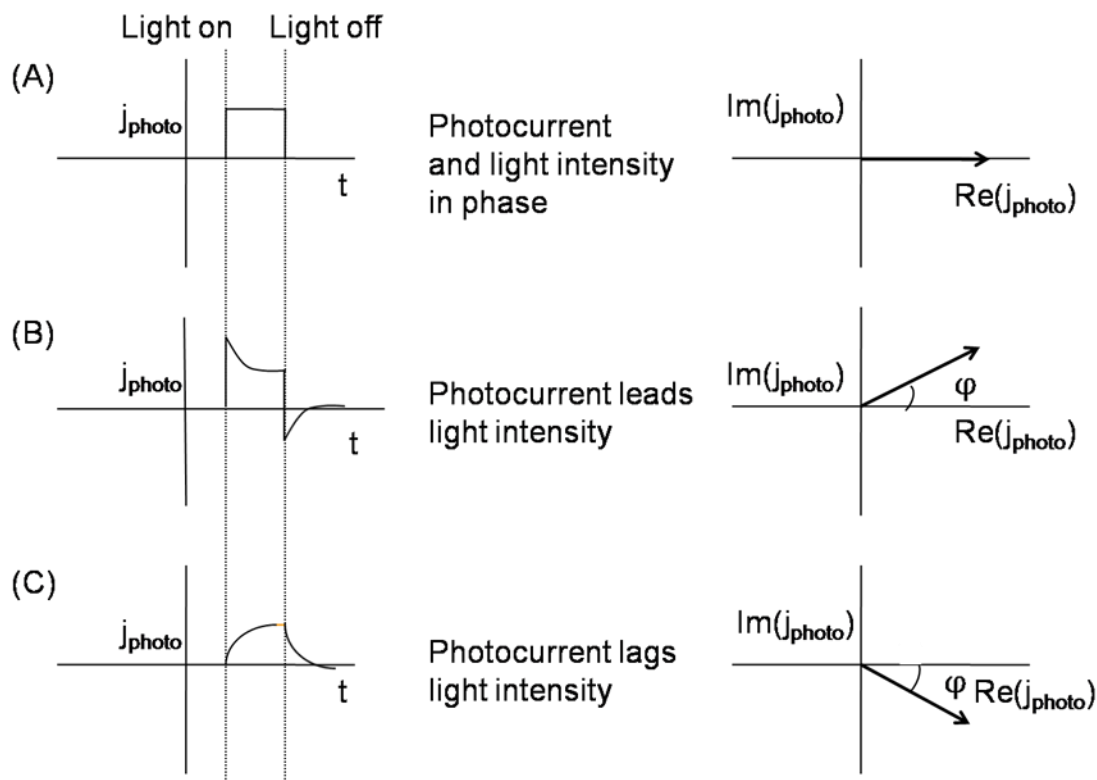


Figure 2-10. Photocurrent transients on the left and their complex plot representation on the right. (A) Left: Light is switched on and immediately reaches steady state. Right: Corresponding IMPS plot is located on real axis with no phase shift. (B) Left: Photocurrent spikes when light is switched on and then decays. Right: IMPS plot is located in the first quadrant in this case (C) Left: Photocurrent lags light intensity and slowly rises with time. Right: The IMPS plot is located in the fourth quadrant in this case.

A typical IMPS spectrum for a semiconductor electrode that exhibits interfacial recombination is illustrated below in Figure 2-11 and a corresponding scheme highlighting the different processes occurring at the interface are shown in Figure 2-12. There are several important parameters that can be extracted from this plot, which are highlighted in Figure 2-11. The first is the point at which the plot crosses over from quadrant IV to quadrant I and is denoted by g_{ac} . This corresponds to the case where no interfacial recombination is occurring and represents the maximum obtainable photocurrent. However, the actual photocurrent that can be obtained from these devices is

represented by the low frequency intercept ReJ_0 and corresponds to steady state conditions. The third parameter that can be extracted from these measurements is the frequency at which the maximum of the imaginary photocurrent is observed and is indicated by ω^* . This parameter relates to the relaxation time of photoexcited carriers at the surface states and usually corresponds to the rate constant for interfacial recombination. Figure 2-12 illustrates two processes that can occur at the interface of a photovoltaic semiconductor.⁵⁹ Ideally, light absorption leads to charge carrier generation and extraction at the corresponding electrodes (case i). However, it is possible that the photogenerated electron will become captured at a surface state. In this case, there are two possible outcomes. It is possible that the electron will become trapped but will then be transferred to the electrode and will still contribute to the photocurrent. Alternatively, once trapped the electron will recombine with the surface trapped hole and will not contribute to the photocurrent.

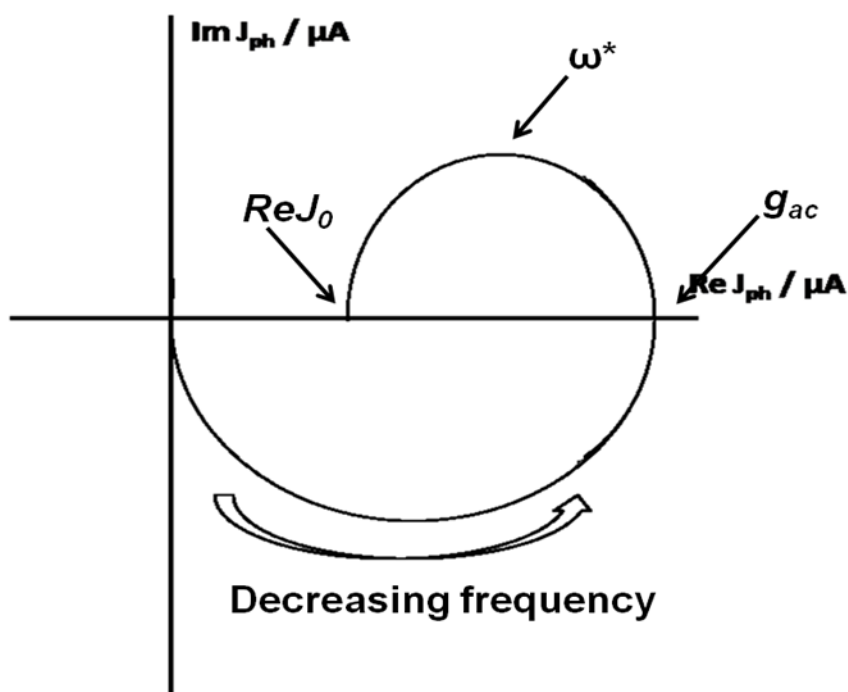


Figure 2-11. A typical IMPS spectrum shown in Nyquist plot representation. The IMPS curve begins at the origin at a high frequency and moves across the fourth quadrant until it crosses over at the real axis into the first quadrant and eventually reaches the steady-state value ReJ_0 .

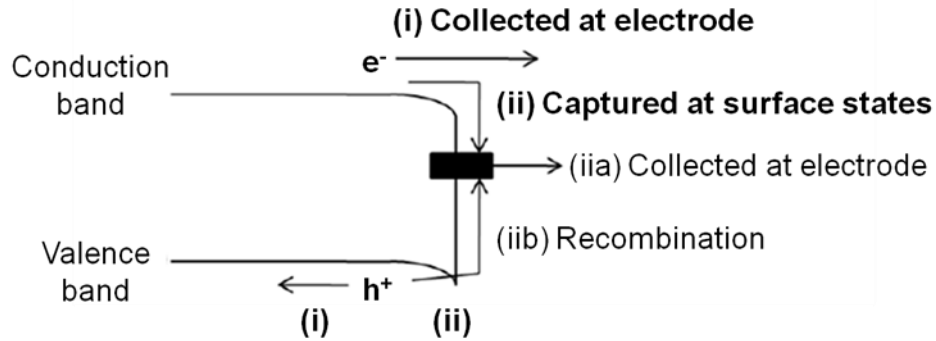


Figure 2-12. Schematic illustrating (i) charge carrier collection at the electrodes, and (ii) charge carrier trapping at an interfacial state leading to (iia) extraction or (iib) interfacial recombination. Adapted from Ref. 59.

Two limiting cases for interfacial recombination are considered in further detail in Chapter 6 to gain a better understanding of the site where interfacial recombination is most likely occurring in bulk heterojunction organic solar cells. In case one it was assumed that once a charge carrier becomes trapped at an interfacial site it is not able to transfer to the electrode and recombines. The frequency dependent photocurrent response in quadrant one for this case was given by:

$$j_{photo}(\omega) = g_{ac} \left(1 - \frac{\gamma}{1 + \frac{i}{\omega k}} \right) \quad (11)$$

Where γ is the fraction of carriers captured by surface states and k is the pseudo first order rate constant for surface recombination. The above expression can be expressed for the real and imaginary components of the frequency dependent photocurrent as:

$$Re(j_{photo}) = g_{ac} \left(1 - \frac{\gamma}{1 + \frac{\omega^2}{k^2}} \right) \quad (12)$$

$$\text{Im}(j_{photo}) = g_{ac} \left(\frac{g\gamma\omega}{k \left(1 + \frac{\omega^2}{k^2} \right)} \right) \quad (13)$$

From equations 12 and 13 it can be seen that in the low frequency limit that $\text{Im}(j_{photo})$ goes to zero while $\text{Re}(j_{photo})$ approaches the value of $g_{ac}(1-\gamma)$, which represents the fraction of charge carriers that are collected in steady-state conditions. In the high frequency limit, $\text{Im}(j_{photo})$ goes to zero while $\text{Re}(j_{photo})$ approaches the value of g_{ac} , which represents the photocurrent that could be obtained if there were no losses due to interfacial recombination. Between these two limiting cases, the value of $\text{Im}(j_{photo})$ passes through a maximum and the frequency at which this occurs represents the pseudo first order rate constant ω^* for interfacial recombination in this case.

In case two it was assumed that electron transfer and recombination involve a common intermediate state at the interface and that charge transfer only occurs via the interfacial state. The frequency dependent photocurrent response in quadrant one for this case was given by:

$$j_{photo}(\omega) = g_{ac} \left(\frac{k_{tr} + i\omega}{k_{tr} + k_{rec} + i\omega} \right) \quad (14)$$

Where k_{tr} represents the charge transfer rate constant and k_{rec} is the recombination rate constant. The above expression can be expressed for the real and imaginary components of the frequency dependent photocurrent as:

$$\text{Re}(j_{photo}) = g_{ac} \left(\frac{(k_{tr} + k_{rec})k_{tr} + \omega^2}{(k_{tr} + k_{rec})^2 + \omega^2} \right) \quad (15)$$

$$\text{Im}(j_{photo}) = g_{ac} \left(\frac{k_{rec}\omega}{(k_{tr} + k_{rec})^2 + \omega^2} \right) \quad (16)$$

Equation 15 shows that $\text{Re}(j_{\text{photo}})$ goes to the value of $k_{tr}/(k_{tr}+k_{rec})$ at the low frequency limit while at the high frequency limit $\text{Re}(j_{\text{photo}})$ approaches the value for g_{ac} , which is the photocurrent that could be obtained if there were no losses due to interfacial recombination. From equation 16 it can be seen that $\text{Im}(j_{\text{photo}})$ goes to zero at the low and high frequency limit. Between these two limiting cases, the value of $\text{Im}(j_{\text{photo}})$ passes through a maximum and the frequency at which this occurs corresponds to the sum of $(k_{tr}+k_{rec})$. Using the experimental IMPS plots it was possible to separate and determine the values for k_{tr} and k_{rec} individually. Comparison of the two different recombination pathways described allowed us to conclude that interfacial recombination most likely occurs at the P3HT/PCBM interface in bulk heterojunction organic solar cells. Further details of these results and the experimental set-up are provided in Chapters 5 and 6.

2.9 References

- (1) Chamberlain, G. A. *Solar Cells* **1983**, 8, 47.
- (2) Gledhill, S. E.; Scott, B.; Gregg, B. A. *Journal of Materials Research* **2005**, 20, 3167.
- (3) Ghosh, A. K.; Morel, D. L.; Feng, T.; Shaw, R. F.; Rowe, C. A. *Journal of Applied Physics* **1974**, 45, 230.
- (4) Theander, M.; Yartsev, A.; Zigmantas, D.; Sundstrom, V.; Mammo, W.; Andersson, M. R.; Inganas, O. *Physical Review B* **2000**, 61, 12957.
- (5) Deussen, M.; Scheidler, M.; Bassler, H. *Synthetic Metals* **1995**, 73, 123.
- (6) Jorgensen, M.; Norrman, K.; Krebs, F. C. *Solar Energy Materials and Solar Cells* **2008**, 92, 686.
- (7) Tang, C. W. *Applied Physics Letters* **1986**, 48, 183.
- (8) Blom, P. W. M.; Mihailetschi, V. D.; Koster, L. J. A.; Markov, D. E. *Advanced Materials* **2007**, 19, 1551.
- (9) MacDiarmid, A. G. *Angewandte Chemie-International Edition* **2001**, 40, 2581.
- (10) Krebs, F. C. *Solar Energy Materials and Solar Cells* **2009**, 93, 394.
- (11) Sariciftci, N. S.; Smilowitz, L.; Heeger, A. J.; Wudl, F. *Science* **1992**, 258, 1474.

- (12) Sariciftci, N. S.; Braun, D.; Zhang, C.; Srdanov, V. I.; Heeger, A. J.; Stucky, G.; Wudl, F. *Appl. Phys. Lett.* **1993**, *62*, 585.
- (13) Halls, J. J. M.; Walsh, C. A.; Greenham, N. C.; Marseglia, E. A.; Friend, R. H.; Moratti, S. C.; Holmes, A. B. *Nature* **1995**, *376*, 498.
- (14) Yu, G.; Gao, J.; Hummelen, J. C.; Wudl, F.; Heeger, A. J. *Science* **1995**, *270*, 1789.
- (15) Hummelen, J. C.; Knight, B. W.; Lepeq, F.; Wudl, F.; Yao, J.; Wilkins, C. L. *Journal of Organic Chemistry* **1995**, *60*, 532.
- (16) Yang, X.; Loos, J. *Macromolecules* **2007**, *40*, 1353.
- (17) van Bavel, S.; Veenstra, S.; Loos, J. *Macromolecular Rapid Communications* **2010**, *31*, 1835.
- (18) Hoppe, H.; Sariciftci, N. S. *Journal of Materials Chemistry* **2006**, *16*, 45.
- (19) Ohkita, H.; Ito, S. *Polymer* **2011**, *52*, 4397.
- (20) Clarke, T. M.; Jamieson, F. C.; Durrant, J. R. *Journal of Physical Chemistry C* **2009**, *113*, 20934.
- (21) Howard, I. A.; Laquai, F. *Macromolecular Chemistry and Physics* **2010**, *211*, 2063.
- (22) Deibel, C.; Dyakonov, V. *Reports on Progress in Physics* **2010**, *73*.
- (23) Jorgensen, M.; Norrman, K.; Gevorgyan, S. A.; Tromholt, T.; Andreasen, B.; Krebs, F. C. *Advanced Materials* **2012**, *24*, 580.
- (24) Boudreault, P. L. T.; Najari, A.; Leclerc, M. *Chemistry of Materials* **2011**, *23*, 456.
- (25) Hadipour, A.; de Boer, B.; Wildeman, J.; Kooistra, F. B.; Hummelen, J. C.; Turbiez, M. G. R.; Wienk, M. M.; Janssen, R. A. J.; Blom, P. W. M. *Advanced Functional Materials* **2006**, *16*, 1897.
- (26) Wienk, M. M.; Kroon, J. M.; Verhees, W. J. H.; Knol, J.; Hummelen, J. C.; van Hal, P. A.; Janssen, R. A. J. *Angewandte Chemie-International Edition* **2003**, *42*, 3371.
- (27) Kim, J. Y.; Kim, S. H.; Lee, H. H.; Lee, K.; Ma, W. L.; Gong, X.; Heeger, A. J. *Advanced Materials* **2006**, *18*, 572-+.
- (28) Pivrikas, A.; Neugebauer, H.; Sariciftci, N. S. *Sol. Energy* **2011**, *85*, 1226.
- (29) Li, G.; Yao, Y.; Yang, H.; Shrotriya, V.; Yang, G.; Yang, Y. *Advanced Functional Materials* **2007**, *17*, 1636.
- (30) Small, C. E.; Chen, S.; Subbiah, J.; Amb, C. M.; Tsang, S. W.; Lai, T. H.; Reynolds, J. R.; So, F. *Nature Photonics* **2012**, *6*, 115.

- (31) Li, G.; Zhu, R.; Yang, Y. *Nat. Photonics* **2012**, *6*, 153.
- (32) Choulis, S. A.; Nelson, J.; Kim, Y.; Poplavskyy, D.; Kreouzis, T.; Durrant, J. R.; Bradley, D. D. C. *Applied Physics Letters* **2003**, *83*, 3812.
- (33) Allemand, P. M.; Koch, A.; Wudl, F.; Rubin, Y.; Diederich, F.; Alvarez, M. M.; Anz, S. J.; Whetten, R. L. *Journal of the American Chemical Society* **1991**, *113*, 1050.
- (34) Kroto, H. W.; Allaf, A. W.; Balm, S. P. *Chemical Reviews* **1991**, *91*, 1213.
- (35) Rispens, M. T.; Meetsma, A.; Rittberger, R.; Brabec, C. J.; Sariciftci, N. S.; Hummelen, J. C. *Chemical Communications* **2003**, 2116.
- (36) Jamieson, F. C.; Domingo, E. B.; McCarthy-Ward, T.; Heeney, M.; Stingelin, N.; Durrant, J. R. *Chemical Science* **2012**, *3*, 485.
- (37) Dupuis, A.; Tournebize, A.; Bussiere, P. O.; Rivaton, A.; Gardette, J. L. *European Physical Journal-Applied Physics* **2011**, *56*.
- (38) Haufler, R. E.; Conceicao, J.; Chibante, L. P. F.; Chai, Y.; Byrne, N. E.; Flanagan, S.; Haley, M. M.; O'Brien, S. C.; Pan, C.; Xiao, Z.; Billups, W. E.; Ciufolini, M. A.; Hauge, R. H.; Margrave, J. L.; Wilson, L. J.; Curl, R. F.; Smalley, R. E. *Journal of Physical Chemistry* **1990**, *94*, 8634.
- (39) Iijima, S. *Nature* **1991**, *354*, 56.
- (40) Novoselov, K. S.; Geim, A. K.; Morozov, S. V.; Jiang, D.; Zhang, Y.; Dubonos, S. V.; Grigorieva, I. V.; Firsov, A. A. *Science* **2004**, *306*, 666.
- (41) Robertson, J. *Materials Science & Engineering R-Reports* **2002**, *37*, 129.
- (42) McCreery, R. L. *Chemical Reviews* **2008**, *108*, 2646.
- (43) Robertson, J.; Davis, C. A. *Diamond and Related Materials* **1995**, *4*, 441.
- (44) Sjostrom, H.; Stafstrom, S.; Boman, M.; Sundgren, J. E. *Physical Review Letters* **1995**, *75*, 1336.
- (45) Robertson, J.; Oreilly, E. P. *Physical Review B* **1987**, *35*, 2946.
- (46) Alibart, F.; Drouhin, O. D.; Debiemme-Chouvy, C.; Benlahsen, M. *Solid State Communications* **2008**, *145*, 392.
- (47) Muhl, S.; Mendez, J. M. *Diamond and Related Materials* **1999**, *8*, 1809.
- (48) Mckenzie, D. R.; Yin, Y.; Marks, N. A.; Davis, C. A.; Pailthorpe, B. A.; Amaratunga, G. A. J.; Veerasamy, V. S. *Diamond and Related Materials* **1994**, *3*, 353.
- (49) Rodil, S. E.; Muhl, S. *Diamond and Related Materials* **2004**, *13*, 1521.

- (50) Gunes, S.; Neugebauer, H.; Sariciftci, N. S. *Chemical Reviews* **2007**, *107*, 1324.
- (51) Shrotriya, V.; Li, G.; Yao, Y.; Moriarty, T.; Emery, K.; Yang, Y. *Advanced Functional Materials* **2006**, *16*, 2016.
- (52) Li, Z.; Gao, F.; Greenham, N. C.; McNeill, C. R. *Advanced Functional Materials* **2011**, *21*, 1419.
- (53) Pivrikas, A.; Sariciftci, N. S.; Juska, G.; Osterbacka, R. *Progress in Photovoltaics* **2007**, *15*, 677.
- (54) Dennler, G.; Mozer, A. J.; Juska, G.; Pivrikas, A.; Osterbacka, R.; Fuchsbauer, A.; Sariciftci, N. S. *Organic Electronics* **2006**, *7*, 229.
- (55) Garcia-Belmonte, G.; Munar, A.; Barea, E. M.; Bisquert, J.; Ugarte, I.; Pacios, R. *Organic Electronics* **2008**, *9*, 847.
- (56) Byers, J. C.; Ballantyne, S.; Rodionov, K.; Mann, A.; Semenikhin, O. A. *ACS Applied Materials & Interfaces* **2011**, *3*, 392.
- (57) Peter, L. M. *Chemical Reviews* **1990**, *90*, 753.
- (58) Dloczik, L.; Ileperuma, O.; Lauermaun, I.; Peter, L. M.; Ponomarev, E. A.; Redmond, G.; Shaw, N. J.; Uhlendorf, I. *Journal of Physical Chemistry B* **1997**, *101*, 10281.
- (59) Rotenberg, Z. A.; Semenikhin, O. A. *Journal of Electroanalytical Chemistry* **1991**, *316*, 165.

Chapter 3

3 Photocurrent Generation in Carbon Nitride and Carbon Nitride/Conjugated Polymer Composites

3.1. Introduction

The motivating factors in the development of next generation photovoltaics are new materials and methods for the fabrication of solar devices on a large scale and at a low cost. Polymer solar cells represent a promising opportunity toward the realization of this goal for several reasons, such as high absorption coefficients that permit the use of extremely thin films, which significantly reduces the materials costs, as well as the ability to use high throughput fabrication techniques such as jet printing, spray-coating, etc.^{1,2} The vast majority of polymer solar cells studied at present use fullerenes and their derivatives as the ubiquitous acceptor materials which enhance exciton dissociation in conjugated polymers upon light absorption.³⁻⁵ The overwhelming use of fullerenes is due to their exceptional electron accepting abilities combined with efficient electron transport properties.^{6,7} The resulting active layer of a polymer solar cell typically contains 50% or more of a fullerene acceptor mixed together with a donor p-type conjugated polymer in a complex fashion forming a so-called bulk heterojunction, with exciton dissociation and photoinduced charge transfer occurring on the nanoscale between the interdispersed and very finely phase segregated donor and acceptor phases.⁸ Another very important role of the fullerene phase is to provide conducting pathways throughout the photoactive film to ensure efficient extraction of photogenerated carriers.

Overall, to ensure high efficiency, a polymer donor-acceptor solar cell should have a very specific and very fine nanostructure, which should also be maintained throughout the cell service life.⁹ The difficulty in creating and maintaining such an intricate nanostructure between the donor and acceptor phases remains one of the limiting factors on the way to commercially viable polymer donor-acceptor solar cells.¹⁰⁻¹³ The other issues with fullerenes as acceptors are their low-lying LUMO that limits the cell output voltage, as well as the need to use high fullerene loading ratios, which increases costs and reduces the absorption of light by the active layer (the majority of solar light in polymer photovoltaic devices is absorbed by the polymer and not by the fullerene).⁵ Therefore, there is a need to search for alternative acceptor materials for polymer donor-acceptor cells.^{14,15} The new acceptor materials should not only possess superior electron-acceptor properties and suitable LUMO position but must also ensure efficient transport of

photogenerated carriers¹⁶ (which has been a major stumbling block for many molecular donor-acceptor systems) while remaining economically viable.

Semiconducting carbon films and their composites have attracted the attention of researchers for their potential use in optical and electronic devices.^{17,18} Vacuum sputtered carbon nitrides (CNx) are a potential new class of semiconductor materials that have not yet received sufficient attention for photovoltaic applications.¹⁹⁻²² The majority of research to date has focused on the outstanding mechanical and electrochemical properties of CNx,²³⁻²⁶ whereas carbon nitrides appear to be a very promising material for potential photovoltaic device applications due to their n-type semiconductor properties,²⁷ high absorption coefficient in the visible region,²⁸ tunable electronic and optical properties,²² chemical robustness and inertness,²⁹ etc.

However, to the best of our knowledge, there has only been one report of a photovoltaic effect observed in a vacuum deposited highly sp² hybridized CNx material, with the photocurrent produced being very low.²⁰ This may be a result of the high defect density present in these materials due to their amorphous nature.³⁰ We ourselves have not succeeded in obtaining appreciable and reproducible photocurrents from vacuum deposited CNx films (see below). However, we were able to show, for the first time, that vacuum deposited CNx can serve as an efficient electron acceptor in organic conjugated polymer-based solar cells. This was also confirmed by electrochemical and photoelectrochemical measurements. Taken together with our data on the nanoscale structure of CNx films deposited onto conjugated polymer substrates,³¹ it is likely that CNx is able to form a bulk heterojunction with the donor conjugated polymer phase. These results suggest that CNx may be an interesting practical alternative to fullerenes as they have the potential to overcome some of the drawbacks associated with such acceptor materials. Moreover, unlike the randomly dispersed films obtained with solution deposited polymer-fullerene mixtures, the interpenetrating network formed by vacuum deposited CNx throughout the polymer matrix should be quite stable. This may be beneficial for the improvement of the lifetime of the bulk heterojunction structure for polymer based solar cells.

The influence of the deposition parameters such as deposition power and nitrogen content on the structure and electronic and optical properties of highly sp^2 hybridized CN_x materials was also studied. It is well known that the deposition parameters for vacuum deposited carbon nitride films have a significant impact on their structure and therefore on their optical and electronic properties.³²⁻³⁷ The incorporation of nitrogen into amorphous carbon promotes the clustering of carbon nitride sp^2 domains, with a variety of possible bonding configurations, while decreasing the long range order of the graphitic domains.^{36,38} The decrease in the graphitic domains and increase in the amount of CN_x nanoclusters should lead to improved semiconductor properties and thus improved photoefficiency.²¹

3.2. Experimental

Substrates. Indium tin oxide (ITO) coated glass electrodes ($R_s = 4 - 8 \Omega$) were purchased from Delta Technologies, Ltd. The electrodes were sonicated successively in detergent, water, acetone, ethanol and deionized water and dried in an oven at 90°C after removing residual water with nitrogen gas. 3,4-Ethylenedioxythiophene (EDOT) (Aldrich, 97 %) was used as received. 2,2'-Bithiophene (BT) (Aldrich, 97 %) was purified by vacuum sublimation. Galvanostatic electrochemical deposition was used to deposit thin films of poly(3,4-ethylenedioxythiophene) (PEDOT) and poly(2,2'-bithiophene) (PBT). PEDOT was prepared from a solution containing 0.37 M EDOT and 0.1 M tetrabutylammonium hexafluorophosphate (TBAPF₆) in acetonitrile. PBT was prepared from a solution containing 5×10^{-3} M 2,2'-bithiophene and 0.1 M TBAPF₆ in acetonitrile. Films were rinsed in pure acetonitrile following deposition to remove excess monomer and electrolyte from the electrode surface.

Vacuum Deposition of Carbon Nitride. Deposition of carbon nitride films was performed using direct current (DC) reactive cathodic magnetron sputtering in a custom built vacuum deposition system or in a commercial reactor (MP 300 S model, Plassys, France). For each CN_x deposition the total pressure in the vacuum chamber was 1 Pa or 10 Pa using a mixture of pure Ar gas with pure N₂ gas. The N₂ partial pressure was varied from 5 % to 50 % of the total deposition pressure to prepare films with different

nitrogen contents. The deposition power was varied at 25 W, 50 W and 100 W. The deposition time was 20 minutes. The nitrogen content in the films increased with an increase in the nitrogen content in plasma and was determined from the atomic ratio of nitrogen and carbon obtained from the XPS spectra (see Appendix A: Supporting Information for Chapter 3).

Film Characterization. The film thicknesses for the deposition conditions employed in this work were determined from the observation of cross sections of the samples using scanning electron microscopy (FEG-SEM, Ultra55, Zeiss) images and are presented in Appendix A: Supporting Information for Chapter 3. A U4001 spectrophotometer (Hitachi) was used to acquire the UV-Vis-IR spectra of CN_x films. All spectra were baseline corrected to take into account absorption by the indium tin oxide coated glass slides. XPS analyses were carried out at ITODYS laboratory (Paris, France) using a VG ESCALAB 250-iXL spectrometer. The X-ray source was monochromatic Al K α radiation (1486.6 eV). The survey spectra were recorded with a pass energy of 100 eV, whereas the high-resolution spectra were recorded with a pass energy of 20 eV in the constant analyzer energy mode. The spot size was ca. 500 μ m. The photoelectron take-off angle was of 90° with respect to the CN_x surface. Each spectrum was background corrected using the Shirley's method. All the binding energy (BE) scales were referenced by setting the C1s main contribution BE to 285 eV.

Device Architecture. Three separate types of device architectures were prepared for measurement in either solution or a solid state configuration. For solution measurements, the substrates consisted of CN_x vacuum deposited onto ITO electrodes (ITO/CN_x) or CN_x films deposited onto PBT coated ITO substrates (ITO/PBT/CN_x). Solid state CN_x based devices were prepared in either a sandwich ITO/CN_x/Au configuration or using a standard photovoltaic architecture of ITO/PEDOT/PBT/CN_x/Al with PBT being a donor conjugated polymer and CN_x being an acceptor. Au and Al contacts were fabricated by thermal evaporation.

Device Characterization. Electrochemical and solid state solar cell measurements were performed using a PAR 263A potentiostat–galvanostat (Princeton Applied Research)

coupled with a Solartron 1250 frequency response analyzer. Steady state measurements were controlled using version 3.1 CorrWare software and frequency domain measurements were controlled using version 2.8 ZPlot software (Scribner Associates Inc.). The light source used was a 405 nm, 20 mW laser diode (LD1510, Power Technology) having a light intensity of 2×10^{17} photons $s^{-1} cm^{-2}$ (90 mW cm^{-2}). Pyrex glass cells without separation of the anodic and cathodic compartments were used for all electrochemical and photoelectrochemical measurements. The cells were purged with Ar gas and sealed prior to measurement. Silver wire quasi-reference electrodes were used for all measurements. To ensure their reproducibility, the reference electrodes were prepared and stored in solutions of the corresponding measurement electrolyte.³⁹⁻⁴² Cyclic voltammetry measurements were performed in acetonitrile (< 35 ppm H₂O) using 0.1 M TBAPF₆ (Fluka, > 99 %) as the supporting electrolyte. A scan rate of 100 mV s^{-1} was used for all measurements. Mott-Schottky and photoelectrochemical measurements were carried out in aqueous solutions made with Millipore deionized water with 0.1 M KCl as the supporting electrolyte. The Mott-Schottky measurements were performed using an ac amplitude of 10 mV rms at a frequency of 6.626 kHz, which was verified to be high enough for the electrode impedance to be well approximated by a serial RC circuit.

Atomic Force Microscopy. Current sensing AFM (CS-AFM) measurements were carried out to characterize the local nanoscale conductivity and distribution of conducting domains in the carbon nitride/conjugated polymer composites. These measurements were performed in air simultaneously with the acquisition of the topography data generating spatially resolved images of the local conductivity and morphology of the samples. A multi-mode AFM (Veeco Metrology) equipped with a Nanoscope IV controller (Veeco) and a CS-AFM extension module was used. The measurements were performed in contact mode using DDESP conducting diamond coated AFM probes (Nanoworld, typical force constant 0.35 N/m). A bias of + 500 mV was applied to the AFM tip with respect to the sample and therefore the conducting regions (regions of higher positive currents) appear bright in these images (the positive current direction is from the sample into the tip).

3.3 Results and Discussion

Characterization of vacuum deposited CNx films

Conductivity of CNx. The electronic properties of carbon nitride are highly dependent upon the local bonding and structure formed throughout the CNx film. Due to the large number of techniques available to create these materials, it is useful to classify CNx as highly sp^2 hybridized carbon nitride, which is quite different from the highly sp^3 hybridized nitrogen doped diamond.³³ The enhanced conductivity of highly sp^3 hybridized nitrogen doped diamond has been attributed to sp^2 rich CNx grain boundaries.⁴³ Therefore, it is of interest to prepare CNx materials that are predominantly sp^2 hybridized as it is the π and π^* states that control the electronic and optical properties of these materials.⁴⁴ There are still many aspects of the deposition process and its impact on the film properties that are not well understood due to the large number of deposition parameters. The target power and nitrogen content in the gas plasma have both been shown to modify the local structure as well as the amount of nitrogen that is incorporated into CNx films.⁴⁵ The amount of nitrogen incorporated into highly sp^2 hybridized DC and RF sputtered CNx is known to modify the local bonding and structure, which directly affects the electronic properties.^{22,36}

Figure 3-1 shows the conductivity as a function of nitrogen content for CNx films prepared at different magnetron powers. For these measurements, we used a solid state architecture that consisted of a CNx layer sandwiched between ITO and Au electrodes taking into account the variations in the film thicknesses with the deposition conditions (see Appendix A: Supporting Information for Chapter 3). The conductivity of CNx did not vary significantly for target powers of 25 W and 50 W. It has been shown previously that carbon nitride films prepared at low deposition powers have a significant graphitic structure.⁴⁶ The higher conductivity observed in films prepared at lower target powers is a result of the graphitic structure which contains a significant density of energy levels in the midgap region, which facilitate electronic conduction. Such graphitic regions may be localized at grain boundaries as discussed in the literature⁴³ and form percolation conduction paths inside the films bypassing semiconducting nitrogen-rich domains. This

can explain the virtual independence of the films conductivity at low powers on the nitrogen content.

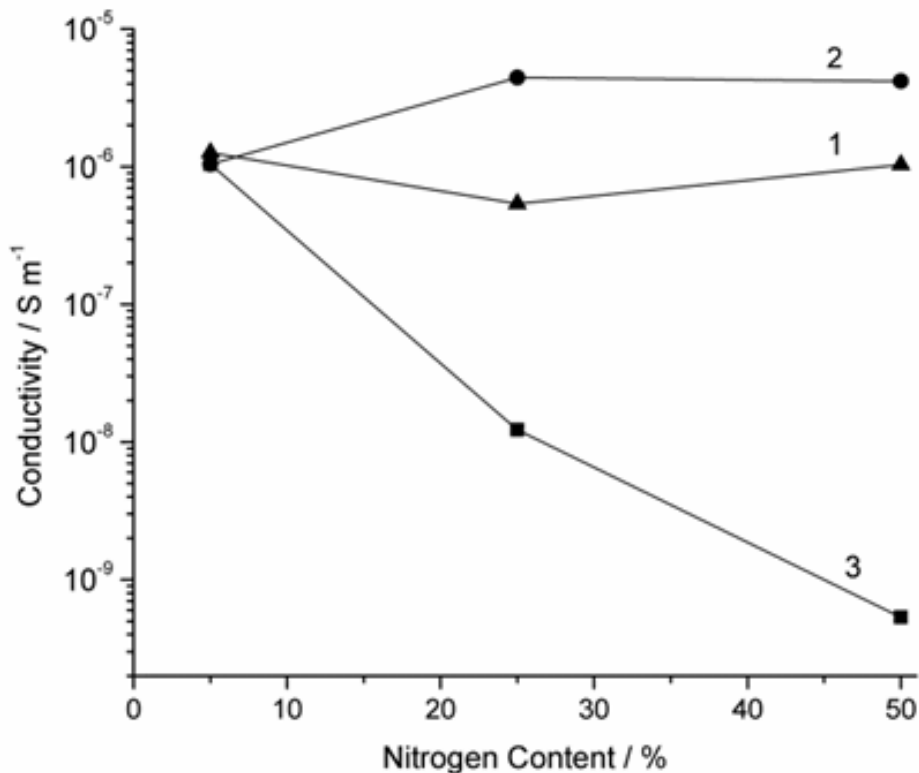


Figure 3-1. Conductivity of CN_x films as a function of N_2 content in the gas mixture for films prepared with a deposition power of 25 W (plot 1), 50 W (plot 2), 100 W (plot 3) during deposition. The deposition time for all films was 20 minutes. The lines are guides for the eye.

For films prepared at 100 W, the conductivity decreases almost three orders of magnitude with increasing nitrogen content. The dramatic decrease in conductivity cannot be attributed to thickness variations as the conductivity values presented were corrected for the differences in film thickness. The significant drop in conductivity at increased target power and nitrogen content can be attributed to structural and chemical modifications of the films. This suggests that films prepared at higher target powers and nitrogen

concentrations contain less graphitic sp^2 hybridized material and therefore less percolation pathways that likely determine the conductivity in materials obtained at lower powers. This hypothesis is further supported by the changes in conductivity for a CNx film under illumination reported below.

Photoconductivity of CNx. For all CNx films, the conductivity was examined in the dark and under illumination. There have been previous reports of photoconductivity in tetrahedral CNx and for highly sp^2 hybridized CNx.^{47,48} In this work it was found that CNx films prepared at low powers showed little or no change in conductivity under illumination for the deposition parameters examined. The curves (not shown) showed Ohmic behavior. It was only films prepared at 100 W and nitrogen contents of 25 % and 50 % that showed a significant change in their conductivity under illumination, or photoconductivity. Figure 3-2 shows typical J-V plots measured in the dark and under illumination for an ITO/CNx/Au sandwich device prepared at 100 W and 50 % N₂. It is seen that the slope of the J-V plots increases under illumination indicating an increase in the film conductivity. However, the linear character of the J-V plots indicates that even at high powers and nitrogen contents the films retain their Ohmic behavior and show no rectification that could be expected for an n-type semiconductor in a Schottky diode configuration. Also, no photovoltage has been detected. Taken together with the lack of photoconductivity in the films prepared at lower target powers, these facts suggest that for all investigated films the conductivity through graphitic percolation pathways still remains the dominant conductivity mechanism. For films prepared at lower powers, the graphitic content is too high for any significant increase in the carrier concentration under illumination. At the same time, the occurrence of photoconductivity at higher powers and nitrogen contents suggests that indeed there is photogeneration of carriers in nitrogen-enriched domains, which therefore do exhibit semiconductor behavior. However, due to the presence of a percolating graphitic phase, these carriers cannot give rise to a photovoltaic effect and produce photoconductivity instead. This hypothesis correlates well with the results of photovoltaic measurements of CNx films deposited onto conjugated polymer substrates presented below and explains why there were no reproducible observations of the photovoltaic effect in CNx films. It can be anticipated that such an effect could still be found if one eliminates the percolation conductivity

pathways due to increased sp^2 graphitic content, perhaps, by means of a post-treatment of CNx materials.

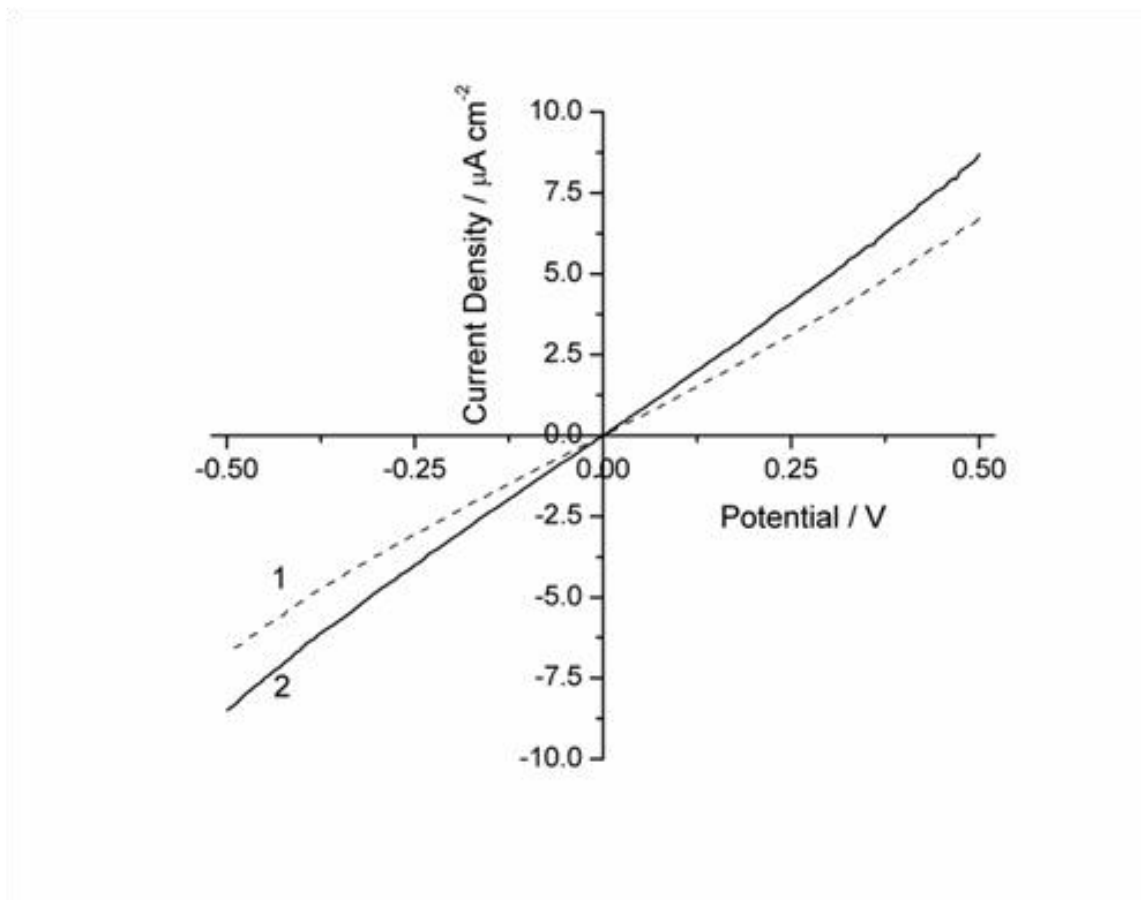


Figure 3-2. Dark conductivity (plot 1) and photoconductivity (plot 2) for ITO/CNx/Au. CNx was prepared at 100 W and 50 % N_2 .

Evidence of space charge formation in CNx films. The above hypothesis is supported by the fact that, despite showing no photovoltaic properties, CNx films were still found to sustain the formation of a space-charge layer consistent with their being n-type semiconductors. This was confirmed by Mott Schottky measurements. The Mott-Schottky measurements analyze the evolution of the capacitance of a semiconductor electrode with the applied bias. If a space-charge region is formed inside the semiconductor electrode, this capacitance should follow the Mott-Schottky law,³⁹ which is given by the following equation:

$$\frac{1}{C_{SC}^2} = \left(\frac{2}{e_0 N_D \epsilon \epsilon_0 A^2} \right) \cdot \left(E - E_{fb} - \frac{kT}{e_0} \right) \quad (1)$$

where C_{SC} is the space charge capacitance, ϵ is the dielectric constant of the semiconductor, ϵ_0 is the permittivity of free space, e_0 is the elementary charge, A is the electrode surface area, $E - E_{fb}$ is the potential drop across the space charge region in the semiconductor, k is the Boltzmann constant and T is the absolute temperature.

It follows from the Mott-Schottky law that, if a space-charge layer is formed in the semiconductor, the experimental dependence of the inversed squared capacitance on the applied bias should have a linear portion (the deviations from linearity are usually related to the finite thickness of the semiconductor layer or potential redistribution at the contacts).^{39,42} In this case, the slopes of the linear portions of the Mott-Schottky plots allow one to find the density of the space charge within the space charge region, or the dopant density. The intercepts of the Mott-Schottky plots on the X-axis produce the value of a so-called flat-band potential, which is related to the work function of the semiconductor material. It is important to emphasize that Mott-Schottky measurements are performed using ac modulation of the applied voltage and thus, unlike steady-state measurements, are able to distinguish between the resistive effects due to heterogeneity of the semiconductor material and the presence of percolation conductivity pathways, and the capacitive behavior originating from the formation of the space-charge region.

The Mott-Schottky measurements were performed in solution with a so-called electrolytic contact.^{39,49} The use of a solution contact is often advantageous for the characterization of semiconductor materials since such an arrangement allows one to avoid complications arising at solid cell contacts (poor energy level matching, high recombination rate, chemical compatibility, etc).

Figure 3-3A shows a typical Mott-Schottky plot for a CNx film in an aqueous solution. Similar plots were obtained for the other CNx films except for CNx films prepared at 100 W and 50 % N₂, which could not be characterized due to the well known delamination in solution of CNx films prepared at higher deposition powers and nitrogen contents.⁵⁰ All

Mott-Schottky plots showed distinct linear portions that had a positive slope with increasing positive potential. This behavior is typical for n-type semiconductor materials and clearly indicates the formation of a space-charge region.⁵¹

Figure 3-3B shows the dependence of the donor density of CN_x extracted from the linear portions of the Mott-Schottky plots on the nitrogen content for target powers of 25 W, 50 W, and 100 W. The deposition power was not found to have a significant effect on the donor density, whereas a clear decrease in the donor density was observed for increasing nitrogen contents. This is a very interesting result as it is nitrogen that functions as an n-type dopant in the carbon film to produce an n-type semiconductor. Therefore, one could expect that the dopant density would increase, not decrease with an increase in the nitrogen content.

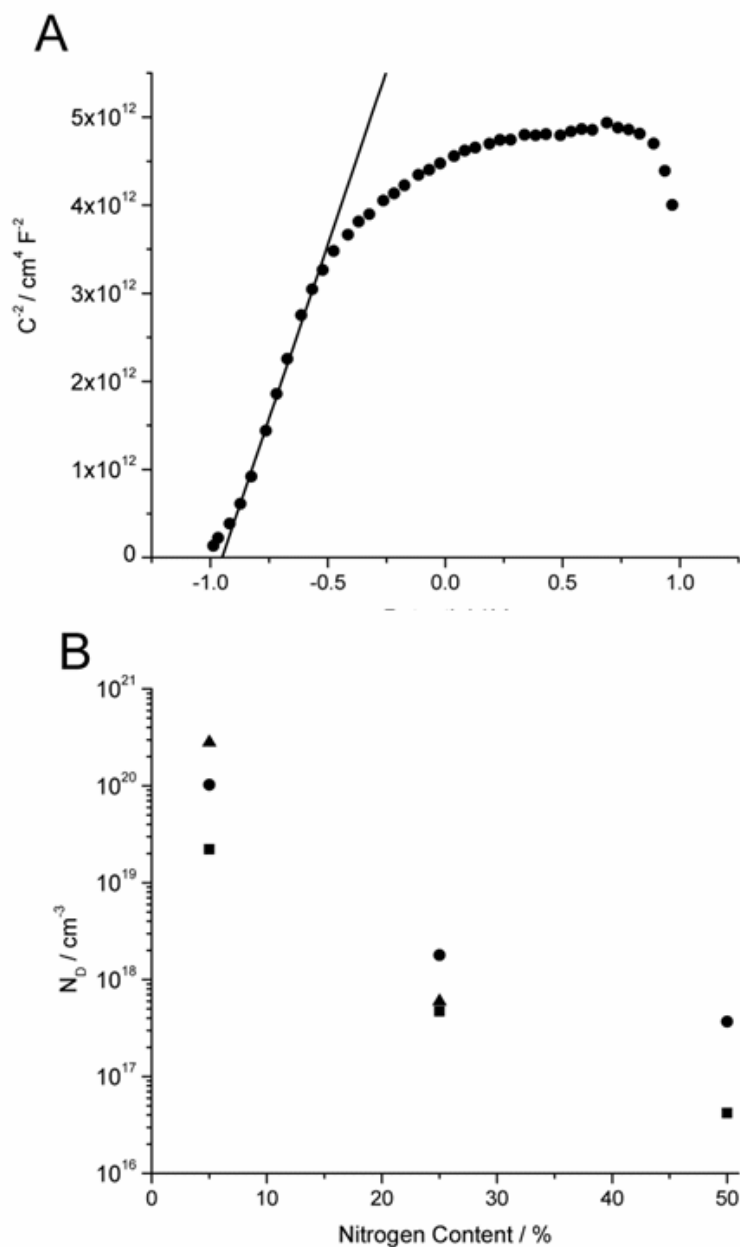


Figure 3-3. (A) Mott-Schottky plot for CN_x on an ITO substrate in aqueous 0.1 M KCl. CN_x was prepared at 50 W and 25 % N₂. (B) Donor density determined from slopes of Mott-Schottky plots for CN_x films as a function of nitrogen content for deposition powers of 25 W (■), 50 W (●) and 100 W (▲).

A possible explanation may be related to the well known fact that nitrogen is able to act as a dopant only in certain bonding configurations.⁵² In addition, the dopant density may

be affected by disorder in a semiconductor material that increases the density of charge trapped in the space-charge layer. It is known that an increase in the nitrogen content in the films is accompanied by an increase in the number of nitrile groups.⁵³ The nitrile groups are bond terminating and thus, with increasing nitrogen content, there should be a decrease in the size of the carbon nitride clusters, which could also be accompanied by a decrease in the degree of disorder. Such changes may or may not be accompanied by an increase in the total nitrogen content in the film. It has been shown that the amount of nitrogen incorporated into CN_x films increases as the nitrogen content used during deposition increases and then plateaus beyond approximately 30 – 40 % N₂ in the gas plasma.⁵⁴ For films prepared at 25 W and 50 W, nitrogen contents in the plasma chamber of 5 % to 50 % led to a nitrogen content in the film of ca. 20 % to 45 %, as determined using XPS (see Appendix A: Supporting Information for Chapter 3). As well, it was found for films prepared at 50 W that the nitrogen sp²/sp³ ratio remained practically constant at ca. 0.44/0.56, regardless of the nitrogen content in the films, which indicates that the main effect of adding nitrogen to the plasma during deposition is to increase the total nitrogen content in the films without significantly modifying the relative proportion of sp² and sp³ nitrogen regions.

Therefore, our results suggest that an increase in the nitrogen content in the gas plasma not only decreased the sp² graphitic content but also increased the total amount of nitrogen contained in the film. Furthermore, the Mott-Schottky experiments demonstrate that the amount of nitrogen used during deposition has a greater affect on the dopant density than does the target power, while the conductivity measurements indicate that the deposition power has a significant impact on the electronic structure of the film. These results once again demonstrate the complexity of the CN_x deposition mechanism and the need for a more detailed understanding of the influence of the deposition conditions on the electronic and semiconductor properties of CN_x films. However, it was demonstrated that the semiconductor properties of CN_x films were the best for films deposited at high power and high nitrogen contents, which featured the lowest parasitic conductivity and the most developed space charge region.

Photocurrent generation in CNx/polymer composites

As was shown above, CNx films alone did not show any photovoltaic effect but still demonstrated the ability of charge carrier photogeneration, as evidenced by the conductivity changes under illumination, and the formation of a space charge layer, as evidenced by Mott-Schottky measurements in solution. These effects were consistent with the anticipated n-type semiconductor behavior. It was therefore of interest to combine n-type CNx materials with a p-type conjugated polymer. In our earlier paper, we demonstrated the possibility of the preparation of such composite materials by vacuum deposition of CNx films onto the conjugated polymer poly(2,2'-bithiophene) (PBT).³¹ In this work, we test similar CNx/polymer composites for photocurrent generation in both solid-state configuration and in solution.

Figure 3-4 shows an energy level diagram expected for a CNx and polybithiophene interface based on the work function, electrochemical and optical data for CNx and PBT. The work function of CNx was shown in the literature to be ca. 5.1 eV and did not depend on nitrogen or sp²/sp³ carbon content.^{55,56} The optical gap can vary to some extent with nitrogen and sp² content (see Appendix A: Supporting Information for Chapter 3), the average value of the bandgap was 1.3 eV. Therefore, the VB and CB edges for CNx were estimated to be -5.75 eV and -4.45 eV, respectively. The HOMO/LUMO levels of PBT have been determined from the onset of electrochemical oxidation and reduction respectively (See Fig. 3-9 below) to be -5.45 eV and -3.35 eV. Therefore, the conduction band edge of CNx lies ca. 1.1 eV lower in energy than the PBT LUMO level, which should make CNx an efficient electron acceptor material.

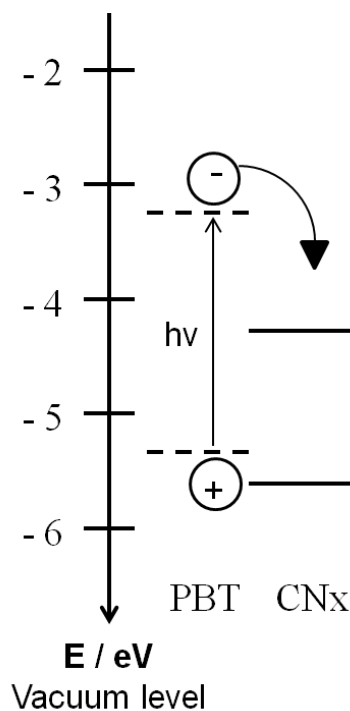


Figure 3-4. Energy level diagram of a CN_x/PBT interface illustrating the proposed photoinduced electron transfer from PBT to CN_x.

Photocurrent measurements in solid state and in solution. Photoelectrochemical measurements were performed in aqueous conditions using KCl as a supporting electrolyte. Polythiophene based electrodes have been shown to exhibit cathodic photocurrents during illumination under these conditions.⁵⁷ For our measurements, carbon nitride films were deposited onto PBT coated ITO substrates. It should be noted that CN_x films deposited onto ITO substrates without PBT exhibited little or no photocurrent generation in aqueous solution, consistent with the results obtained in solid-state sandwich devices. Therefore, photocurrent generation will occur due to light absorbed in the PBT layer. Figure 3-5 shows photocurrent measurements for films prepared at 25 W and nitrogen contents of 5 %, 25 %, and 50 %. The electrodes were illuminated through the CN_x layer. It can be seen that the CN_x/PBT composite films exhibit a substantially higher photocurrent than the pristine PBT film. Since the measured photocurrent remained cathodic, and in view of the demonstrated inability of CN_x films alone to generate a photocurrent, this fact suggests that the enhanced photocurrent

generation observed with the CNx/PBT composite films should be attributed to CNx functioning as an acceptor material when incorporated with a donor conjugated polymer such as polybithiophene. The same behavior is also observed for a solid state configuration. Figure 3-6 shows photocurrent-voltage curves obtained for two solid state organic photovoltaic devices with and without CNx. The results clearly demonstrate the improvement in photocurrent generation when CNx is incorporated into a polymer based solar cell (plot 1) compared to a device without CNx (plot 2).

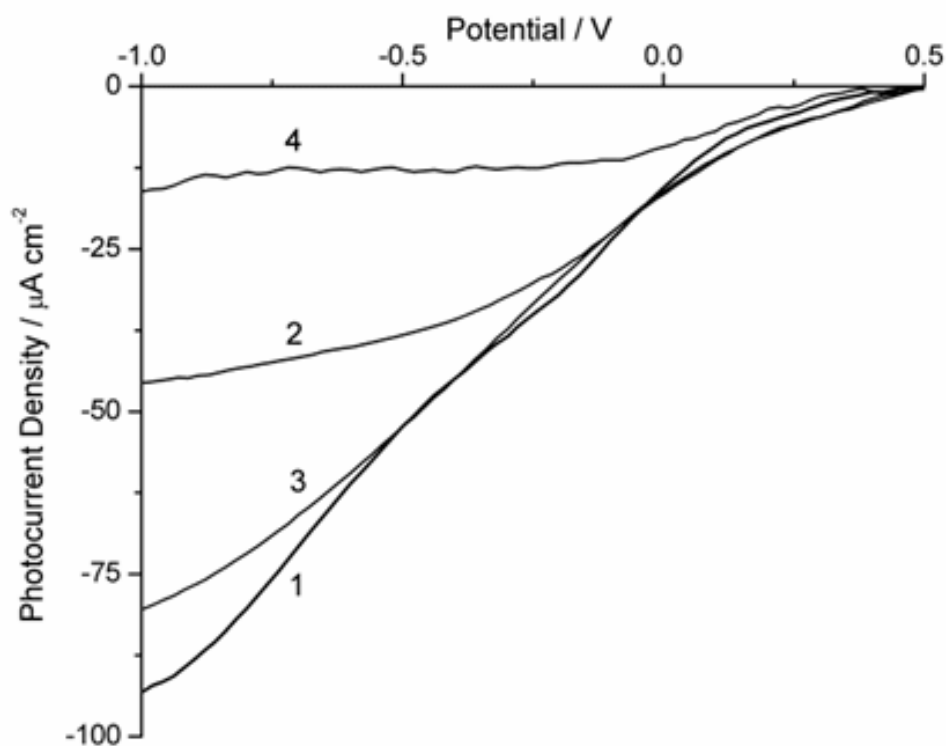


Figure 3-5. Net photocurrent generation of PBT/CNx composites on ITO substrates in aqueous 0.1 M KCl. CNx films were prepared at 25 W and nitrogen contents of 5 % (plot 1), 25 % (plot 2), and 50 % (plot 3). Photocurrent generation of a pristine PBT film is included for comparison (plot 4).

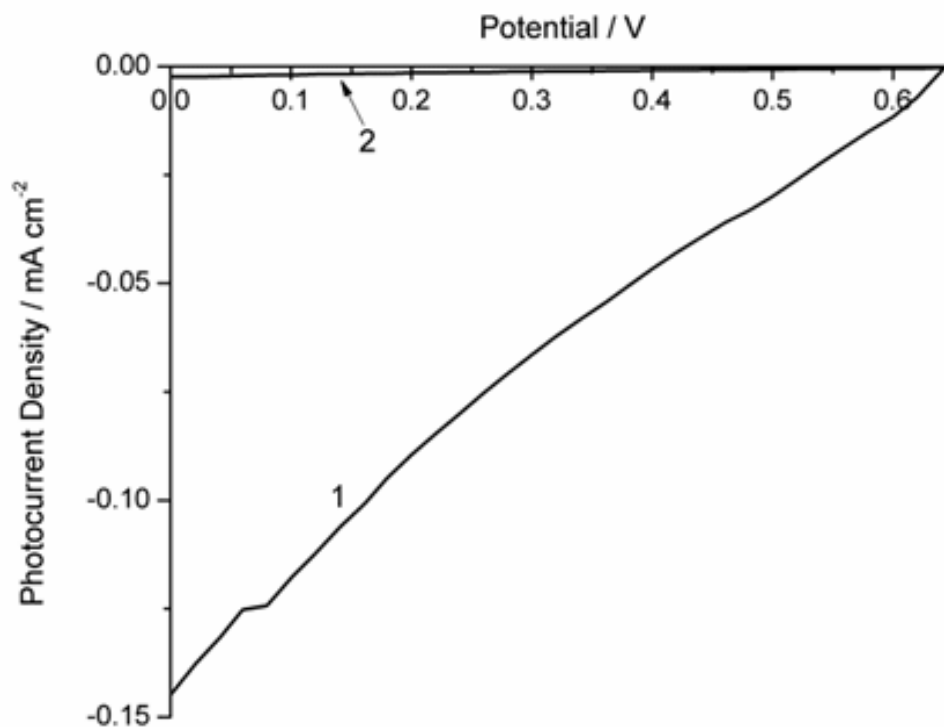


Figure 3-6. Current-Voltage plot of a solid state ITO/PEDOT/PBT/CNx/Al (plot 1) and a ITO/PEDOT/PBT/Al (plot 2) photovoltaic device. CNx film was prepared at 25 W and 10 % N₂.

It is natural to assume that the magnitude of the photocurrent enhancement will correlate with the improvement in the semiconductor properties of CNx films and therefore the greatest enhancement will be observed for films with the highest nitrogen content. The results of Figure 3-5 do not suggest such an outcome. However, we must remember that variations in the deposition conditions affect the CNx film thickness and therefore, since the illumination for films measured in Figure 3-5 was performed from the CNx side, the amount of light that was absorbed by the donor PBT phase will be reduced by light absorbed in the CNx layer. The required correction can be performed using the data on CNx film thicknesses and absorption coefficient that are found in Appendix A: Supporting Information for Chapter 3. The results are presented in Figure 3-7. It is seen

that, after the correction, the improvement in the photocurrent clearly correlates with an increase in the nitrogen concentration and therefore in the carbon nitride content in the films. One can see that the external quantum efficiency of the best photoelectrochemical cell at 50% nitrogen content exceeds 1%, which is a relatively good result taking into consideration that no optimization of the cell structure and composition, especially that of the donor layer, was performed. Future work will focus on tuning the properties and nanostructure of the bulk heterojunction layer, for instance, by thermal annealing, as well as exploring inverse architecture devices with polymer layers deposited onto CN_x using high work function metal electrodes. However, the results of this work allow us to conclude that vacuum deposited CN_x films may eventually become a viable alternative to PCBM and other fullerene-based acceptors in polymer donor-acceptor photovoltaic cells.

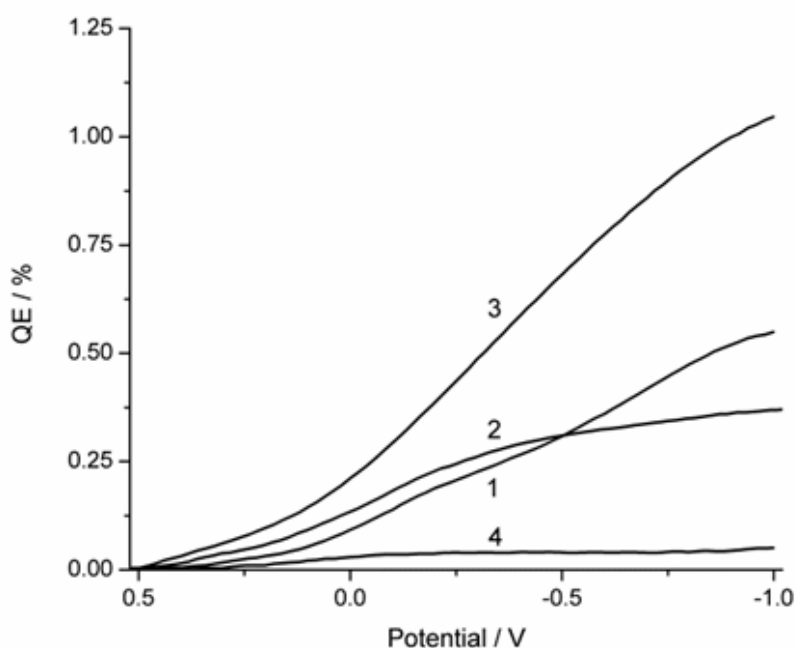


Figure 3-7. Quantum efficiency of PBT/CN_x composites on ITO substrates in aqueous 0.1 M KCl. CN_x films were prepared at 25 W and nitrogen contents of 5 % (plot 1), 25 % (plot 2), and 50 % (plot 3). A pristine PBT film is included for comparison (plot 4). Scan rate: 100 mV s⁻¹.

Nanoscale structure of CNx/polymer composites. Furthermore, there is evidence to suggest that the vacuum-deposited CNx films penetrate through the conjugated polymers forming a kind of bulk heterojunction rather than a bilayer structure. The ability to form a bulk heterojunction between the donor and acceptor phases is an important feature for polymer based solar cells due to the short exciton lifetimes and limited electron and hole mobility.⁸ Specifically, it was shown using nanoscale conductivity measurements through a conducting AFM tip that the CNx/conjugated polymer composites exhibit a complex structure coherent with CNx penetrating into the conjugated polymer as a consequence of the deposition technique and forming a nanoscale blend with alternating regions of high and low conductivity and nitrogen content.

The observed structure is illustrated in Figure 3-8, which presents simultaneous topography (left) and CS-AFM current (right) images of a PBT/CNx composite film. The conductivity image clearly shows finely segregated nanoscale regions of high and low conductivity that can be attributed to conducting and semiconducting CNx domains within the PBT film. Such complex structures were not found for either CNx films deposited onto ITO substrates or PBT films alone.³¹ Importantly, the conductivity of the same PBT films without CNx was much lower indicating that CNx indeed penetrated the polymer layer and formed a kind of interpenetrating bulk heterojunction structure. Importantly, CNx did penetrate the PBT films but did not short-circuit them, as evidenced by electrochemical data (see below). At the same time, as was evidenced by our previous XPS measurements,³¹ the outmost layers of CNx/polymer composites contained CNx only without PBT (no sulfur was found on the composite surface), which suggested that we could have a hybrid structure combining bilayer and bulk heterojunction architectures. However, regardless of the type of nanostructure, CNx/polymer composites under study were able to provide an efficient donor-acceptor charge separation as described in the previous sections.

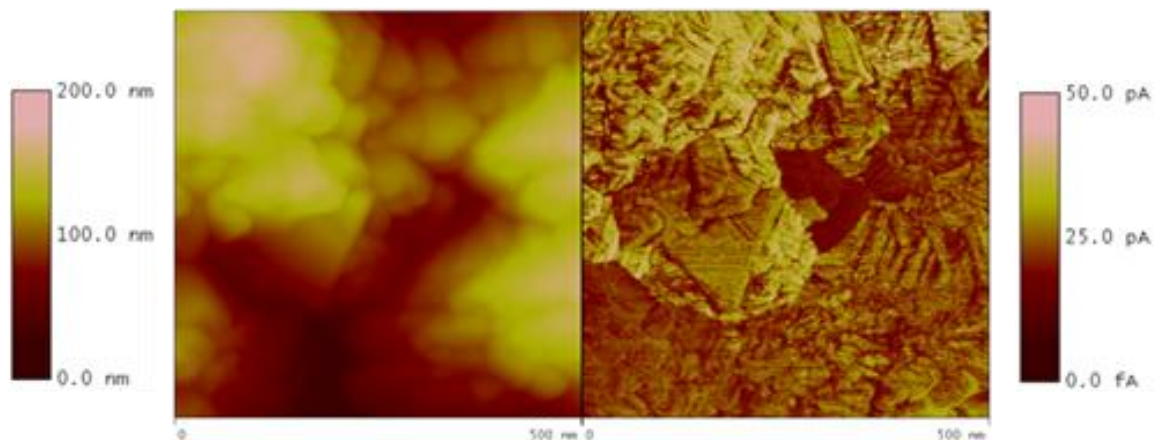


Figure 3-8. 500 nm by 500 nm topography (left) and CS-AFM current (right) images of a CN_x film on PBT. A bias of + 500 mV was applied to the tip. Height scale bar: 200 nm. CS-AFM current scale bar: 50 pA.

Electrochemical evidence of the donor-acceptor effect. The occurrence of the donor-acceptor effect in CN_x/PBT composites was supported by electrochemical measurements of the anodic and cathodic doping of the PBT polymer with and without CN_x. The corresponding cyclic voltammograms for a PBT electrode and PBT/CN_x composite electrode in acetonitrile are shown in Figure 3-9. A cyclic voltammogram of carbon nitride on its own is not included as it is well established in the literature that these films do not show significant currents in the potential regions examined here.²⁶ The voltammogram for PBT clearly shows broad anodic and cathodic doping/undoping peaks that are typical of the PBT polymer in non-aqueous conditions.⁵⁸ In the anodic region, anodic doping occurs, which corresponds to oxidation of the polymer backbone. In the cathodic region, reduction and n-doping of the polymer backbone takes place, with the electrons being injected from the contact and driving the reduction process.

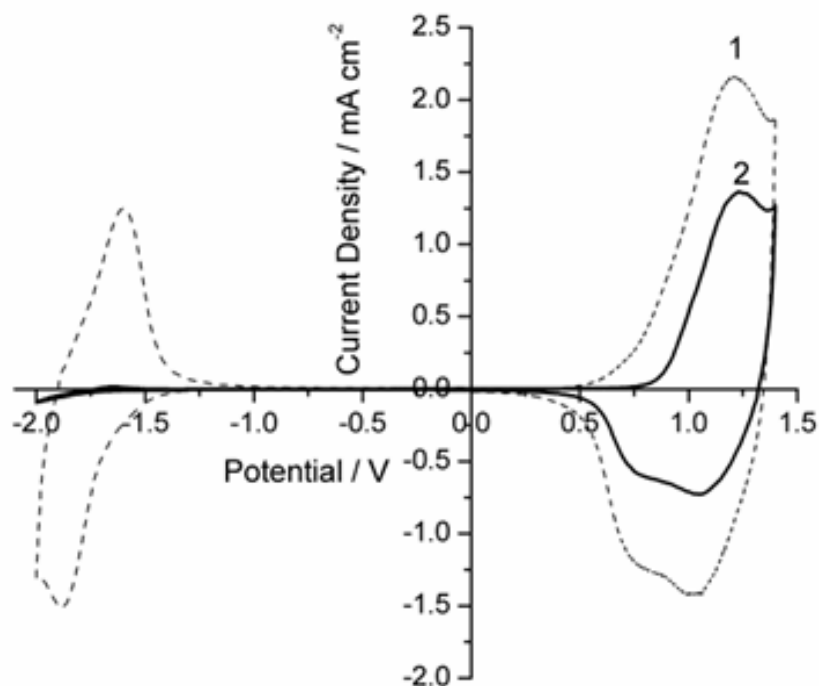


Figure 3-9. Cyclic voltammograms of (1) ITO/PBT and (2) ITO/PBT/CNx in acetonitrile and 0.1 M TBAPF₆.

The voltammetric response for a PBT/CNx film features similar electrochemical behavior to a pristine PBT film in the anodic region. This indicates that electrolyte and solvent are able to penetrate into the PBT through CNx allowing for oxidation to occur, although to a lesser degree than in the case of pristine PBT film. The presence of a pronounced anodic polymer oxidation peak in the voltammogram for the composite material and the absence of current in the potential range where the polymer is not conducting indicate that CNx sputtering did not damage the underlying PBT substrate. This was also demonstrated in our previous paper by AFM and conducting AFM measurements.³¹ The composite material is oxidized across the entire film and not only at the edges of the electrode as a visual change in color is observed across the whole film during oxidation. Additionally, repeated cycling led to a cracking of the CNx film, which was attributed to the well

known swelling and shrinking of the polymer film in the course of its doping-undoping. These results indicate that the CN_x layer adheres well to the PBT layer as it does not delaminate from the surface throughout the entire process, further emphasizing the formation of a stable composite film.

In the cathodic region, however, the behavior of the PBT/CN_x composite is strikingly different from that of pristine PBT. Specifically, the composite film showed no ability to be doped in the cathodic region. This is an interesting phenomenon that has been previously observed for donor polymers incorporating an acceptor material,^{40,42} and can be related to the fact that electrons injected from the contact are scavenged by the acceptor component and are not able to reduce the polymer phase. This phenomenon is broadly analogous to the well-known fact of fluorescence quenching in donor-acceptor systems (depopulation of the excited states of the donor due to the donor-acceptor electron transfer). These results suggest that CN_x behaves as an electron acceptor material with PBT and prevents the n-doping of the polymer film. In the absence of doping, the polymer remains semiconducting and no or very little dark current can flow through the polymer/CN_x composite, as compared to the pristine polymer film that becomes fully doped and therefore conducting at negative potentials (Figure 3-9). Furthermore, the fact that the cathodic doping is not just reduced but is abolished altogether suggests that the acceptor material is located not only at the interface with the donor material but throughout the entire thickness of the composite film. Therefore, we may conclude that CN_x indeed can function as an effective electron acceptor material and forms an interpenetrating heterojunction with a conjugated donor polymer such as polybithiophene. Furthermore, CN_x vacuum deposition did not damage the polymer film. CN_x can also perform well another very important function of the acceptor component and provide efficient conductivity pathways for the captured charge carriers.

3.4 Conclusions

The photocurrent generation in composite carbon nitride/conjugated polymer composite films was reported for the first time both in solution and in solid state devices. It was attributed to the occurrence of the donor-acceptor effect in such composite films with the

conjugated polymer acting as a donor and carbon nitride acting as an acceptor. Furthermore, nanoscale structural investigations revealed that such composites may feature a bulk heterojunction structure between PBT and CN_x with CN_x penetrating the PBT layer and forming finely segregated conducting and semiconducting domains. The results suggest that carbon nitride materials have the potential to become an alternative to fullerenes in organic bulk heterojunction solar cells.

Without the polymer, CN_x films did not show any photovoltaic effect, which was related to the abundance of graphitic domains that short-circuited the semiconducting domains where charge photogeneration could occur. At the same time, CN_x films prepared at high nitrogen content and magnetron power did show photoconductivity. Mott-Schottky measurements in electrolyte solution also revealed the formation of a space charge layer consistent with these materials being n-type semiconductors.

The variations in the film properties with the deposition conditions were attributed to the structural reorganization of the film that occurs during the deposition process. It was found that film thickness increased with both the target power and total nitrogen content, while the conductivity of the films decreased. The best semiconductor properties were observed for films prepared using increased magnetron power and nitrogen content. The dopant density in such films was also lower. At low deposition powers and nitrogen contents, a significant amount of graphitic carbon was present.

3.5 References

- (1) Nielsen, T. D.; Cruickshank, C.; Foged, S.; Thorsen, J.; Krebs, F. C. *Solar Energy Materials and Solar Cells* 2010, 94, 1553.
- (2) Helgesen, M.; Sondergaard, R.; Krebs, F. C. *Journal of Materials Chemistry* 2010, 20, 36.
- (3) Yu, G.; Gao, J.; Hummelen, J. C.; Wudl, F.; Heeger, A. J. *Science* 1995, 270, 1789.
- (4) Gunes, S.; Neugebauer, H.; Sariciftci, N. S. *Chemical Reviews* 2007, 107, 1324.
- (5) Brabec, C. J.; Cravino, A.; Meissner, D.; Sariciftci, N. S.; Fromherz, T.; Rispen, M. T.; Sanchez, L.; Hummelen, J. C. *Advanced Functional Materials* 2001, 11, 374.
- (6) Sariciftci, N. S.; Smilowitz, L.; Heeger, A. J.; Wudl, F. *Science* 1992, 258, 1474.

- (7) Mihailetschi, V. D.; van Duren, J. K. J.; Blom, P. W. M.; Hummelen, J. C.; Janssen, R. A. J.; Kroon, J. M.; Rispens, M. T.; Verhees, W. J. H.; Wienk, M. M. *Advanced Functional Materials* 2003, 13, 43.
- (8) Blom, P. W. M.; Mihailetschi, V. D.; Koster, L. J. A.; Markov, D. E. *Advanced Materials* 2007, 19, 1551.
- (9) Yang, X.; Loos, J. *Macromolecules* 2007, 40, 1353.
- (10) Krebs, F. C.; Norrman, K. *Progress in Photovoltaics* 2007, 15, 697.
- (11) Jorgensen, M.; Norrman, K.; Krebs, F. C. *Solar Energy Materials and Solar Cells* 2008, 92, 686.
- (12) Bertho, S.; Janssen, G.; Cleij, T. J.; Conings, B.; Moons, W.; Gadisa, A.; D'Haen, J.; Goovaerts, E.; Lutsen, L.; Manca, J.; Vanderzande, D. *Solar Energy Materials and Solar Cells* 2008, 92, 753.
- (13) Brabec, C. J.; Heeney, M.; McCulloch, I.; Nelson, J. *Chemical Society Reviews* 2011, 40, 1185.
- (14) Schwenn, P. E.; Gui, K.; Nardes, A. M.; Krueger, K. B.; Lee, K. H.; Mutkins, K.; Rubinstein-Dunlop, H.; Shaw, P. E.; Kopidakis, N.; Burn, P. L.; Meredith, P. *Advanced Energy Materials* 2011, 1, 73.
- (15) Sonar, P.; Lim, J. P. F.; Chan, K. L. *Energy & Environmental Science* 2011, 4, 1558.
- (16) Li, Z.; Gao, F.; Greenham, N. C.; McNeill, C. R. *Advanced Functional Materials* 2011, 21, 1419.
- (17) Avouris, P.; Chen, Z. H.; Perebeinos, V. *Nature Nanotechnology* 2007, 2, 605.
- (18) Tung, V. C.; Huang, J. H.; Tevis, I.; Kim, F.; Kim, J.; Chu, C. W.; Stupp, S. I.; Huang, J. X. *Journal of the American Chemical Society* 2011, 133, 4940.
- (19) Silva, S. R. P.; Rafferty, B.; Amaratunga, G. A. J.; Schwan, J.; Franceschini, D. F.; Brown, L. M. *Diamond and Related Materials* 1996, 5, 401.
- (20) Zhou, Z. B.; Cui, R. Q.; Pang, Q. J.; Hadi, G. M.; Ding, Z. M.; Li, W. Y. *Solar Energy Materials and Solar Cells* 2002, 70, 487.
- (21) Alibart, F.; Drouhin, O. D.; Benlahsen, M.; Muhl, S.; Rodil, S. E.; Camps, E.; Escobar-Alarcon, L. *Applied Surface Science* 2008, 254, 5564.

- (22) Alibart, F.; Drouhin, O. D.; Lejeune, M.; Benlahsen, A.; Rodil, S. E.; Camps, E. *Diamond and Related Materials* 2008, 17, 925.
- (23) Sjostrom, H.; Hultman, L.; Sundgren, J. E.; Hainsworth, S. V.; Page, T. F.; Theunissen, G. S. A. M. *Journal of Vacuum Science & Technology A-Vacuum Surfaces and Films* 1996, 14, 56.
- (24) Yoo, K. S.; Miller, B.; Kalish, R.; Shi, X. *Electrochemical and Solid State Letters* 1999, 2, 233.
- (25) Broitman, E.; Hellgren, N.; Wanstrand, O.; Johansson, M. P.; Berlind, T.; Sjostrom, H.; Sundgren, J. E.; Larsson, M.; Hultman, L. *Wear* 2001, 248, 55.
- (26) Lagrini, A.; Deslouis, C.; Cachet, H.; Benlahsen, M.; Charvet, S. *Electrochemistry Communications* 2004, 6, 245.
- (27) Monclus, M. A.; Cameron, D. C.; Barklie, R.; Collins, M. *Surface & Coatings Technology* 1999, 116, 54.
- (28) Friedrich, M.; Welzel, T.; Rochotzki, R.; Kupfer, H.; Zahn, D. R. T. *Diamond and Related Materials* 1997, 6, 33.
- (29) Hultman, L.; Neidhardt, J.; Hellgren, N.; Sjostrom, H.; Sundgren, J. E. *Mrs Bulletin* 2003, 28, 194.
- (30) Alibart, F.; Lejeune, M.; Drouhin, O. D.; Zellama, K.; Benlahsen, M. *Journal of Applied Physics* 2010, 108.
- (31) Byers, J. C.; Tamiasso-Martinhon, P.; Deslouis, C.; Pailleret, A.; Semenikhin, O. A. *Journal of Physical Chemistry C* 2010, 114, 18474.
- (32) Zheng, W. T.; Sjostrom, H.; Ivanov, I.; Xing, K. Z.; Broitman, E.; Salaneck, W. R.; Greene, J. E.; Sundgren, J. E. *Journal of Vacuum Science & Technology A-Vacuum Surfaces and Films* 1996, 14, 2696.
- (33) Muhl, S.; Mendez, J. M. *Diamond and Related Materials* 1999, 8, 1809.
- (34) Hellgren, N.; Johansson, M. P.; Broitman, E.; Hultman, L.; Sundgren, J. E. *Physical Review B* 1999, 59, 5162.
- (35) Lejeune, M.; Durand-Drouhin, O.; Charvet, S.; Grosman, A.; Ortega, C.; Benlahsen, M. *Thin Solid Films* 2003, 444, 1.
- (36) Alibart, F.; Lejeune, M.; Zellama, K.; Benlahsen, M. *Diamond and Related Materials* 2011, 20, 409.

- (37) Alibart, F.; Drouhin, O. D.; Debiemme-Chouvy, C.; Benlahsen, M. *Solid State Communications* 2008, 145, 392.
- (38) Ferrari, A. C.; Rodil, S. E.; Robertson, J. *Physical Review B* 2003, 67.
- (39) Semenikhin, O. A.; Hossain, M. M. D.; Workentin, M. S. *Journal of Physical Chemistry B* 2006, 110, 20189.
- (40) DiCarmine, P. M.; Wang, X.; Pagenkopf, B. L.; Semenikhin, O. A. *Electrochemistry Communications* 2008, 10, 229.
- (41) Tindale, J. J.; Holm, H.; Workentin, M. S.; Semenikhin, O. A. *Journal of Electroanalytical Chemistry* 2008, 612, 219.
- (42) Byers, J. C.; DiCarmine, P. M.; Moustafa, M. M. A.; Wang, X.; Pagenkopf, B. L.; Semenikhin, O. A. *Journal of Physical Chemistry B* 2009, 113, 15715.
- (43) Arenal, R.; Stephan, O.; Bruno, P.; Gruen, D. M. *Applied Physics Letters* 2009, 94.
- (44) Robertson, J.; Oreilly, E. P. *Physical Review B* 1987, 35, 2946.
- (45) Rodil, S. E.; Muhl, S. *Diamond and Related Materials* 2004, 13, 1521.
- (46) Lazar, G.; Clin, M.; Charvet, S.; Therasse, M.; Godet, C.; Zellama, K. *Diamond and Related Materials* 2003, 12, 201.
- (47) Cheah, L. K.; Shi, X.; Liu, E.; Shi, J. R. *Applied Physics Letters* 1998, 73, 2473.
- (48) Katsuno, T.; Nitta, S.; Habuchi, H.; Stolojan, V.; Silva, S. R. P. *Applied Physics Letters* 2004, 85, 2803.
- (49) Peat, R.; Peter, L. M. *Applied Physics Letters* 1987, 51, 328.
- (50) Peponas, S.; Guedda, M.; Benlahsen, M. *Solid State Communications* 2008, 146, 78.
- (51) Pleskov, Y. V.; Pimenov, S. M.; Lim, P. Y.; Ralchenko, V. G. *Russian Journal of Electrochemistry* 2008, 44, 861.
- (52) Robertson, J.; Davis, C. A. *Diamond and Related Materials* 1995, 4, 441.
- (53) Alibart, F.; Peponas, S.; Charvet, S.; Benlahsen, M. *Thin Solid Films* 2011, 519, 3430.
- (54) Kusano, Y.; Evetts, J. E.; Somekh, R. E.; Hutchings, I. M. *Thin Solid Films* 1998, 332, 56.
- (55) Ilie, A.; Hart, A.; Flewitt, A. J.; Robertson, J.; Milne, W. I. *Journal of Applied Physics* 2000, 88, 6002.

- (56) Miyajima, Y.; Tison, Y.; Giusca, C. E.; Stolojan, V.; Watanabe, H.; Habuchi, H.; Henley, S. J.; Shannon, J. M.; Silva, S. R. P. *Carbon* 2011, 49, 5229.
- (57) ElRashiedy, O. A.; Holdcroft, S. *Journal of Physical Chemistry* 1996, 100, 5481.
- (58) Semenikhin, O. A.; Ovsyannikova, E. V.; Ehrenburg, M. R.; Alpatova, N. M.; Kazarinov, V. E. *Journal of Electroanalytical Chemistry* 2000, 494, 1.

Chapter 4

4 Nitrogen Rich Carbon Nitride Photovoltaic Materials

4.1 Introduction

Organic materials are a promising platform for the economical production of solar cell devices, offering reduced materials cost due to very thin photoactive layers (~100 - 200 nm) combined with high-throughput manufacturing methods.¹⁻³ Organic solar cells typically consist of a light absorbing conjugated polymer or small molecule that is mixed with a fullerene or fullerene derivative to create a nanoscale interpenetrating bulk heterojunction material,⁴⁻⁶ which is necessary to overcome the binding energy of the exciton that is created in the light absorbing material.⁷ So far, fullerenes have been the most effective materials for exciton dissociation in conjugated polymers exhibiting efficiencies of ca. 9 %, while alternatives such as small organic molecules, conjugated polymers and quantum nanocrystals exhibit much lower device efficiencies when used as an acceptor material.⁸⁻¹¹ While fullerenes are able to efficiently dissociate excitons and transport charge carriers throughout the photoactive layer to the appropriate electrodes, these composite films are prepared in a way that produces a metastable bulk heterojunction film which eventually leads to a decrease in efficiency with time as a result of photoactive layer segregation and degradation.¹² In addition, fullerenes exhibit a short wavelength absorption maximum in the visible spectrum due to their molecular nature.¹³ As a result, fullerenes themselves contribute a negligible amount towards the photocurrent generated in the films, while typically making up half of the total photoactive layer composition.¹⁴ This is a considerable drawback in the development of organic solar cell technology, where a minimum of 10 % efficiency, with 10 year service life, is needed before serious practical exploitation of these devices can be realized.¹⁵ Therefore, the continued development of new materials that may overcome the limitations of fullerenes while also effectively promoting exciton dissociation and acting as effective charge carrier transport materials is an important area of research to realize the potential of organic solar cell technology.¹⁶ It was demonstrated in the previous chapter that carbon nitride (CN_x) can function as an electron acceptor in organic bulk heterojunction solar cells.¹⁷ In this work we show that nitrogen rich photovoltaic carbon nitride materials can be prepared that exhibit n-type semiconductor properties. Furthermore, we were able to demonstrate for the first time working photovoltaic cell prototypes based on carbon nitride only without conjugated polymers, which opens up

many new opportunities for the realization of photovoltaic devices that are not limited to organic bulk heterojunction architectures. These could now include composites with quantum nanocrystals, inorganic nanowire devices or even all carbon solar cells.

Carbon nitride represents an extremely promising material for photovoltaic device applications as it has been demonstrated to be extremely robust and chemically inert.¹⁸ The electronic properties of amorphous carbon are significantly modified by nitrogen incorporation into the film, transitioning from a semi-metallic graphitic like material to a more semiconducting material for increasing nitrogen content.¹⁹ However, there is not a clear understanding of the role of nitrogen content and bonding in the film which is suitable for creating semiconductor materials for photovoltaic applications.²⁰ CN_x materials prepared with high nitrogen content typically exhibit band-gaps in the range of 0 - 1.5 eV which make them ideal light absorbing materials over the entire solar spectrum.¹⁹ Carbon nitride can be prepared using a variety of techniques²¹ including vacuum sputtering which produces materials that are primarily sp² hybridized and permits the opportunity to directly deposit CN_x thin films onto a variety of substrates, such as a conjugated polymer, creating a stable and robust heterojunction.²² As well, amorphous carbon has also been shown to be an effective electron acceptor material when combined with quantum nanocrystals reflecting the significant potential of amorphous carbon and nitrogen modified carbon materials for photovoltaic applications.²³

There have been two other demonstrations of photoconductive carbon nitride thin films prepared using plasma enhanced chemical vapor deposition and reactive magnetron sputtering.²⁴⁻³⁴ However, none of these films exhibited photovoltaic properties. In fact, to the best of our knowledge there has been only one report of a photovoltaic effect observed in a carbon nitride thin film.³⁵ However, in that work an ion beam sputtering process was used for deposition, whereas reactive magnetron sputtering techniques, like those which have been used to prepare photoconductive CN_x thin films above are preferable for high throughput deposition of photovoltaic devices. Recently we have shown that vacuum sputtered carbon nitride films can be combined with conjugated polymers to enhance photocurrent generation.²² In all cases, an increase in photocurrent

generation was observed when these films were combined with a conjugated polymer demonstrating their potential as electron acceptor materials in organic photovoltaic devices. However, it was found that the CN_x films studied in that work would only show photoconductivity under certain deposition conditions and there were no observations of a photovoltaic effect. One of the limiting factors highlighted was the significant amount of graphitic material that was obtained in the as prepared films that limited the occurrence of photoconductivity in the materials, and completely prevented any observation of a photovoltaic effect. It is the presence of graphitic regions that can form a percolation network in these films which can dominate the electronic properties of these materials. In this work we show that it is possible to prepare nitrogen rich carbon nitride films with a significantly reduced number of graphitic domains through optimization of the deposition process along with post-deposition annealing of the thin films. Through the formation of nitrogen rich materials, a reduction of the graphitic domains was observed that limited the formation of highly conductive percolation networks across the bulk of the film and permitted the observation of a photovoltaic effect in vacuum sputtered carbon nitride materials for the first time.

A further change in the electronic properties of carbon nitride can be realized by structural modification and relaxation. This can be accomplished through the adjustment of the deposition parameters, aging of the thin films as well as thermal annealing.^{36,37} Current-voltage measurements and impedance spectroscopy were used to characterize the changes in the electronic properties of carbon nitride as a function of these parameters. It was found that structural relaxation by film aging led to photovoltaic carbon nitride materials. As well, the intentional reduction of graphite in the films was promoted by modifying the plasma composition; and through post-deposition annealing, we show that it is possible to prepare photovoltaic carbon nitride materials directly without any aging. These materials exhibited hole minority carrier generation under illumination, which indicates an n-type semiconductor material was formed. Further evidence for the formation of an n-type material is provided by XPS measurements where it was found that nitrogen is incorporated into a graphitic network, which is known to be a n-type doping configuration of nitrogen in amorphous carbon.³⁸ When these n-type photovoltaic materials were combined with a p-type conjugated polymer, rectification was observed in

their current-voltage plots indicating the formation of a p-n heterojunction device. In addition, an improvement in the photocurrent generation in these heterojunction devices relative to devices using only an individual CN_x or a conjugated polymer layer was observed, representing the development of a new type of photovoltaic device based on carbon nitride materials.

4.2 Experimental

Substrate cleaning

Indium tin oxide coated glass slides (Delta Technologies, Ltd) with a surface resistance of 8 -12 Ω were used for solid state devices. Prior to use, the substrates were sonicated sequentially in soap and water, deionized water, acetone, and ethanol. The electrodes were dried using nitrogen gas and placed in an oven at 90°C to remove any residual solvent.

4.2.2. Spin-coating of poly(3,4-ethylenedioxythiophene) and poly(3-hexylthiophene)

A 1.3 % by weight poly(3,4-ethylenedioxythiophene) solution (Sigma-Aldrich), conductive grade, was filtered through a 0.45 μm syringe filter prior to spin-coating. A film thickness of 40 nm was obtained by spin-coating for 90 seconds at a speed of 3000 RPM. Film thickness was determined using AFM to image a scratch across the surface of the film. Electronic grade regioregular (93-95%, MW = 40 - 60 kDa) poly(3-hexylthiophene) (Solaris Chem Inc) was used as received. Poly(3-hexylthiophene) was dissolved in anhydrous 1,2,4-trichlorobenzene (Sigma-Aldrich, > 99%) at a concentration of 20 mg mL⁻¹ and heated for one hour at 80°C to ensure complete dissolution. Poly(3-hexylthiophene) was spin-coated at 1200 RPM for 300 seconds to obtain a film thickness of 70 nm. The thickness of the film was determined from the transmission spectrum of a spin-coated P3HT film on an ITO coated glass slide assuming an absorption coefficient for P3HT of $6 \times 10^4 \text{ cm}^{-1}$ at 405 nm.³⁹

Vacuum deposition of carbon nitride and aluminum

A custom built vacuum deposition system was used for radiofrequency magnetron sputtering of carbon and aluminum. The vacuum system was directly connected to a

glovebox with a separate load-lock chamber for the introduction of substrates into the system. The target was biased at a negative potential while the substrate was grounded. The substrate to target distance was 7 cm. The substrate temperature was not controlled and it is known that the substrate temperature would not be expected to exceed 100°C for the deposition powers used in this work.⁴⁰ The base pressure prior to deposition was below 2×10^{-6} Torr. Ultrahigh purity argon and nitrogen gas were used as gas sources. A 5 cm diameter carbon target (Goodfellow, 99.997 % purity) was used as a carbon source and a 2.5 cm diameter aluminum target (Kurt J. Lesker, 99.9995 % purity) was used as an aluminum source. The total chamber pressure during deposition was varied from 7.5 – 37.5 mTorr, and the deposition powers were in the range from 25 W to 150 W. The partial pressure of nitrogen was varied by adjusting the rates of mass flow of nitrogen gas and argon gas as expressed in equation 1:

$$\% \text{N}_2 = \frac{\text{Flow Rate of N}_2}{\text{Flow Rate of N}_2 + \text{Flow Rate of Ar}} \times 100 \% \quad (1)$$

The flow rate, measured in SCCM, was controlled using a mass flow controller (MKS Type 1179A). RF magnetron sputtering of aluminum was done in a pure argon plasma to deposit an aluminum electrode on the carbon nitride surface at a deposition power of 25 W and a deposition pressure of 15 mTorr.

Annealing of carbon nitride films

Carbon nitride was annealed using a custom-built oven with independent control of the temperature above and below the substrate to allow uniform heating. The oven was located inside a glovebox that was directly attached to the vacuum system to ensure samples were not exposed to the atmosphere during annealing. The films were annealed between 100 - 200°C for 60 minutes, removed from the oven and allowed to cool to room temperature in the glovebox for several hours.

Device characterization

Completed solid state devices were loaded into a sealed holder inside a glovebox without any exposure of the samples to the atmosphere before measurements were performed. The sealed holder contained electrical pins, which allowed electrical connection of the devices to an external measurement circuit, as well as a quartz optical window for sample illumination for photovoltaic measurements. This set-up allowed measurements to be performed in an inert atmosphere. Measurements of the solid state devices were performed using a PAR 263A potentiostat–galvanostat (Princeton Applied Research) coupled with a Solartron 1250 frequency response analyzer. Steady-state measurements were controlled using version 3.1 CorrWare software and frequency domain measurements were controlled using version 2.8 ZPlot software (Scribner Associates Inc.). The light source used was a 405 nm, 20 mW laser diode (LD1510, Power Technology) having a light intensity of 2×10^{17} photons $\text{s}^{-1} \text{cm}^{-2}$ (90 mW cm^{-2}).

4.3 Results and Discussion

The structure and bonding of vacuum sputtered carbon nitride are highly dependent upon the plasma composition which can be controlled through a variety of deposition parameters including deposition power or target bias, nitrogen partial pressure, target to substrate separation, substrate temperature or bias, and total plasma pressure.⁴⁰ Addition of nitrogen to amorphous carbon thin films modifies the film structure and bonding, which leads to changes in the π and π^* states as well as their distribution.⁴¹ A change in the distribution of these states modifies the electronic and optical properties of the films. In particular, a transition from a semi-metallic to semiconducting conductivity has been observed when the amount of nitrogen in the film was increased.¹⁹ In this work we examine the influence of deposition power, nitrogen partial pressure and total plasma pressure. Figure 4-1 shows J-V plots for a series of carbon nitride films prepared using deposition powers of 25 W, 50 W, 100 W and 150 W and a range of nitrogen partial pressures from 1% N_2 to 100% N_2 . The device architecture was ITO/CNx/Al without any interfacial layers between the CNx and the anode/cathode. Figure 4-1A shows the J-V plots for all films prepared at 25 W and it can be seen that these films show a decrease in current density with increasing nitrogen content in the films. For films prepared in pure

nitrogen discharge plasma without any argon, a significantly lower conductivity was observed relative to any of the other films. The decrease in the conductivity of the films with increasing nitrogen content is due to a reduction in the graphitic domains present in the films as more nitrogen substitutes for carbon.⁴² Comparison of the current-voltage plots of the 25 W films with those obtained at higher deposition powers in Fig. 4-1B – Fig. 4-1D shows that there is some variation between nitrogen partial pressure and deposition power, however this is not nearly as pronounced as what was observed in the films shown in Fig. 4-1A. This can be explained by the fact that an increase in the deposition power increases the kinetic energy of the bombarding species at the growing film surface, which decreases the nitrogen content in the film as a result of chemical re-sputtering at the substrate surface where nitrogen is preferentially etched away from the growing film.³⁷ As well, an increase in the target bias results in an increase in disorder of the film and limits the reactivity of carbon and nitrogen in the plasma.⁴¹ This generates films that contain a significant amount of graphitic content as well as a significant film disorder, which lead to photoconductive materials only in some cases and prevent the observation of a photovoltaic effect. It is possible that there are photovoltaic CNx domains in these films, however due to the presence of a significant graphitic content, these domains could be short-circuited and prevent the observation of a photovoltaic effect. This highlights the need to reduce or eliminate their presence.

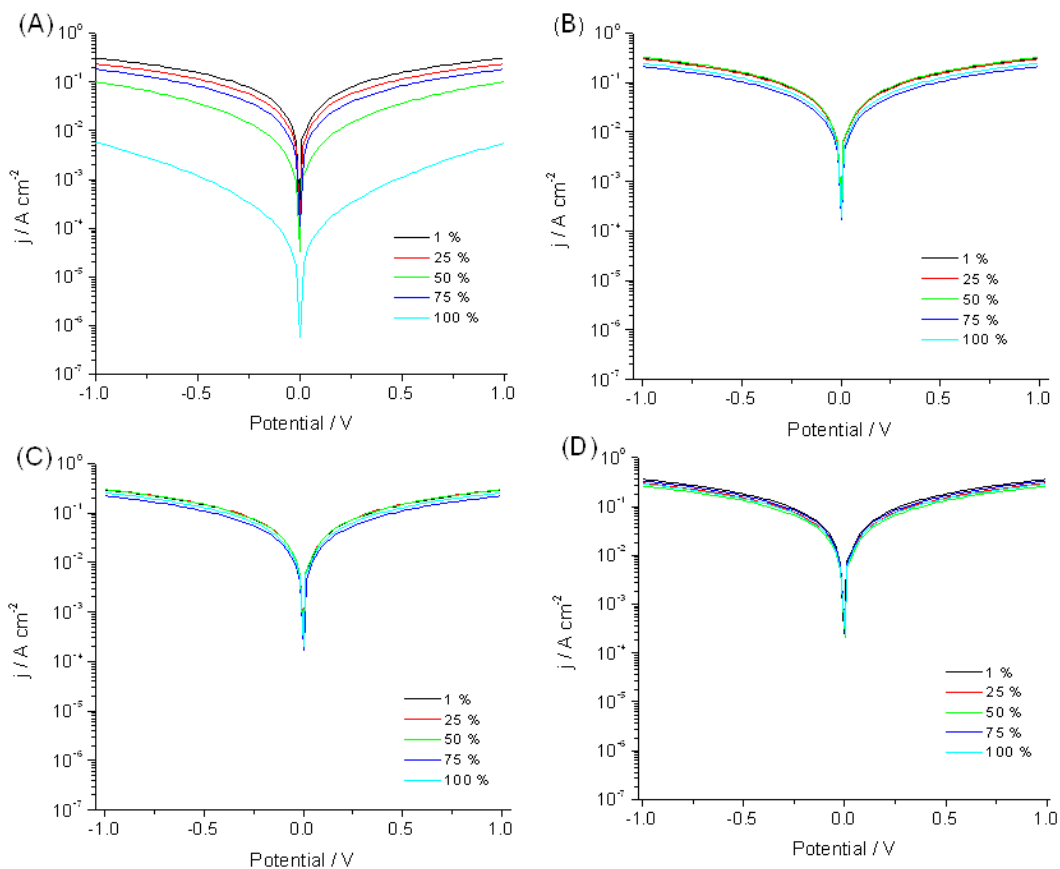


Figure 4-1. Dark J-V plots of CN_x films prepared at (A) 25 W, (B) 50 W, (C) 100 W and (D) 150 W for nitrogen plasma compositions indicated.

The substantial decrease in conductivity observed for films prepared at the lowest deposition power and highest nitrogen content can be attributed to a disruption of a graphitic percolation network across the bulk of the films. This is in contrast to films prepared at low nitrogen contents and high deposition powers where the presence of a significant amount of graphitic material was able to form a percolation network across the entire film leading to a higher conductivity. It is the conductive pathways provided by the graphitic domains, that if present in a high enough concentration, will determine the current-voltage behavior of carbon nitride films. The size of the graphitic clusters is in the range of 1 – 10 nm.^{43,44} The film thicknesses used in this work ranged from 20 – 100 nm and it can be anticipated that graphite should be able to form an effective percolation network across the entire film for lower nitrogen contents and higher

deposition powers. As a result, the current density measured in these films will be dominated by the highly conductive graphitic pathways and explains the independence of the conductivity of these films for higher deposition powers and lower nitrogen contents. However, it is well established that for higher nitrogen content plasmas, more nitrogen is incorporated into the film. Therefore, the presence of these graphitic domains may circumvent the observation of the electronic properties of the CN_x domains making it difficult to observe a photoconductive or photovoltaic effect. Increasing the nitrogen content in the plasma and decreasing the deposition power promoted nitrogen incorporation into the films and limited the formation of carbon rich graphitic domains, which explains the significant decrease in conductivity for these films. It is important to point out that none of the materials prepared at a deposition power of 50 W or more in a 1 Pa total discharge pressure showed any photoconductive or photovoltaic effects. Only films that were prepared at 25 W and high nitrogen plasma discharge contents showed any changes in their electronic properties under illumination using RF magnetron sputtering for the deposition conditions examined here. The focus of this chapter is on films prepared at low deposition power and high nitrogen contents.

Figure 4-2 shows the current-voltage plots for three different carbon nitride films prepared at 25 W and with nitrogen contents in a plasma of 1 % N₂, 50 % N₂, and 100 % N₂. These figures illustrate the change in conductivity of the films with increasing nitrogen content from ohmic to semiconducting, exhibiting some rectification at higher nitrogen contents. The change in shape of the current voltage plots is a clear indication of the modification in the electronic properties of the carbon nitride films with increasing nitrogen content, changing from semi-metallic to semiconducting. A decrease in conductivity in the carbon nitride films with increasing nitrogen content was also observed using impedance spectroscopy measurements. All measurements were made under open-circuit conditions in the dark.

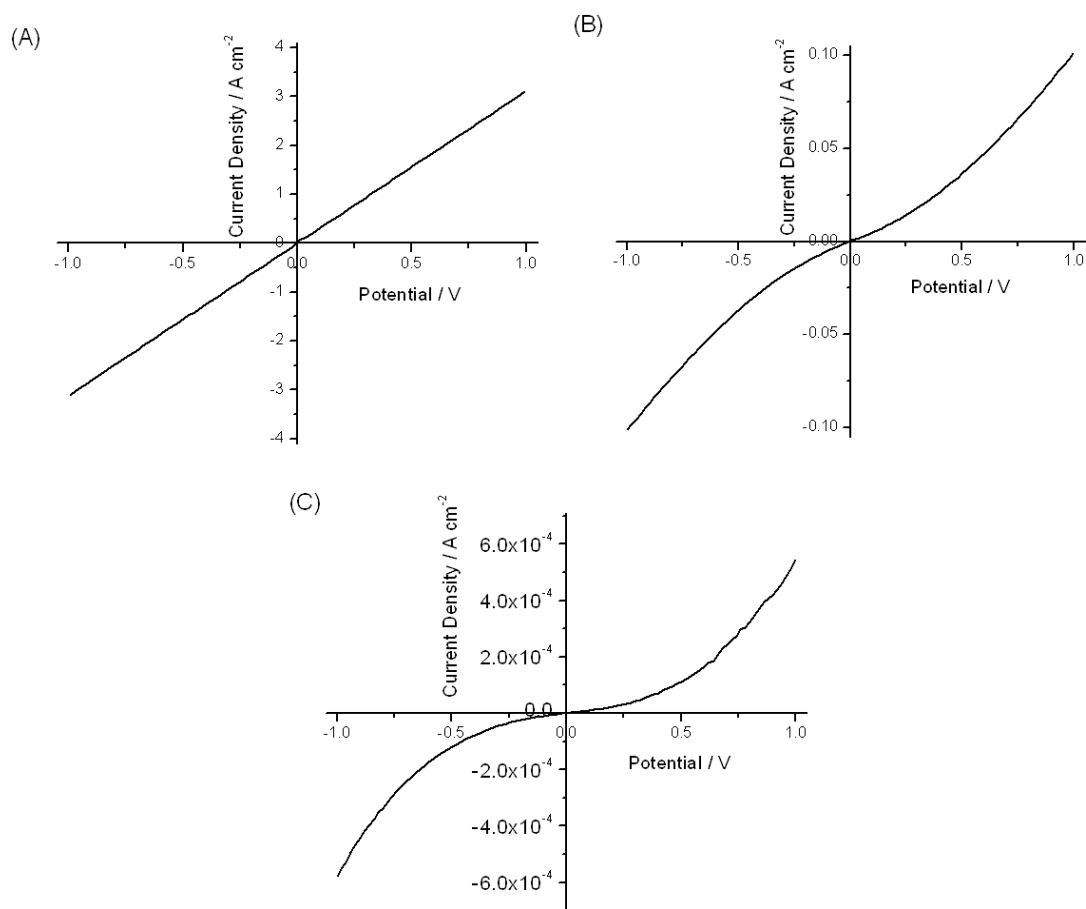


Figure 4-2. Dark J-V plots of CN_x films prepared using a deposition power of 25 W and nitrogen contents of (A) 1 % N₂, (B) 50 % N₂, (C) 100 % N₂.

Figure 4-3 shows the (A) Nyquist plot and (B) Bode plot for the same carbon nitride films whose current-voltage curves are shown in Figure 4-2. Dark impedance measurements were made at an applied potential of 0 V. The experimental data are shown as scatter points on the plot and the solid lines represent a fit of the data using a Randles equivalent circuit for films prepared at 50 % N₂ and 100 % N₂. The equivalent circuit that was used to fit the data is shown in Figure 4-3C with the series resistance R_s assigned to contact resistance of the electrodes, with the parallel capacitance C_p and parallel resistance R_p terms attributed to the CN_x film. A constant phase element with a value of $n \geq 0.93$ was used to fit the data. A clear change in the shape of the Nyquist plots can be observed in Figure 4-3A upon going from 1 % N₂ to higher nitrogen contents. The

impedance of the film prepared at 1 % N₂ shows a single point in the Nyquist plot without any significant phase shift indicating primarily resistive behavior, which could be expected for a highly conducting graphitic material. However, for CN_x films prepared at higher nitrogen contents (50 % N₂ and 100 % N₂), a semicircle in the Nyquist plot was observed due to the contributions of the film resistance and capacitance, which is attributed to the increasing amount of CN_x regions in the film. As well, as the nitrogen content increases, the size of the semicircle increases due to an increase in the film resistance which further shows that increasing nitrogen content in the film leads to a decrease in the conductive graphitic domains.

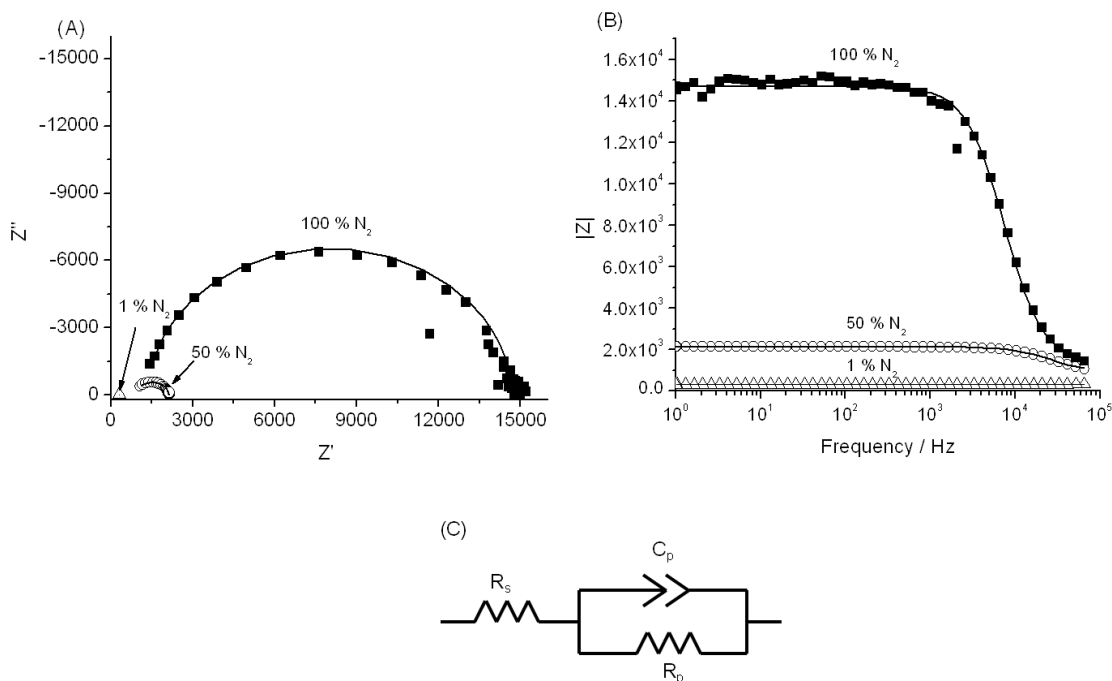


Figure 4-3. (A) Nyquist plot and (B) Bode plot of CN_x films prepared at 25 W and nitrogen content of 1 % N₂, 5 % N₂ and 100 % N₂ (1 Pa total pressure). (C) Equivalent circuit element used to fit the data. Applied potential was 0 V in dark.

Figure 4-3B shows the amplitude of the impedance for the three different films which clearly illustrates the increase in impedance with increasing nitrogen content. While the increase in film resistance with increasing nitrogen content indicates a decrease in the conductive graphitic domains, it does not suggest their elimination as the film would not

be expected to show any resistive component at low frequencies if there were not any current pathways available in the film. This is an important consideration, particularly in view of the potential application of carbon nitride as a photovoltaic material. As discussed in further detail below, the emergence of photovoltaic properties in carbon nitride was only observed for films that showed an extremely large or infinitely large value for the film resistance at open-circuit conditions in the dark.

Figure 4-4 shows the current-voltage plots of a CN_x film prepared with 100 % N₂ in the dark and under illumination. The film exhibits photoconductive behavior but does not show any photovoltaic behavior, which indicates that illumination increases the number of charge carriers in the film leading to an increase in conductivity. However, a photovoltaic effect is not observed due to the presence of graphitic domains. With time, CN_x films undergo a further structural modification as a result of film relaxation.⁴⁶ Figure 4-5 shows the current-voltage plot for a freshly prepared CN_x film as well as the current-voltage plot for the same film after aging for approximately 30 days. It can be seen that the conductivity of the film is significantly reduced upon aging as reflected by the decrease in current density in Figure 4-5. As well, impedance measurements of the aged film (Figure 4-6) is best described by a series R-C circuit whose imaginary component increases with decreasing frequency and does not have a parallel resistance component, instead only showing capacitive behaviour that is offset by a high frequency series resistance. This indicates that structural relaxation of carbon nitride with aging is accompanied by a change in the electronic structure and/or morphology of these materials and it is this change that leads to the emergence of a photovoltaic effect in carbon nitride films.

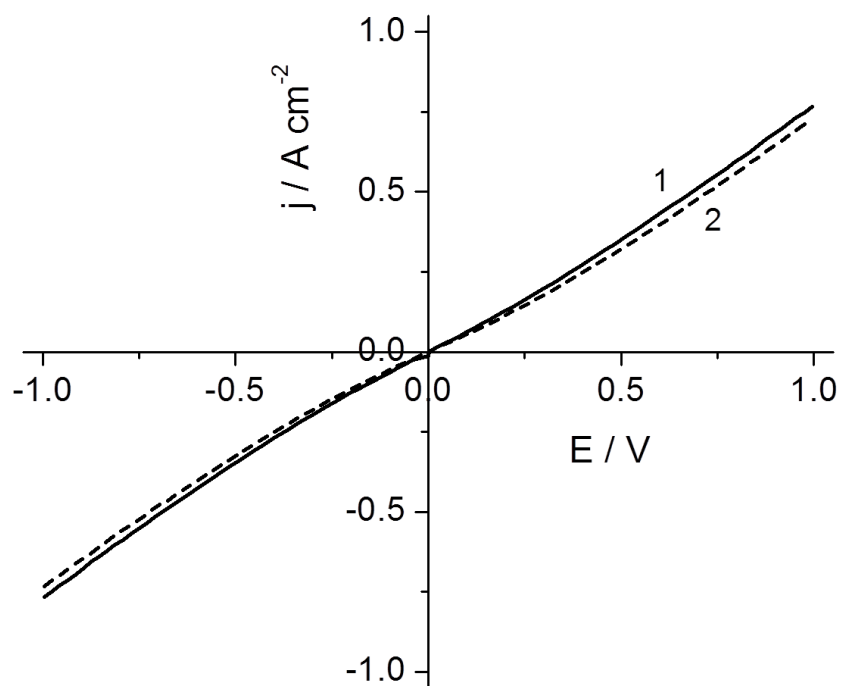


Figure 4-4. Illuminated (1) and dark (2) J-V plots of a CN_x film prepared using a deposition power of 25 W in a 100% (1 Pa total pressure) nitrogen discharge plasma.

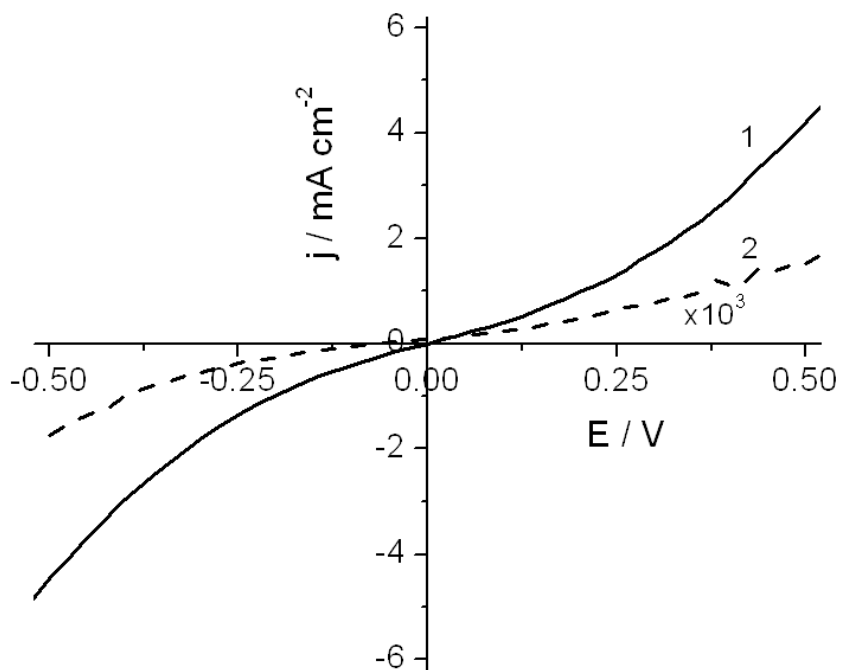


Figure 4-5. Dark J-V plots of a CN_x film prepared using a deposition power of 25 W in a 100 % nitrogen discharge plasma for a (1) fresh film and an (2) aged film (1 Pa total pressure). Note the current density of the aged film has been multiplied by a factor of 10^3 .

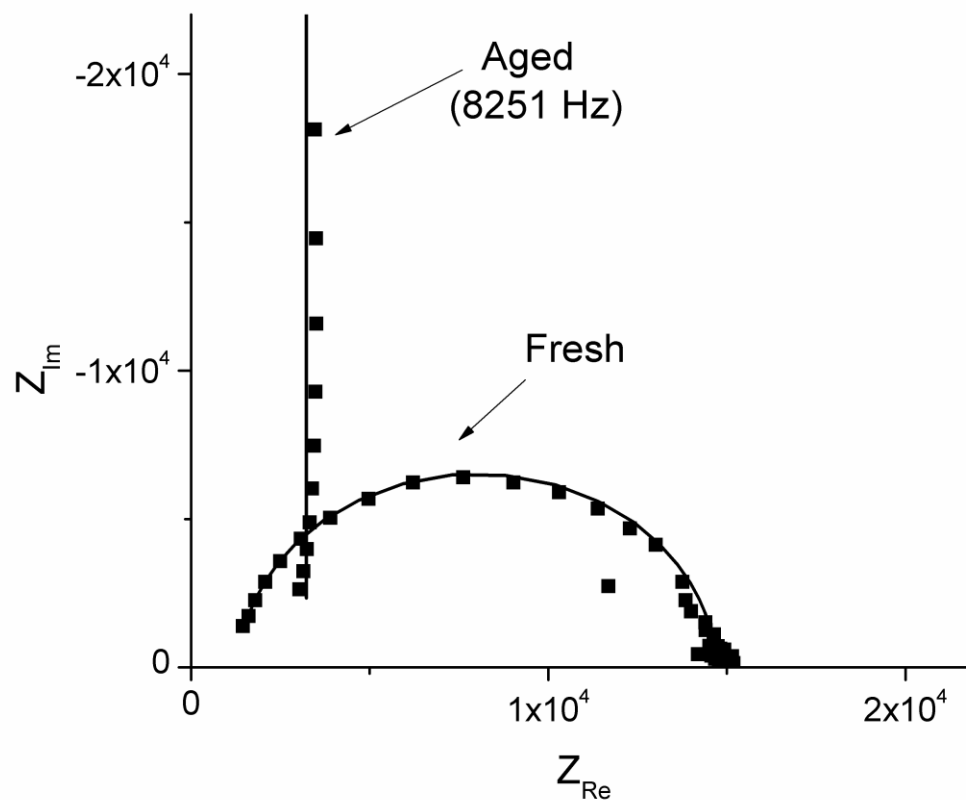


Figure 4-6. Nyquist plot of an aged CN_x film prepared using a deposition power of 25 W in a 100 % nitrogen discharge plasma.

Most importantly, the aged films start to show a pronounced photovoltaic effect, as is clearly seen in Figure 4-7 for an aged carbon nitride film. It should be noted that the open-circuit voltage is negative in this figure while the current density is positive. This demonstrates that structural relaxation of carbon nitride with aging leads to a transition from a photoconductive material to an n-type photovoltaic material. Structural relaxation of the film promotes a structural modification as a result of the release of the significant stress present in the as deposited films, which has the effect of breaking up the graphitic domains.

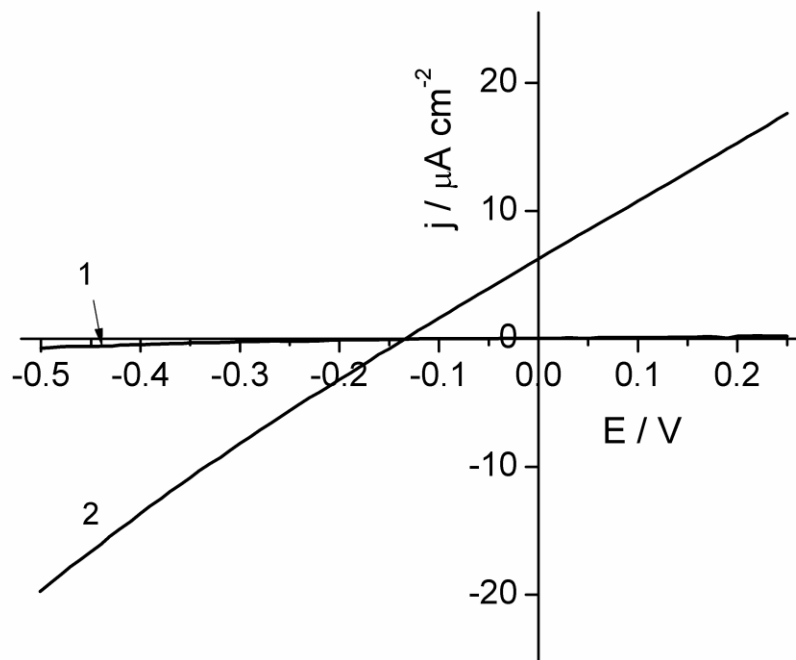


Figure 4-7. Dark (1) and illuminated (2) J-V plots of a CN_x film prepared using a deposition power of 25 W in a 100 % nitrogen containing plasma at 1 Pa after aging.

It is useful to compare the open-circuit voltage transients and short-circuit transients of the photoconductive and photovoltaic films as shown in Figure 4-8. Figure 4-8A shows the short-circuit photocurrent transients obtained at a cell bias of 0 V. For the photoconductive carbon nitride film (transient 1), it can be seen that even in the dark, there is still some positive anodic background current, attributed to the presence of conductive graphitic percolation networks. Upon illumination, the current increases to a more positive value clearly demonstrating an increase in the number of charge carriers in the film, which lead to an increase in film conductivity. It is important to highlight that the sign of the dark current and the photocurrent under illumination are the same for the photoconductive film. This is characteristic of photoconductive behaviour whereby the current under illumination is proportional to the dark current following Ohm's law.

However, for the aged film the background current was effectively zero at 0 V (transient 2), reflecting the absence of conductive domains across the bulk of the film, and upon illumination a significant increase in the anodic current was observed indicating an increase in the number of charge carriers. The positive sign of the net photocurrent indicates that the photogenerated minority carriers are holes.

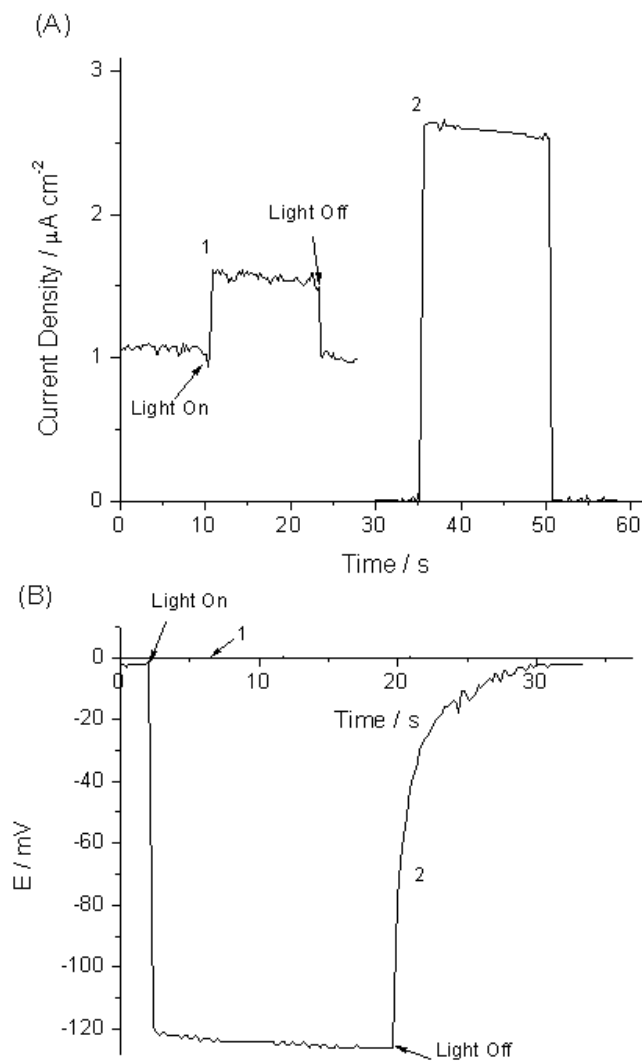


Figure 4-8. (A) Photocurrent and (B) photovoltage transients for photoconductive (plot 1 - fresh) and photovoltaic (plot 2 - aged) CN_x films prepared in 100 % N₂ plasma at 1 Pa.

Figure 4-8B shows the open-circuit voltage transients for a freshly prepared CN_x film (plot 1) and an aged CN_x film (plot 2) under illumination. The open-circuit voltage of the freshly prepared CN_x film does not change under illumination as would be expected for a photoconductive material. However, a significant change in the open-circuit voltage of the aged CN_x film was observed under illumination reaching a value of approximately -120 mV. It is the presence of graphitic domains that strongly influence the electronic properties of CN_x, and through their reduction or elimination by aging it was possible to reveal the electronic properties of the carbon nitride film. Building upon this observation, several routes were explored for the deposition of nitrogen rich carbon nitride materials that had a reduction of the graphitic domains.

One method to further modify the plasma composition for CN_x films during their growth and to increase the nitrogen content in the film is to increase the total deposition pressure.⁴⁰ An increase in the total discharge pressure can lead to a further increase in the nitrogen content in the film as a result of an increased likelihood of nitrogen reacting with carbon at the target as well as a reduction of the mean free path of the ejected CN species from the target leading to the possibility that they will further react during their travel toward the substrate. Higher pressures will also reduce the energy of the incident species arriving at the substrate limiting the chemical re-sputtering of nitrogen in the growing film.⁴⁰ We explored several different total deposition pressures in a pure nitrogen discharge plasma to examine the influence on the electronic properties of the resulting CN_x films. Figure 4-9 shows the dark J-V curves for carbon nitride films prepared at a total deposition pressure of 1 Pa, 3 Pa and 5 Pa. It was observed that the current-voltage plots show a pronounced decrease in current density as the total deposition pressure increases indicating a decrease in the electronic conductivity of the films with increasing plasma pressure as a result of an increase in the nitrogen content in the film. While the films show a decrease in their conductivity with increasing deposition pressure, none of the as prepared films showed photovoltaic properties when measured under illumination. In some cases photoconductivity was observed for these films. Therefore, these films were subjected to a thermal annealing process to promote structural modification of the carbon nitride film to further disrupt the graphitic percolation network.

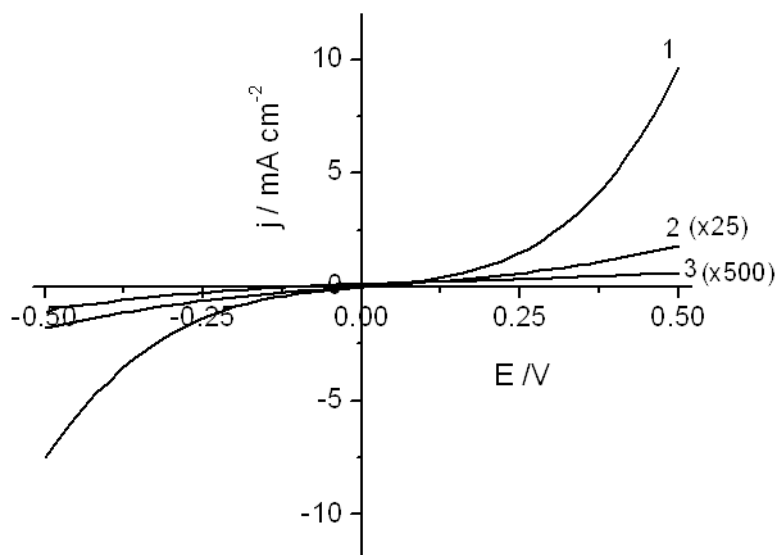
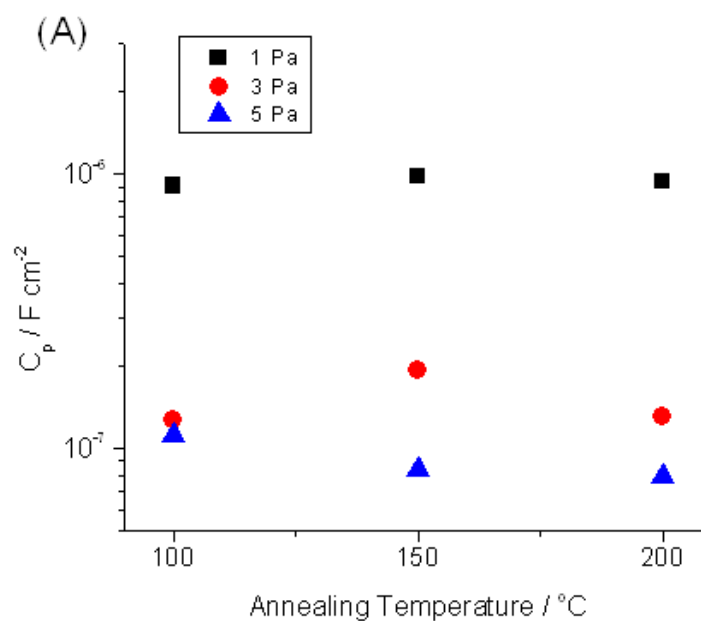


Figure 4-9. Dark current-voltage plots of CN_x prepared at 1 Pa (plot 1), 3 Pa (plot 2) and 5 Pa (plot 3) pure nitrogen plasma discharge pressures. Current density values for films prepared at 3 Pa and 5 Pa have been multiplied by a factor of 25 and 500 respectively to more clearly display on the same plot.

Figure 4-10 shows the parallel capacitance and resistance determined from impedance spectroscopy measurements at open-circuit conditions in the dark for films prepared at different total pressures in a 100% nitrogen discharge plasma and annealed in the temperature range of 100°C to 200°C for 60 minutes. A Randles equivalent circuit was used to fit all of the data. Figure 4-10A and 4-10 B show the values for the parallel capacitance and resistance as a function of the annealing temperature for films prepared using different plasma pressures. It can be seen that the films prepared at higher pressures (3 Pa and 5 Pa) exhibit an increased parallel resistance and decreased parallel capacitance relative to films prepared at a lower deposition pressure (1 Pa). R_p was found to increase in value with increasing annealing temperature indicating a reduction in the conductive pathways with annealing. However, C_p did not show a significant dependence on the annealing temperature. Figure 4-10C re-plots the value of C_p as a function of the plasma pressure, which shows that film capacitance depends more strongly on the plasma pressure and the nitrogen incorporation into the film. While none of the films exhibited

photovoltaic properties after annealing at 100°C, films prepared at 3 Pa and 5 Pa, and annealed at 150°C and 200°C generally exhibited a photovoltaic effect. This is due to a decrease in the percolation network of graphite as reflected in the increased parallel resistance along with a decrease in the film capacitance which suggests the formation of a space charge layer, apparently, in the nitrogen-rich domains of the film. Both of these properties are beneficial for the observation of a photovoltaic effect in CNx.



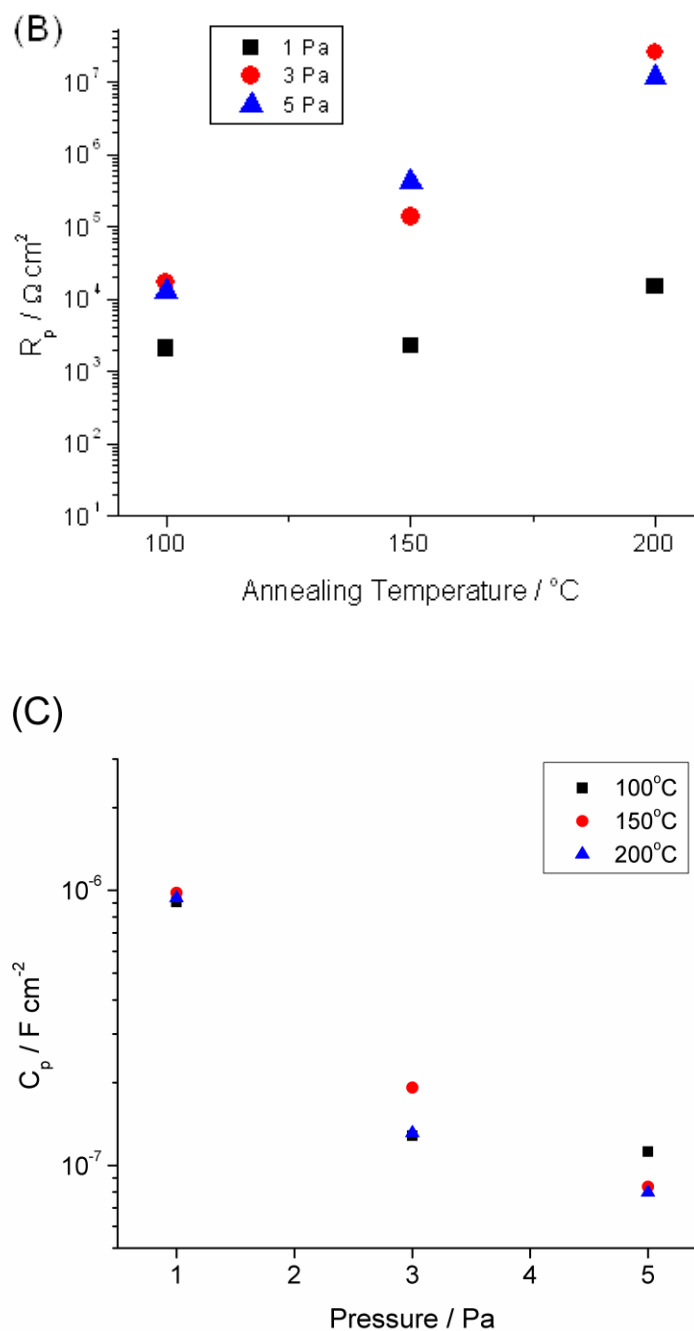


Figure 4-10 Values for the (A) parallel capacitance and (B) parallel resistance as a function of annealing temperature determined using a Randles equivalent circuit for CN_x films prepared at 1 Pa, 3 Pa, and 5 Pa pure nitrogen plasma discharge pressures. All films were annealed for 60 minutes. (C) Figure 4-10A re-plotted as a function of total plasma pressure.

The architecture of the films studied so far has consisted of an ITO/CNx/Al architecture. The work function of indium tin oxide has been reported to be in the range of 4.4 – 4.7 eV while aluminum is known to have a work function of 4.1 eV. This should lead to a difference in the work function of the two electrodes in the range of 0.3 V to 0.6 V. It would be expected that an open-circuit voltage for the CNx films would be in this range if it was determined by the difference in electrode work function. However, the largest value of the open-circuit voltage that was observed for any of the films was approximately - 0.15 V. This may indicate a poor alignment of the conduction band and valence band energy levels of the CNx films with the electrodes. To better control the interfacial energy level, a thin layer of poly(3,4-ethylenedioxythiophene) : polystyrene sulfonate (PEDOT:PSS) was spin-coated on the ITO electrode prior to CNx deposition. This material is commonly used in organic electronic devices as an electron blocking interfacial material and was used to ensure that electrons are extracted at the aluminum electrode and not at the ITO electrode. A photovoltaic effect was observed for annealed films that contained a PEDOT:PSS layer as well as films that did not contain a PEDOT:PSS layer. However, films that contained the PEDOT:PSS interfacial layer showed more reproducible photovoltaic properties.

Carbon nitride films were annealed at several different temperatures to promote structural modification of the films. Figure 4-11 shows typical J-V plots of CNx films of the same thickness (ca. 40 nm) under illumination deposited at pressures of 3 Pa and 5 Pa and annealed at 150°C for 60 minutes with a PEDOT:PSS interfacial layer. It was determined that annealing temperatures of 150°C were more effective than annealing temperatures of 200°C when a PEDOT:PSS layer was incorporated, probably, due to degradation of PEDOT:PSS at high temperatures. It can be clearly seen that under illumination the films show photovoltaic properties similar to the aged films as discussed above. However, in this case no aging of the device was necessary to observe a photovoltaic effect. This highlights the importance that nitrogen content and conductive percolation networks have in controlling the properties of the film. Ideally the carbon rich graphitic regions should be minimized to obtain a photovoltaic effect. This can be accomplished by increasing the nitrogen content present in the film through an increased total discharge pressure and their connectivity can be further disrupted with post-deposition annealing.

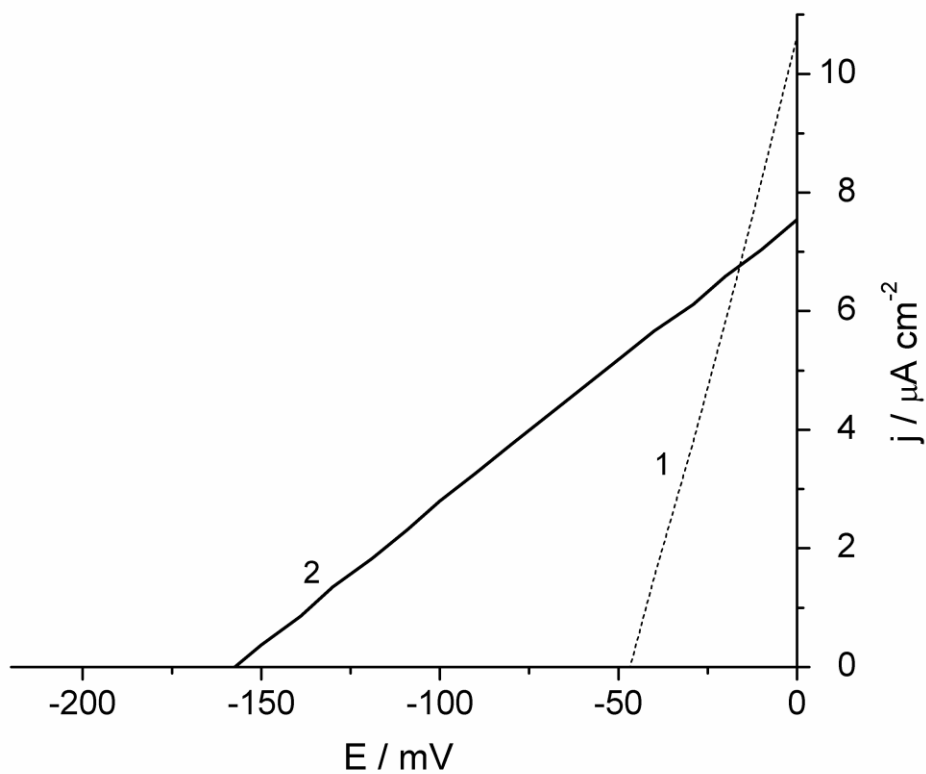


Figure 4-11. Typical J-V plot under illumination for CNx films prepared at 3 Pa (plot 1) and 5 Pa (plot 2) pure nitrogen plasma discharge pressures. The films were annealed for 60 minutes at 150°C.

In general, it was observed that CNx films prepared at 3 Pa showed a higher short-circuit current density and a lower open-circuit voltage, while films prepared at 5 Pa showed a smaller value of the short-circuit current density and a larger value of the open-circuit voltage. This difference in film properties can be attributed to their difference in conductive pathways in the film which will act as a source of a leakage current. For films prepared at 3 Pa, more graphitic content is expected, which will decrease film resistance and increase the dark current leading to a reduced value for the open-circuit voltage. On the other hand, for films prepared at 5 Pa, an increase in open-circuit voltage is accompanied by a decrease in the short-circuit current density, reflecting increased film resistance. Ideally, films should exhibit a high open-circuit voltage and short-circuit

current density to maximize power generation. These factors highlight the need for balance in charge transporting pathways provided by the graphitic regions to maximize current extraction, without acting as a detrimental source of current leakage that limits the maximum open-circuit voltage.

As highlighted above, the sign of the photocurrent of photoconductive materials does not change sign from that of the dark current. However, for photovoltaic materials the photogenerated carriers would be expected to be of opposite sign of the dark current in the film under forward bias conditions. Figure 4-12 shows a photocurrent transient for a photovoltaic CN_x film under forward bias conditions at a negative bias. The dark current is cathodic at a negative bias as has been observed for all the current-voltage plots of these materials. Upon illumination of the film, the sign of the current changes from cathodic to anodic indicating that the film shows photovoltaic rather than photoconductive behavior (the current under illumination is not proportional to the dark current and is opposite in sign). The occurrence of the anodic photocurrent indicates that the minority carriers in these devices are holes. In addition, it was observed in the current-voltage plots that it was necessary to apply a negative bias to the ITO electrode for the dark current to equal the photocurrent. This bias was in the range of – 50 to – 150 mV depending on the deposition conditions. Considered together with the change in sign of the photocurrent, these results indicate that a CN_x photovoltaic material with n-type properties was created.

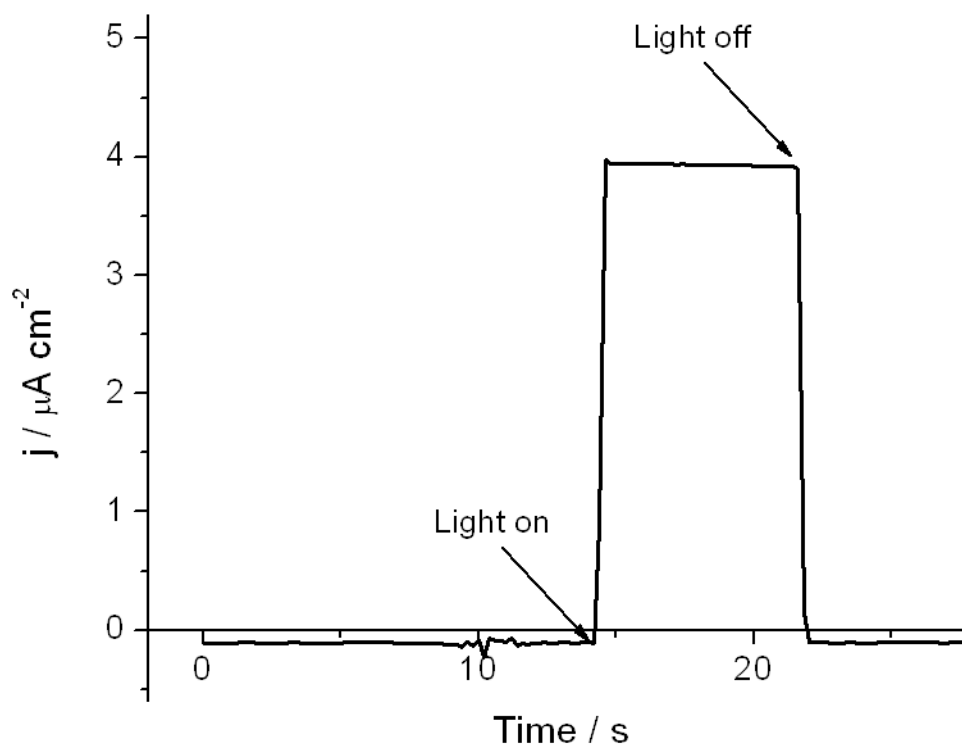


Figure 4-12. Photocurrent transient for a CN_x film at an applied bias of – 70 mV. The film was prepared in a 5 Pa pure nitrogen discharge plasma and annealed for 60 minutes at 150°C.

Bonding of CN_x determined from XPS

To better understand the bonding and structure of the photovoltaic CN_x materials, XPS was carried out for films prepared at 5 Pa and the spectra of the as deposited and annealed films were compared. XPS is a valuable technique for the investigation of the bonding in carbon nitride as a result of nitrogen incorporation.⁴⁷ It has also been shown that the surface bonding structure determined using XPS is representative of the bulk composition of the film, as previously demonstrated using elastic recoil detection and nuclear reaction analysis.⁴⁸ The C 1s spectra of amorphous carbon materials typically consist of one large broad peak that is a result of a distribution of the many different carbon bonding environments in the films.⁴⁹ Nitrogen incorporation leads to a chemical

shift to higher binding energies of the C 1s spectra due to the increased electronegativity of nitrogen. On the other hand the N 1s spectra exhibit two peaks that overlap to a varying extent depending on the amount of nitrogen incorporated into the film.⁵⁰ Table 4-1 shows the composition of the films as determined from the XPS survey scan. Despite efforts to minimize atmospheric exposure, there was still some post-deposition contamination of the surface of the films by oxygen. However, its value is quite low at approximately 6% of the atomic mass present in the film. Comparing the carbon to nitrogen ratio it can be seen that the as prepared films exhibit a C:N ratio of 1:0.73 which decreases slightly to 1:0.67 with annealing. This rather small change in nitrogen content, along with a reduction in the oxygen content, can have quite a large impact on the bonding in the film as discussed in further detail below.

Table 4-1. CN_x film composition determined for XPS survey spectra.

	C 1s / At. %	N 1s / At. %	O 1s / At. %
As deposited	54.0	39.4	6.10
Annealed	56.4	37.6	5.20

Figure 4-13 shows the C 1s and N 1s spectra for an as deposited CN_x film prepared using a 100% nitrogen discharge plasma at 5 Pa total pressure. As noted above the C 1s spectra of vacuum sputtered carbon nitride films typically exhibit one large broad peak, however for the deposition conditions used in this work it can be seen that there are two distinct peaks visible in the C 1s spectrum of our film. While these peaks have not been observed for vacuum sputtered carbon nitride, they have been observed in the C 1s spectra of melamine, as well as in graphitic carbon nitride materials prepared from molecular precursors where carbon is in an extended 6 fold ring structure and bonded to three nitrogen atoms.^{51,52} In References 51 and 52 the higher binding energy peak in these spectra at 288 eV are attributed to carbon bonded to three nitrogen atoms in an sp² configuration, while the first peak centered at 284.5 eV is due to carbon-carbon bonding in an aromatic configuration, which may or may not contain nitrogen in the ring structure. In our sputtered carbon nitride materials the nitrogen content is lower than in graphitic

carbon nitride, which has a C_3N_4 stoichiometry. As a result, the second peak centred at approximately 287 eV in our C 1s spectrum is shifted to lower binding energy and much broader due to the many different carbon bonding environments that contribute to this signal. The second peak is much larger in size than the graphitic peak reflecting the significant amount of nitrogen incorporation in the film. Two smaller peaks centred at 286.47 eV (C1) and 287.94 eV (C2) have been used to fit the data and reflect carbon bonded to one and two nitrogen atoms respectively.⁵⁰ While it is quite difficult to determine the specific bonding of carbon in the film from the C 1s spectrum as a result of the many possible bonding arrangements, further insight can be gained from the N 1s spectrum shown in Figure 4-13B.

For low nitrogen content films, one peak centred around 399 eV is usually observed. However, for increasing nitrogen content, the peak at 399 eV shifts to a higher binding energy around 400 eV, which is accompanied by the emergence of a second peak around 398 eV. As a result, the binding energies for the two components in the N 1s spectra of nitrogen rich carbon nitride films are generally found around ca. 399 and ca. 400 eV.⁴⁷ The peak centred around 400 eV (N3) is attributed to tetrahedrally coordinated nitrogen having three neighbours, such as nitrogen substituted in a graphite sheet, which is a n-type doping configuration of nitrogen in carbon nitride. The peak centered around 398 eV (N2) is assigned to nitrogen having two neighbours such as a pyridine-like bonding configuration.⁵³ Two peaks were used to fit the N 1s spectrum and the binding energy and area of each peak are shown in Table 4-2 along with those for the C 1s spectrum in Table 4-3.

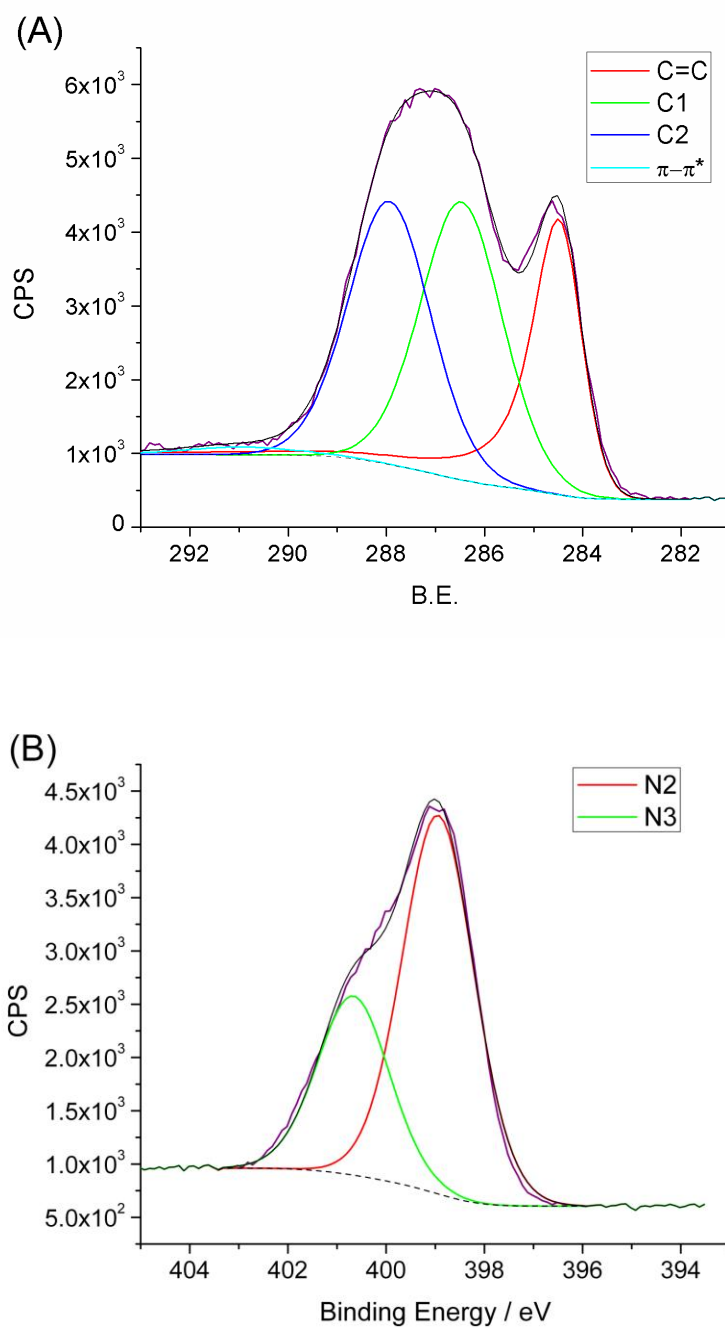


Figure 4-13. (A) C 1s XPS spectrum for an as deposited CN_x film prepared in a 5 Pa discharge plasma. (B) N 1s XPS spectrum for an as deposited CN_x film prepared in a 5 Pa discharge plasma.

Table 4-2. Binding energies and peak areas for peaks used to fit N 1s spectra.

N1s	N3		N2	
	BE / eV	Area / %	BE / eV	Area / %
Non-Annealed	400.67	32.10	398.94	67.9
Annealed	400.42	31.7	398.77	68.3

Table 4-3. Binding energies and peak areas for peaks used to fit C 1s spectra.

C1s	C2		C1		C=C	
	BE / eV	Area / %	BE / eV	Area / %	BE / eV	Area / %
Non-Annealed	287.94	37.4	286.47	39.5	284.5	21.6
Annealed	287.69	34.6	286.23	32.3	284.5	30.9

Figure 4-14 shows the C 1s and N 1s spectra for an annealed CN_x film prepared using a 100 % nitrogen discharge plasma at 5 Pa total pressure. The film was annealed at 150°C for 60 minutes. The C 1s spectrum for this film is shown in Figure 4-14A and again two peaks are visible. However, the shapes of the two peaks are quite different from the as deposited films. It can be seen that upon annealing the peak centred at 284.5 eV (C=C), which shows carbon-carbon bonding has increased in intensity relative to the second higher binding energy peak. As well, the second peak at higher binding energy has decreased in intensity, is less broad and is slightly shifted to a lower binding energy as a result of thermal annealing. This is a direct result of the slight decrease in nitrogen, as well as oxygen, present in the film that are more electronegative than carbon and which have the effect of increasing the binding energy in the C 1s spectra. Considering first the graphitic peak at 284.5 eV: it is observed for an as deposited film that the area is 21.6 % and that upon annealing this increased to 30.9 %, which is a 10 % increase in size. Concomitantly, the contribution of the two higher binding energy peaks decrease by the same amount from 76.9 % to 66.9 % indicating that one of the main effects of thermal annealing is to increase the carbon-carbon C=C bonding. This signal may be due to either graphitic or aromatic carbon bonding configurations, which may also contain nitrogen in the ring structure. The increase in intensity of the peak at 284.5 eV therefore indicates an

increase in the aromatic carbon in the film with thermal annealing. As shown above, a decrease in film conductivity was also observed upon thermal annealing, which would not be expected for an increase in the graphitic content in the film. These factors suggest that the main effect of thermal annealing is to induce morphological changes in the film that disrupt the graphitic percolation network and explain the observed decrease in conductivity with thermal annealing.

This hypothesis is consistent with the changes in the nitrogen bonding as revealed in the N1s spectra for the annealed films shown in Figure 4-14B. Again, the N 1s spectrum shows one large peak that is due to the overlap of two smaller peaks. The higher binding energy peak at 400.42 eV due to tetrahedrally coordinated nitrogen has shifted down slightly in energy and represents a slightly smaller fraction of the total signal compared to the as deposited films. At the same time the peak at 398.77 eV assigned to pyridine-like nitrogen has increased slightly in intensity and shows a narrower distribution. Overall, no significant change in the N 1s spectrum was observed, which indicates little change in the chemical environment of the nitrogen atoms and is consistent with the suggestion that thermal annealing induces a structural modification. In summary, thermal annealing of carbon nitride leads to a slight decrease in the nitrogen content present in the film along with an increase in carbon-carbon bonding, which is likely accompanied by some morphological changes in the film microstructure. Future studies of the local film morphology and composition with thermal annealing are needed to explore this behaviour in more detail.

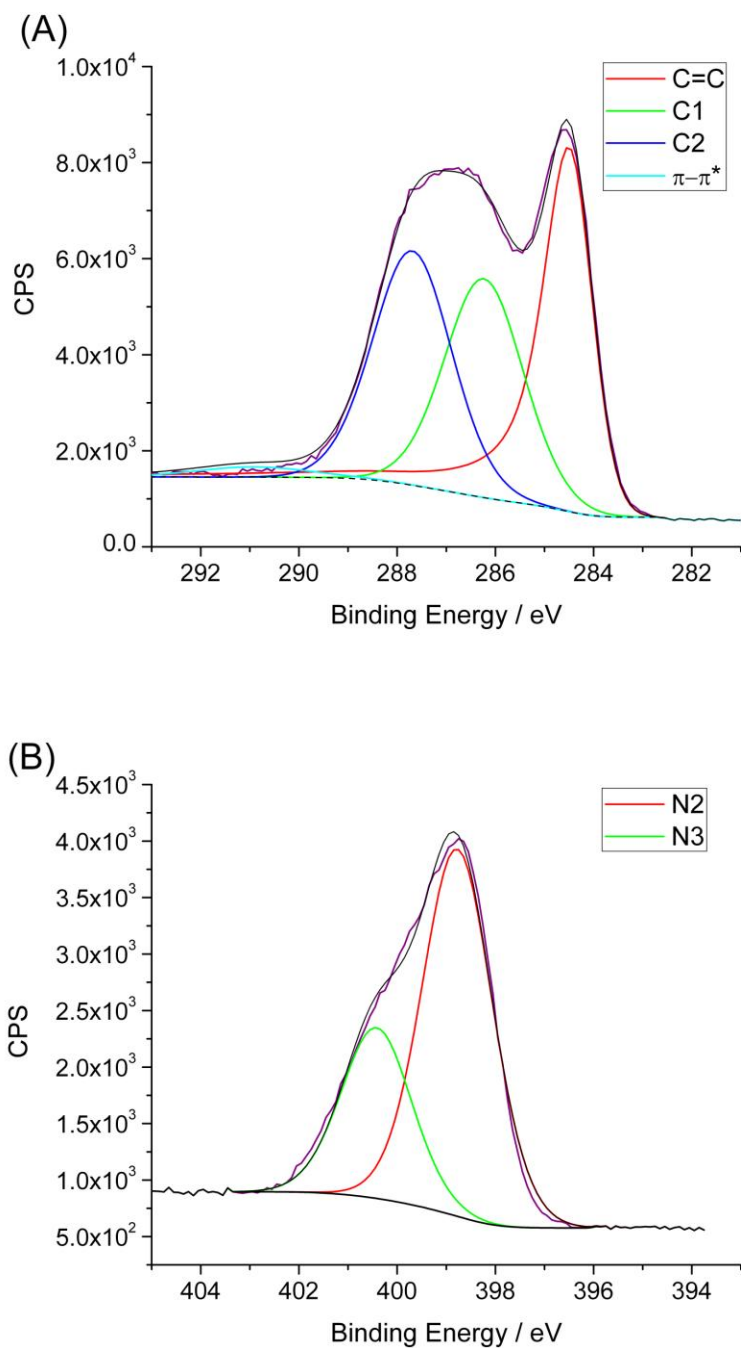


Figure 4-14. (A) C 1s XPS spectrum for an annealed CN_x film prepared in a 5 Pa discharge plasma. Films were annealed for 60 minutes at 150°C. (B) N XPS 1s spectrum for an annealed CN_x film prepared in a 5 Pa discharge plasma. Films were annealed for 60 minutes at 150°C.

P3HT:CNx bulk heterojunction composite organic solar cells

It was shown in the previous chapter that carbon nitride can act as an effective electron acceptor material when combined with a conjugated polymer leading to an enhancement in photocurrent generation in these composite films.¹⁷ However, in the previous case the CNx materials themselves did not show any photovoltaic properties. Ideally, alternative acceptor materials that could replace fullerenes should also exhibit photovoltaic properties to maximize device efficiency. We have prepared three separate solid-state devices to compare the photovoltaic response of single layer CNx or P3HT device with a P3HT/CNx heterojunction device. Figure 4-15 shows the photocurrent transients obtained for ITO/CNx/Al, ITO/PEDOT/P3HT/Al as well as a composite ITO/PEDOT/P3HT:CNx/Al device obtained at short-circuit conditions. For all of the films, the background current is zero in the dark. Several important features can be observed for these films upon illumination.

In the case of the P3HT only device, a sharp increase in the cathodic photocurrent, expected for a p-type semiconductor, is observed which decays with time. This decay is indicative of surface state recombination in the P3HT film and has been observed previously for single layer polythiophene devices.⁵⁴ In the case of the CNx only device, it can be seen that the photocurrent immediately increases under illumination and that it is anodic which would be expected for an n-type semiconductor. As well, there is no decay in the current density over time reflecting the excellent stability of this material. Finally, if we look at the composite P3HT:CNx film we can see that a cathodic photocurrent is obtained whose magnitude is larger than either the P3HT film or CNx film on their own. It should be noted that a constant P3HT thickness of 70 nm was used and a constant thickness of 30 nm was used for the CNx film and there would not be any differences in photocurrent generation expected due to film thickness. The increase in photocurrent generation can be attributed to CNx acting as an electron acceptor material, as was previously demonstrated for this material, as well as providing a significant photocurrent on its own as reflected in its photocurrent transient. In addition, CNx exhibits a much more stable response under illumination compared to P3HT, which is one of the significant barriers that has limited organic solar cells. The prototype devices shown here

demonstrate the significant potential of n-type carbon nitride photovoltaics for a wide variety of possible materials combinations that can extend beyond conjugated polymers.

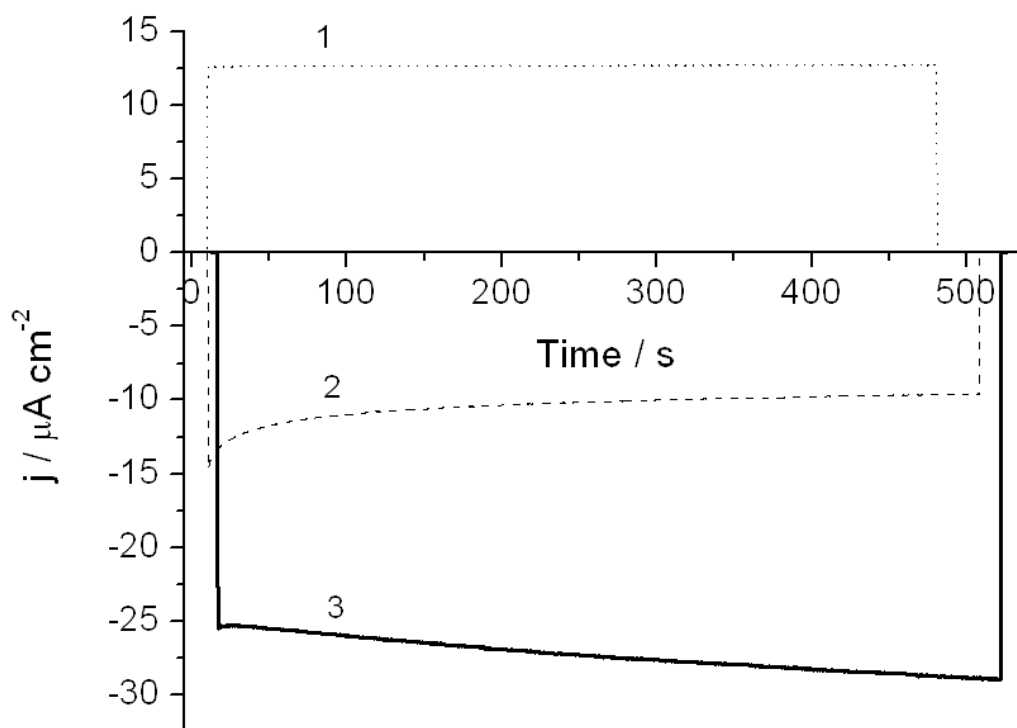


Figure 4-15. Photocurrent transients for a CN_x single layer device (plot 1), P3HT single layer device (plot 2) and a CN_x-P3HT heterojunction device (plot 3) measured at short-circuit conditions. All films were annealed at 150°C for 60 minutes.

4.4 Conclusions

Carbon nitride materials have been prepared that exhibit a photovoltaic effect and n-type semiconductor properties for the first time. It was found that the elimination of conductive graphitic pathways was necessary to observe photocurrent generation in these films. This was accomplished by increasing the nitrogen content in the films using a pure nitrogen plasma discharge at elevated deposition pressures and low deposition powers to create photoconductive CN_x materials. The as deposited films contained a significant amount of film disorder that was reduced through structural relaxation by film aging and

thermal annealing, which allowed the observation of a photovoltaic effect in CN_x. The materials showed an anodic photocurrent and negative photovoltage indicating that the minority carriers were holes and that these materials are n-type semiconductors. The bonding structure and configuration in carbon nitride as determined by XPS measurements showed that these materials contained high amounts of nitrogen (ca. 40 %) in a graphitic network, which is a known n-type doping configuration for amorphous carbon nitride materials. These materials were deposited onto a P3HT substrate to create a prototype p-n heterojunction device that exhibited enhanced photocurrent generation compared to the single layer devices. These results clearly demonstrate that nitrogen rich carbon nitride materials show exceptional promise not only for organic solar cells but may also be combined with other materials such as inorganic oxides, quantum nanocrystals, etc. where their useful electronic properties may be exploited.

4.5 References

- (1) Dennler, G.; Scharber, M. C.; Brabec, C. J. *Advanced Materials* **2009**, *21*, 1323.
- (2) Nielsen, T. D.; Cruickshank, C.; Foged, S.; Thorsen, J.; Krebs, F. C. *Solar Energy Materials and Solar Cells* **2010**, *94*, 1553.
- (3) Li, G.; Zhu, R.; Yang, Y. *Nature Photonics* **2012**, *6*, 153.
- (4) Yu, G.; Gao, J.; Hummelen, J. C.; Wudl, F.; Heeger, A. J. *Science* **1995**, *270*, 1789.
- (5) Walker, B.; Kim, C.; Nguyen, T. Q. *Chemistry of Materials* **2011**, *23*, 470.
- (6) Gunes, S.; Neugebauer, H.; Sariciftci, N. S. *Chemical Reviews* **2007**, *107*, 1324.
- (7) Sariciftci, N. S.; Smilowitz, L.; Heeger, A. J.; Wudl, F. *Science* **1992**, *258*, 1474.
- (8) Ooi, Z. E.; Tam, T. L.; Shin, R. Y. C.; Chen, Z. K.; Kietzke, T.; Sellinger, A.; Baumgarten, M.; Mullen, K.; Demello, J. C. *Journal of Materials Chemistry* **2008**, *18*, 4619.
- (9) Halls, J. J. M.; Walsh, C. A.; Greenham, N. C.; Marseglia, E. A.; Friend, R. H.; Moratti, S. C.; Holmes, A. B. *Nature* **1995**, *376*, 498.
- (10) Huynh, W. U.; Dittmer, J. J.; Alivisatos, A. P. *Science* **2002**, *295*, 2425.

- (11) Li, Z.; Gao, F.; Greenham, N. C.; McNeill, C. R. *Advanced Functional Materials* **2011**, *21*, 1419.
- (12) Ebadian, S.; Gholamkhash, B.; Shambayati, S.; Holdcroft, S.; Servati, P. *Solar Energy Materials and Solar Cells* **2010**, *94*, 2258.
- (13) Janssen, R. A. J.; Hummelen, J. C.; Wudl, F. *Journal of the American Chemical Society* **1995**, *117*, 544.
- (14) Nicolaidis, N. C.; Routley, B. S.; Holdsworth, J. L.; Belcher, W. J.; Zhou, X. J.; Dastoor, P. C. *Journal of Physical Chemistry C* **2011**, *115*, 7801.
- (15) Sondergaard, R.; Hosel, M.; Angmo, D.; Larsen-Olsen, T. T.; Krebs, F. C. *Materials Today* **2012**, *15*, 36.
- (16) Sonar, P.; Lim, J. P. F.; Chan, K. L. *Energy & Environmental Science* **2011**, *4*, 1558.
- (17) Byers, J. C.; Billon, F.; Debiecme-Chouvy, C.; Deslouis, C.; Pailleret, A.; Semenikhin, O. A. *Acs Applied Materials & Interfaces* **2012**, *4*, 4579.
- (18) Hultman, L.; Neidhardt, J.; Hellgren, N.; Sjostrom, H.; Sundgren, J. E. *Mrs Bulletin* **2003**, *28*, 194.
- (19) Mubumbila, N.; Tessier, P. Y.; Angleraud, B.; Turban, G. *Surface & Coatings Technology* **2002**, *151*, 175.
- (20) Silva, S. R. P.; Rafferty, B.; Amaratunga, G. A. J.; Schwan, J.; Franceschini, D. F.; Brown, L. M. *Diamond and Related Materials* **1996**, *5*, 401.
- (21) Muhl, S.; Mendez, J. M. *Diamond and Related Materials* **1999**, *8*, 1809.
- (22) Byers, J. C.; Tamiasso-Martinhon, P.; Deslouis, C.; Pailleret, A.; Semenikhin, O. A. *Journal of Physical Chemistry C* **2010**, *114*, 18474.
- (23) Jander, S.; Kornowski, A.; Weller, H. *Nano Letters* **2011**, *11*, 5179.
- (24) Nitta, S.; Takada, N.; Sugiyama, K.; Itoh, T.; Nonomura, S. *Journal of Non-Crystalline Solids* **1998**, *227*, 655.
- (25) Katsuno, T.; Nitta, S.; Habuchi, H.; Iwasaki, T.; Itoh, T.; Nonomura, S. *Amorphous and Nanostructured Carbon* **2000**, *593*, 499.
- (26) Naruse, Y.; Nitta, S. *Diamond and Related Materials* **2002**, *11*, 1210.
- (27) Katsuno, T.; Nitta, S.; Habuchi, H. *Diamond and Related Materials* **2002**, *11*, 1215.

- (28) Katsuno, T.; Nitta, S. *Diamond and Related Materials* **2003**, *12*, 1887.
- (29) Nitta, S.; Aono, M.; Katsuno, T.; Naruse, Y. *Diamond and Related Materials* **2003**, *12*, 219.
- (30) Katsuno, T.; Nitta, S.; Habuchi, H.; Stolojan, V.; Silva, S. R. P. *Applied Physics Letters* **2004**, *85*, 2803.
- (31) Iwasaki, T.; Aono, M.; Nitta, S.; Habuchi, H.; Itoh, T.; Nonomura, S. *Diamond and Related Materials* **1999**, *8*, 440.
- (32) Aono, M.; Goto, T.; Tamura, N.; Kitazawa, N.; Watanabe, Y. *Diamond and Related Materials* **2011**, *20*, 1208.
- (33) Iwasaki, C.; Aono, M.; Tamura, N.; Kitazawa, N.; Watanabe, Y. *Japanese Journal of Applied Physics* **2012**, *51*.
- (34) Tamura, N.; Aono, M.; Kishimura, H.; Kitazawa, N.; Watanabe, Y. *Japanese Journal of Applied Physics* **2012**, *51*.
- (35) Zhou, Z. B.; Cui, R. Q.; Pang, Q. J.; Hadi, G. M.; Ding, Z. M.; Li, W. Y. *Solar Energy Materials and Solar Cells* **2002**, *70*, 487.
- (36) Lejeune, M.; Benlahsen, M. *Diamond and Related Materials* **2008**, *17*, 29.
- (37) Durand-Drouhin, O.; Lejeune, M.; Clin, M.; Ballutaud, D.; Benlahsen, M. *Solid State Communications* **2001**, *118*, 179.
- (38) Robertson, J.; Davis, C. A. *Diamond and Related Materials* **1995**, *4*, 441.
- (39) Kim, Y.; Cook, S.; Tuladhar, S. M.; Choulis, S. A.; Nelson, J.; Durrant, J. R.; Bradley, D. D. C.; Giles, M.; McCulloch, I.; Ha, C. S.; Ree, M. *Nature Materials* **2006**, *5*, 197.
- (40) Kaltofen, R.; Sebald, T.; Weise, G. *Thin Solid Films* **1996**, *290*, 112.
- (41) Lazar, G.; Clin, M.; Charvet, S.; Therasse, M.; Godet, C.; Zellama, K. *Diamond and Related Materials* **2003**, *12*, 201.
- (42) Alibart, F.; Peponas, S.; Charvet, S.; Benlahsen, M. *Thin Solid Films* **2011**, *519*, 3430.
- (43) Robertson, J.; O'Reilly, E. P. *Physical Review B* **1987**, *35*, 2946.
- (44) Kaltofen, R.; Sebald, T.; Weise, G. *Thin Solid Films* **1997**, *308*, 118.
- (45) Durand-Drouhin, O.; Benlahsen, M. *Solid State Communications* **2004**, *131*, 425.
- (46) Peponas, S.; Benlahsen, M.; Guedda, M. *Journal of Applied Physics* **2009**, *106*.

- (47) Ronning, C.; Feldermann, H.; Merk, R.; Hofsass, H.; Reinke, P.; Thiele, J. U. *Physical Review B* **1998**, *58*, 2207.
- (48) Lejeune, M.; Durand-Drouhin, O.; Charvet, S.; Grosman, A.; Ortega, C.; Benlahsen, M. *Thin Solid Films* **2003**, *444*, 1.
- (49) Rodil, S. E.; Muhl, S. *Diamond and Related Materials* **2004**, *13*, 1521.
- (50) Hellgren, N.; Guo, J. H.; Luo, Y.; Sathe, C.; Agui, A.; Kashtanov, S.; Nordgren, J.; Agren, H.; Sundgren, J. E. *Thin Solid Films* **2005**, *471*, 19.
- (51) Dementjev, A. P.; de Graaf, A.; van de Sanden, M. C. M.; Maslakov, K. I.; Naumkin, A. V.; Serov, A. A. *Diamond and Related Materials* **2000**, *9*, 1904.
- (52) Guo, Q. X.; Xie, Y.; Wang, X. J.; Zhang, S. Y.; Hou, T.; Lv, S. C. *Chemical Communications* **2004**, 26.
- (53) Neidhardt, J.; Hultman, L.; Czigany, Z. *Carbon* **2004**, *42*, 2729.
- (54) DiCarmine, P. M.; Semenikhin, O. A. *Electrochimica Acta* **2008**, *53*, 3744.

Chapter 5

5 The Mechanism of Recombination Losses in Bulk Heterojunction P3HT:PCBM Solar Cells Studied Using Intensity Modulated Photocurrent Spectroscopy

5.1 Introduction

Despite impressive improvements over the past 10 years, the efficiency and the service life of organic solar cells still remain too low for them to compete successfully with other solar cell technologies.¹⁻³ It is estimated³ that the organic solar cells will become competitive with other thin film technologies only at efficiencies of more than 10% and the lifetimes more than 3-5 years. The low efficiency of organic solar cells is directly related to losses that occur at every step of the photogeneration, separation and collection processes. However, there remains a considerable controversy concerning the mechanism of the recombination losses (geminate or non-geminate, bulk or interfacial) in organic solar cells.⁴⁻²⁰ It is widely considered that the main loss mechanism is the geminate recombination of the primary photoexcitons.^{6,13-15,17,20,21} However, recent data^{8,12,14} show that in photovoltaic blends with proper nanomorphology and phase segregation, the probability of fast exciton dissociation into free charge carriers approaches unity and therefore other loss mechanisms need to be considered to further improve the efficiency of organic bulk heterojunction solar cells. One of these loss channels is interfacial recombination and poor charge extraction at the contacts. However, surprisingly, these processes have attracted little attention in the literature. Earlier this year, Street et al. published a paper²² in which they suggested that the dominant recombination mechanism is through interfacial states at the polymer/PCBM (phenyl C₆₀-butyric acid methyl ester) interface. This finding was made on the basis of measurements of the intensity dependence of steady-state photocurrents, which prompted certain discussion^{10,18} stemming from an assertion that a steady-state technique cannot unambiguously determine the loss mechanism. In this work, we study the mechanism of the recombination losses in poly(3-hexylthiophene) (P3HT):PCBM bulk heterojunction organic solar cells using two non-steady-state techniques, namely, intensity modulated photocurrent spectroscopy (IMPS) and intensity modulated photovoltage spectroscopy (IMVS). We show that indeed one of the dominant loss mechanisms is non-geminate recombination via interfacial states. Furthermore, we demonstrate that the interfacial recombination is to a large extent responsible for the drastic loss in the cell efficiency upon ageing.

A rapid deterioration of the photovoltaic performance of typical organic solar cells upon their ageing is recognized as a very important issue that limits the competitiveness of organic solar cells.^{3,23-27} While it is generally agreed that this deterioration is due to incorporation of atmospheric oxygen and moisture into the active layer and recently a number of detailed studies,^{26,27} including spatial and depth profiling of the physico-chemical changes that occur upon ageing^{24,25} appeared in the literature, still there is insufficient knowledge of the specific degradation mechanisms and especially how ageing affects various steps of the photocurrent generation and collection processes in organic solar cells.

IMPS and IMVS are well-known techniques that were successfully used in the past for the studies of the photoprocesses at various semiconductor electrodes^{28-33,33-36} including organic single-layer or bi-layer polymer solid-state solar cells,^{36,37} and are actively used at present for studies of dye-sensitized solar cells.³⁸⁻⁴⁴ At the same time, we are aware of only one paper that describes an IMPS study of a bulk heterojunction organic solar cell,⁴⁵ which appeared when this manuscript was in preparation. However, the interpretation of the IMPS measurements in this paper was somewhat deficient. For instance, the analytical expression for the photocurrent obtained by Bag et al.⁴⁵ should result in the phase of the photocurrent staying negative at all frequencies, whereas the experimental data presented in this paper clearly showed a positive phase shift at low frequencies. To account for this, the authors introduced a certain effective parallel capacitance with an unclear physical meaning. Furthermore, Bag et al. interpreted their data in terms of primary exciton dissociation and recombination times, which are known to be in the nanosecond to picosecond range or even shorter¹⁵ and thus can hardly be analyzed by IMPS measurements with the high frequency limit of 100 kHz as was done by Bag et al.¹⁵

The IMPS technique analyzes an *ac* photocurrent response of a photovoltaic system to intensity modulated illumination as a function of the modulation frequency. Since IMPS is a frequency domain technique, it is capable of characterizing the dynamic behavior of photovoltaic systems, as opposed to various *dc* methods like I-V curve measurements/simulations. IMPS also offers distinct advantages over measurements of

transient photocurrent/photovoltage/photoconductivity/time-of-flight/photo-CELIV (charge extraction by linearly increasing voltage) response to short illumination pulses since it allows one to separate the bulk (such as transport) and interfacial (such as surface recombination and charge extraction) processes. Furthermore, IMPS measurements are easier to relate to regular steady-state photocurrent measurements since they are essentially performed under normal working conditions of a solar cell, just using a modulated illumination. While IMPS cannot characterize the ultrafast processes related to primary photoexcitation and exciton dissociation, it is an excellent tool for studies of the transport and recombination processes as well as the processes of carrier recombination and extraction at the contacts. Furthermore, since IMPS uses a small *ac* harmonic perturbation, which can be easily superimposed onto a larger *dc* signal, IMPS offers a unique opportunity to investigate non-linear behavior of photovoltaic systems with great accuracy.^{31,32,40,46}

Towards this end, the IMPS response to such an *ac+dc* perturbation is analyzed as a function of both the modulation frequency of the *ac* component of the light intensity and the magnitude of the *dc* component. Since the *ac* perturbation is typically much smaller than the *dc* component, IMPS spectra represent a quasi-linear approximation, with the non-linear behavior of the photovoltaic system manifesting itself through dependencies of the kinetic parameters of the photoprocess, as determined by IMPS, on the *dc* light intensity. In this work, this approach allowed us to separately evaluate the effect of the light intensity on different stages of the photoprocess. Specifically, it was found that the rate of the interfacial recombination of photoexcited electrons has two components, one of which increases linearly with the light intensity. This indicates that one of the dominant mechanisms of the recombination losses under these conditions is the interfacial recombination of electrons with photogenerated holes trapped at or near the interface. This finding was supported by Mott-Schottky measurements in the dark and under illumination that showed that the density of hole-occupied deep traps in the photovoltaic layer also increased with the light intensity.

5.2 Experimental

Materials and Device Fabrication

The solid state organic photovoltaic devices were prepared using a glass (1.1 mm)/ITO(100 nm) /PEDOT:PSS(70 nm)/P3HT:PCBM(90 nm)/Al (130 nm) architecture. Indium tin oxide (ITO) coated glass slides (Kintec, surface resistance $< 10 \text{ Ohm}/\square$) were used as a transparent conducting anode. The ITO coated glass slides were cleaned by sonicating in a soap solution and rinsing multiple times with deionized water, followed by successive sonication for 20 minutes each in acetone, methanol and isopropanol. The ITO slides were then activated by UV ozone treatment for 20 min prior to PEDOT:PSS deposition. PEDOT:PSS (Clevios PH1000 PEDOT grade, H.C. Stark) was filtered through a $1 \mu\text{m}$ glass filter to remove polymer aggregates, spin coated onto ITO coated glass slides in ambient conditions and dried for 15 min at 95°C . The samples were transferred to a glove box with an inert Ar atmosphere ($< 1 \text{ ppm O}_2$ and H_2O). The photoactive layer consisted of a 1:1 mass ratio of P3HT ($> 95\%$ regioregular, Solaris Chem) and PCBM (Solaris Chem) dissolved in dichlorobenzene and stirred overnight at 60°C . The solution was filtered through a $0.45 \mu\text{m}$ PTFE filter to remove aggregates and spin coated onto the PEDOT:PSS layer. Samples were dried for 12 minutes at 90°C and transferred without being exposed to ambient conditions under an inert Ar atmosphere to a vacuum chamber (base pressure $< 4 \times 10^{-6}$ Torr). Aluminum was deposited using thermal evaporation and the completed devices were annealed at 150°C for 11 minutes. Up to 5 cells were prepared from one PV slide by evaporating 5 independent Al electrodes. The bottom ITO glass electrode was also divided into 5 independent electrodes by selectively removing the conducting ITO layer between the cells. The geometric area of one cell was 0.26 cm^2 . The cells were not encapsulated. After the fabrication, the cell efficiencies were evaluated using a Sciencetech solar simulator under the simulated AM1.5 solar light. Samples were stored under an inert Ar environment or in vacuum; however, they were briefly exposed to ambient conditions when they were loaded to the IMPS sample holder.

Measurement Procedures

For this work, we selected two representative cells that were prepared in identical conditions on the same photovoltaic slide. A number of other slides were also measured which generally produced similar results, with slight variations in the values of characteristic times, photocurrent magnitude and other photovoltaic parameters. Two sets of measurements were performed, one a few days after the cell fabrication, and the other 2 months after the cell fabrication. All measurements were performed in an inert argon atmosphere using the aluminum electrode as a counter electrode and the ITO electrode as a working electrode. Cathodic photocurrents (electrons extracted at the Al electrode) were taken as having the positive sign in the IMPS plots. The IMPS measurements were performed under short-circuit conditions in the 1 MHz – 1 Hz frequency range using a stand-alone Solartron 1260 frequency response analyzer. The light source was a 405 nm 20 mW laser diode (LD1510, Power Technology). The *ac* component of the light intensity was maintained constant at 8.0×10^{15} photons $s^{-1} cm^{-2}$, whereas the *dc* component increased stepwise from 8.2×10^{15} to 6.4×10^{16} photons $s^{-1} cm^{-2}$, or from ca. 4 to 31 mW cm^{-2} . The chosen *ac* light intensity was shown in a separate experiment to be small enough to ensure the linear character of the cell response. The illuminated cell area was $0.03 cm^2$. For the bias dependencies, IMPS spectra were acquired using a different setup that included a Solartron 1250 frequency response analyzer coupled with a PAR 263A potentiostat–galvanostat (Princeton Applied Research). Both setups were controlled by a version 2.8 ZPlot software (Scribner Associates Inc.). The IMVS spectra were acquired in open-circuit conditions in the 1 MHz – 1 Hz frequency range using a stand-alone Solartron 1260 frequency response analyzer.

The Mott-Schottky measurements were performed in the dark and under the same *dc* light intensities as the IMPS measurements using a Solartron 1250 frequency response analyzer coupled with a PAR 263A potentiostat–galvanostat. The *dc* bias range was +0.6 V to -0.25 V. The amplitude of the *ac* voltage perturbation was 10 mV. A frequency of 6.626 kHz was used that was found high enough for the cells to be adequately represented by a serial RC circuit.

Procedures for determination of relaxation time τ and the exponent α

In the case of photocurrent relaxation at surface states with a single mean relaxation time, the IMPS photocurrent complex plane plots lay entirely within the 1st quadrant of the complex plane and can be described by the general equation of the form (31,32,34,36,46):

$$j = g \left(1 - \frac{\gamma}{1+(i\omega\tau)^\alpha} \right) \quad (1)$$

where g is the *ac* generation current (the flux of photogenerated carriers to the interface), τ is the characteristic relaxation time of the photogenerated carriers, γ is the fraction of carriers involved in the relaxation, ω is the angular light modulation frequency, and i is the imaginary unit. The exponent $0 \leq \alpha \leq 1$ is introduced to account for a distribution of relaxation times of the surface states, for instance, due to structural inhomogeneity or fractal nature of the interface.³² For an ideal interface with a single type of surface states, $\alpha = 1$ and the IMPS complex plane plot takes shape of a semicircle. When α is less than unity, the centre of the semicircle is located below the real axis resulting in the appearance of a depressed semi-circle shape in the IMPS spectra.

The parameters γg , τ and α can be determined by fitting the experimental frequency dependencies of the real and imaginary components $Re(j)$ and $Im(j)$ of the *ac* photocurrent using Eq. (1). Specifically, the following procedure was used:³²

First, the experimental values of $Re(j)$ and $Im(j)$ were used to calculate the value of the function:

$$Y = (j - Re(j)_0)^{-1} \quad (2)$$

where $Re(j)_0$ is the low-frequency limit of the *ac* photocurrent, $Re(j)_0 = g(1-\gamma)$.

From (1) and (2) one can obtain frequency dependencies of the real $Re(Y)$ and imaginary $Im(Y)$ components of function Y , as well as function Φ :

$$Re(Y) = \frac{1}{\gamma g} \left(1 + (\omega\tau)^{-\alpha} \cos\left(\frac{\alpha\pi}{2}\right) \right) \quad (3)$$

$$Im(Y) = \frac{1}{\gamma g} (\omega\tau)^{-\alpha} \cos\left(\frac{\alpha\pi}{2}\right) \quad (4)$$

$$\Phi = \frac{Re(Y)}{Im(Y)} \operatorname{ctg}\left(\frac{\alpha\pi}{2}\right) = \frac{\omega^\alpha \tau^\alpha}{\sin\left(\frac{\alpha\pi}{2}\right)} \quad (5)$$

Then the exponent α can be found from the slope of the plot of $\ln(Im(Y))$ vs. $\ln(\omega)$ (see Eq. 4) and the relaxation time τ and thus the recombination rate constant $k=1/\tau$ can be found from the slope of a linear plot of Φ versus ω^α . For IMPS plots studied in this work, the values of the exponent α varied from 0.65 to 0.8, the average value being $\alpha = 0.75$. This is easily understood since the interfacial recombination most likely occurs at the bulk heterojunction interface between PCBM and P3HT phases (see below), which should feature a considerable fractal behavior as well as pronounced inhomogeneity.

The standard deviations σ and confidence intervals for parameters τ and k were determined from the same Φ, ω^α plots using the well-known equation for the standard deviations for the slope of a linear regression:

$$\sigma = \sqrt{\frac{\frac{1}{n-2} \sum_{i=1}^n \hat{\varepsilon}_i^2}{\sum_{i=1}^n (x_i - \bar{x})^2}} \quad (6)$$

where $\hat{\varepsilon}_i$ are the residuals of the linear model, n is the number of points, \bar{x} is the average value of the argument. The approximate 3 sigma rule was then used to determine the confidence intervals.

It should be noted that equations (3) – (5) are valid only if the experimental IMPS plots correspond to relaxation at a single type of surface states. If the experimental frequency response of the photocurrent is distorted by the presence of additional relaxations such as carrier transport /recombination in the bulk, or relaxation at more than one type of surface states, care should be taken to select the frequency range where the effects of these additional relaxations can be disregarded.

5.3 Results and Discussion

In this work, we have been interested in the following goals:

- (1) To analyze the *ac* photocurrent/photovoltage response of bulk-heterojunction P3HT:PCBM solar cells to intensity modulated illumination;
- (2) To characterize using IMPS measurements at various *dc* light intensity levels the main mechanisms of recombination losses in the cells and separate the contributions of the bulk and interfacial processes;
- (3) To gain insight into the changes in the carrier generation, separation, recombination and extraction upon ageing.

The shape of IMPS response and the correlation between IMPS plots and cell efficiency

For this analysis we selected two cells that were prepared in identical conditions on the same photovoltaic slide but nevertheless featured a somewhat different photovoltaic performance. Figure 5-1 presents the photocurrent-voltage curves for the two cells selected for this manuscript. Specifically (Fig. 5-1), one of the cells that will be referred to as cell A showed V_{oc} of 0.51 V, I_{sc} of 5.00 mA cm⁻² and fill factor FF=0.32, with the resulting power conversion efficiency of 0.82% (AM 1.5 simulated solar radiation immediately following cell fabrication). The other cell (cell B) showed a quite better efficiency of 1.4 %, with V_{oc} of 0.55 V, I_{sc} of 5.91 mA cm⁻² and fill factor FF=0.43. The goal was to understand what the reasons for such a difference in performance are and specifically, whether it related to variability in the properties of the photovoltaic layer, or the contacts, or to some other factors.

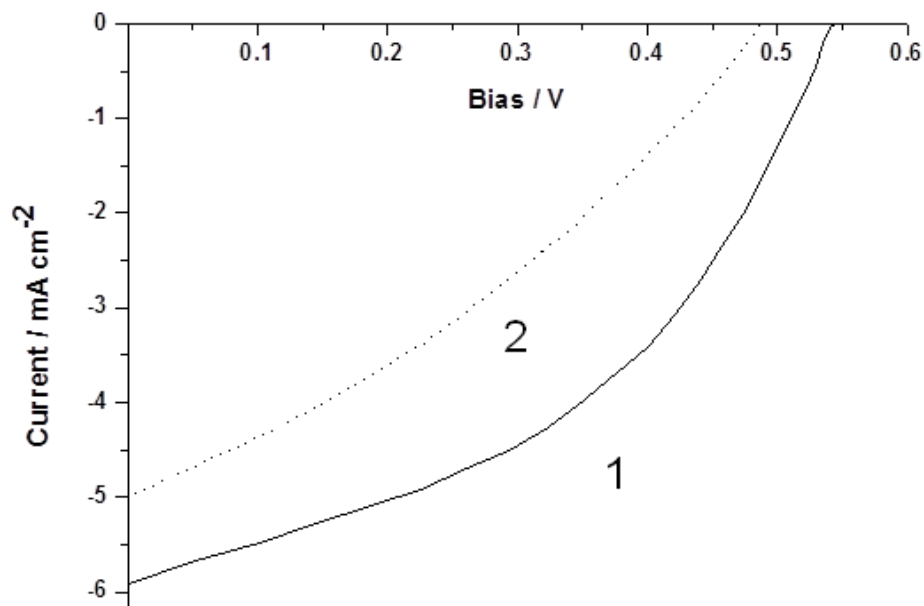
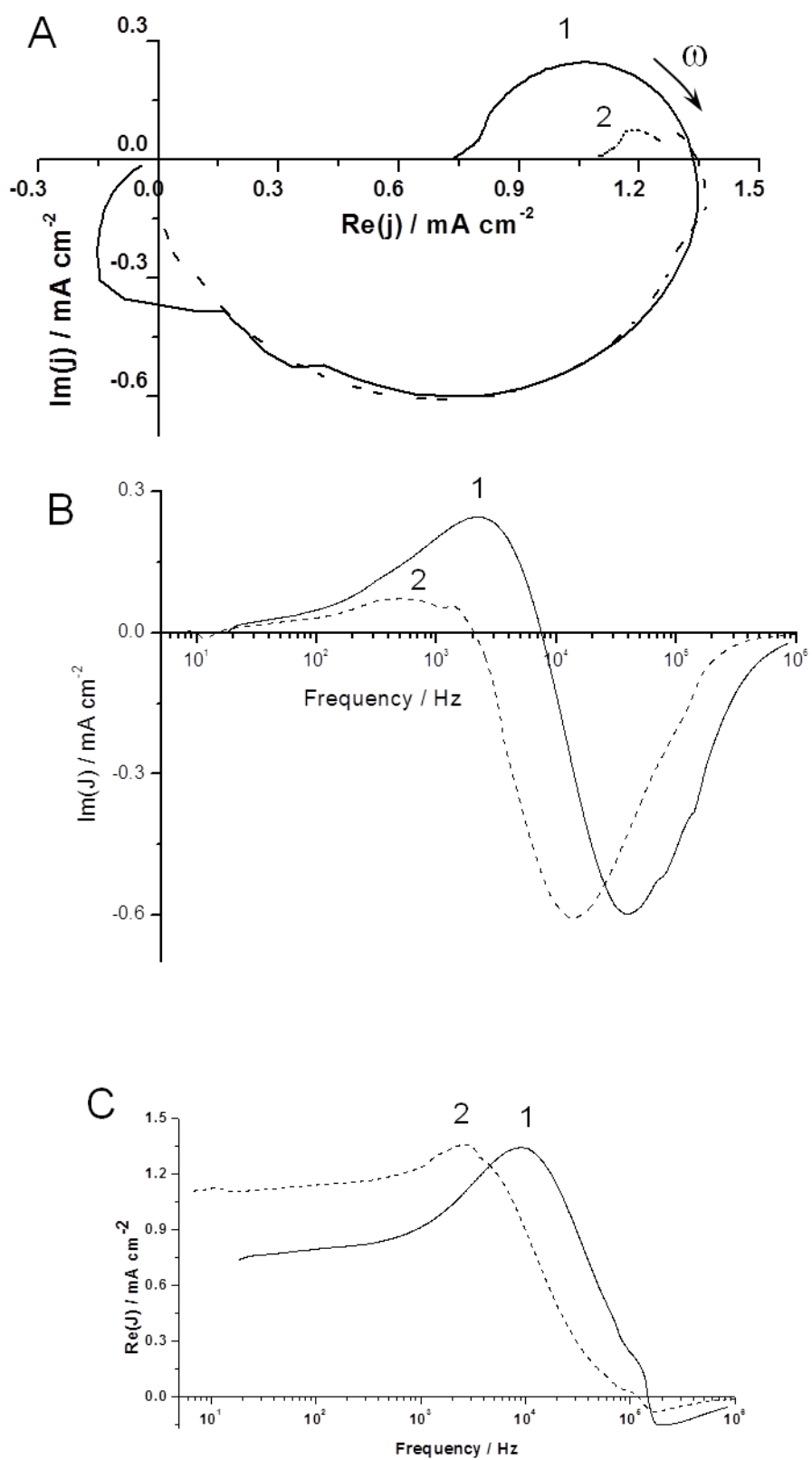


Figure 5-1. Experimental I-V curves for two P3HT:PCBM cells after fabrication (plot 1, cell B; plot 2, cell A) prepared on the same photovoltaic slide.

Figure 5-2 shows the IMPS complex plane plots (A) and the corresponding Bode plots (B-C) obtained in identical conditions for cells A and B after their fabrication. The IMPS complex plane plots show similar shapes for the two cells, with the high-frequency regions located below the real axis in quadrants III and IV and the low-frequency arcs located above the real axis in quadrant I. The corresponding Bode plots of the imaginary component of the photocurrent (Fig. 5-2B) shows characteristic maxima and minima, which correspond to the maxima and minima of the two portions of the IMPS complex plane plot located in the I and IV quadrant, respectively. From Fig. 5-2B one can estimate the characteristic relaxation times for the processes that correspond to the two portions of the plot. The high-frequency portions of the IMPS plots are similar to those observed with nanocrystalline systems,³⁸⁻⁴¹ and can be related to the processes of carrier transport in the bulk of the photovoltaic layer. While there exists a fairly advanced understanding of these processes in systems such as dye-sensitized solar cells, including the necessary mathematical analysis^{35,38} the situation with organic photovoltaic systems is significantly

different. Specifically, one needs to take into account the transport of excitons, holes and electrons rather than electrons only; also, the assumption that there is no electric field in the semiconductor bulk that is customarily made with nanocrystalline systems may not hold here as well. At present, as far as we know, there is no mathematical analysis available in the literature that would allow adequate interpretation of the high-frequency portions of the IMPS responses under such circumstances, and it is likely that development of such analysis will take some time. The characteristic times of the high-frequency IMPS relaxation will therefore be interpreted broadly as a kind of carrier life time that should generally depend on the efficiency of carrier transport and extraction; however, at present, no further analysis of these phenomena is possible without an adequate mathematical analysis. The only fact we can note here is that this lifetime is shorter in less efficient cell A.



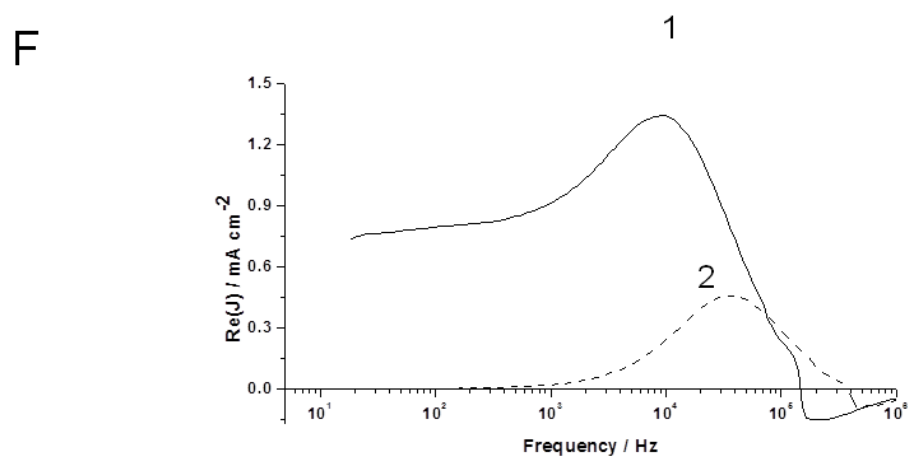
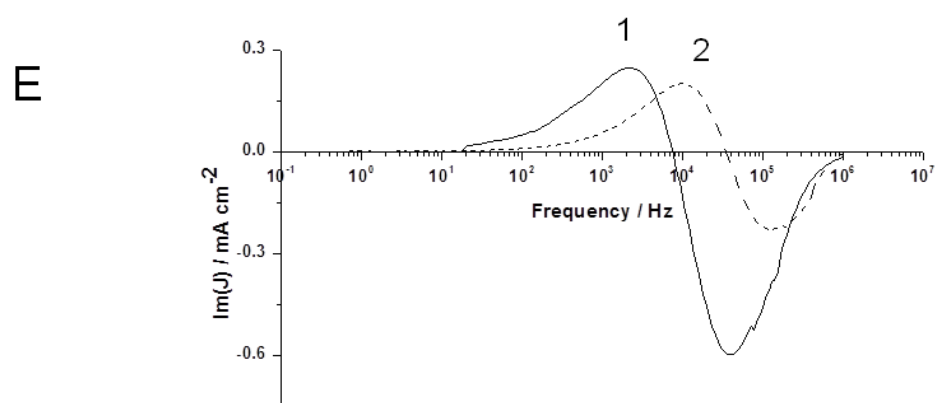
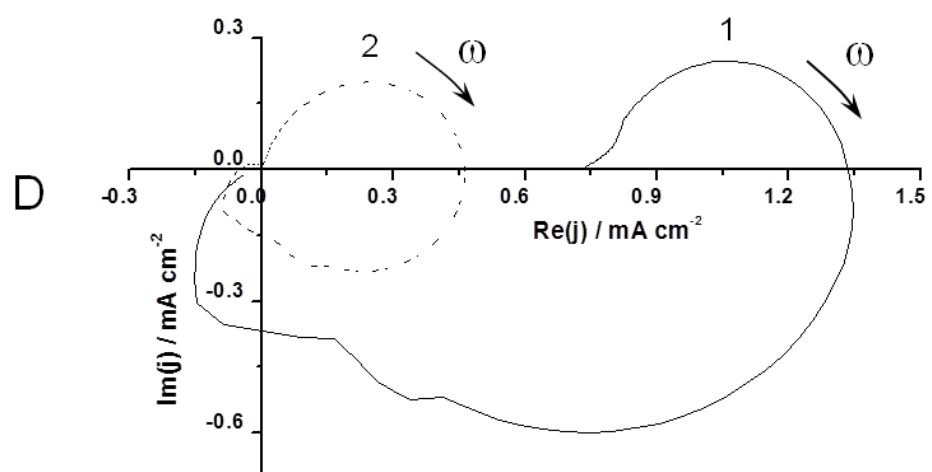


Figure 5-2. (A) Experimental IMPS spectra obtained at short-circuit conditions for two P3HT:PCBM photovoltaic cells (plot 1, cell A; plot 2, cell B) prepared on the same photovoltaic slide. (D) Comparison of experimental IMPS spectra for cell A (1) after fabrication and (2) after ageing for 2 months. The arrows indicate the direction of increasing frequency. IMPS spectra are presented as Bode plots of (B,E) the imaginary and (C,F) the real components of the photocurrent response vs. the modulation frequency. The *dc* light intensity for all spectra was $8.2 \times 10^{15} \text{ s}^{-1} \text{ cm}^{-2}$.

In the further discussion we concentrate on the low-frequency portions of the experimental IMPS response, which are located in the first quadrant of the complex plane. Importantly, as opposed to the IMPS response in nanocrystalline systems such as dye-sensitized solar cells where the IMPS response is largely determined by carrier transport and thus the photocurrent lags the light intensity, the photocurrent in this region leads the light intensity (both the real and imaginary components are positive thus producing a positive phase shift), and the photocurrent magnitude increases with the modulation frequency. Such behavior is hardly observed in nanocrystalline solar cells and is a signature of the occurrence of interfacial recombination.^{28-32,34,36} Furthermore, the fact that the photocurrent leads the light intensity suggests that the observed recombination is non-geminate. The photogenerated carriers first separate and charge the interface, which is seen as the growth of the photocurrent magnitude with a decrease in the modulation frequency in the high-frequency range; the interfacial recombination occurs only later (at lower frequencies) and involves the carriers that have already been separated and trapped at the surface/interfacial states. If the carriers were to remain bound or spatially correlated as in the case of geminate recombination, the separation of charges and the corresponding interfacial charging current would not be observed and the photocurrent would have lagged the light intensity and had a negative phase shift in the whole frequency range. Therefore, the fact that all experimental IMPS plots featured the low-frequency portions in quadrant I provides a direct evidence of the occurrence of non-geminate interfacial recombination in bulk heterojunction solar cells.

Furthermore, the IMPS results suggest that the interfacial recombination is a factor that to a large extent determines the cell efficiency. This can be seen by comparing the value of

the *ac* photocurrent at the point at which the IMPS plot crosses the real axis from quadrant IV into quadrant I (often called the generation current) with the low-frequency limit of the photocurrent. The generation current indicates the maximum photocurrent that could be produced by a cell in the absence of interfacial recombination, whereas the low-frequency limit corresponds to the steady-state photocurrent that determines the actual cell conversion efficiency. From Fig. 5-2 one can see that the photocurrent losses due to interfacial recombination can reach almost 50% in the case of the less efficient cell A. Furthermore, while the high-frequency portions of plots 1 and 2 of Fig. 5-2A are nearly identical indicating that the bulk processes in these cells are very similar, it is the low-frequency portions due to interfacial recombination that determine the difference in the power conversion efficiencies between cells A and B. Furthermore, the frequency at the low-frequency maximum of the imaginary component of the photocurrent (Fig. 5-2B) can be related to the rate of decay of photogenerated minority carriers at the surface states and in the first approximation can be considered equal to the pseudo-first-order rate constant k of the interfacial recombination^{28-32,34,36} assuming that there is no carrier extraction through the interfacial states. As follows from the figure, the recombination rate constant is also higher for less efficient cell A as compared to cell B. These facts suggest that the difference between these cells are not due to the bulk properties of the photovoltaic layer but rather is related to the processes at the contacts or at the interface between the donor and acceptor components of the photovoltaic blend.

A similar conclusion of the importance of the interfacial recombination for the organic solar cell efficiency was reached recently by R.A. Street et al.^{22,47} but on the basis of steady-state measurements. In this work, the use of IMPS allowed us to separate the bulk and interfacial photoprocesses that occur in different frequency domains and obtain direct evidence that non-geminate interfacial recombination is an important loss mechanism.

IMPS evidence of increased interfacial recombination rate in aged cells

Moreover, the interfacial recombination is more pronounced in aged cells. Figures 5-2D-F show that while both the generation and steady-state photocurrents decrease upon cell ageing, the low-frequency portion in the IMPS plots is much more pronounced for the

aged cell with the low-frequency intercept being close to zero. This correlates well with the regular photocurrent-voltage curves obtained for the aged cell under steady-state conditions using a solar simulator, which did not show any photocurrents whatsoever (the curves not presented). The frequency at the maxima of the low-frequency portions also increases with ageing (Fig. 5-2E) by about an order of magnitude indicating a considerable increase in the interfacial recombination rate. This means that interfacial recombination becomes a dominant loss mechanism in aged cells. At the same time, the high frequency portions of the photocurrent are greatly affected too: the photocurrent magnitude is smaller at virtually all frequencies and the frequency at the minimum of the high-frequency portion increases too indicating a shorter carrier lifetime in the bulk and presumably higher bulk recombination rate. All these facts suggest that ageing affects all aspects of the operation of a solar cell; however, it should be pointed out that even aged cells would still be able to produce quite measurable photocurrent if not for the occurrence of interfacial recombination, as evidenced by the non-zero photocurrent values in the intermediate transitional region between the high and low frequency portions of the *ac* response. In other words, if the surface recombination could be suppressed, the aged cell efficiency would decrease significantly (perhaps, ca. 3 times as follows from Fig. 5-2F) but still would not be zero. Again, this important conclusion could not be reached without IMPS allowing us to separate the bulk and interfacial processes through photocurrent analysis in the frequency domain.

IMPS and IMVS responses at varying dc light intensities

To gain a further insight into the mechanism of interfacial recombination, IMPS measurements at varying *dc* light intensities were performed (Fig. 5-3). For a linear system, the *ac* IMPS response should not vary with the *dc* intensity; however, as follows from Fig. 5-3, this is not the case. Specifically, the magnitude of the *ac* photocurrent, including its low-frequency limit that corresponds to the steady-state photocurrent, decreased with the light intensity, while the frequency at the extrema of the imaginary component of the photocurrent increased for both the high-frequency and low-frequency portions of the IMPS response (Fig. 5-3B). In particular, there is a pronounced increase in

the frequency at the maxima of the low frequency portions of the IMPS complex-plane plots, which

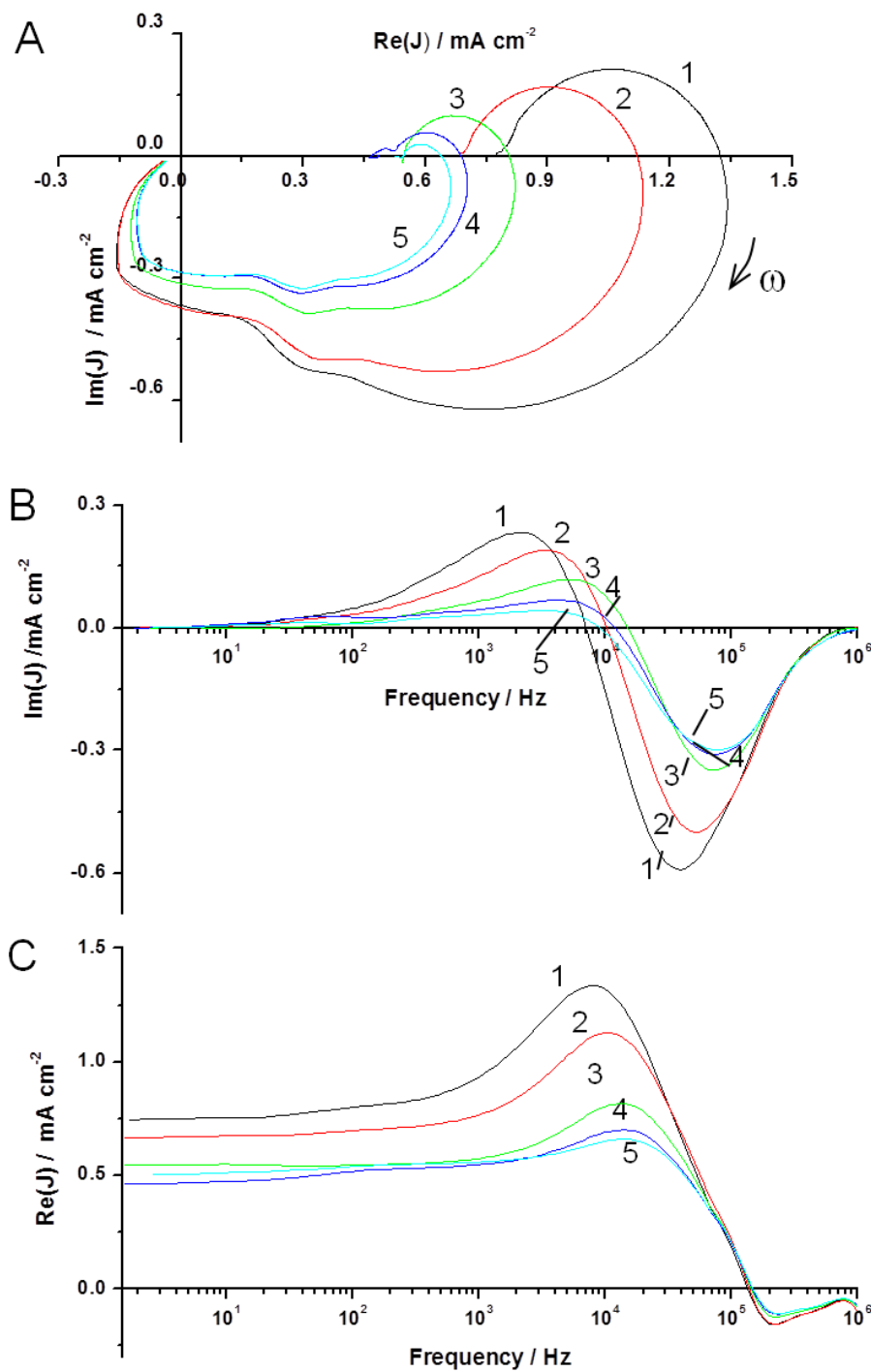
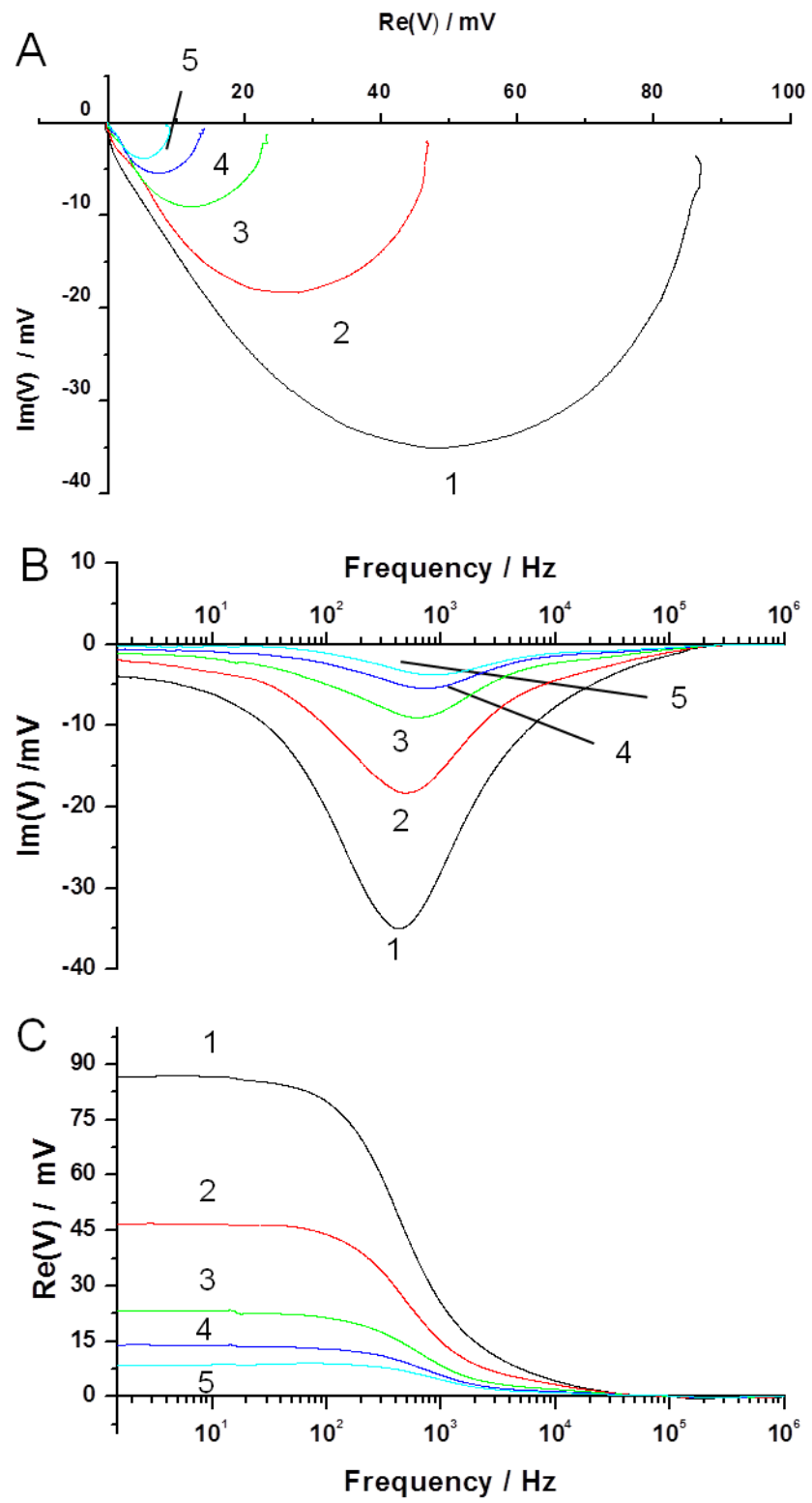


Figure 5-3. The intensity dependence of IMPS spectra measured at short-circuit conditions for photovoltaic cell A. The dc light intensities were (1) $8.2 \times 10^{15} \text{ s}^{-1} \text{ cm}^{-2}$; (2) $2.2 \times 10^{16} \text{ s}^{-1} \text{ cm}^{-2}$; (3) $3.5 \times 10^{16} \text{ s}^{-1} \text{ cm}^{-2}$; (4) $5.0 \times 10^{16} \text{ s}^{-1} \text{ cm}^{-2}$ and (5) $6.4 \times 10^{16} \text{ s}^{-1} \text{ cm}^{-2}$. The IMPS spectra are presented as (A) a Nyquist complex plane plot as well as Bode plots of (B) the imaginary and (C) the real components of the photocurrent response vs. the modulation frequency. The arrow indicates the direction of increasing frequency.

indicates that increasing the *dc* light intensity increases the recombination rate constant k . It should be remembered that rate constant k is a pseudo-first-order rate constant that implicitly includes the population of the interfacial states with the majority carriers (holes in the case of P3HT). In linear systems it is independent of the light intensity since there is an excess of majority carriers at the interfacial states; however, if the surface state density or population can be modulated by light, the pseudo-first-order recombination rate constant will also have an intensity-dependent component.

Similar behavior is observed for the intensity modulated photovoltage (IMVS) response. Figures 5-4 A-C show the complex plane as well as Bode plots of the *ac* photovoltage measured for photovoltaic cell A. It should be remembered that while IMPS spectra are measured at short-circuit conditions, IMVS spectra are measured at open circuit. Therefore, there is no carrier extraction and IMVS spectra just show accumulation of charge at the interface. Then the characteristic frequency at the minimum of the imaginary component of the photovoltage can be in the first approximation taken as the lifetime of carriers at the surface states,⁴⁰ which is the inverse of the pseudo-first-order recombination rate constant at open circuit. Figure 5-4 again suggests, now on the basis of IMVS data, that the recombination rate constant k increases with the light intensity. Furthermore, as follows from Fig. 5-4D, the frequencies at maxima and thus the lifetimes of carriers at the interfacial states derived from IMPS and IMVS data are quite close. This may suggest, among other facts, that there is no extraction of photogenerated carriers through the interfacial states (the lifetime is determined by the recombination rate only).



D

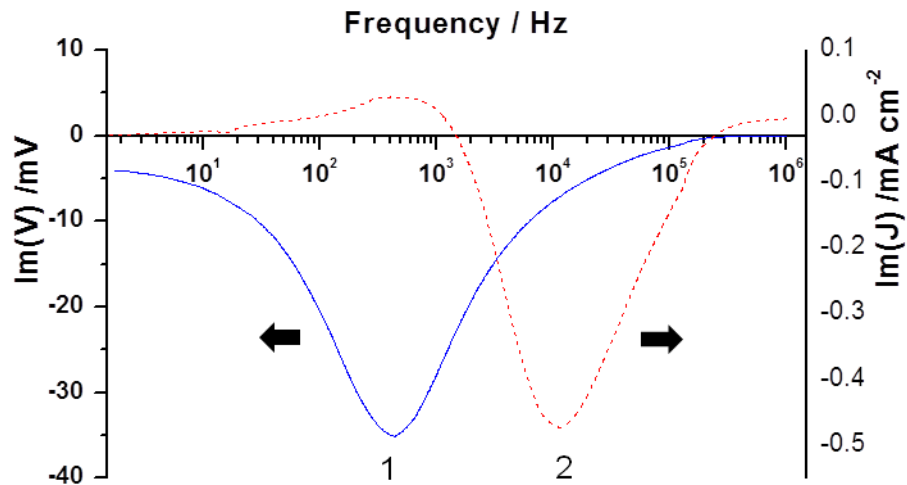


Figure 5-4. The intensity dependence of IMVS spectra measured at open-circuit conditions for photovoltaic cell A. The *dc* light intensities were (1) $8.2 \times 10^{15} \text{ s}^{-1} \text{ cm}^{-2}$; (2) $2.2 \times 10^{16} \text{ s}^{-1} \text{ cm}^{-2}$; (3) $3.5 \times 10^{16} \text{ s}^{-1} \text{ cm}^{-2}$; (4) $5.0 \times 10^{16} \text{ s}^{-1} \text{ cm}^{-2}$ and (5) $6.4 \times 10^{16} \text{ s}^{-1} \text{ cm}^{-2}$. The IMVS spectra are presented as (A) a Nyquist complex plane plot as well as Bode plots of (B) the imaginary and (C) the real components of the photovoltage response vs. the modulation frequency. (D) Comparison of the frequency dependencies of the imaginary components of (1) IMVS photovoltage and (2) IMPS photocurrent response at a *dc* light intensity of $8.2 \times 10^{15} \text{ s}^{-1} \text{ cm}^{-2}$.

If there were noticeable carrier extraction through the surface states, then the characteristic relaxation times derived from IMPS and IMVS spectra would have been quite different (IMPS is measured when carriers are extracted giving rise to photocurrent and IMVS is measured at open circuit when no extraction is possible). At the same time, this conclusion needs further justification, especially given the fact that the recombination constant is bias-dependent (see below) and IMPS and IMVS are measured at different bias values. However, the IMVS data unambiguously suggest that it is the recombination rate and not the rate of the carrier extraction that increases with the light intensity since no carrier extraction is possible in these conditions.

Bias dependence of IMPS response

Figure 5-5 shows the evolution of IMPS spectra under applied bias. It should be noted that these data had to be obtained with a different setup that included a potentiostat, which reduced the bandwidth and affected the measurement frequency range. Nevertheless, one can clearly see that the recombination rate constant increased when the bias was changed from short-circuit ($E=0.0\text{V}$) to near open-circuit conditions ($E=+0.5\text{V}$). This indicated that the population of the interfacial states or their density is not only intensity but also bias-dependent. The photocurrent magnitude also decreased, as could be expected in view of the bias dependence of the photocurrent (Fig. 5-1). While a decrease in the photocurrent alone could be attributed to a lower probability of exciton dissociation with a decrease in the electric field, this mechanism cannot explain the corresponding changes in the interfacial recombination rate revealed by IMPS. This again highlights the importance of interfacial recombination as a major loss channel. Moreover, the increase in the recombination rate near the open circuit should have a detrimental effect on the cell fill factor and further reduce the efficiency.

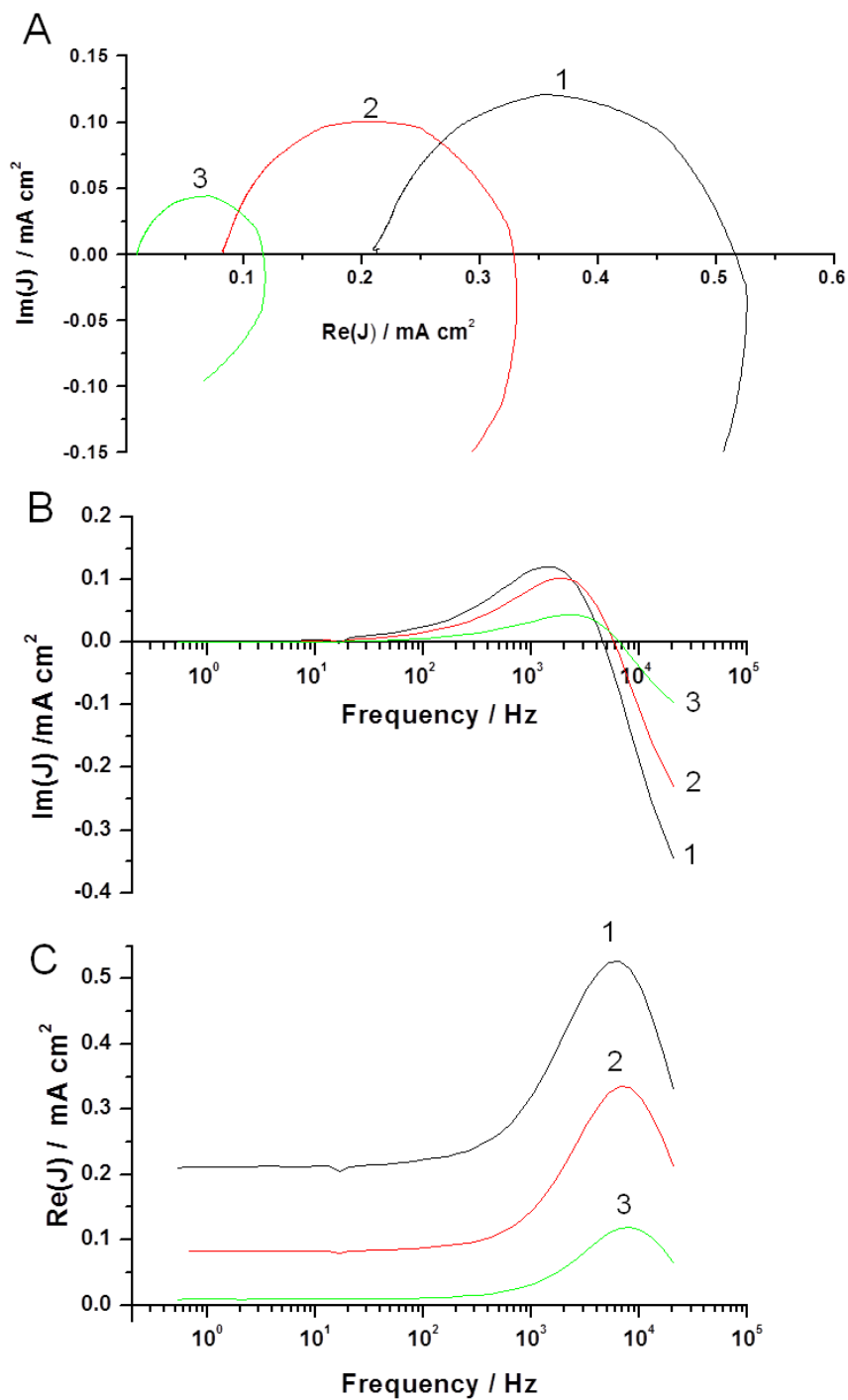


Figure 5-5. (A) Experimental IMPS spectra obtained at cell biases of 0.0 V (plot 1), +0.25 V (plot 2), +0.5 V (plot 3) as well as Bode plots of (B) the imaginary and (C) the real components of the photocurrent response obtained at these bias values vs. the modulation frequency.

Mott-Schottky measurements in the dark and under illumination

In order to find an explanation for the observed light intensity dependence of the recombination rate constant k , dependencies of the cell capacitance C on the applied bias E were measured in the dark and under illumination. The corresponding C^{-2} , E plots for cell A in the dark and for a series of *dc* light intensities are presented in Fig. 5-6. If a C^{-2} , E (Mott-Schottky) plot is linear, this indicates that there is a space charge region in the semiconductor near the contact, which is set up by ionized donor or acceptor species and the width of which increases as the square root of the applied bias. The Mott-Schottky behavior may occur within a limited bias range only due to potential drop redistribution or other factors such as a finite semiconductor layer thickness. The slope of the linear portions of Mott-Schottky plots is inversely proportional to the dopant density in the films.⁴⁸ For a p-type conjugated polymer semiconductor, the dopant density does not represent dopant ions but instead is due to positively charged polarons/bipolarons in the film.^{49,50} Such polarons/bipolarons may form due to trapping of photoexcited holes at certain portions of the polymer backbone or, for instance, oxygen-induced doping.²⁷

As follows from Fig. 5-6, the experimental Mott-Schottky plots all had linear portions at more negative bias values, in agreement with the literature data^{26,49,50} and the anticipated p-type semiconductor behavior. Furthermore, the slopes of the Mott-Schottky plots decreased with the light intensity. This indicates that illumination results in an increase in the density of trapped holes near the interface. Similar changes in the slope of Mott-Schottky plots due to illumination were recently observed in the literature.²⁶ Indeed, charge trapping is known to occur in such relatively disordered media as organic semiconducting polymers.^{51,52} Furthermore, illumination changes the shape of the C^{-2} , E dependencies. As seen in the inset in Fig. 5-6, under illumination the decrease in the C^{-2} values with the applied bias is interrupted from ca. 0.2 V to ca. 0.5 V, and the Mott-Schottky plot shows a plateau. The occurrence of such a plateau is usually attributed to the Fermi level pinning by the interfacial states. When a Fermi level passes through a set of interfacial states with a relatively high density, the applied bias will be localized at the capacitance of these states, and there will be little or no change in the potential drop in the space charge region and correspondingly little change in its capacitance. The Fermi

level will stay pinned to the interfacial states until all such states are charged. Therefore, the occurrence of the Fermi level pinning under illumination indicates formation of a large density of interfacial states under illumination. Such midgap states formation was observed by Schafferhans et al. in P3HT:PCBM blends under illumination using thermally stimulated current technique.²⁷ They also found that such states had their activation energy within a range from 0.2 to 0.4 eV, which agrees quite well with our data (inset in Fig. 5-6).

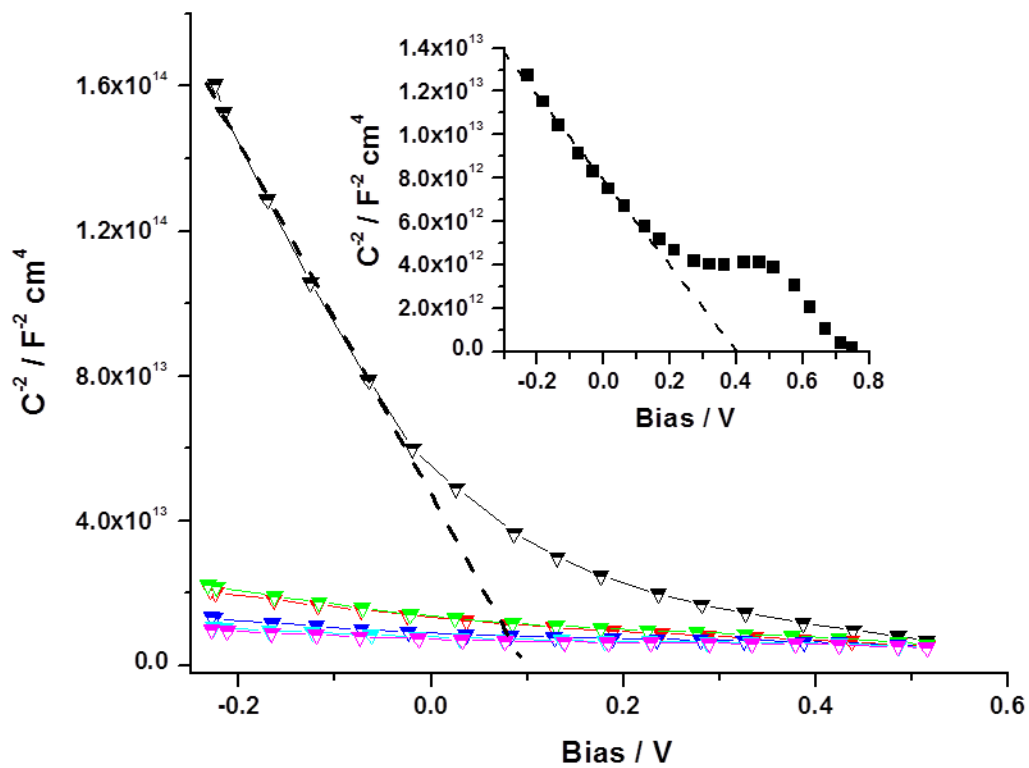


Figure 5-6. Mott-Schottky plots for photovoltaic cell A measured in the dark (plot 1) and as a function of the *dc* light intensity (plots 2-6). The light intensity values were (2) $8.2 \times 10^{15} \text{ s}^{-1} \text{ cm}^{-2}$; (3) $2.2 \times 10^{16} \text{ s}^{-1} \text{ cm}^{-2}$; (4) $3.5 \times 10^{16} \text{ s}^{-1} \text{ cm}^{-2}$; (5) $5.0 \times 10^{16} \text{ s}^{-1} \text{ cm}^{-2}$ and (6) $6.4 \times 10^{16} \text{ s}^{-1} \text{ cm}^{-2}$. The inset shows an enlarged Mott-Schottky plot at a *dc* light intensity of $5.0 \times 10^{16} \text{ s}^{-1} \text{ cm}^{-2}$.

Correlation between the interfacial recombination rate and the charged trap density

Therefore, it was found that illumination facilitates trapping of photogenerated holes at and near the P3HT:PCBM interface. These holes may be able to participate in recombination with photogenerated electrons, which could be the reason of the non-linear photocurrent and photovoltage response and the experimentally observed increase in the apparent pseudo-first-order recombination constant with the light intensity. In order to support this line of reasoning, we looked into the dependencies of the recombination constant k and the charged trap density N_D on the light intensity. Such data are given in Fig. 5-7.

The values of k in Fig. 5-7 were determined by fitting the frequency dependencies of the real and imaginary components of the photocurrent as described in Experimental section. The corresponding dependencies of k vs. dc light intensity for the two cells under study are shown in Fig. 5-7A. One can see that both cell types showed a linear increase in the recombination rate with the dc intensity. At the same time, the values of k extrapolated to zero dc intensity were not zero. This means that the interfacial recombination rate has two components, one of which is dependent and the other independent of the light intensity. The k values were higher for the aged cell, as could be expected.

Similar dependencies were found for the trapped holes density N_D . Figure 5-7B presents the dependencies of the trap density on the dc light intensity for cell A after fabrication (plot 2) and after ageing (plot 1). Again, N_D values were found to scale linearly with the light intensity. Furthermore, the dependencies again showed non-zero intercepts at zero dc light intensity, which was especially pronounced in the aged cell. This means that the trap density, like the recombination constant, has two components, one dependent and another independent of the light intensity. Furthermore, one can see that the trap density is much higher in the aged cell even in the dark, which may be another factor responsible for the increase in the interfacial recombination rate upon ageing.

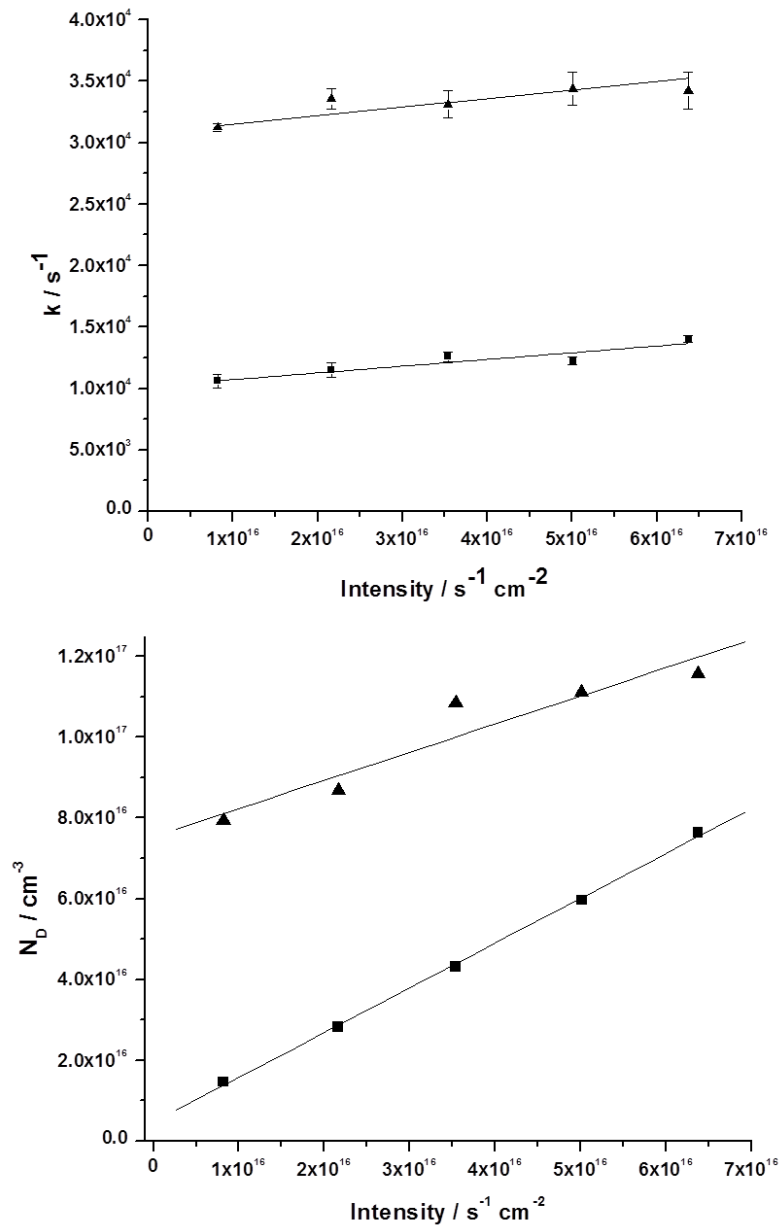


Figure 5-7. Dependencies on the *dc* light intensity of (A) interfacial recombination rate constant derived from the IMPS plots and (B) trap density obtained from the Mott-Schottky plots for photovoltaic cell A. For each graph, plot 1 corresponds to the photovoltaic cell after ageing for 2 months and plot 2 corresponds to a photovoltaic cell after fabrication.

Localization of the interfacial states

An organic bulk heterojunction solar cell is a complex device that contains many interfaces. Therefore, it is important to determine the localization of the interfacial states that are responsible for the observed recombination losses in order to be able to further improve the cell efficiency. In our opinion, the most likely location of the interfacial states responsible for recombination evidenced by the IMPS and IMVS data is the interface between the PCBM and P3HT phases. The reason is that it is the interface at which the separation of the primary photoexcitons occurs and at which the electrons are transferred into the PCBM phase. Furthermore, efficient cells are vertically organized in such a way that the majority of the PCBM phase is located closer to the top metal contact. For an electron to recombine at the ITO/PEDOT or PEDOT/P3HT:PCBM interfaces, it would have to transfer back into the P3HT phase and travel across the photovoltaic layer, which seems unlikely. It is possible that some electrons that are photogenerated in the P3HT phase without the use of the donor-acceptor mechanism may recombine at these interfaces, as was demonstrated for single layer polymer solar cell without the acceptor component,³⁶ but the photocurrents in this case are very small and cannot account for the relaxations seen in Figs. 2-4.

The recombination cannot happen at the Al/PCBM interface as well because PCBM forms an Ohmic contact with Al;^{53,54} furthermore, there should be no holes in the PCBM phase. The only other possible location would be the portions of the Al contact where the metal is in direct contact with P3HT. Such locations are essentially defects but they are found in bulk heterojunction cells. Then the recombination could occur at Al/P3HT interface with PCBM clusters located in the close proximity or with electrons provided through the metal contact. Further studies are required to investigate this possibility, for instance, by introducing barrier interfacial layers such as LiF.

The conclusion about the most likely localization of the interfacial states is also supported by the results with the aged cells. The increase in the interfacial recombination rate can be attributed to an increase in the density of states at the interface, as well as increased charge trapping near the interface upon ageing. Both these processes are likely

to be related to chemical and structural changes induced by illumination in the presence of oxygen and moisture.²⁴⁻²⁷ The specific mechanisms involved in these processes are yet to be fully understood. However, recent measurements of the distribution of the oxygen and water intake in bulk heterojunction cells during their degradation²⁴ show a considerable accumulation of oxygen at the Al/P3HT:PCBM interface (the resolution of the mapping in this study was not high enough to distinguish between P3HT and PCBM components of the photovoltaic layer).

5.4 Conclusions

1. The IMPS and IMVS measurements in the frequency domain allowed us to separate the contribution of the bulk and interfacial processes and provide direct evidence of the occurrence of non-geminate recombination through interfacial states. This recombination appears to be a major loss mechanism, especially, in aged cells. While the geminate recombination of primary excitons remains an important process, especially, in photovoltaic films with poor morphology and phase separation, the latest data suggest that almost all primary excitons in the best photovoltaic cells give rise to free carriers, and then the recombination losses through interfacial states analyzed here become especially important as an untapped resource for further efficiency improvements.
2. The interfacial recombination shows a mixture of the first order and second-order kinetics. The reason for the latter process exhibited through non-linear dependence of the photocurrent on the light intensity is the trapping of photoexcited holes in P3HT phase at and near the interface with PCBM and/or Al.
3. The interfacial recombination centers are located either at the P3HT:PCBM internal heterojunction interface or at the Al contact with the photovoltaic layer with both P3HT and PCBM domains being in close proximity to the contact. Further studies are needed to clarify this point, for instance, using modification of the contacts with various sub-layers such as LiF. However, the most likely location of the interfacial states responsible for the recombination is at the interface between the PCBM and P3HT phases. In this case, the increase in the interfacial recombination rate may be due to nanoscale structural changes

and specifically changes in the phase segregation in the P3HT:PCBM layer upon ageing. Further studies of these processes are required.

4. The rate of the interfacial recombination greatly increases with ageing to the point that it effectively controls the efficiency of aged cells. This fact may be related to formation of recombination centers facilitated by oxygen/water intake and illumination.

5. Our findings enable us to make the following recommendations concerning the ways to further improve the efficiency of bulk heterojunction organic solar cells:

(i) Reduce trapping of charges in the photovoltaic layer. The means may be better morphological control, improving mobilities, etc.

(ii) Reduce the density of interfacial states at the interface. Possible means may include strict control of exposure to oxygen and water, as well as surface modification.

(iii) Improve the carrier extraction efficiency at contacts. If the rate of charge extraction is high enough, it should be able to compete efficiently with carrier capture by the interfacial states and interfacial recombination. Our results indicate that the typical relaxation times at the interfacial states are 0.1-1 ms, which means that the cross-section of the electron capture by the interfacial states cannot be very high. This recommendation is not new but it gains new significance in view of our results showing the importance and the extent of recombination losses at the interfaces.

6. IMPS and IMVS techniques show significant potential for studies of the mechanism of photocurrent generation and recombination losses in organic solar cells in the intermediate time/frequency range. With the recent research efforts resulting in drastic improvements of the charge separation processes on the ultrafast time scale, the losses due to slow transport, poor carrier extraction and interfacial recombination should become the primary targets to further improve the efficiency of bulk heterojunction organic solar cells.

5.5 References

- (1) Dennler, G.; Scharber, M. C.; Brabec, C. J. *Advanced Materials* 2009, 21, 1323.
- (2) Deibel, C.; Dyakonov, V. *Reports on Progress in Physics* 2010, 73.
- (3) Nielsen, T. D.; Cruickshank, C.; Foged, S.; Thorsen, J.; Krebs, F. C. *Solar Energy Materials and Solar Cells* 2010, 94, 1553.
- (4) Pivrikas, A.; Juska, G.; Mozer, A. J.; Scharber, M.; Arlauskas, K.; Sariciftci, N. S.; Stubb, H.; Osterbacka, R. *Physical Review Letters* 2005, 94.
- (5) Koster, L. J. A.; Smits, E. C. P.; Mihailetschi, V. D.; Blom, P. W. M. *Physical Review B* 2005, 72.
- (6) Koster, L. J. A.; Mihailetschi, V. D.; Blom, P. W. M. *Applied Physics Letters* 2006, 88.
- (7) Deibel, C.; Wagenpfahl, A.; Dyakonov, V. *Physical Review B* 2009, 80.
- (8) Bakulin, A. A.; Hummelen, J. C.; Pshenichnikov, M. S.; van Loosdrecht, P. H. M. *Advanced Functional Materials* 2010, 20, 1653.
- (9) Collins, B. A.; Gann, E.; Guignard, L.; He, X.; McNeill, C. R.; Ade, H. *Journal of Physical Chemistry Letters* 2010, 1, 3160.
- (10) Deibel, C.; Wagenpfahl, A. *Physical Review B* 2010, 82.
- (11) Deibel, C.; Strobel, T.; Dyakonov, V. *Advanced Materials* 2010, 22, 4097.
- (12) Guo, J. M.; Ohkita, H.; Benten, H.; Ito, S. *Journal of the American Chemical Society* 2010, 132, 6154.
- (13) Hamilton, R.; Shuttle, C. G.; O'Regan, B.; Hammant, T. C.; Nelson, J.; Durrant, J. R. *Journal of Physical Chemistry Letters* 2010, 1, 1432.
- (14) Howard, I. A.; Mauer, R.; Meister, M.; Laquai, F. *Journal of the American Chemical Society* 2010, 132, 14866.
- (15) Howard, I. A.; Laquai, F. *Macromolecular Chemistry and Physics* 2010, 211, 2063.
- (16) Shoaee, S.; Eng, M. P.; Espildora, E.; Delgado, J. L.; Campo, B.; Martin, N.; Vanderzande, D.; Durrant, J. R. *Energy & Environmental Science* 2010, 3, 971.
- (17) Shuttle, C. G.; Hamilton, R.; O'Regan, B. C.; Nelson, J.; Durrant, J. R. *Proceedings of the National Academy of Sciences of the United States of America* 2010, 107, 16448.
- (18) Street, R. A. *Physical Review B* 2010, 82.
- (19) Hilczler, M.; Tachiya, M. *Journal of Physical Chemistry C* 2010, 114, 6808.

- (20) Clarke, T. M.; Ballantyne, A. M.; Shoaee, S.; Soon, Y. W.; Duffy, W.; Heeney, M.; McCulloch, I.; Nelson, J.; Durrant, J. R. *Advanced Materials* 2010, 22, 5287.
- (21) Shuttle, C. G.; O'Regan, B.; Ballantyne, A. M.; Nelson, J.; Bradley, D. D. C.; Durrant, J. R. *Physical Review B* 2008, 78.
- (22) Street, R. A.; Schoendorf, M. *Physical Review B* 2010, 81.
- (23) Jorgensen, M.; Norrman, K.; Krebs, F. C. *Solar Energy Materials and Solar Cells* 2008, 92, 686.
- (24) Norrman, K.; Gevorgyan, S. A.; Krebs, F. C. *Acs Applied Materials & Interfaces* 2009, 1, 102.
- (25) Norrman, K.; Madsen, M. V.; Gevorgyan, S. A.; Krebs, F. C. *Journal of the American Chemical Society* 2010, 132, 16883.
- (26) Seemann, A.; Sauermann, T.; Lungenschmied, C.; Armbruster, O.; Bauer, S.; Egelhaaf, H. J.; Hauch, J. *Solar Energy* 2010
- (27) Schafferhans, J.; Baumann, A.; Wagenpfahl, A.; Deibel, C.; Dyakonov, V. *Organic Electronics* 2010, 11, 1693.
- (28) Li, J.; Peter, L. M. *Journal of Electroanalytical Chemistry* 1985, 193, 27.
- (29) Li, J.; Peter, L. M. *Journal of Electroanalytical Chemistry* 1986, 199, 1.
- (30) Peter, L. M. *Chemical Reviews* 1990, 90, 753.
- (31) Rotenberg, Z. A.; Semenikhin, O. A. *Journal of Electroanalytical Chemistry* 1991, 316, 165.
- (32) Semenikhin, O. A.; Rotenberg, Z. A. *Soviet Electrochemistry* 1992, 28, 992.
- (33) de Jongh, P. E.; Vanmaekelbergh, D. *Journal of Physical Chemistry B* 1997, 101, 2716.
- (34) Semenikhin, O. A.; Kazarinov, V. E.; Jiang, L.; Hashimoto, K.; Fujishima, A. *Langmuir* 1999, 15, 3731.
- (35) Vanmaekelbergh, D.; de Jongh, P. E. *Physical Review B* 2000, 61, 4699.
- (36) DiCarmine, P. M.; Semenikhin, O. A. *Electrochimica Acta* 2008, 53, 3744.
- (37) Manoj, A. G.; Alagiriswamy, A. A.; Narayan, K. S. *J. Appl. Phys.* 2003, 94, 4088.
- (38) Dloczik, L.; Ileperuma, O.; Lauermann, I.; Peter, L. M.; Ponomarev, E. A.; Redmond, G.; Shaw, N. J.; Uhlendorf, I. *Journal of Physical Chemistry B* 1997, 101, 10281.

- (39) Peter, L. M.; Ponomarev, E. A.; Franco, G.; Shaw, N. J. *Electrochimica Acta* 1999, 45, 549.
- (40) Kruger, J.; Plass, R.; Gratzel, M.; Cameron, P. J.; Peter, L. M. *Journal of Physical Chemistry B* 2003, 107, 7536.
- (41) Dunn, H. K.; Peter, L. M. *Journal of Physical Chemistry C* 2009, 113, 4726.
- (42) Schlichthorl, G.; Huang, S. Y.; Sprague, J.; Frank, A. J. *Journal of Physical Chemistry B* 1997, 101, 8141.
- (43) Zhu, K.; Neale, N. R.; Miedaner, A.; Frank, A. J. *Nano Letters* 2007, 7, 69.
- (44) Zhu, K.; Neale, N. R.; Halverson, A. F.; Kim, J. Y.; Frank, A. J. *Journal of Physical Chemistry C* 2010, 114, 13433.
- (45) Bag, M.; Narayan, K. S. *Physical Review B* 2010, 82.
- (46) Rotenberg, Z. A. *Soviet Electrochemistry* 1992, 28, 1307.
- (47) Street, R. A.; Cowan, S.; Heeger, A. J. *Physical Review B* 2010, 82.
- (48) Bard, A. J.; Memming, R.; Miller, B. *Pure Appl. Chem.* 1991, 63, 569.
- (49) Semenikhin, O. A.; Ovsyannikova, E. V.; Alpatova, N. M.; Rotenberg, Z. A. *Journal of Electroanalytical Chemistry* 1996, 408, 67.
- (50) Semenikhin, O. A.; Hossain, M. M. D.; Workentin, M. S. *Journal of Physical Chemistry B* 2006, 110, 20189.
- (51) Blom, P. W. M.; Vissenberg, M. C. J. M. *Materials Science & Engineering R-Reports* 2000, 27, 53.
- (52) Chiguvare, Z.; Dyakonov, V. *Physical Review B* 2004, 70.
- (53) Mihailetchi, V. D.; van Duren, J. K. J.; Blom, P. W. M.; Hummelen, J. C.; Janssen, R. A. J.; Kroon, J. M.; Rispens, M. T.; Verhees, W. J. H.; Wienk, M. M. *Advanced Functional Materials* 2003, 13, 43.
- (54) Mihailetchi, V. D.; Blom, P. W. M.; Hummelen, J. C.; Rispens, M. T. *J. Appl. Phys.* 2003, 94, 6849.

Chapter 6

6 Influence of Preparation Conditions of Bulk Heterojunction Solar Cells Studied using Intensity Modulated Photocurrent Spectroscopy

6.1 Introduction

Bulk heterojunction organic solar cells incorporating conjugated polymers and fullerene derivatives as a composite photoactive layer represent a promising platform for high-throughput, low cost alternative energy generation. Organic photovoltaic devices require the use of two materials in the photoactive layer due to the formation of excitons, instead of free charge carriers, upon light absorption in the conjugated polymer. Due to the short lifetimes of excitons, it is necessary to form an intimately mixed three dimensional bulk heterojunction of the two materials to maximize the interfacial area while ensuring the formation of uninterrupted pathways for charge carriers to be transported across the film. However, photoactive layer morphology is far from ideal and losses can occur at the interface between the donor and acceptor materials as well as at the electrodes where charge is extracted.¹ Compared to more traditional devices, organic solar cells exhibit low efficiencies along with limited lifetimes, which have so far limited their application. The importance of degradation and stability on device performance is highlighted by a target of 10 % efficiency combined with a lifetime of 10 years for commercial development.² Device efficiency has been shown to decrease with time, especially under illumination, and this detrimental effect is further accelerated when measurements are performed in ambient conditions.³⁻⁹ Practical devices will require a sustained efficiency with time that are not affected by external factors such as moisture and oxygen. Possible solutions to this problem include more stable photoactive materials,¹⁰ inverse architectures,¹¹ interfacial layers for improved charge extraction,¹² as well as device encapsulation.¹³ In addition, these factors must be considered in the context of low-cost and high-throughput manufacturing. To identify and exploit the most effective architectures requires a fundamental understanding of the loss mechanisms which have so far limited device lifetime and stability. Intensity modulated photocurrent spectroscopy is a particularly powerful technique, which has recently been shown to be an effective method for the investigation of charge transport and carrier recombination in organic solar cells, particularly as it relates to device stability.¹ Using this technique it is possible to separate the contributions of bulk transport from interfacial recombination to better understand the role that each of these processes have on device efficiency.

In the previous chapter it was shown that device aging led to an increase of the interfacial recombination as reflected by an increase in value of the recombination rate constant and an increasing fraction of carriers that were not extracted. Several studies have examined the chemical and physical degradation of the photoactive layer as well as the interfacial contacts where charge is extracted in these devices.^{6,14,15} The conjugated polymer that is used in the photoactive layer is susceptible to photochemical modification in the presence of water and can also undergo a reversible doping in the presence of oxygen while under illumination. These two atmospheric contaminants can also react with the interfacial layer and charge extracting electrodes. All of these effects have been shown to reduce device efficiency as reflected by a reduction in the measured short-circuit current and fill factor. In addition, chemical and physical degradation of the photoactive layer can promote modification of the interface at the charge collecting electrodes, which can be further accelerated for photoactive layers prepared using low PCBM contents.¹⁶ In our previous work we tentatively attributed the site for interfacial recombination to be the P3HT:PCBM internal heterojunction interface or at the Al contact with both P3HT and PCBM domains being in close proximity to the contact. To explore this effect further, and to better understand where interfacial recombination is likely occurring, a series of devices containing varying ratios of P3HT and PCBM were prepared with and without encapsulation. It was found that exclusion of atmospheric contaminants through encapsulation was effective in significantly reducing interfacial recombination, whereas devices that were not encapsulated demonstrated a significant amount of interfacial recombination that was dependent on the photoactive layer composition.

Typically P3HT and PCBM are combined in equal or nearly equal mass ratios as this has been shown to lead to the highest efficiency devices through the formation of an efficient nanoscale phase separated heterojunction, with a percolation network formed by each material throughout the entire active layer that can transport charge to the corresponding electrodes. However, this high mass ratio of PCBM may be undesirable if further improvements in efficiency are to be realized given its small contribution to photocurrent generation while making up half the photoactive layer composition. In this work we

found that comparable efficiencies could be obtained with lower PCBM contents than is typically used. However, higher PCBM containing films showed less of a decrease in efficiency with time suggesting the importance of their high loading ratios on long term stability. Almost all reports of organic solar cells use J-V plots to determine device efficiency. To understand the influence of the photoactive layer composition on efficiency and stability we have varied the P3HT:PCBM mass ratios and studied comparatively the commonly reported steady state J-V curves with their corresponding IMPS spectra. The influence of active layer composition, device aging and short-circuit current density are discussed in relation to the non-steady state results that were obtained using intensity modulated photocurrent spectroscopy and highlight the valuable insights that can be gained from these types of measurements, particularly as it relates to device degradation and stability.

6.2 Experimental

Materials

ITO-coated glass substrates (CEC20S, $\leq 20 \Omega \text{ sq}^{-1}$) from Präzisions Glass & Optik GmbH were cleaned in an ultrasonic bath with, sequentially, detergent deionized water (DI water), acetone and isopropyl alcohol, followed by UV ozone cleaning for 10 minutes. PEDOT:PSS (Bayer Baytron Co.), P3HT (98.5% regioregular from Sigma Aldrich Co.), and PCBM (Solenne BV Co.) were used as received without further purification.

Device fabrication

Bulk heterojunction solar cells were fabricated using an ITO/PEDOT:PSS/P3HT:PCBM/Al architecture. A PEDOT:PSS hole transport layer was spin-coated onto ITO and annealed in an oven at 120°C for 15 minutes prior to spin-coating the P3HT:PCBM photoactive layer. The ratio of the P3HT:PCBM photoactive layer was varied from 1:0.5 to 1:0.8 by varying the mass ratio of P3HT and PCBM dissolved in dichlorobenzene leading to films with a thickness of approximately 120 nm.¹⁷ The total mass of the P3HT and PCBM was always 40 mg mL⁻¹. An aluminum cathode was evaporated on-top of the photoactive layer to complete the cell. The

completed devices were annealed in an inert atmosphere and were not exposed to ambient conditions following fabrication. For some of the cells, a UV curable epoxy resin was used to encapsulate the devices.

Steady-state J-V measurements

Photocurrent measurements were performed using a 20 mW monochromatic 405 nm laser diode (LD1510, Power technology). The range of light intensity used was 3.07×10^{16} to 2.95×10^{17} photons $\text{cm}^{-2}\text{s}^{-1}$, which corresponds to an incident power of 15 mW cm^{-2} to 145 mW cm^{-2} . Steady-state J-V measurements were collected using a PAR 263A potentiostat–galvanostat (Princeton Applied Research) that was controlled using version 3.1 CorrWare software (Scribner Associates Inc.).

Intensity modulated photocurrent measurements

Intensity modulated photocurrent/photovoltage measurements were made using either a PAR 263A potentiostat–galvanostat (Princeton Applied Research) coupled with a Solartron 1250 frequency response analyzer or a stand-alone Solartron 1260 frequency response analyzer. The dc light intensity was varied from 3.07×10^{16} to 2.95×10^{17} photons $\text{s}^{-1} \text{ cm}^{-2}$, while the ac was kept constant at $3.07 \times 10^{16} \text{ s}^{-1} \text{ cm}^{-2}$, which was determined to be small enough to ensure a linear cell response.

6.3 Results

It is well known that device efficiency drops off with time, reflected by a substantial decrease in the short circuit current density and device fill factor; with this process being accelerated by exposure to oxygen and water. To explore this effect we have prepared several series of devices that were either encapsulated or not encapsulated to further understand the relationship between atmospheric contamination and device performance. The J-V plots for both encapsulated and non-encapsulated devices measured using a laser diode are shown in Figures 6-1 and 6-2, and the relevant parameters extracted from these plots are summarized in Table 6-1 along with device efficiencies obtained using an AM 1.5 solar simulator. For the photoactive layer compositions used in this work, device efficiencies in the range of 1.7 – 2.5 % were obtained under AM 1.5 solar simulator

conditions following device fabrication for both encapsulated and non-encapsulated devices. It was found that the lowest PCBM content films (1:0.5) exhibited the lowest efficiencies of 1.7 %, while all other compositions exhibited efficiencies of approximately 2.0 - 2.5%. The lower efficiency observed for the 1:0.5 P3HT:PCBM mass ratio is attributed to the inefficient formation of a percolation network throughout the film. Shortly following solar simulator measurements, devices were again measured using a monochromatic laser diode ($\lambda = 405$ nm) and their efficiencies determined from the corresponding J-V plots. Measurements were made using this light source because it was also used for the IMPS measurements that are discussed further below. Encapsulated devices showed similar efficiencies when measured shortly following fabrication using the monochromatic laser diode. However, non-encapsulated devices showed a substantial reduction in efficiency that was dependent on PCBM content in the films. The efficiency was also found to decrease after further aging in the dark as discussed in more detail below.

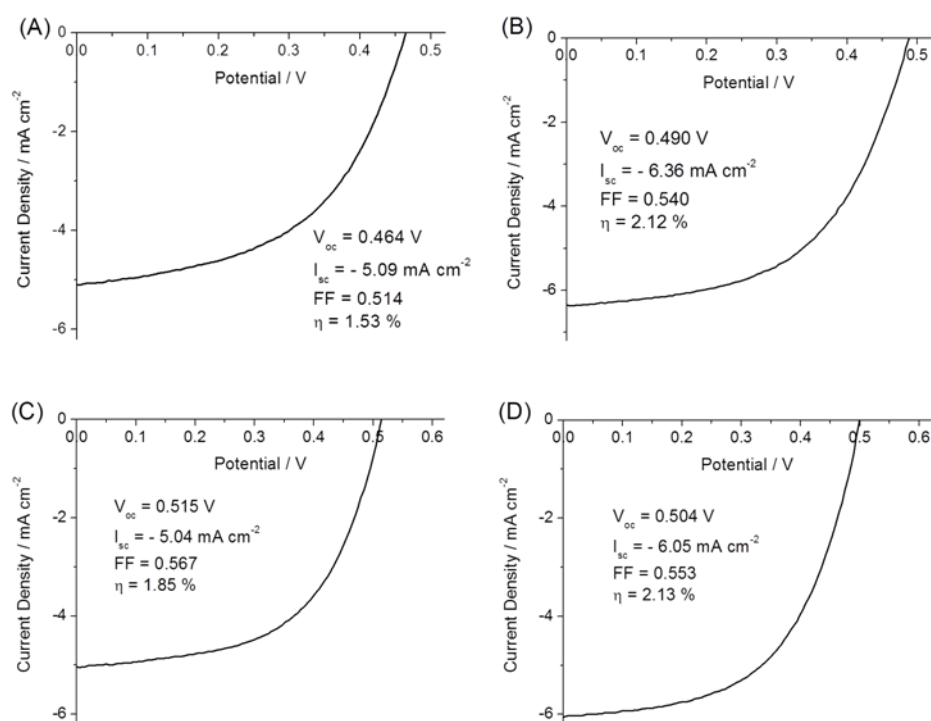


Figure 6-1. J-V plots of encapsulated bulk heterojunction devices containing a P3HT:PCBM mass ratio of (A) 1:0.5, (B) 1:0.6, (C) 1:0.7, and (D) 1:0.8.

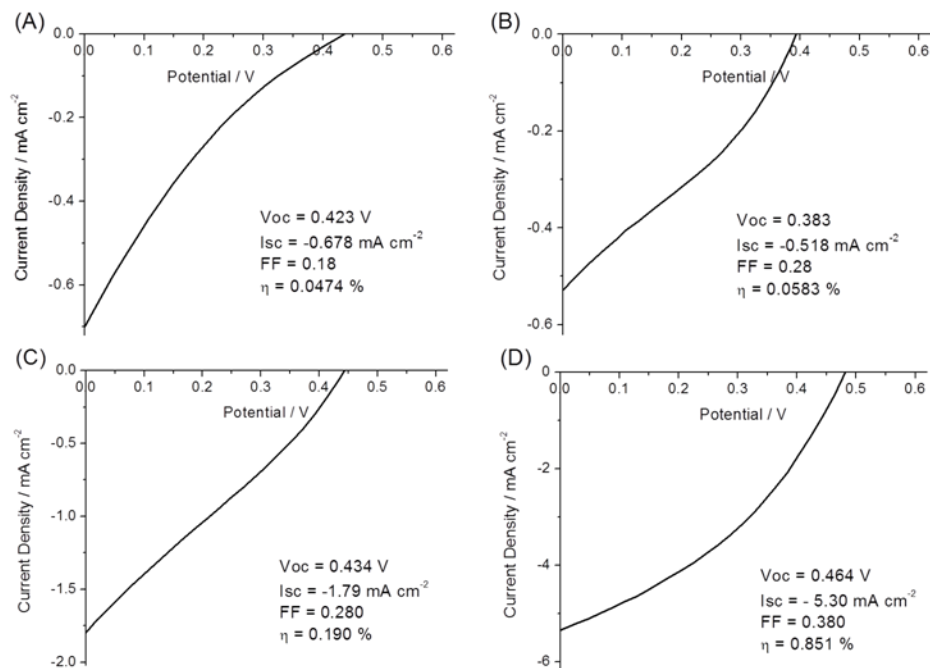


Figure 6-2. J-V plots of non-encapsulated bulk heterojunction devices containing a P3HT:PCBM mass ratio of (A) 1:0.5, (B) 1:0.6, (C) 1:0.7, and (D) 1:0.8.

Table 6-1. Device efficiencies for bulk heterojunction devices measured shortly after fabrication.

P3HT:PCBM	Encapsulated				Non-Encapsulated (fresh)			
	(1:0.5)	(1:0.6)	(1:0.7)	(1:0.8)	(1:0.5)	(1:0.6)	(1:0.7)	(1:0.8)
AM 1.5								
Efficiency / %	1.92	2.25	2.35	2.03	1.73	2.51	2.4	2.46
Fill Factor / %	52.6	54.5	57.8	55.7	47.5	55.2	55.8	59.2
Laser Diode*								
Efficiency / %	1.53	2.12	1.85	2.13	0.0583	0.0474	0.190	0.851
Fill Factor / %	51.4	54.0	56.7	55.3	34.0	18.0	27.8	38.0

*Encapsulated cells were measured using a power of 79.4 mW cm^{-2} . Non-encapsulated cells were measured using a power of 114 mW cm^{-2} .

All solid state devices were continuously stored in a glovebox under nitrogen, however devices that were not encapsulated exhibited a substantial decrease in efficiency when measured using the laser diode compared to those devices that were encapsulated. While efforts were made to limit exposure to atmospheric conditions, it was not possible to completely eliminate their introduction into the transfer vessels during transport and storage, which led to a decrease in device efficiency between measurements made with the AM 1.5 solar simulator and the laser diode. Efficiencies in the range of 1.7 – 2.5 % were observed for the encapsulated and non-encapsulated devices when characterized using an AM 1.5 solar light simulator shortly following their fabrication. However, it can be seen in Figure 6-2 that device efficiency was much lower for non-encapsulated devices when measured using the laser diode, and a trend emerged between the short-circuit current density, fill factor and device efficiency that was dependent on the PCBM content in the photoactive layer. This was in contrast to what was observed for the encapsulated devices, where device efficiency was quite similar for all cells. Upon aging of the non-encapsulated devices in the dark a further decrease in efficiency was observed as shown in the J-V plots of Figure 6-3. The short-circuit current and device efficiency of non-encapsulated cells exhibited a similar dependence on PCBM content following aging and these parameters are summarized in Table 6-2. It has been shown that atmospheric oxygen or moisture, if present, is able to penetrate into the photoactive layer through grain boundaries and pinholes present in the aluminum cathode layer. Studies of aging in the dark have found that oxygen will be found predominantly at the interface between the cathode and the photoactive layer.⁶ Subsequent illumination of the device promotes the diffusion of oxygen throughout the entire photoactive layer. For the non-encapsulated devices, it can be expected that oxygen will be located not only at the cathode/photoactive layer interface but also throughout the entire bulk of the film.

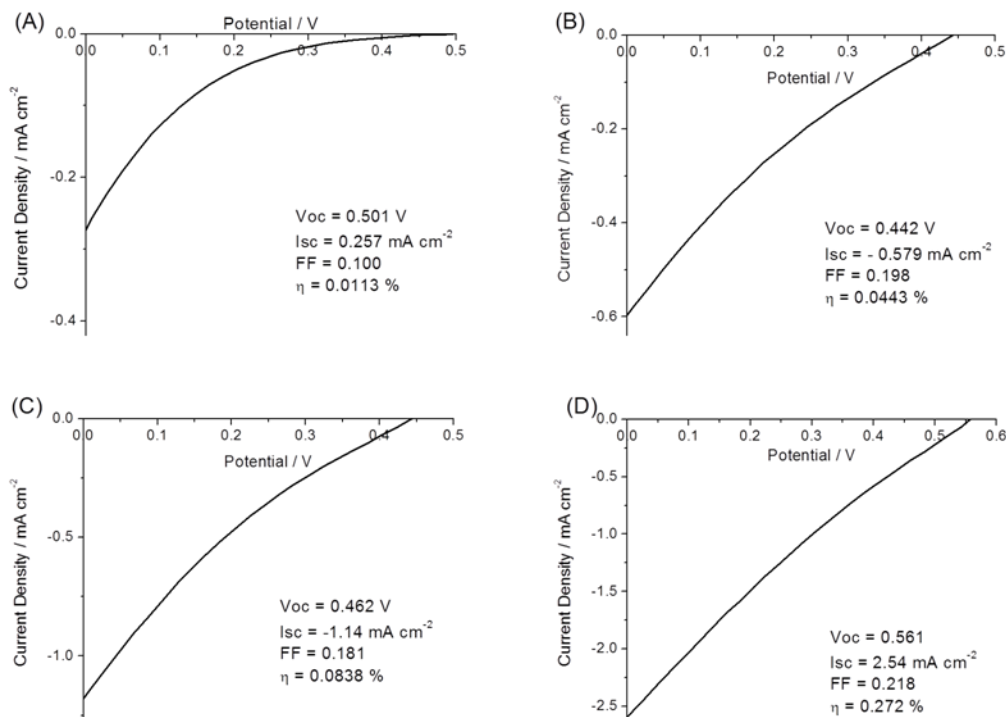


Figure 6-3. J-V plots of aged non-encapsulated bulk heterojunction devices containing a P3HT:PCBM mass ratio of (A) 1:0.5, (B) 1:0.6, (C) 1:0.7, and (D) 1:0.8.

Table 6-2. Device efficiencies for bulk heterojunction devices measured aging.

P3HT:PCBM	Non-encapsulated (aged)			
	(1:0.5)	(1:0.6)	(1:0.7)	(1:0.8)
Laser Diode*				
Efficiency / %	0.0113	0.0443	0.0838	0.273
Fill Factor / %	10.000	19.8	18.1	21.8

As discussed in further detail below, the encapsulated devices did not exhibit any features in quadrant I of the IMPS spectra, which indicates the absence of interfacial recombination due to the effective exclusion of atmospheric contaminants. The non-encapsulated devices showed evidence of interfacial recombination in their IMPS spectra shortly following fabrication and with aging, and will be the primary focus in the remainder of this chapter. The differences observed for the encapsulated and non-

encapsulated devices highlights the role of atmospheric contamination on device efficiency which can be directly attributed to interfacial recombination.

Intensity modulated photocurrent spectroscopy of non-encapsulated devices

Measurements were made using intensity modulated photocurrent spectroscopy to further understand the origin of the differences in the short-circuit current density for fresh and aged non-encapsulated devices. Typical IMPS plots obtained at different dc light intensities are shown in the Nyquist and Bode plot representations in Figure 6-4 for a film composition of 1:0.7 P3HT:PCBM mass ratio. The IMPS plots follow similar trends to those observed in Chapter 5 with increasing dc light intensity. Specifically, the maximum of the imaginary photocurrent shifts to higher frequencies with increasing dc light intensity as shown in Figure 6-4C. The frequency that occurs for the maximum of the imaginary photocurrent corresponds to the pseudo first order rate constant for interfacial recombination and is represented by ω^* similar to Chapter 5. Figure 6-5 shows the frequency corresponding to the maximum of the imaginary photocurrent in quadrant I for all cells as a function of dc light intensity. It can be seen that the recombination rate increases with increasing dc light intensity for all cells, but it does not appear to show a significant variation or dependence on the PCBM content. It is important to point out that

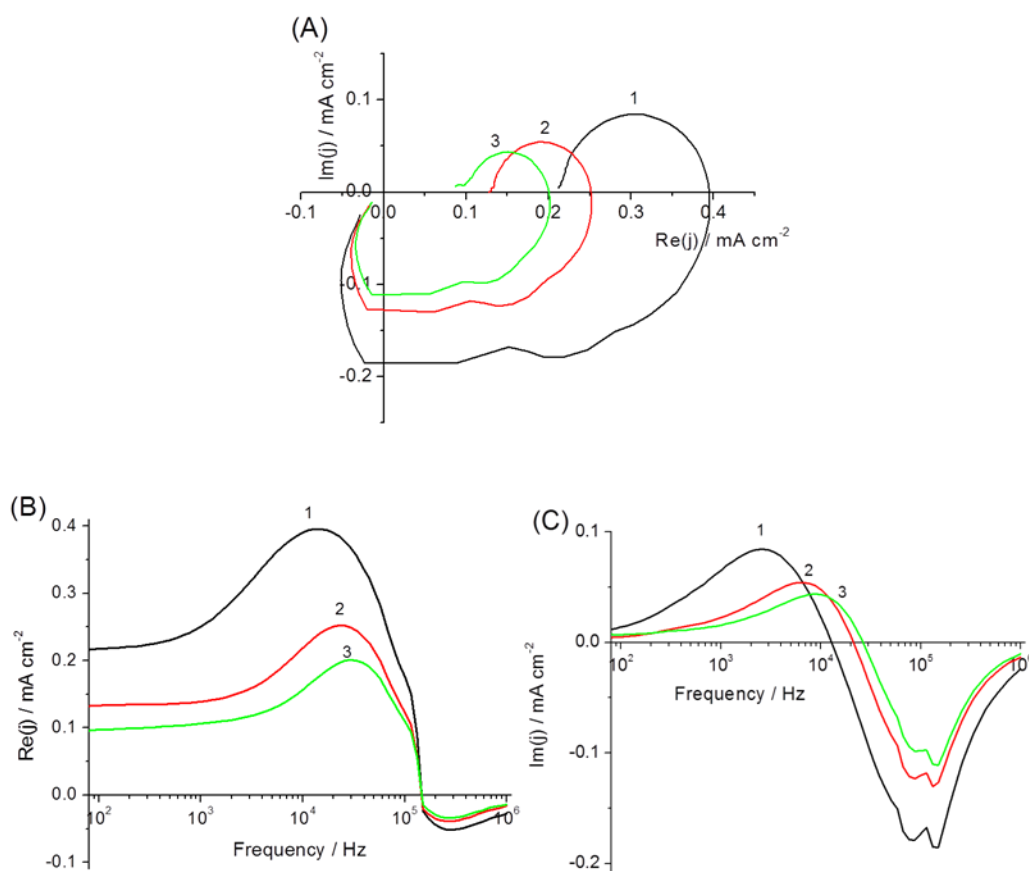


Figure 6-4. Experimental IMPS spectra obtained at short-circuit conditions for a P3HT:PCBM ratio of 1:0.7 in (A) Nyquist and (B,C) Bode plot representation. The *dc* light intensity used was (1) 3.07×10^{16} , (2) 1.62×10^{17} , and (3) $2.95 \times 10^{17} \text{ s}^{-1} \text{ cm}^{-2}$.

the pseudo-first order rate constant ω^* implicitly includes the majority carrier concentration. Therefore, these data suggest that recombination involves not only photogenerated minority carriers but photogenerated majority carriers (holes) as well. These carriers should be located in the p-type P3HT phase. Normally, photogenerated majority carriers are rapidly swept away by the electric field; however, the carrier mobilities in a conjugated organic semiconductor such P3HT could be lower and thus some photogenerated majority carriers may be trapped near the interface and contribute to the recombination with photogenerated electrons. Our data suggest that this is a predominant recombination mechanism since the values of the recombination rate constant under illumination are significantly higher than those in the dark (found as the

extrapolation of the recombination rate to zero light intensity, Fig. 6-5). The independence of ω^* on PCBM content for a given dc light intensity suggests that the rate constant for the interfacial recombination does not depend on the PCBM or P3HT concentration. However, the short-circuit current density does exhibit a dependence on the PCBM content as observed in their steady-state J-V plots, with films containing a greater fraction of PCBM showing higher efficiencies. It could be expected that the recombination rate constant should increase for decreasing PCBM contents if interfacial recombination were occurring at the PCBM/Al interface, which would lead to a dependence of the recombination rate constant on the PCBM content in the active layer and at the interface. This possibility is considered further in the discussion as one of the possible mechanisms for interfacial recombination.

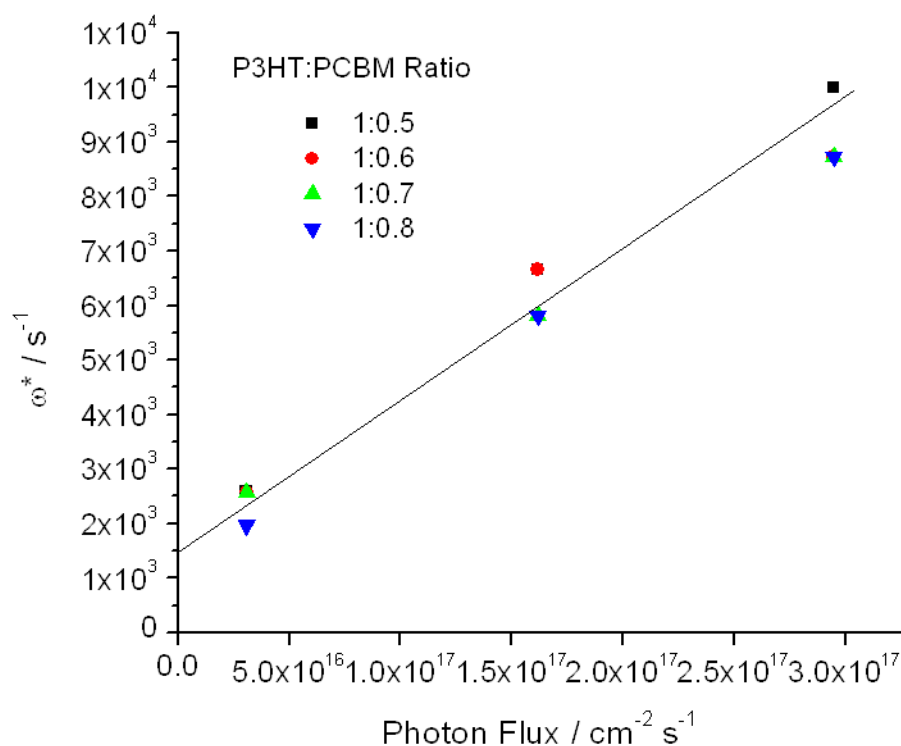


Figure 6-5. The value of the rate constant for recombination ω^* for P3HT:PCBM mass ratios of 1:0.5, 1:0.6, 1:0.7 and 1:0.8 as a function of the *dc* light intensity. The line is not a fit and is a guide for the eyes.

Figure 6-6 shows the IMPS spectra for P3HT:PCBM films with increasing ratios of PCBM content in the photoactive layer. Several trends can be observed in these figures. The Bode plot in Figure 6-6B shows that for increasing PCBM content, the low frequency portion of the real photocurrent is greater in magnitude, which is similar to the trend observed in the steady state J-V plots (Fig. 6-2) above. As well, Figure 6-6C shows that ω^* does not vary significantly with the P3HT:PCBM ratio, which would suggest that an increase in the rate constant for recombination with decreasing PCBM content cannot explain the decrease in device efficiency. The shape of the IMPS spectra (Fig 6A) in the first quadrant shows that higher PCBM content films exhibit a smaller semicircle than lower PCBM content films. This is indicative of reduced recombination in the films, but this is not accompanied by a change in the value of ω^* as observed in Figure 6-6C.

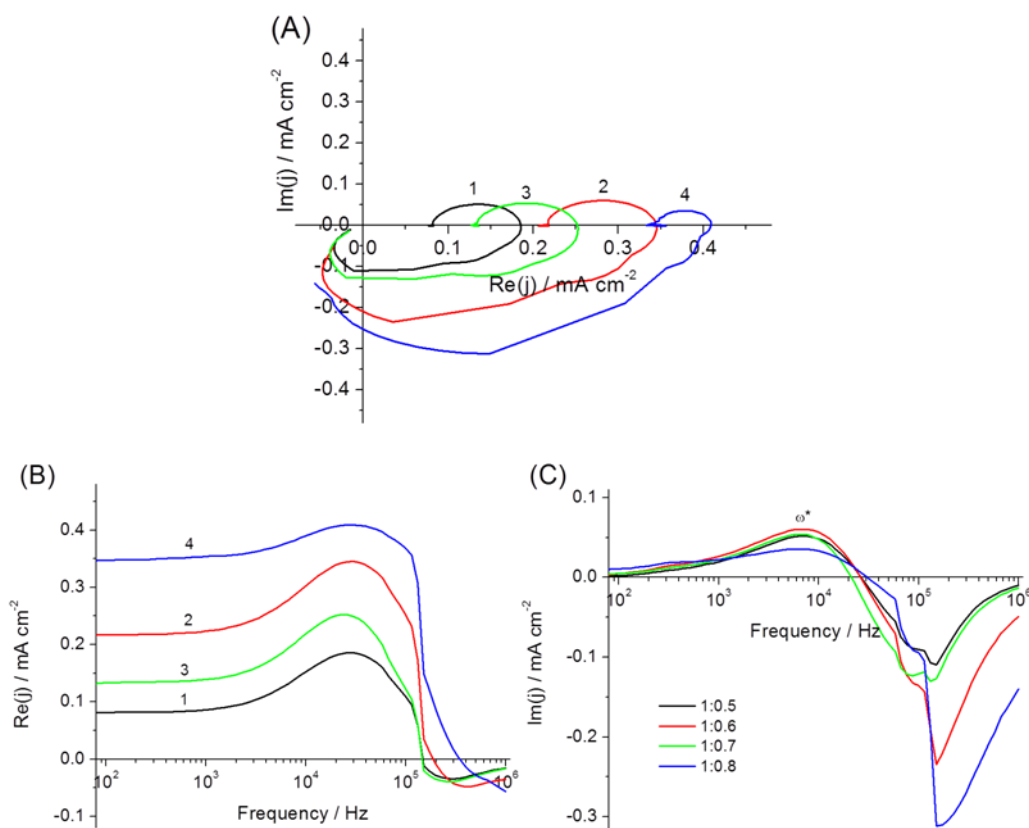


Figure 6-6. Experimental IMPS spectra obtained at short-circuit conditions for P3HT:PCBM ratios of (1) 1:0.5, (2) 1:0.6, (3) 1:0.7, and (4) 1:0.8 in (A) Nyquist and (B,C) Bode plot representation. The dc light intensity for all spectra was $1.62 \times 10^{17} \text{ s}^{-1} \text{ cm}^{-2}$.

Figure 6-7 shows the normalized IMPS spectra for a series of P3HT:PCBM cells at a light intensity of $1.62 \times 10^{17} \text{ s}^{-1} \text{ cm}^{-2}$. Normalizing the data allows a comparison between the size and shape of the spectra, which are due to differences in interfacial recombination. The semicircle in the first quadrant increases in size with decreasing PCBM content, which indicates that an increasing number of charge carriers are being lost to a surface recombination process for lower PCBM containing films. To further understand the role of interfacial recombination it is useful to define three parameters as indicated in Figure 6-7. The three parameters are the (1) high frequency intercept g_{ac} , (2)

the low frequency intercept ReJ_0 , and (3) the frequency corresponding to maximum of the imaginary photocurrent in the first quadrant ω^* .

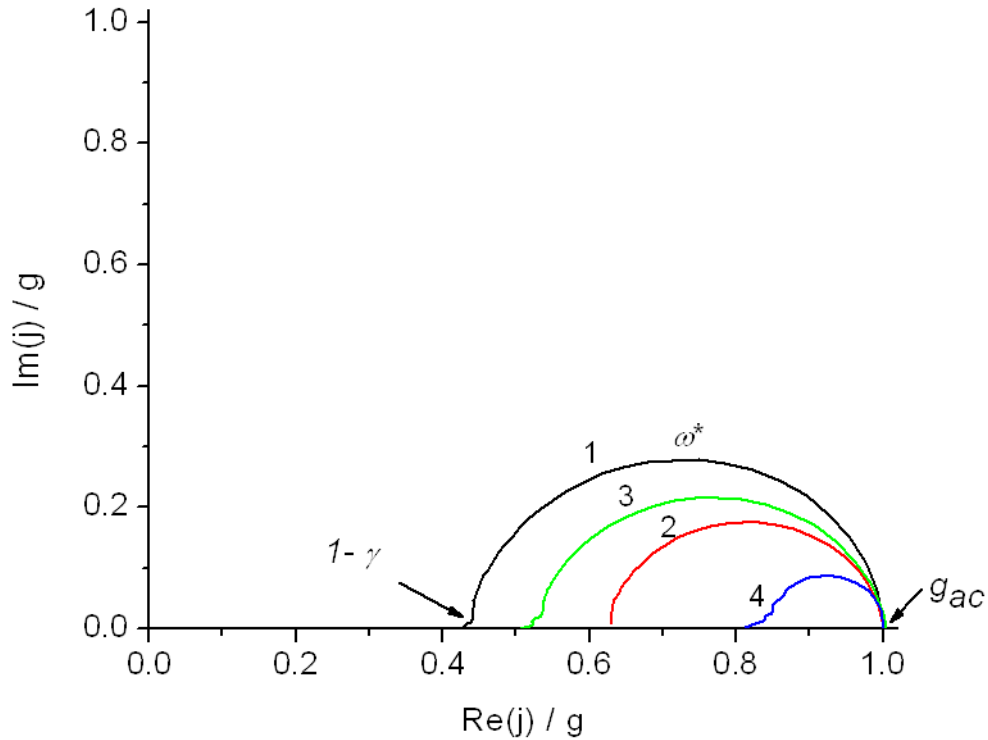


Figure 6-7. Normalized IMPS spectra (from Figure 6-6 (A)) obtained at short-circuit conditions for P3HT:PCBM ratios of (1) 1:0.5, (2) 1:0.6, (3) 1:0.7, and (4) 1:0.8 in Nyquist plot representation. The dc light intensity for all spectra was $1.62 \times 10^{-17} \text{ s}^{-1} \text{ cm}^{-2}$. The high frequency intercept g_{ac} , low frequency intercept $1-\gamma$ and the maximum of the imaginary photocurrent ω^* are indicated .

The high frequency intercept is determined by the point at which the imaginary photocurrent crosses over from quadrant IV to quadrant I and corresponds to the maximum of the real photocurrent. This is indicated in Figure 6-7 as g_{ac} , which is unity in the normalized plots, and represents the maximum attainable photocurrent if no interfacial recombination were occurring. The next parameter is the frequency that corresponds to the maximum for the imaginary photocurrent in quadrant I, indicated by

ω^* in Figure 6-7. The final parameter is the real photocurrent ReJ_0 measured at low frequency and represents the situation where the steady-state photocurrent would be measured. In the normalized plots this is the fraction of charge carriers that are not lost to interfacial recombination and are extracted at the electrode. This is represented by $(I - \gamma)$, where γ denotes the fraction of charge carriers that recombine. A smaller value of $(I - \gamma)$ indicates a greater number of charge carriers have been lost to interfacial recombination. The parameters ReJ_0 , g_{ac} , and $g_{ac}(I - \gamma)$ are related through the following expression:

$$ReJ_0 = g_{ac}(I - \gamma) \quad (1)$$

Which can be arranged in the following form:

$$(I - \gamma) = ReJ_0 / g_{ac} \quad (2)$$

The values of these parameters are given in Table 6-3 along with the experimental values for the low frequency ReJ_0 and high frequency g_{ac} of the photocurrent determined from the IMPS plots.

Table 6-3. Values for the low frequency ReJ_0 , high frequency g_{ac} , and $(I - \gamma)$ determined from the IMPS plots. A dc light intensity of $1.62 \times 10^{17} \text{ s}^{-1} \text{ cm}^{-2}$ was used.

P3HT:PCBM	Fresh				Aged			
	(1:0.5)	(1:0.6)	(1:0.7)	(1:0.8)	(1:0.5)	(1:0.6)	(1:0.7)	(1:0.8)
$g_{ac} / \text{mA cm}^{-2}$	0.186	0.342	0.250	0.408	0.202	0.238	0.262	0.280
$ReJ_0 / \text{mA cm}^{-2}$	0.082	0.218	0.133	0.348	0.011	0.078	0.090	0.141
$1 - \gamma$	0.44	0.63	0.52	0.83	0.06	0.32	0.35	0.50

It is clear from Figure 6-7 and Table 6-3 that that the value $(I - \gamma)$ increases as the amount of PCBM in the film is increased indicating that the contribution of the interfacial recombination increases at low PCBM contents, which is reflected in a lower device efficiency. Therefore, we conclude that while the rate of interfacial recombination per se does not depend significantly on the PCBM content, an increase in the PCBM content reduces the recombination losses by decreasing the fraction of photogenerated carriers trapped at the surface states. This mechanism will be discussed in more detail below.

Furthermore, an increase in the PCBM content increases the generation current g_{ac} thus suggesting an increase in the efficiency of exciton dissociation with the PCBM content or improved bulk transport.

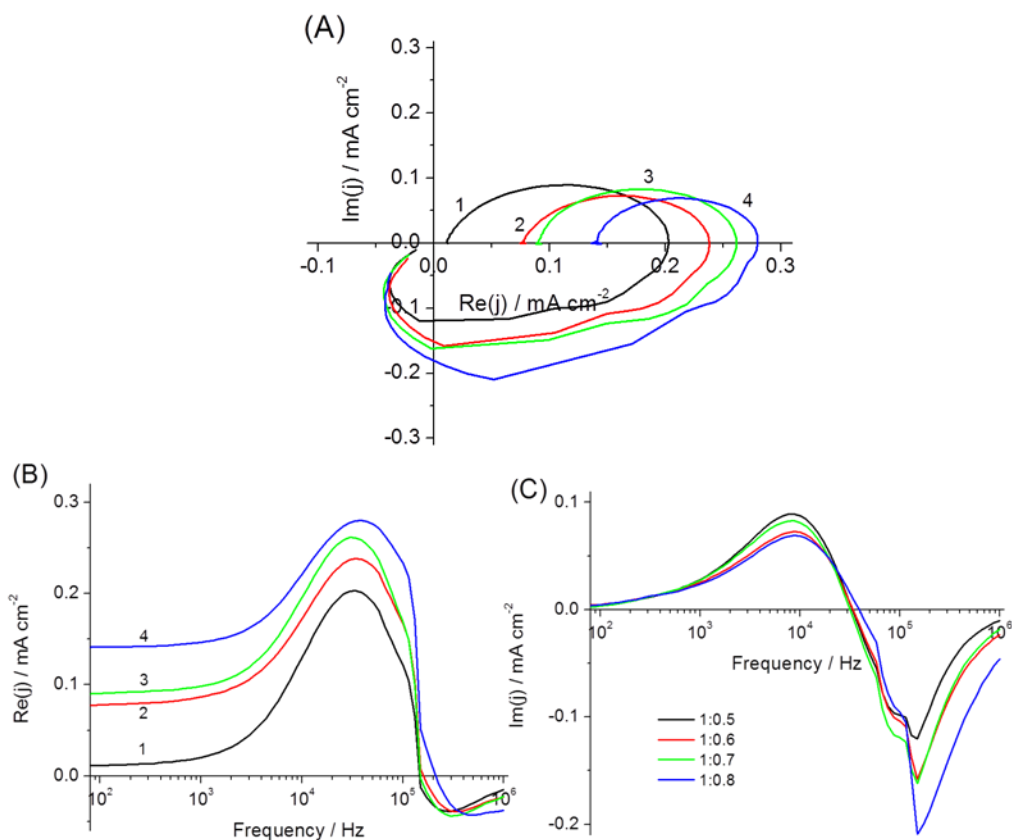


Figure 6-8. Experimental IMPS spectra of aged films obtained at short-circuit conditions for P3HT:PCBM ratios of (1) 1:0.5, (2) 1:0.6, (3) 1:0.7, and (4) 1:0.8 in (A) Nyquist and (B,C) Bode plot representation. The dc light intensity for all spectra was $1.62 \times 10^{-17} \text{ s}^{-1} \text{ cm}^{-2}$.

While encapsulated devices showed little or no surface recombination due to the exclusion of atmospheric contaminants, it was observed that non-encapsulated devices exhibited a pronounced reduction in the short-circuit current density as a result of surface recombination as revealed by the IMPS plots in Figure 6-7. It was shown in Chapter 5 that aging of non-encapsulated devices can lead to an increase in the surface state density in P3HT, which was responsible for surface recombination. Figure 6-8 shows the IMPS

spectra for a series of devices that were measured following aging in a controlled glovebox environment that limited further atmospheric exposure. Figure 6-8B shows that the real component of the photocurrent follows a similar trend to the fresh cells, with the photocurrent decreasing with decreasing PCBM content. As well, the aged cells show a reduction in both their high frequency and low frequency intercept values for the real component of the photocurrent indicating both a reduction in the number of generated charge carriers and their poorer extraction with aging. As shown in Figure 6-8C, the frequency at the maximum in the imaginary photocurrent does not vary significantly with the PCBM content, similar to what was observed for the fresh cells. However, it can also be seen that the frequency at the maximum for the imaginary photocurrent has shifted to a much higher frequency for the aged cells in comparison to the fresh cells. This indicates that aging of the film leads to an increase in the recombination rate similar to what was observed in Chapter 5. However, the recombination rate remains independent of the PCBM content in the film. Figure 6-9 shows the normalized IMPS spectra for the aged cells and it can be seen that the semicircles for the aged cells increase in size with decreasing PCBM content, similar to the fresh cells. However, the semicircle for the aged cells is now much larger than for the fresh cells, indicating a further increase in the fraction of charge carriers that are lost to interfacial recombination.

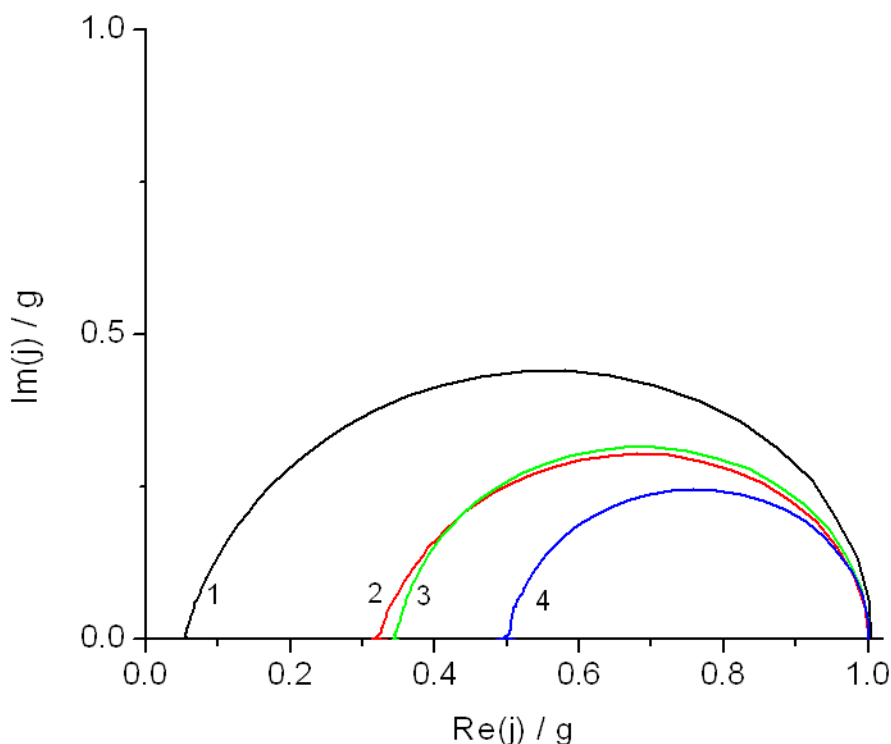


Figure 6-9. Normalized IMPS spectra of aged films obtained at short-circuit conditions for P3HT:PCBM ratios of (1) 1:0.5, (2) 1:0.6, (3) 1:0.7, and (4) 1:0.8 in (A) Nyquist and (B,C) Bode plot representation. The *dc* light intensity for all spectra was $1.62 \times 10^{-17} \text{ s}^{-1} \text{ cm}^{-2}$.

6.4 Discussion

Steady-state measurements

Figure 6-10 shows the short-circuit current density (Fig. 6-10A) and the open-circuit voltage (Fig. 6-10B) for the non-encapsulated devices as a function of the PCBM content measured using the laser diode for cells shortly following fabrication (fresh cells) as well as after aging (aged cells), with the short-circuit current density increasing with the PCBM content for fresh and aged cells. However, aged cells show a decreased value of the short-circuit current density compared to the fresh cells, with the differences becoming more pronounced at higher PCBM contents. Figure 6-10B shows that the open

circuit voltage does not vary significantly with PCBM content and increases slightly for aged cells. The relative independence of the open circuit voltage with PCBM content can be expected as its value is a function of the difference between the LUMO level of the PCBM and HOMO level of P3HT which do not change with variations of the PCBM content. This slight increase in V_{oc} with aging can be attributed to an increased shunt resistance of the film that occurs due to film degradation and explains the slight increase that was observed.⁸

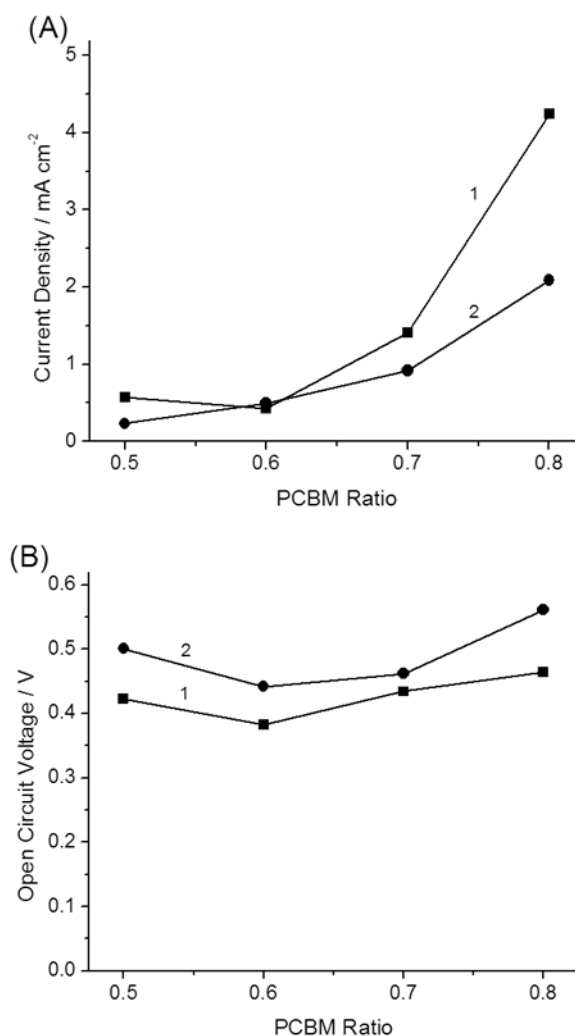


Figure 6-10. (A) Short-circuit current density and (B) open-circuit voltage as a function of PCBM content for (1) fresh cells and (2) aged cells. A light intensity of $1.62 \times 10^{17} \text{ s}^{-1} \text{ cm}^{-2}$ was used.

The increase in the short-circuit current density with PCBM content could be attributed to several factors. It has been shown that increasing the PCBM content in the films limits phase segregation in the composite layer.¹⁹ One possibility could be that phase segregation between P3HT and PCBM is decreased at higher PCBM contents which would ensure a greater interfacial area between the two phases leading to a larger photogeneration in the films. As well, this will ensure the stability of the percolation network. However, encapsulated devices did not exhibit a similar dependence with the PCBM content suggesting that differences in phase segregation or interfacial mixing between the two materials is not the origin of the device efficiency dependence on PCBM content. As well, it has been shown that photogeneration is not the limiting process in device efficiency with aging, which suggests another process is responsible for the reduction in efficiency.¹⁶ Alternatively, as the PCBM mass ratio is increased in the film, the mass of the P3HT is reduced because the total mass ratio is held constant as detailed in the experimental section. This has two important consequences on the resulting film morphology. First, at low PCBM contents, it can be expected that PCBM will be dispersed throughout the film and will not form as efficient a percolation network and this will also not allow for its uniform coverage at the aluminum interface. Deviations from the expected shape for the J-V plots has been shown to be due to poor interface formation between the photoactive layer and the cathode.²⁰ This was also observed in our J-V plots and in fact, it was only for films prepared with the highest PCBM ratio that significant deviations were not observed, reinforcing the importance of PCBM loading on the formation of a stable interface at the cathode. As well, it is known that oxygen is able to dope P3HT and form a charge transfer complex under illumination.¹⁴ As discussed above it can be expected that oxygen is present throughout the bulk of the film and is able to diffuse in through the aluminum cathode of the non-encapsulated devices. Therefore, as the PCBM content in the film is increased, the amount of P3HT that could undergo oxidation by oxygen in the film is decreased and this would help to reduce the overall degradation of the photoactive layer and sites where recombination may occur.

IMPS measurements

To better understand which interface is primarily responsible for the occurrence of the surface recombination, PCBM/Al or P3HT/PCBM, two separate models are used to interpret the IMPS spectra that correspond to different interfaces where recombination could occur. In both models it is important to state that we are discussing the trapping of an electron at an interfacial state. In this case, recombination of photoexcited electrons cannot occur at the interfacial states formed between P3HT and the aluminum cathode, as P3HT is a hole majority carrier with low exciton dissociation efficiency on its own and will have no or very few photogenerated electrons. Therefore, electron recombination from P3HT at the aluminum cathode cannot explain the significant amount of charge that is being generated and collected in our measurements. The two remaining interfaces where interfacial recombination can occur are the P3HT/PCBM interface or the PCBM/Al interface. These two separate cases are illustrated below in Figure 6-11.

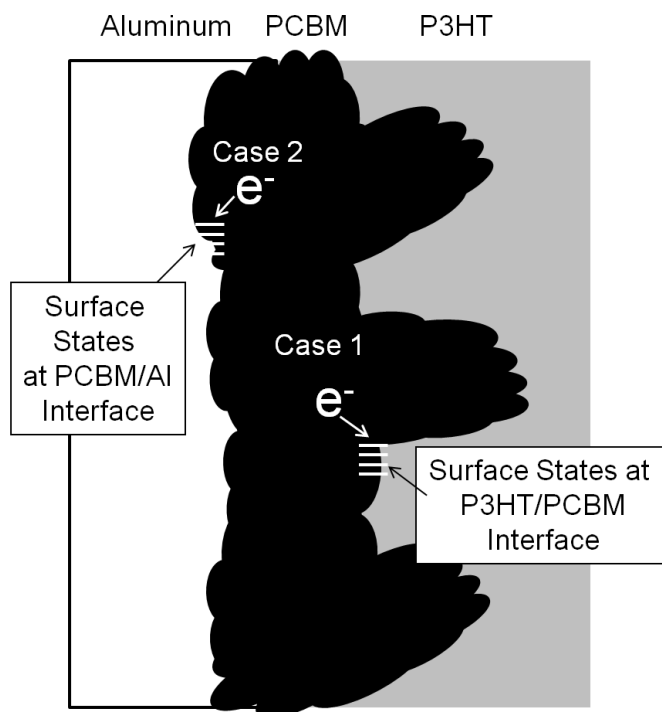


Figure 6-11. Schematic showing the possible interfaces where interfacial recombination may occur in a bulk heterojunction P3HT:PCBM device.

Case 1: No extraction from interfacial states

In case 1, the interfacial states responsible for the recombination are assumed to be located at the P3HT/PCBM interface. Therefore, all charge carriers trapped at the interfacial states recombine and cannot be extracted. In this case, the low frequency intercept of the real component of the photocurrent ReJ_0 , will correspond to carriers that escape trapping at the surface states and are extracted directly at the PCBM/Al interface. The corresponding fraction of carriers that escape trapping and recombination will be equal to $g_{ac}(I - \gamma)$ as described above. Figure 6-12A plots the experimental values for the real photocurrent for the low and high frequency intercepts in quadrant I as a function of the PCBM content for aged cells (data for fresh cells demonstrated similar behavior and are not shown), while Figure 6-12B plots the corresponding values of $I - \gamma$ for both the fresh and the aged cells.

Figure 6-12A presents the values of ReJ_0 and g_{ac} for an aged cell. It can be seen that g_{ac} decreases with decreasing PCBM content indicating that carriers are not being generated as efficiently and/or being lost to bulk recombination as the PCBM content in the film is decreased. This would suggest that some morphological rearrangement does occur with aging that is detrimental to either exciton dissociation or bulk charge transport. However, examination of the value of ReJ_0 in Figure 6-12A shows that its value decreases more rapidly compared to g_{ac} with decreasing PCBM content. The difference in the slope for the values of ReJ_0 compared to g_{ac} demonstrates that losses due to interfacial recombination are greater for low PCBM containing films.

Figure 6-12B plots the value of $I - \gamma$, which represents the fraction of photogenerated charges that are extracted at the electrode. One can see that this value increases significantly with an increase in the PCBM content. This indicates enhanced carrier extraction in the device. At the same time, as was shown above, the pseudo first order rate constant for interfacial recombination did not depend or showed only a slight dependence on the PCBM content in the film. Taken together, these two facts indicate that an increase in the cell efficiency at high PCBM contents is not due to suppression of

interfacial recombination but rather originates from enhanced carrier extraction at the PCBM/Al interface.

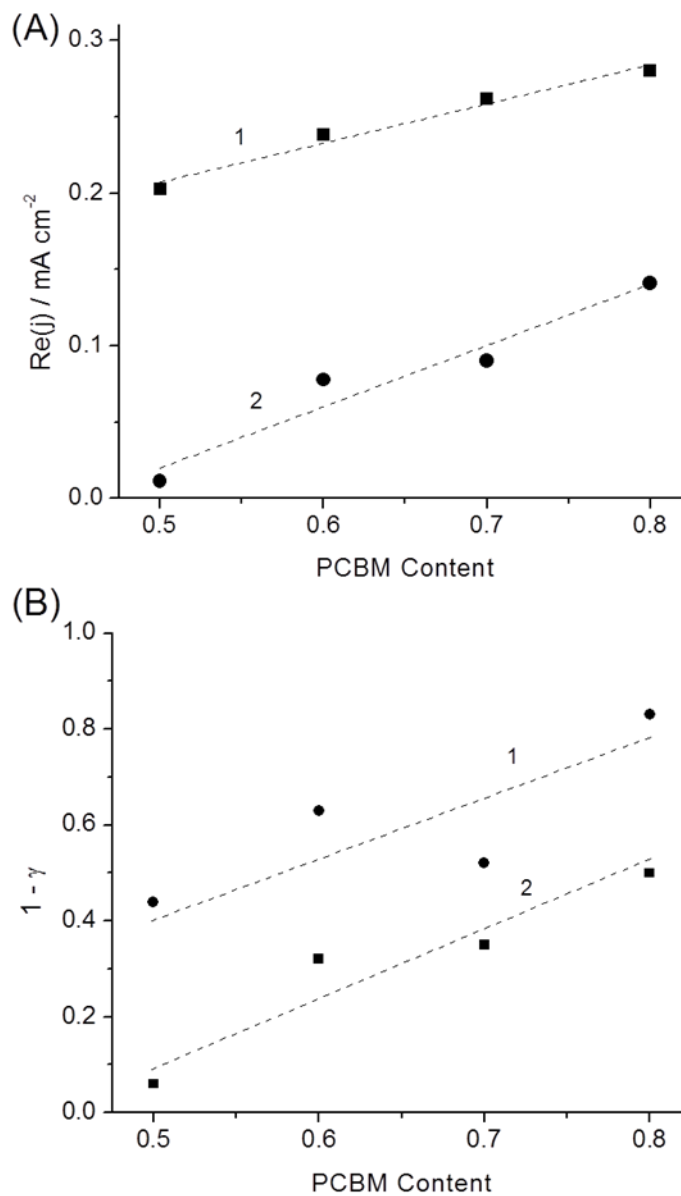


Figure 6-12. (A) Values for the (1) high frequency intercept g_{ac} and the (2) low frequency intercept ReJ_0 for aged cells as a function of PCBM content in the film. (B) Fraction of charge carriers collected as a function of PCBM content for (1) fresh cells and (2) aged cells. A light intensity of $1.62 \times 10^{17} \text{ s}^{-1} \text{ cm}^{-2}$ was used.

This mechanism is further corroborated by the light intensity dependencies of parameters $I - \gamma$ and ω^* . As has been discussed above (see Fig. 6-5), ω^* that represents in this model the pseudo-first order recombination rate constant, increases significantly with the light intensity, whereas $I - \gamma$ was found to be virtually independent of the light intensity. The light intensity dependence of ω^* was attributed to contribution from majority carriers (holes) trapped in the P3HT phase. Therefore, these facts suggest that carrier extraction indeed should occur at the PCBM/Al interface where no contribution from carriers trapped in P3HT could be expected, whereas the recombination should occur at the PCBM/P3HT interface.

The rate of the interfacial recombination increases with aging, which suggests that either further chemical modification of the active layer or morphological changes in the film/at the interfaces are occurring with time. While oxygen can modify the conjugated polymer under illumination, this process does not occur in the dark.¹⁴ These devices were stored in a glovebox in the dark during aging and photochemical modification is not likely in this case. It would seem more likely that aging leads to modification of the bulk heterojunction layer and that this is most pronounced at the cathode interface with the low work function metal. As well, it has also been shown that the presence of atmospheric contaminants accelerates the roughening of the morphology at the interface leading to segregation of the nanoscale domains, with this process most pronounced for films containing lower PCBM contents.¹⁶ Both of these factors can be expected to lead to increased interfacial recombination as was measured here using intensity modulated photocurrent spectroscopy. Taking all of this into consideration for case 1 it can be suggested that interfacial recombination is occurring at the P3HT/PCBM interface, with this process being most significant near the cathode with aging.

Case 2: All carriers are extracted through interfacial states only

In the previous case it was assumed that carriers cannot be extracted once they become trapped at an interfacial site and the charge transfer occurs directly from PCBM to Al without involvement of interfacial states. Case 2 considers the opposite situation that photogenerated charge carriers are extracted through interfacial states only.²¹ In this case

there is a competition between charge carrier recombination and charge carrier transfer from the interfacial state and the interfacial recombination would occur at the PCBM/Al interface where there is the possibility that there would a competition between charge carrier recombination in PCBM or extraction at the aluminum electrode. Therefore, the parameter ω^* will no longer be simply a pseudo first order recombination rate constant and should incorporate two separate components that include a rate constant for charge transfer k_{tr} from the surface states to the Al electrode along with a rate constant for interfacial recombination k_{rec} . The values of these two rate constants can be determined from the experimental IMPS plots by taking the sum of the charge transfer rate constant and the surface recombination rate constant and equating them to ω^* as shown in equation 3:

$$\omega^* = k_{tr} + k_{rec} \quad (3)$$

Where k_{tr} is the rate constant for charge transfer and k_{rec} is the rate constant for surface recombination. Separation of these two components requires the use the value of the low frequency intercept of the real photocurrent, which represents the fraction of electrons that are collected at the electrode and do not recombine. Since case 2 assumes that all carriers are extracted through surface states, this fraction for this model is expressed as:

$$ReJ_0 = (k_{tr} / (k_{tr} + k_{rec}))g_{ac} \quad (4)$$

Using Equations 3 and 4, it is possible to determine k_{tr} from k_{rec} from the experimental values of the high and low frequency intercepts and frequency at the maximum of the imaginary component of the photocurrent for quadrant I.

The corresponding values of k_{tr} from k_{rec} are shown in Table 6-4. However, the analysis of the results for case 2 shows a light intensity dependence not only for the recombination rate constant k_{rec} but also for the rate constant of the charge extraction k_{tr} , which does not have a clear physical meaning. The recombination rate constant could depend on the light intensity through the contribution of the majority carriers trapped in the P3HT phase, as discussed above; however, this should not affect the values of the charge transfer rate constant since majority carriers are not involved in charge extraction that occurs at the

PCBM/Al interface. Therefore, we must conclude that case 2 is not corroborated by the experimental data and therefore the photoprocess in our devices should be described by the mechanism outlined in case 1. Namely, the interfacial states where the charge recombination occurs are located at the P3HT/PCBM and not the PCBM/Al interface; there is no charge extraction through these interfacial states; all charge is extracted directly from PCBM at the PCBM/Al interface.

Table 6-4. Values for the rate constant for charge transfer k_{tr} from the surface states to the Al electrode along with a rate constant for interfacial recombination k_{rec} .

P3HT:PCBM		Non-Encapsulated (fresh)							
		kt				kr			
		(1:0.5)	(1:0.6)	(1:0.7)	(1:0.8)	(1:0.5)	(1:0.6)	(1:0.7)	(1:0.8)
Photon Flux / cm ² s ⁻¹									
	3.07x10 ¹⁶	1073	1521	1382	1923	1508	1060	1199	331
	1.62x10 ¹⁷	3267	4058	3450	6339	4360	2602	3211	1288
	2.95x10 ¹⁷	2298	5752	3683	7505	7702	2981	5051	2495

P3HT:PCBM		Non-Encapsulated (aged)							
		kt				kr			
		(1:0.5)	(1:0.6)	(1:0.7)	(1:0.8)	(1:0.5)	(1:0.6)	(1:0.7)	(1:0.8)
Photon Flux / cm ² s ⁻¹									
	3.07x10 ¹⁶	418	1290	1150	1415	2537	2094	1805	1166
	1.62x10 ¹⁷	491	2846	2943	4228	8243	5887	5790	4505
	2.95x10 ¹⁷	400	3452	2812	5835	11050	9659	8638	7276

The significant amount of charge that is generated but which is not collected at the electrodes as reflected by the value of γ highlights the significant impact that interfacial recombination has on device performance and particularly stability. It is clear from the normalized IMPS spectra that interfacial recombination increases further with aging for all PCBM contents. However, this detrimental process increases for low PCBM concentrations in the film, which highlights the importance of film morphology and composition on stability. It is possible for films with lower PCBM content to exhibit comparable efficiencies to those with a higher PCBM content as was observed for the efficiency measurements made using an AM 1.5 solar simulator. However, a reduction in efficiency was immediately observed due to atmospheric contamination and aging that

depended on the PCBM content. It has been recently shown that addition of a fullerene layer between the photoactive layer and cathode led to more reproducible bulk heterojunction organic photovoltaic devices.²⁰ This increase in reproducibility is due to the formation of a more stable interface being formed between the photoactive layer and cathode material, which limits the morphological rearrangement in the film. It has also been shown that a C₆₀ layer is able to prevent the diffusion of oxygen into the active layer, which would help to reduce degradation and interfacial recombination.⁶ Taken into consideration with our results presented here, we think that such an interfacial C₆₀ layer can also modify the PCBM/Al interface and improve carrier extraction. It could be expected that stable bulk heterojunction films with lower PCBM contents could be prepared if an interfacial layer between the photoactive layer and cathode was incorporated and the morphology did not change significantly. This may be a useful consideration when evaluating alternative acceptor materials to exclude interfacial effects. In addition, this may provide new opportunities to engineer the morphology and composition of the photoactive layer using new materials, if such high loading ratios are not required.

6.5 Conclusions

Bulk heterojunction organic solar cells containing varying amounts of PCBM were investigated using steady-state J-V measurements in combination with the non-steady-state technique intensity modulated photocurrent spectroscopy. It was found that effective encapsulation of the devices could prevent interfacial recombination from occurring. However, for devices that were not encapsulated it was shown that interfacial recombination is a significant process for all PCBM contents. Two different possible mechanisms were considered to identify the site where interfacial recombination was occurring. It was determined that interfacial recombination occurs at the P3HT/PCBM interface and that this process is accelerated for lower PCBM contents. This work highlights the role film morphology and composition has on device stability. These results demonstrate the importance of the active layer/cathode interface and suggest possible areas where intensity modulated photocurrent spectroscopy could be further applied to better understand new interfacial cathode materials to enhance device

efficiency and stability. Photoactive layers that contained the highest PCBM fraction showed the greatest stability with time and exhibited greater charge carrier collection. This highlights the stabilizing effect of PCBM in organic solar cells that is sometimes overlooked when considering alternative acceptor materials. It was found that a greater fraction of generated charge carriers were not extracted for low PCBM content films and that this was a major loss mechanism in these devices. It is quite clear from these results, that a high PCBM content is necessary for the formation of stable bulk heterojunction devices. However, this aspect of PCBM content is not usually considered when discussing their role in organic solar cells. It is clearly demonstrated here that higher PCBM contents enhance device stability by reducing interfacial recombination. This is an extremely important observation as it suggests in one instance an important stabilizing effect of PCBM but also the limitation in its use for further improvements in device efficiency due to its high loading ratio, while contributing a negligible amount towards light absorption and carrier generation. However, the search for alternative acceptor materials should also take into consideration the stabilizing effect provided by PCBM which can help prevent losses due to surface state formation. The fact that the charge transfer through surface states is not possible is very important because it shows that the best way to improve the device efficiency is to suppress the formation of the surface states. Our data also suggest surface state formation is likely to be due to reactions with atmospheric oxygen and moisture, as shown by a significant increase in both ω^* and γ for aged devices. In fact, other systems such as all polymer bulk heterojunction devices exhibit much lower efficiencies and show characteristic decays of interfacial recombination in their photocurrent transients likely due to their increased susceptibility to reaction with atmospheric oxygen and moisture, which could lead to surface state formation in these devices. These results highlight the utility in the use of IMPS for the characterization of various bulk heterojunction systems to assess the role of alternative acceptors and new interfacial materials.

6.5 References

- (1) Byers, J. C.; Ballantyne, S.; Rodionov, K.; Mann, A.; Semenikhin, O. A. *ACS Applied Materials & Interfaces* **2011**, *3*, 392.
- (2) Jorgensen, M.; Norrman, K.; Gevorgyan, S. A.; Tromholt, T.; Andreasen, B.; Krebs, F. C. *Advanced Materials* **2012**, *24*, 580.
- (3) Rosch, R.; Tanenbaum, D. M.; Jorgensen, M.; Seeland, M.; Barenklau, M.; Hermenau, M.; Voroshazi, E.; Lloyd, M. T.; Galagan, Y.; Zimmermann, B.; Wurfel, U.; Hosel, M.; Dam, H. F.; Gevorgyan, S. A.; Kudret, S.; Maes, W.; Lutsen, L.; Vanderzande, D.; Andriessen, R.; Teran-Escobar, G.; Lira-Cantu, M.; Rivaton, A.; Uzunoglu, G. Y.; Germack, D.; Andreasen, B.; Madsen, M. V.; Norrman, K.; Hoppe, H.; Krebs, F. C. *Energy & Environmental Science* **2012**, *5*, 6521.
- (4) Teran-Escobar, G.; Tanenbaum, D. M.; Voroshazi, E.; Hermenau, M.; Norrman, K.; Lloyd, M. T.; Galagan, Y.; Zimmermann, B.; Hosel, M.; Dam, H. F.; Jorgensen, M.; Gevorgyan, S.; Kudret, S.; Maes, W.; Lutsen, L.; Vanderzande, D.; Wurfel, U.; Andriessen, R.; Rosch, R.; Hoppe, H.; Rivaton, A.; Uzunoglu, G. Y.; Germack, D.; Andreasen, B.; Madsen, M. V.; Bundgaard, E.; Krebs, F. C.; Lira-Cantu, M. *Physical Chemistry Chemical Physics* **2012**, *14*, 11824.
- (5) Norrman, K.; Krebs, F. C. *Solar Energy Materials and Solar Cells* **2006**, *90*, 213.
- (6) Norrman, K.; Larsen, N. B.; Krebs, F. C. *Solar Energy Materials and Solar Cells* **2006**, *90*, 2793.
- (7) Norrman, K.; Gevorgyan, S. A.; Krebs, F. C. *Acs Applied Materials & Interfaces* **2009**, *1*, 102.
- (8) Jorgensen, M.; Norrman, K.; Krebs, F. C. *Solar Energy Materials and Solar Cells* **2008**, *92*, 686.
- (9) Krebs, F. C.; Norrman, K. *Progress in Photovoltaics* **2007**, *15*, 697.
- (10) Petersen, M. H.; Gevorgyan, S. A.; Krebs, F. C. *Macromolecules* **2008**, *41*, 8986.
- (11) Zimmermann, B.; Wurfel, U.; Niggemann, M. *Solar Energy Materials and Solar Cells* **2009**, *93*, 491.

- (12) Steim, R.; Kogler, F. R.; Brabec, C. J. *Journal of Materials Chemistry* **2010**, *20*, 2499.
- (13) Krebs, F. C. *Solar Energy Materials and Solar Cells* **2006**, *90*, 3633.
- (14) Seemann, A.; Sauermann, T.; Lungenschmied, C.; Armbruster, O.; Bauer, S.; Egelhaaf, H. J.; Hauch, J. *Solar Energy* **2011**, *85*, 1238.
- (15) Schafferhans, J.; Baumann, A.; Wagenpohl, A.; Deibel, C.; Dyakonov, V. *Organic Electronics* **2010**, *11*, 1693.
- (16) Manceau, M.; Rivaton, A.; Gardette, J. L.; Guillerez, S.; Lemaitre, N. *Solar Energy Materials and Solar Cells* **2011**, *95*, 1315.
- (17) Jouane, Y.; Colis, S.; Schmerber, G.; Kern, P.; Dinia, A.; Heiser, T.; Chapuis, Y. A. *Journal of Materials Chemistry* **2011**, *21*, 1953.
- (18) Chirvase, D.; Parisi, J.; Hummelen, J. C.; Dyakonov, V. *Nanotechnology* **2004**, *15*, 1317.
- (19) Zhao, J.; Swinnen, A.; Van Assche, G.; Manca, J.; Vanderzande, D.; Van Mele, B. *Journal of Physical Chemistry B* **2009**, *113*, 1587.
- (20) de Villers, B. T.; Tassone, C. J.; Tolbert, S. H.; Schwartz, B. J. *Journal of Physical Chemistry C* **2009**, *113*, 18978.
- (21) Peter, L. M.; Wijayantha, K. G. U.; Tahir, A. A. *Faraday Discussions* **2012**, *155*, 309.

Chapter 7

7 Conclusions

7.1 Conclusions

In this work it was shown that vacuum sputtering of carbon in a nitrogen plasma can be used as a method to prepare photovoltaic carbon nitride (CN_x) materials. The electronic properties were found to depend significantly on the formation of a graphitic percolation network across the bulk of the film. Higher nitrogen containing plasmas showed increased the nitrogen content in the carbon nitride thin films as shown using X-ray photoelectron spectroscopy (XPS). Higher nitrogen containing films exhibited a reduced film conductivity as demonstrated using current-voltage measurements and impedance spectroscopy (IS). Further studies of the deposition process showed that nitrogen rich CN_x films prepared in a pure nitrogen discharge plasma at elevated pressures showed reproducible photoconductive and photovoltaic properties. XPS measurements showed that a significant amount of nitrogen was incorporated into the films under these conditions reaching approximately 40%. As well, XPS showed that nitrogen was incorporated into a graphitic carbon nitride network, which is a known n-type doping configuration for this material. Post-deposition modification through thermal annealing generated CN_x films that exhibited a photovoltaic effect, with the minority carriers being positively charged holes, which further supports the formation of an n-type material. Impedance spectroscopy showed that a further reduction in film conductivity occurred upon thermal annealing, while XPS showed that the amount of nitrogen in the film did not significantly change, which indicates that structural or morphological rearrangement of the film was also occurring.

The photocurrent generation in composite carbon nitride/conjugated polymer composite films was reported for the first time both in solution and in solid state devices. While the majority of deposition conditions used did not generate carbon nitride films that showed reproducible photovoltaic properties, it was demonstrated using current-sensing atomic force microscopy and cyclic voltammetry that direct deposition of CN_x onto the conjugated polymer polybithiophene formed a donor-acceptor composite heterojunction. These composite films exhibited enhanced photocurrent generation, with high nitrogen content films exhibiting external quantum efficiencies of 1% when measured in solution.

A series of solid state prototype devices were prepared to compare the photovoltaic response of single layer CN_x or poly(3-hexylthiophene) (P3HT) devices with a P3HT/CN_x heterojunction device. Photocurrent transients showed that single layer CN_x devices exhibited a stable response with time, whereas single layer P3HT transients decayed with time showing characteristic features of interfacial recombination. The CN_x/P3HT heterojunction device exhibited enhanced photocurrent generation relative to the single layer devices that was stable with time, highlighting the potential of carbon nitride photovoltaic devices.

In addition to exploring new materials for photovoltaic devices, this thesis investigated the use of the frequency resolved measurements intensity modulated photocurrent/photovoltage spectroscopy (IMPS/IMVS) to study charge carrier transport and recombination in organic solar cells. While these methods have been applied to other nanostructured devices such as dye sensitized solar cells, their application in bulk heterojunction organic solar cells had not been reported prior to the start of this thesis. Device service life and stability represent one of the limiting factors in the development of new photovoltaic technologies and it is important to develop and apply new methods that can study these devices under normal working conditions. This is particularly true for bulk heterojunction organic solar cells whose composite high surface area active layer forms many interfaces in the bulk and at the electrodes where recombination can occur, which reduces device efficiency, especially with aging.

IMPS and IMVS measurements were used to study bulk heterojunction organic solar cells using the prototypical photoactive layer materials P3HT and PCBM (phenyl C₆₁-butyric acid methyl ester). These measurements allowed us to separate the contribution of the bulk and interfacial processes and provided direct evidence that non-geminate recombination through interfacial states represents a significant loss mechanism in these devices especially with aging. The interfacial recombination was shown to have a light intensity dependence which was due to the trapping of photogenerated holes in the P3HT phase at the interface with PCBM or Al. The exposure to atmospheric oxygen and moisture with aging increased the rate of interfacial recombination, which became a dominant factor in limiting the steady-state device efficiency.

To better identify the interface where recombination was most likely occurring, a series of photoactive layers containing varying ratios of P3HT:PCBM were studied using IMPS. Encapsulated and non-encapsulated devices were measured and it was found that interfacial recombination did not occur for the encapsulated devices. This provided direct evidence that atmospheric oxygen and moisture were responsible for the creation of surface states in these devices, which led to interfacial recombination in the non-encapsulated devices. Steady-state current-voltage measurements showed that device efficiency increased with increasing PCBM contents in the film due to improved carrier extraction as was shown using IMPS measurements. The P3HT/PCBM interface was identified as the site where recombination was occurring, with surface states located on P3HT being responsible for the interfacial recombination.

7.2 Future Work

The work presented here demonstrates the potential of CN_x as a new type of photovoltaic material for solar cell applications. Thin films of these materials are resilient, chemically stable and can be conducting or semi-conducting depending on the deposition conditions used in their preparation. Thermal annealing was found to promote a photovoltaic effect that was accompanied by structural or morphological changes in these films. More detailed studies of the local structure using scanning probe techniques such as atomic force microscopy as a function annealing would be very useful to better understand how the film structure or morphology may be changing. The observation of a photovoltaic effect in nitrogen rich CN_x films opens the door towards new types of solar cell architectures that are not only limited to conjugated organic polymers. In addition, vacuum sputtering is a conformal deposition technique which allows the direct deposition of CN_x onto high aspect ratio nanostructured substrates, which no longer necessarily need to be an organic material, to develop high surface area heterojunction devices. The use of a substrate that can be annealed at higher temperatures than those used here may allow for further optimization of the CN_x stoichiometry and structure leading to further improvements in its photovoltaic properties.

IMPS was shown to be a valuable technique for the characterization of P3HT:PCBM bulk heterojunction organic solar cells. Future work could involve the application of this

technique to other bulk heterojunction devices such as all polymer solar cells whose photocurrent transients show characteristic signatures of interfacial recombination. Due to the significant reduction in device efficiency with aging, new interfacial materials are increasingly being explored to limit cathode degradation which promotes enhanced device efficiency and stability. IMPS is an ideal technique for evaluating new interfacial materials in bulk heterojunction devices. As was shown in Chapter 4, CNx/P3HT solid state devices exhibit enhanced stability relative to the P3HT only devices which could be further explored using IMPS to examine the role of CNx as a possible interfacial material for organic photovoltaics.

Appendix A: Supporting Information for Chapter 3: Photocurrent Generation in Carbon Nitride and Carbon Nitride Conjugated/Polymer Composites

Thicknesses of vacuum deposited carbon nitride (CN_x) films

The deposition conditions such as the magnetron power, pressure and plasma composition are known to have a considerable effect on the film properties and their thickness.^{1,2} The film thickness is an important parameter that may affect all other film properties. In this work, the film thicknesses were determined from the observation of the cross-section of the samples using scanning electron microscopy (FEG-SEM, Ultra55, Zeiss) images. Figure SI1 shows the effect of the deposition conditions used in this work on the film thickness. It can be seen that the film thickness clearly increases with the magnetron power and the nitrogen content. Although the power dependencies appear to be linear, more work is required to find out the exact type of these dependencies.

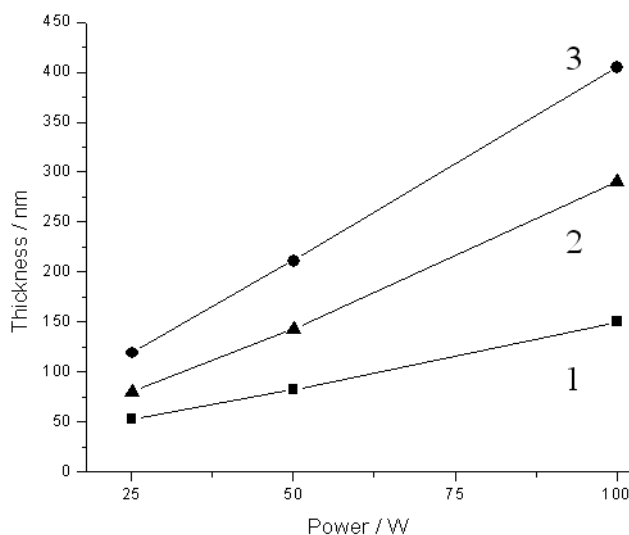


Figure SI2. The thicknesses for CN_x films deposited at various target powers and nitrogen contents of (1) 5% (■), (2) 25% (▲), and (3) 50% (●). The deposition time for all films was 20 minutes. The lines represent a guide for the eye.

Nitrogen content in CN_x films from X-ray photoelectron spectroscopy

Figure SI2 shows the nitrogen content in the film as a function of nitrogen used in the plasma during deposition. The nitrogen content was determined from the atomic ratio of nitrogen and carbon obtained from the XPS survey spectra.

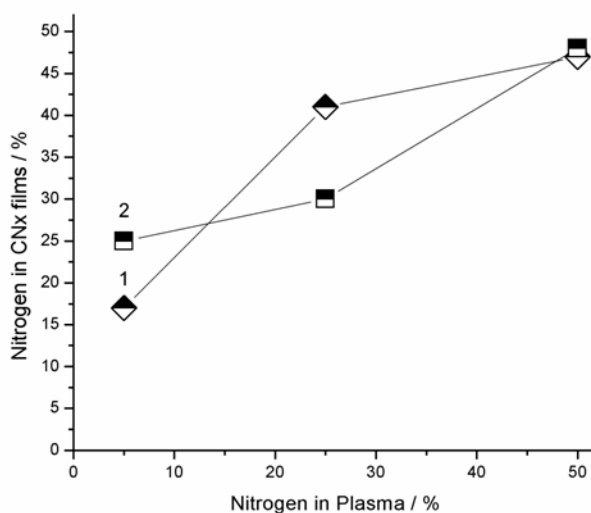


Figure SI2. The nitrogen content in CN_x films as a function of the nitrogen in the plasma used during deposition for target powers of (1) 25 W (Σ) and (2) 50 W (◊). The deposition time for all films was 20 minutes. The lines represent a guide for the eye.

UV-Vis spectra of CN_x and PBT/CN_x films

Figure SI3 shows the UV-Vis spectra of CN_x films as a function of nitrogen content and deposition power. The films were deposited onto an ITO coated glass slide. A correction was made to take into account absorption by the ITO coated glass substrate. Figure SI4 shows the UV-Vis spectra for a PBT/CN_x film as well as individual CN_x and PBT films. It can be seen that the absorption spectrum for the composite film is a superposition of the two individual layers. As well, the PBT absorption peak is still present in the composite indicating its stability during the CN_x sputtering process.

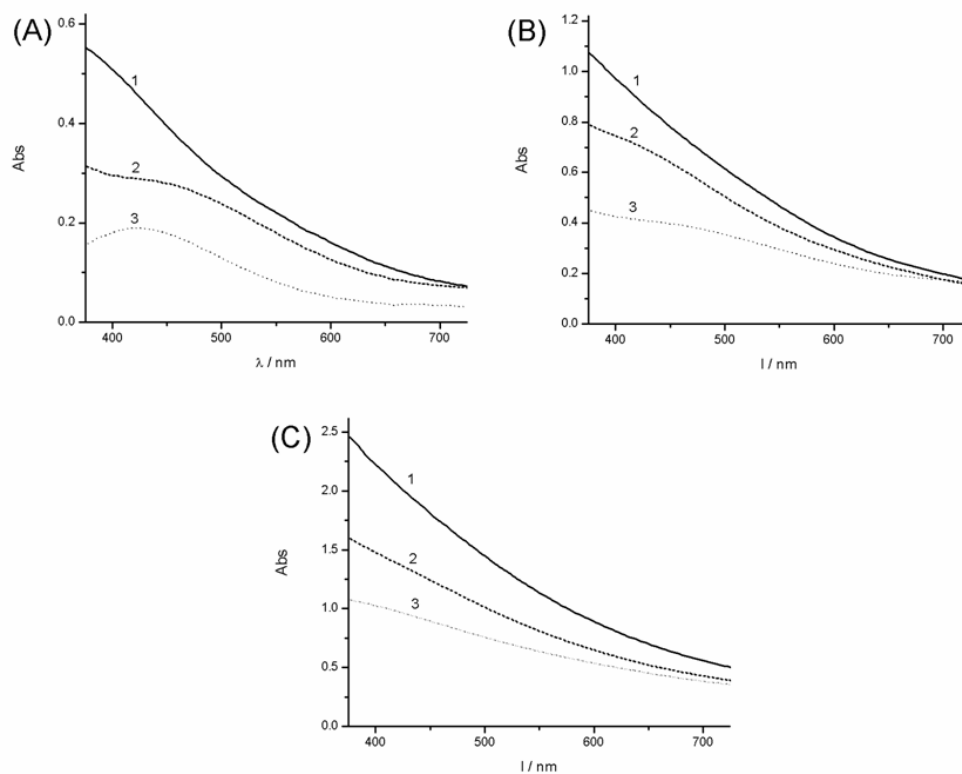


Figure SI3. UV-Vis spectra for CNx films deposited at (A) 25 W, (B) 50 W, and (C) 100 W. In each plot the nitrogen content in the plasma used during deposition was (1) 50 %, (2) 25 %, and (3) 5 %. The deposition time for all films was 20 minutes.

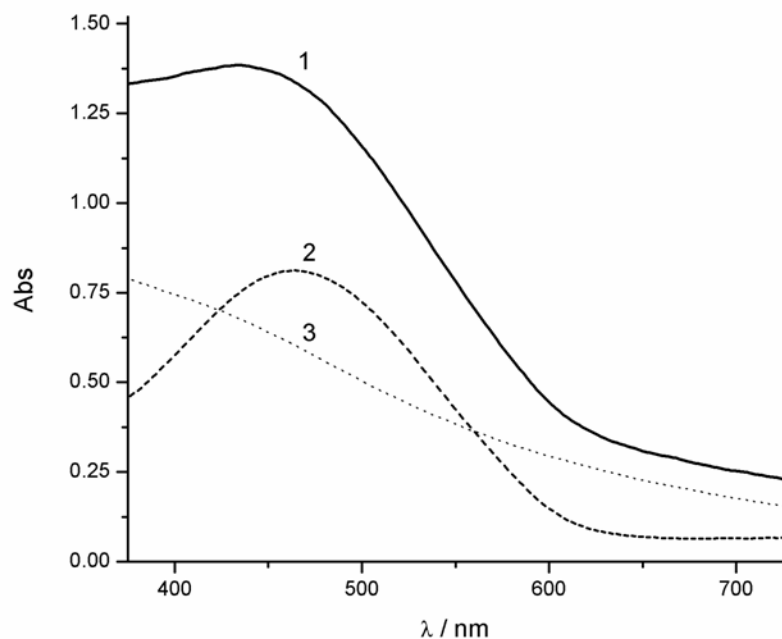


Figure SI4. UV-Vis spectra for (1) PBT/CNx, (2) PBT, and (3) CNx films on ITO coated glass substrates. All CNx films were deposited at 50 W with 25 % N₂ in plasma for 20 minutes.

Absorption Coefficient

The increase in the film thickness with increasing deposition power and nitrogen content in the gas mixture is consistent with the UV-vis transmittance spectra of the films, which showed a decrease in transmission with increasing target power and nitrogen content. Figure SI5 plots the value of the natural logarithm of the transmittance $-\ln(T)$, obtained from the transmittance spectra at 405 nm, as a function of the film thickness. It turned out that all data values studied in this work can be well approximated by a single straight line. Amorphous carbon and sp^2 carbon nitrides exhibit similar broad absorptions over the entire visible light spectrum. As a result, it is not possible to distinguish between the absorption of light due to C=C bonds versus that of C=N bonds. From the slope of this plot we extracted the absorption coefficient α of the carbon nitride films, which was found to be $1.19 \cdot 10^5 \text{ cm}^{-1}$ at 405 nm. This value is consistent with other highly sp^2

hybridized carbon materials and demonstrates the significant fraction of sp^2 bonding of the films investigated in this work.

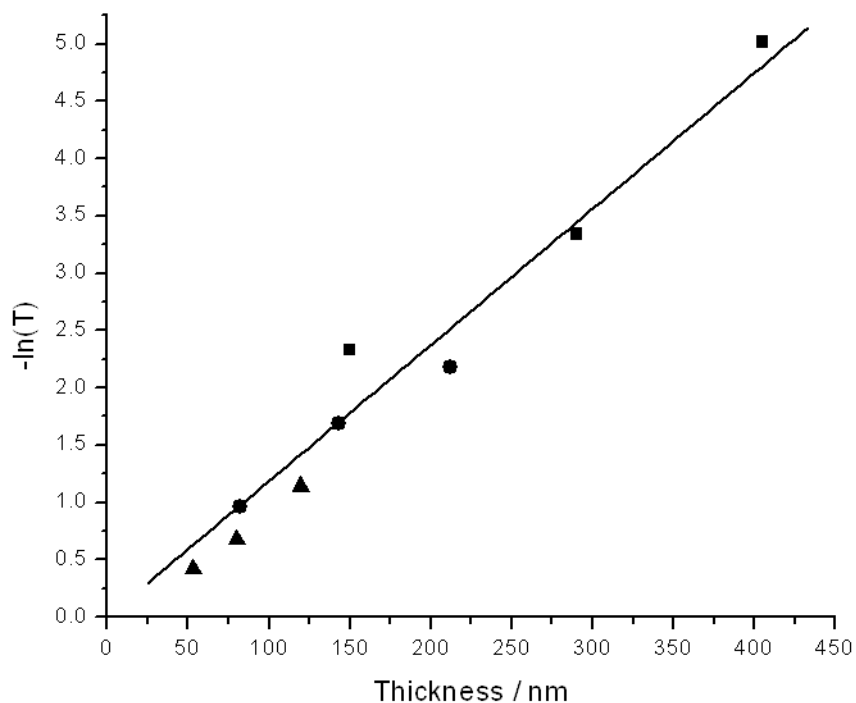


Figure SI5. Plot of $-\ln(T)$ versus film thickness for CNx films deposited at various nitrogen contents and target powers of 25 W (▲), 50 W (●) and 100 W (■). The line represents a linear fit of the experimental data points.

Optical Properties

The optical properties of CNx films have been well documented and two common values used to evaluate these materials are the E_{04} optical gap and E_g which is the Tauc optical band-gap.² A Tauc plot can be used to determine the optical band-gap E_g of an amorphous semiconductor.³ The intercept of a linear fit with the X-axis of the linear portion of a Tauc plot can be used to extract the optical band-gap energy. These plots are obtained by plotting $(\alpha h\nu)^{1/2}$ versus the photon energy $h\nu$ as shown in Figure SI6 (α represents the absorption coefficient, h is Planck constant and ν is the photon frequency).

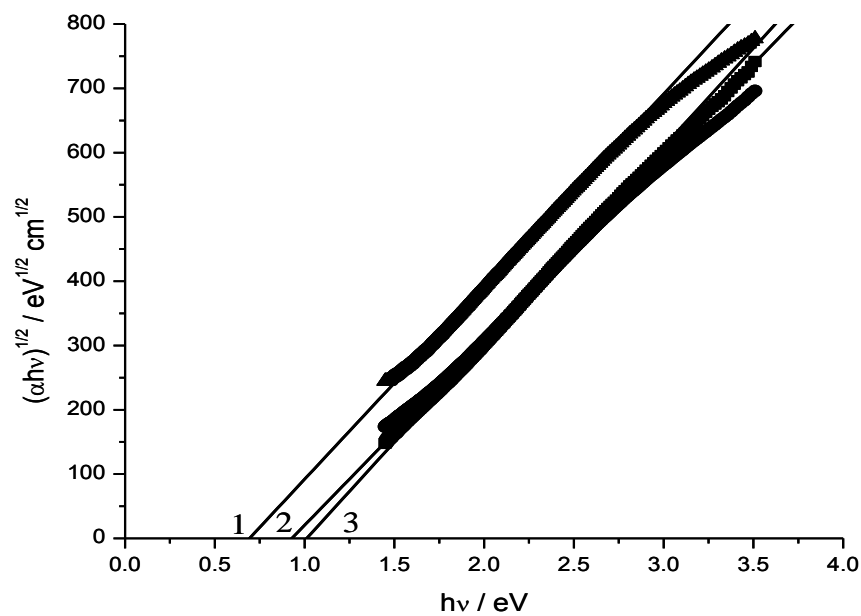


Figure SI6. Tauc plots and linear fit of data for CN_x films prepared at 100 W and (1) 5% N₂, (2) 25% N₂, and (3) 50% N₂.

The E_{04} optical gap represents the onset of the photon energy at which the optical absorption coefficient α is equal to 10^4 cm^{-1} . The results of both measurements are summarized in Table SI1.

Table SII. Values of the optical gap (E_{04}) and Tauc optical gap (E_{Tauc}) for CNx films prepared at 25 W, 50 W, 100 W and nitrogen contents of 5 %, 25 %, and 50 %.

Nitrogen content used during deposition / %	Power					
	25 W		50 W		100 W	
	E_{04} / eV	E_{Tauc} / eV	E_{04} / eV	E_{Tauc} / eV	E_{04} / eV	E_{Tauc} / eV
5	1.3	1.5	0.98	0.78	0.85	0.66
25	1.1	1.26	1.0	0.83	1.0	0.94
50	1.0	1.22	1.1	0.85	1.1	1.01

The Tauc optical band-gap E_g and the optical gap E_{04} exhibit different behavior at low target power (25 W) as compared to higher target powers (50 W and 100 W). For low target power the Tauc optical band-gap is greater than the E_{04} optical gap. This result is expected for films that exhibit larger graphitic clusters and less disorder in the film.² For higher target powers, the Tauc optical band-gap is less than the E_{04} optical gap. This is likely a result of the significant disorder caused by the greater incorporation of nitrogen which is known to cause a distortion of the graphitic planes and their clustering. Taken together with the decrease of the film conductivity with increasing nitrogen contents at 100 W, it can be concluded that the reduction in conducting pathways through the film is a result of the decrease in the graphitic portions of the film.⁴

References

- (1) Zheng, W.; Sjostrom, H.; Ivanov, I.; Xing, K.; Broitman, E.; Salaneck, W.; Greene, J.; Sundgren, J. *Journal of Vacuum Science and Technology A* **1996**, *14*, 2696-2701.
- (2) Lejeune, M.; Durand-Drouhin, O.; Charvet, S.; Grosman, A.; Ortega, C.; Benlahsen, M. *Thin Solid Films* **2003**, *444*, 1-8.
- (3) Tauc, J.; Grigorov, R.; Vancu, A. *Physica Status Solidi* **1966**, *15*, 627-637.
- (4) Dos Santos, M.; Alvarez, F. *Physical Review B* **1998**, *58*, 13918-13924.

Appendix B: Copyright Release from Publisher for Chapter 3**ACS Publications**
High quality. High impact.

Title: Photocurrent Generation in Carbon Nitride and Carbon Nitride/Conjugated Polymer Composites

Author: Joshua C. Byers, Florence Billon, Catherine Debiemme-Chouvy, Claude Deslouis, Alain Pailleret, and Oleg A. Semnikhin

Publication: Applied Materials

Publisher: American Chemical Society

Date: Sep 1, 2012

Copyright © 2012, American Chemical Society

PERMISSION/LICENSE IS GRANTED FOR YOUR ORDER AT NO CHARGE

This type of permission/license, instead of the standard Terms & Conditions, is sent to you because no fee is being charged for your order. Please note the following:

- Permission is granted for your request in both print and electronic formats, and translations.
- If figures and/or tables were requested, they may be adapted or used in part.
- Please print this page for your records and send a copy of it to your publisher/graduate school.
- Appropriate credit for the requested material should be given as follows: "Reprinted (adapted) with permission from (COMPLETE REFERENCE CITATION). Copyright (YEAR) American Chemical Society." Insert appropriate information in place of the capitalized words.
- One-time permission is granted only for the use specified in your request. No additional uses are granted (such as derivative works or other editions). For any other uses, please submit a new request.

Appendix C: Copyright Release from Publisher for Chapter 5

Title: Mechanism of Recombination Losses in Bulk Heterojunction P3HT:PCBM Solar Cells Studied Using Intensity Modulated Photocurrent Spectroscopy

Author: Joshua C. Byers, Scott Ballantyne, Konstantin Rodionov, Alex Mann, and O. A. Semnikhin

Publication: Applied Materials

Publisher: American Chemical Society

Date: Feb 1, 2011

Copyright © 2011, American Chemical Society

PERMISSION/LICENSE IS GRANTED FOR YOUR ORDER AT NO CHARGE

This type of permission/license, instead of the standard Terms & Conditions, is sent to you because no fee is being charged for your order. Please note the following:

- Permission is granted for your request in both print and electronic formats, and translations.
- If figures and/or tables were requested, they may be adapted or used in part.
- Please print this page for your records and send a copy of it to your publisher/graduate school.
- Appropriate credit for the requested material should be given as follows: "Reprinted (adapted) with permission from (COMPLETE REFERENCE CITATION). Copyright (YEAR) American Chemical Society." Insert appropriate information in place of the capitalized words.
- One-time permission is granted only for the use specified in your request. No additional uses are granted (such as derivative works or other editions). For any other uses, please submit a new request.

Curriculum Vitae

Name:	Joshua Byers	
Post-secondary Education and Degrees:	University of Western Ontario London, Ontario, Canada 2009-2013 Ph.D. Physical Chemistry	
	The University of Western Ontario London, Ontario, Canada 2007-2009 M.Sc. Physical Chemistry	
	The University of Western Ontario London, Ontario, Canada 2003-2007 Honors B.Sc. Materials Science	
Honours and Awards:	Ontario Graduate Scholarship	2012 - 2013
	UWO Graduate thesis research award	2012
	Ontario Graduate Scholarship	2011 - 2012
	Curriculum Development Fellowship	2010 - 2011
	France Government Award	2010
	Western Graduate Research Scholarship	2010
	UWO Christian Sivertz Entrance Scholarship	2009
	Graduate Tuition Scholarship in Science	2009
	A Special International Research Experience (ASPIRE) Award	2009
	Graduate Student Teaching Assistants Union Award Nominee	2008 - 2009
	Faculty of Science Graduate Student Teaching Award	2008 - 2009
	Graduate Tuition Scholarship in Science	2007
	Dean's Honour List	2004 - 2007
	UWO Entrance Scholarship	2003

Related Work Experience

Teaching Assistant
The University of Western Ontario
2007-2012

Chemistry 1200B: First Year Chemistry Tutorial	Summer 2012
Chemistry 1200A: First Year Chemistry Tutorial	Summer 2012
Chemistry 3372: Third Year Analytical Chemistry Laboratory	Winter 2012
Curriculum Development: Faculty of Science Fellowship	Fall 2010/ Winter 2011
Chemistry 1050: First Year Chemistry Tutorial	Summer 2010
Chemistry 3372: Third Year Analytical Chemistry Laboratory	Winter 2010
Chemistry 1050: First Year Chemistry Tutorial	2008/ 2009
Chemistry 020, 022, 024: First Year Chemistry Tutorial	Fall 2007/ Winter 2008

Publications:

1. Byers, J.C., Billon, F., Debiemme-Chouvy, C., Deslouis, C. Pailleret, A., Semenikhin, O.A. Photocurrent generation in carbon nitride (CN_x) and carbon nitride/conjugated polymer composites. *ACS Applied Materials & Interfaces*, 2012, 4, 4579–4587.
2. Kantzas, T.K., Byers, J.C., Semenikhin, O.A. Photocurrent Enhancement in Polythiophene-Based Photoelectrodes through Electrochemical Anodic Halogenation. *Journal of the Electrochemical Society*, 2012, 159, H885-H892.
3. Ostrakhovitch, E.A., O'Neil, K.D., Byers, J.C., Semenikhin, O.A. Differentiation of embryonic P19 and neural stem cells into neural lineage on conducting substrates. *Archives of Biochemistry and Biophysics*, 2012, 528, 21–31.
4. Byers, J.C., Ballantyne, S., Rodionov, K., Mann, A. Semenikhin, O.A. The Mechanism of Recombination Losses in Bulk Heterojunction P3HT:PCBM Solar Cells Studied Using Intensity Modulated Photocurrent Spectroscopy. *ACS Applied Materials & Interfaces*, 2011, 3, 392-401.
5. Byers, J.C., Tamiasso-Martinhon, P., Pailleret, A., Deslouis, C., Semenikhin, O.A. Atomic Force Microscopy Studies of Carbon Nitride (CN_x) Films Deposited on a Conducting Polymer Substrate. *Journal of Physical Chemistry C*, 2010, 114, 18474-18480.
6. Byers, J.C., DiCarmine, P.M., Moustafa, M.M.A, Wang, X., Pagenkopf, B.L., Semenikhin, O.A. Electrochemical and Photovoltaic Properties of Electropolymerized Poly(thienylsilole)s. *Journal of Physical Chemistry B*, 2009, 113, 15715-15723.